UNIVERSIDAD NACIONAL AUTÓNOMA DE MEXICO

PROGRAMA DE MAESTRÍA Y DOCTORADO EN CIENCIAS QUÍMICAS

SÍNTESIS MECANOQUÍMICA Y SOLVOTERMAL DE NANOCOMPÓSITOS DE ÓXIDO DE GRAFENO Y GRAFITO CON LANTÁNIDOS

TESIS

PARA OPTAR POR EL GRADO DE

DOCTOR EN CIENCIAS

PRESENTA

M. en C. DIEGO ARMANDO ACEVEDO GUZMAN

DRA. ELENA GOLOVATAYA DZHYMBEEVA
INSTITUTO DE CIENCIAS APLICADAS Y TECNOLOGÍA

DRA. PETRA RUDOLF
ZERNIKE INSTITUTE FOR ADVANCED MATERIALS

Ciudad de México, 2024

UNIVERSIDAD NACIONAL AUTÓNOMA DE MÉXICO

PROGRAMA DE MAESTRÍA Y DOCTORADO EN CIENCIAS QUÍMICAS

Síntesis mecanoquímica y solvotermal de nanocompósitos de óxido de grafeno y grafito con lántanidos

T E S I S
PARA OPTAR POR EL GRADO DE

DOCTOR EN CIENCIAS

P R E S E N T A

M. en C. DIEGO ARMANDO ACEVEDO GUZMÁN

Prof. Dr. Elena Golovataya Dzhymbeeva (E. V. Basiuk)
Instituto de Ciencias Aplicadas y Tecnología, UNAM

Prof. Dr. Petra Rudolf
Zernike Institute for Advanced Materials, University of Groningen

Ciudad de México, 2024.

Comité tutor
Dra. Lioudmila Fomina
Dra. María del Pilar Carreón Castro

Comité evaluador

Presidente	Dra. María del Pilar Carreón Castro
Vocal	Dr. José René Rangel Méndez
Vocal	Dr. Rodolfo Zanella Specia
Vocal	Dr. Roberto Ysaac Sato Berrú
Secretario	Dr. Alfonso Ramón García Márquez

Mechanochemical and Solvothermal Synthesis of Graphene Oxide and Graphite Nanocomposites with Lanthanides

PhD thesis

to obtain the degree of PhD at the
University of Groningen
on the authority of the
Rector Magnificus Prof. J.M.A. Scherpen
and in accordance with
the decision by the College of Deans

and

to obtain the degree of PhD of the
Universidad Nacional Autónoma de México
on the authority of the
Rector Dr. L. Lomelí Vanegas
and in accordance with
the decision of the Assessment Committee of the
Master and Doctoral Program of Chemical Sciences

Double PhD degree

This thesis will be defended in public on
Friday 12 July 2024 at 14:30 hours

by

Diego Armando Acevedo Guzmán
born on 17 June 1994
in Mexico City, Mexico

Supervisors
Prof. E. Golovataya Dzhymbeeva
Prof. P. Rudolf

Assessment committee
Prof. T. Da Ros
Prof. P. J. Deuss
Prof. M. Quintana Ruíz
Prof. E. Rivera García

MECHANOCHEMICAL AND SOLVOTHERMAL SYNTHESIS OF GRAPHENE OXIDE AND GRAPHITE NANOCOMPOSITES WITH LANTHANIDES

M.Sc. Diego Armando Acevedo Guzmán
PhD thesis
Universidad Nacional Autónoma de México
University of Groningen

Acknowledgements

I would like to thank my two supervisors, prof. Dr. Elena Golovataya Dzhymbeeva and prof. Dr. Petra Rudolf, as well as prof. Dr. Vladimir Basiuk, none of these would have been possible without you.

This path started a long time ago, **Elena**. I remember the first time I went to your lab, there was a group meeting and you practically received me with pizza, since that day I knew that everything would be awesome. All your kindness, support and guidance through these years have been of great importance in my development as a researcher and person, thanks to you I have come this far.

Petra, thank you for giving me the opportunity to join and finish my PhD project in your group. Your guidance, suggestions and advice are invaluable. Moreover, always your positive energy and enthusiasm have been encouraging. It has been a wonderful experience.

All this began with you **Vladimir** when I expressed my intentions to join the group, we talked and you said yes, that I could work simultaneously with you and Elena. All your guidance and support have helped me a lot in my career as a researcher.

Prof. Dr. **Lioudmila Fomina** and prof. Dr. **Pilar Carreón Castro**, having you on my Tutor Committee has been a pleasure. I will always be grateful for all your comments, feedback, and support during these four years and double-degree journey.

Thanks, Dr. **Victor Meza** for your support with the SEM measurements, thanks, Dra. **Selene Islas** for your technical support with the FTIR and Raman measurements and all your advice, kind words and good chatting, you have known me since I was a

young bachelor's student. Thanks, **Lázaro Huerta** for your time and support with the XPS characterisation during my time in Mexico, you always invited me to your lectures and laboratory to learn more about the XPS technique.

I also would like to thank the people who provide administrative and technical support at RUG. **Hilda Riemens**, thanks for your excellent management of the group administration. Thank you, Dr. **Dominic Gerlach**, for your support and help with the XPS equipment, lab issues, and all the nice stories you have. Thank you, Dr. **Mihaela Enache**, for always smiling at the Mexican duo in the kitchen and corridors. Thanks to Ing. **Jacob Baas** for your help and training for the XRD equipment. Thank you Dr. **Václav Ocelik**, for the training and willing to help me during the SEM and STEM measurements. Thank you, Dr. **Gert ten Brink**, for all your support, all your help, all your words, all the knowledge and all the enthusiasm that you have shared with me.

Thanks to the assessment committee in Groningen prof. **T. Da Ros**, prof. **P. J. Deuss**, prof. **M. Quintana Ruíz**, and prof. **E. Rivera García**, as well as my committee in Mexico Dr. **Pilar Carreón Castro**, Dr. **José René Rangel Méndez**, Dr. **Rodolfo Zanella Specia**, Dr. **Roberto Ysaac Sato Berrú** and Dr. **Alfonso Ramón García Márquez**, all your comments have enriched this dissertation.

Now, it is fair to give a warning for high levels of corniness, so keep reading at your own risk…

Aaron, what can I say that people do not know already? Although we both know that the constant presence in each other´s lives delayed the process of finishing our thesis, we have had the best moments because we know that *el chismesito da vida*. Fruit of the unexpected compatibility between us, we have created uncountable memories during all lunch times, morning coffee breaks, morning tea breaks, afternoon coffee breaks, afternoon tea breaks, parties, gatherings, trips, and concerts, *pero ya no hay que vernos tan seguido*. Thanks for everything, my friend.

Martina, I never imagined I would meet someone so smart, wonderful, awesome, amazing, nice, special, intelligent, gorgeous, kind, and talented as you (I am afraid there are not enough incredible adjectives to describe you, languages are limited), also, the best housemate anyone could ask for. I can still remember the first time I saw you and the first time you joined a group meeting because I felt so fortunate to live and work in the same place. Despite the distance, baking reminds me of you, I hope I will be as good as you one day. Thank you for sharing your thoughts and your soul. Thank you for including me in your life even knowing that I like pineapple on pizza. Also, thank you

for opening your heart to me and accompanying me during this journey, you touched my heart and changed my life.

Carito, you volunteered to receive and guide me in Zernike after I arrived, and now look at us, I am delighted to have you as my paranymph. Thank you for everything, all the moments, for always saying what you think and for your friendship. Thanks for joining the breaks and lunch times, of course, you were one of my favourite housemates. I admire all the passion you live with, thank you for putting up with my *dark* humour and laughing at my jokes.

Giovanna, you made me feel so happy when you accepted to be my paranymph. You have always been so nice and kind, I am more than grateful, and I would like to add that you have one of the sweetest smiles I have ever seen. Thank you for sharing the treats you baked, everything was delicious. Also, it is so cool we have similar types of humour, I admire you as a person and scientist.

Alida, I am so thankful you accepted to be my paranymph as well, it is a great honour for me. I remember the first time I saw you because I was presenting at one of the group meetings and you were the first person who raised a hand and started asking questions, I have admired you since that moment. Also, thank you for your willingness to try the things I baked and for sharing your honest feedback, it was priceless. Thank you for sharing the delicious things you baked.

Now is the turn to thank the people from the Surface and Thin Films group. What are you doing here **Aaron**? This is not your group! **Lina,** you initiated everything, thank you so much for your warm welcome and support when I arrived in Groningen, and for all the gossip at home and work. *A la morra que se llama* **Dinorah,** thanks for all the laughs, this time would not have been the same without your unpredictable and sometimes inexplicable experiences. Thank you for everything **Yindi**, I am glad we could share many moments inside and outside the lab. Thank you, **Xiaojing**, for being such a nice person, it was a pleasure that we could be officemates during my last months in this group. **Melina, Yaoting, Franziska, Mohammed, Roberto, Diego I, Xiaolong, Baoxin, Amara, Hamoon, Feng, Kaleem**, all these two years have been an awesome experience, the group meetings, working with you in the lab, measuring XPS or even just meeting you in the corridors to chat, thanks for everything. Thank you **Diego III** and **Sanchari**, it was great that you could join the group even if only for a couple of months, you are amazing. **Antonija**, since the first moment, since my first presentation in the group meetings you supported me and showed me kindness, I will be eternally grateful for that, thank you for all your words and for being so inspiring, I

hope you enjoyed my little baking experiments.

Thanks to my officemates, you made me feel our office was the nicest. **Wenbo** thanks for your friendship, your honesty, the good and aimless chatting, all the movies and anime, for changing my name, but especially for inviting me to attend your wedding in China, it was an unforgettable trip, you are the best, even though I am still waiting for my green noodles. Thank you, **Koen,** for all the interesting conversations in the office and your kindness, Fridays were awesome days because of you. Thank you, **Dan,** for all your cheerfulness, you always have the best attitude. *Muchas gracias* **Douwe** for your contribution to the office environment, it was awesome that you joined the group, I enjoyed working together in the XPS, and I am glad you were not assigned to the office for masters' students but to ours. **Veronika**, you were the last to join such an amazing office, thank you for being so friendly. Thank you, **Adam**, you were the best officemate. *Claro que sí* **Joris,** it was awesome that we could travel together to China and get to know each other better, thank you.

Groningen is a beautiful city, that's a fact, but it's also full of amazing people, so thanks to all the friends I have made in this lovely place. Again here, **Aaron**? **Angel**, you were the one who created the UNAM-RUG WhatsApp group**,** it was amazing, thank you. **Cédric**, my most handsome half-French friend, thank you for all the moments, the gossip during the breaks, your unconditional support and kind words, it has been awesome. **Gustavo**, thank you for the *conchas* and *roscas* you baked, everything was delicious, and because of you I also started baking, it makes gossiping better. **Mees**, **Brenda**, **Vicente**, **Ana Lau**, **Rubí**, **Amalia**, **Charito**, **Emmanuel, Liliana, Denisse, Alex, Karen, Enrique, Diego, t**hank you for all the moments, parties, trips, food, and laughs, you are awesome. A special mention to **Mireny**, I am glad we could also train together at the gym, you are super strong.

It is more than a well-known rumour that I like exercising, so it is time to thank the friends I made at the gym. How should I start this **Henrike**? I have told you before that you are one of the most extraordinary people I have ever met in my entire life and I will keep saying it, however, all the things I would like to tell you are beyond words. Thank you for brightening up all my mornings for almost two years. After all this time, you have taught me so many things and even if you are not aware of it, I have become a better version of myself because of you, I think I have lost count of all the times you have inspired me (just kidding, I remember all of them). I feel immensely proud of you, all your passion, all your strength, all your kindness, all your "*ambitiousness*", working out beside you has been an absolute pleasure. Thank you for sharing movies, series, and your books, I have enjoyed all of them. since you are already so exceptional, I cannot

even imagine the person you will become, thank you for letting me be part of your life, you are unstoppable. My dearest darling **Peter**, what´s the gas? *¿Cómo estás mi amigo?* I have never seen such an enthusiastic, curious, and well-looking man in my whole career. All the time working out with you has been amazing, as well as the good chatting, I enjoy all your crazy ideas and I am glad we could share many sunrises, love brother, *buenas noches*. My dear **Sander**, I enjoyed our time together and training with you, many nice moments and conversations, I will not forget your most famous phrase *I think you can do more* which was true, indeed. **Henk,** the man who knows all the songs playing at the gym, thanks for all your good vibes and great attitude. **Jeroen**, I am glad we could spend time together; it was awesome. Thank you, **Dahise**, I am delighted we met, I enjoyed training with someone as charming as you.

Naturally, I would like to say thank you to the Goudlaan party as well. **Aaron, Caro, Nick,** and **Stefan**, thank you for inviting me to your home for the gatherings, parties, movies, and game nights you organised, it was an absolute pleasure spending time together, it was the best time, you all are wonderful people.

Thanks to the lovely people from the FND group, **Teresa, Rick, Jan, Sytze, Rixt, Krishna, Anna, Sharma, Ishitro, Maxen, Stella, Job, Denis, Samer,** I am glad you joined for lunch on Fridays, many good moments.

Thanks to my friends in Mexico **Huidobro, Manolo, Yoliztli, Cristina, Ernesto, Chema, Jess, Jeanette, Gustavo, Toñito, and Jorge,** we have been together for a long time, and it is priceless. **Jess,** you were the first person I talked to about this new adventure I wanted to start, thank you for all your support.

I would like to express my gratitude to my beloved family. Thanks to my **Mom** and **Dad,** I am so thankful because you always have supported me unconditionally during my whole life, I feel so proud of being your son. Also, I would like to thanks to my sister and brother, **Tania** and **Julio**, you are the best. We have always been together. I appreciate all our moments and weekend video calls during these two years. Thanks to my two little dogs **Mila** and **Paloma** for not forgetting me despite not being with you.

Who knows, perhaps the PhD is about the friends we make along the way.

Thank you everyone!

The road so far...

Table of Contents

—— CHAPTER 1 ——
Introduction

This chapter serves as a general introduction to graphene materials and highlights the motivation for the research presented in this thesis. Finally, a concise summary of each of the upcoming chapters in this dissertation is given, highlighting the results and their implications from a fundamental point of view.

1

This dissertation reports on the green synthesis of graphene-based nanocomposites with lanthanide species. This is why in this introduction we first present a short overview of green chemistry, then explain why composites of nanometer-sized carbon and lanthanide species are interesting and introduce the constituents of the composites we produced, namely graphene, graphite, graphene oxide, lanthanides, and lanthanide oxides.

1.1. Green chemistry

The evolution of chemistry throughout history has allowed us to modify matter to benefit society and enrich life quality from creating compounds present in the clothes we wear every day to the synthesis of pharmaceutical agents to combat threatful diseases. However, such endeavour has led to the waste of high amounts of global natural resources as well as the production of hazardous pollutants, therefore, sustainability is one of the biggest challenges for science nowadays [1]. As a response, two decades ago [2] green chemistry emerged as a scientific multidisciplinary approach focused on designing processes and chemical products that reduce or eliminate the use or the generation of hazardous and polluting substances, as well as to increase the efficiency and efficacy of chemical products. While no reaction or chemical process can be completely "green", green chemistry has been divided into the 12 principles shown in Figure 1.1 [2]. Thus, it is highly desirable that synthesis techniques are designed so that they do not require elevated temperatures or long reaction times, use safer solvents or are even solvent-free.

The solvothermal method is among the most appealing environmentally friendly techniques since it is a one-step process. In solvothermal synthesis, a chemical reaction occurs in aqueous or non-aqueous solvents heated close to or above the solvent boiling temperature within a sealed autoclave [3]. Under these conditions, the solvent can be converted into a supercritical fluid, and the temperature and pressure conditions facilitate the dissolution of reagents and their posterior crystallization of the product [4]. Changing experimental parameters like temperature, solvent, reaction time, and precursors allow control over the crystallinity, size, distribution, and shape in the synthesis of nanomaterials [5].

Another technique with great potential is ball milling since it is a simple, fast, and cost-effective technology. In ball milling, solids are ground into nanostructured fine powders [6,7] and because high-energy collisions occur between the powder and

Figure 1.1. Green chemistry principles

grinding balls inside a grinding jar [8], the mechanical forces at play can induce chemical and structural changes in the materials. In a planetary ball mill, the grinding jars are located above a wheel, and both rotate in opposite directions at uniform speeds and rotation ratios. As a result, centrifugal forces change in a motion known as Coriolis motion, where the resulting interaction product of frictional and impact forces produces an effective size reduction and increases the reactivity of the materials inside [8,9].

In this thesis, we employed solvothermal and ball milling methods as environmentally friendly synthesis routes to synthesise graphene-based lanthanide-containing nanocomposites.

1.2. Graphene

Graphene is a single layer of sp^2-hybridised carbon atoms arranged in a hexagonal two-dimensional lattice (Figure 1.2). It is the basic building block of other graphitic materials like fullerenes, carbon nanotubes (CNTs) and graphite [10]. Since Novoselov and Geim employed mechanical cleavage to obtain graphene, also called the Scotch tape method, several top-down and bottom-up approaches to prepare graphene

1

have been developed [11–13], resulting in graphene with different sizes and thicknesses. Top-down methods like micromechanical cleavage [10,14–19] and direct sonication of graphite [20–22] allow to obtain large graphene sheets with lateral sizes of μm to sub-μm and low defect concentration, but they are not easily upscalable. Electrochemical exfoliation [23–28], despite being a simple and eco-friendly process, needs high-cost reagents like ionic liquids. Through bottom-up methods like unzipping CNTs [29–31], it is possible to obtain graphene with different sizes and number of layers depending on which multi-walled or single-walled nanotubes are employed as precursors (μm to nm), but it is a costly process. The arc discharge method [32–37] is cost-effective and environmentally friendly but has a low yield and requires further separation steps. One of the most employed methods is chemical vapour deposition (CVD) [38–46], which produces large graphene sheets, even cm of lateral size, with high quality but necessitates specialised and costly equipment. Therefore, the search for eco-friendly, low-cost, and high-yield synthesis routes for graphene still remains a challenge.
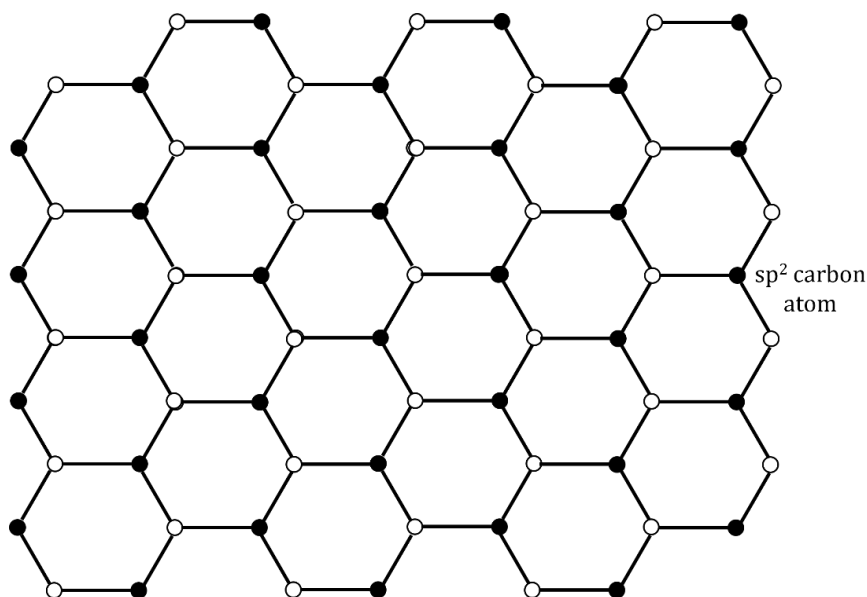
Figure 1.2. Sketch of the structure of graphene

1.3. Graphite

Graphite is the most common carbon allotrope in the Earth's crust and the most stable under standard conditions. However, graphite can also be synthesised [47] and it is normally used in pencils, lubricants, and electrodes. Graphite consists of graphene layers that are mainly stacked in an AB sequence (Figure 1.3), meaning that the position of the adjacent layers is shifted with respect to one another; and the interplanar distance of 3.35 Å [48]. The adjacent graphene layers are weakly bonded through van der Waal forces, resulting in a high anisotropy, where the mechanical, electrical, and thermal properties are determined by the covalently bonded planes and the delocalised π-electrons above and below each plane. As already mentioned above, graphite can serve as a starting material for graphene production by direct solvent exfoliation [20–22] or through oxidation/exfoliation/reduction [49–51]. Both are promising synthesis routes for industry since they can be scaled up at a relatively low cost and could thus also be considered for the development of more environmentally friendly synthetic methodologies.
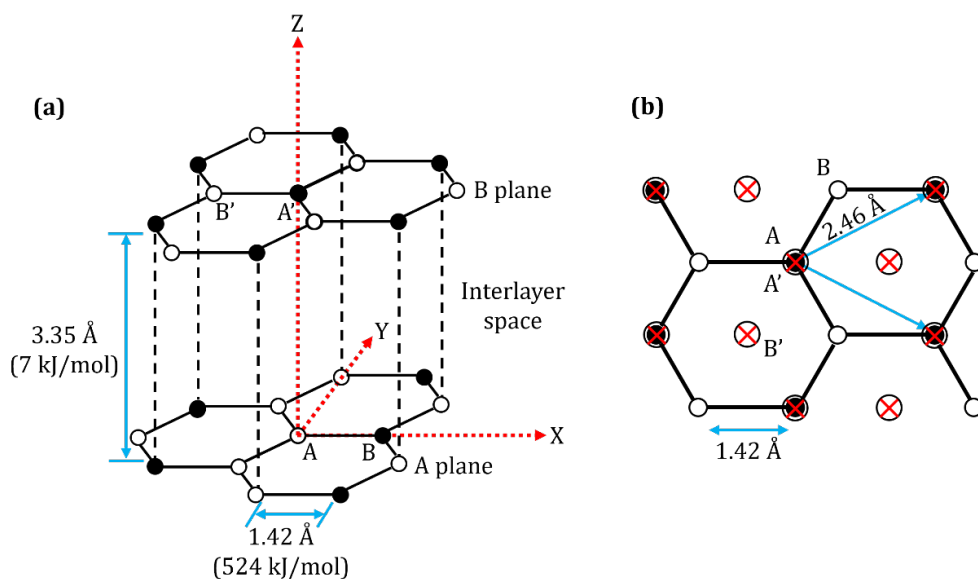
Figure 1.3. Sketch of the structure of graphite (a) 3D structure, (b) 2D structure of an individual plane

1

1.4. Graphene oxide

Graphene oxide (GO) is the oxidised form of graphene, which consists of domains predominantly with sp^2-hybridised carbon atoms, delimited and surrounded by sp^3-hybridised carbon atoms covalently bonded with different oxygen functional groups. Carbonyl (C=O) and carboxyl (COOH) groups are mainly present at the edges of the layers, while hydroxyl (C-O) and epoxy (C-O-C) groups are bound to the basal planes [52] (Figure 1.4). Due to these functional groups GO is hydrophilic, meaning that it can be easily dispersed in polar solvents like water due to the formation of hydrogen bonds. Among the synthesis routes of GO, the most famous are the methods developed by Brodie [53], Staudenmaier [54], Hofmann [55], and Hummers [56] where first graphite flakes are treated with strong oxidants like $KClO_3$, $NaNO_3$, or $KMnO_4$ to obtain graphite oxide (see details in Table 1.1), which is then exfoliated by stirring or sonication to obtain single GO sheets. Unfortunately, these methods are unsafe and environmentally unfriendly due to the formation of acid fog, explosive ClO_2 or toxic gases like NO_X in the process, as well as the presence of residual ions that are difficult to remove from the produced wastewater [57,58].

The presence of oxygen-containing groups allows for the covalent or non-covalent functionalisation of GO and for tuning its chemical and physical properties through several types of reactions [59–61]. In particular, the coordination of metal cations with oxygenated groups as nucleation sites and the subsequent nanoparticle growth [62] yields GO nanocomposites where nanometre-sized metal or metal oxide particles are anchored to the GO layers.

Table 1.1. Common methods for GO synthesis

Method	Oxidant	Reaction media	Temperature	Reaction Time
Brodie	$KClO_3$	Fuming HNO_3	60 °C	4 days
Staudenmaier	$KClO_3$	$HNO_3 + H_2SO_4$	40 °C	4 days
Hofmann	$KClO_3$	HNO_3	45 °C	4 days
Hummers	$KMnO_4 + NaNO_3$	Concentrated H_2SO_4	< 45 °C	< 2 hours
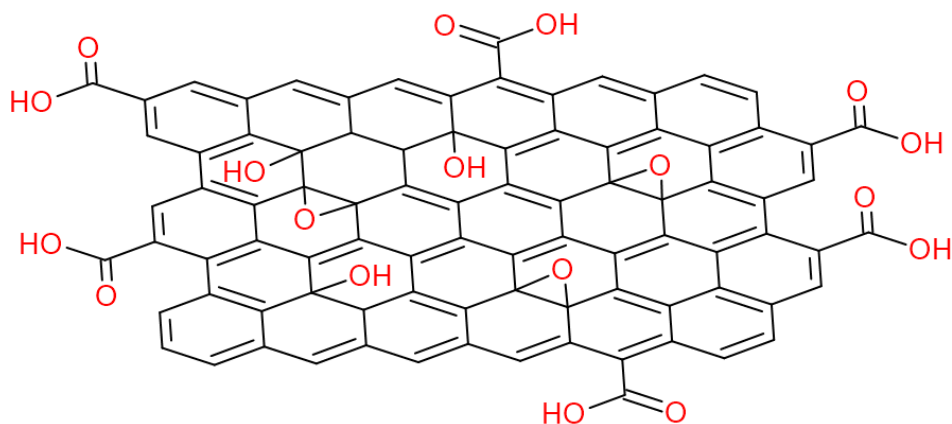
Figure 1.4. Structural representation of graphene oxide

1.5. Lanthanides and lanthanide oxides

The lanthanide series consists of 14 elements, from lanthanum (La; Z = 57) to lutetium (Lu; Z = 71), characterised by the gradual filling of the $4f$ subshell. The abundance of some lanthanides in the earth's crust is higher than that of for gold, silver and even lead, as seen in Table 1.2 [63]. Lanthanides have the propensity to form +3 cations but with similar reactivity; this tendency to form +3 ions is stronger than for transition metals [64]. Europium and ytterbium can also present the oxidation state +2 due to the stability provided by the half-filled $4f^7$ and filled $4f^{14}$ subshell [65].

Table 1.2. Abundance of some metals throughout the Earth's crust.

Element	Atomic number	Abundance
Copper (Cu)	29	0.006 %
Lanthanum (La)	57	0.0039 %
Lead (Pb)	82	0.0014 %
Gadolinium (Gd)	64	0.00062 %
Europium (Eu)	63	0.0002 %
Terbium (Tb)	65	0.00012 %
Lutetium (Lu)	71	0.00008 %
Silver (Ag)	47	0.0000075 %
Gold (Au)	79	0.0000004 %

1

The decrease of atomic radius as the atomic number increases, known as lanthanide contraction, stems from the 5s and 5p orbitals penetrating the 4f orbital and thereby introducing a poor shielding of the 4f electrons from the increasing nuclear charge [66]. Lanthanides form primarily ionic compounds and typically behave as hard acids, meaning that they have high charge densities and are weakly polarizable, which causes them to bind preferentially to elements with high electronegativity, like fluoride and oxygen donor ligands, normally with coordination numbers from 6 to 9 [67].

Explore the functionalisation of graphene materials with lanthanide species then arises as an attractive way to prepare hybrid materials with advantageous properties in the fields of medical diagnosis [68,69], bioimaging [70], environmental remediation [71–74], clinical sensors [75,76], solar cells [77], magnetic resonance imaging [78–80], catalysis [81], and supercapacitors [82–86]. Thus, in this thesis, we focussed on the synthesis of graphene-based materials with lanthanide species employing environmentally friendly techniques.

1.6. Research aims and hypothesis of this dissertation

As discussed in the preceding sections, the functionalisation of graphene nanomaterials with lanthanides results in hybrid materials with useful properties for application in different fields. Therefore, the primary objective of this dissertation is to synthesize graphite and graphene oxide nanocomposites incorporating different lanthanide-containing species via environmentally friendly synthetic routes.

Given the high charge density of lanthanide ions, we hypothesize that the non-covalent attachment of lanthanide species to graphite and graphene oxide will occur through the oxygen-containing groups present in their structures. Consequently, we anticipate that these nanocomposites will exhibit different cytotoxicity, compared to pristine materials.

The specific goals of this research endeavour are as follows:

To functionalise graphene oxide with lanthanide oxide/hydroxide nanoparticles employing the solvothermal approach, followed by comprehensive characterisation of the nanocomposites obtained.

1

Tosynthesise graphite-lanthanide oxide nanocomposites utilizing the mechanochemical approach and thoroughly characterise the resultant products.

To assess the potential bactericidal effects of the graphene oxide-lanthanide oxide/hydroxide nanocomposites and evaluate the cell viability of these graphite-lanthanide oxide nanocomposites.

1.7. Thesis outline

This thesis is organised as follows:

Chapter 2 presents a brief description of the principles of the techniques employed for the characterisation of the nanocomposites synthesised in this dissertation and gives the experimental details of these measurements.

Chapter 3 describes the synthesis of graphene oxide-lanthanide oxide/ hydroxide nanocomposites using a solvothermal method. We detail how we could obtain the desired products with short reaction times, safer solvents, and temperatures below 200 °C. The characterisation gave evidence that the oxygen-containing functional groups in GO serve as nanoparticle growth sites and showed important differences in the distribution and size of the lanthanide-containing nanoparticles depending on the lanthanide and the conditions employed. Therefore, the solvothermal approach can be considered a versatile and successful green approach for the synthesis of graphene oxide-lanthanide oxide/hydroxide nanocomposites.

Chapter 4 is devoted to the exploration of one possible application of these graphene oxide-lanthanide oxide/hydroxide nanocomposites, namely the exploitation of their antimicrobial properties. Remarkably differences were observed in the bactericidal effect against Gram$^-$ and Gram$^+$ bacteria depending on the distribution and size of the lanthanide-containing nanoparticles on the GO surface. We tentatively attribute these different properties to a different interaction between the bacteria membranes and the nanocomposites tested.

Chapter 5 presents the first approach to the synthesis of graphite-lanthanide oxide nanocomposites through a high-energy ball milling technique. The size of the graphite crystallites was greatly reduced and the oxygen content increased through the mechanochemical processing, while micro- and nanometre-sized lanthanide oxide

1

particles were formed on them. Density functional theory calculation provided insight into the interaction between graphene sheets and the lanthanide ions that explained these results.

Chapter 6 details an improved methodology for the synthesis of graphite-lanthanide oxide nanocomposites by changing the ball milling conditions explored in Chapter 5. Graphite was successfully exfoliated into a few-layer graphene that was slightly oxidised and decorated with lanthanide oxide nanoparticles. Therefore, the mechanochemical approach can be considered an environmentally friendly methodology to achieve the simultaneous exfoliation and functionalisation of graphite with lanthanide oxides. We also studied the cell viability of mammal cells in the presence of the nanocomposites to determine if the presence of lanthanide ions increases the toxicity of these nanocomposites.

The thesis concludes with a short summary of the results obtained and an outlook on future research.

References

[1]   J.H. Clark, Green chemistry: challenges and opportunities, Green Chemistry 1 (1999) 1–8. https://doi.org/10.1039/A807961G.

[2]   P.T. Anastas, J.C. Warner, Green Chemistry: Theory and Practice, (2000). https://doi.org/10.1093/OSO/9780198506980.001.0001.

[3]   A. Kashyap, N.K. Singh, M. Soni, A. Soni, Deposition of thin films by chemical solution-assisted techniques, Chemical Solution Synthesis for Materials Design and Thin Film Device Applications (2021) 79–117. https://doi.org/10.1016/B978-0-12-819718-9.00014-5.

[4]   S. Choudhury, S. Paul, S. Goswami, K. Deb, Methods for nanoparticle synthesis and drug delivery, Advances in Nanotechnology-Based Drug Delivery Systems (2022) 21–44. https://doi.org/10.1016/B978-0-323-88450-1.00005-3.

[5]   S.F. Shaikh, M. Ubaidullah, R.S. Mane, A.M. Al-Enizi, Types, Synthesis methods and applications of ferrites, Spinel Ferrite Nanostructures for Energy Storage Devices (2020) 51–82. https://doi.org/10.1016/B978-0-12-819237-5.00004-3.

[6]   S.O. Amusat, T.G. Kebede, S. Dube, M.M. Nindi, Ball-milling synthesis of biochar and biochar–based nanocomposites and prospects for removal of emerging contaminants: A review, Journal of Water Process Engineering 41 (2021) 101993. https://doi.org/10.1016/J.JWPE.2021.101993.

[7]   O. Faye, J. Szpunar, U. Eduok, A critical review on the current technologies for the generation, storage, and transportation of hydrogen, Int J Hydrogen Energy 47 (2022) 13771–13802. https://doi.org/10.1016/J.IJHYDENE.2022.02.112.

1

[8]   V.A. Sadykov, N. V. Mezentseva, L.N. Bobrova, O.L. Smorygo, N.F. Eremeev, Y.E. Fedorova, Y.N. Bespalko, P.I. Skriabin, A. V. Krasnov, A.I. Lukashevich, T.A. Krieger, E.M. Sadovskaya, V.D. Belyaev, A.N. Shmakov, Z.S. Vinokurov, V.A. Bolotov, Y.Y. Tanashev, M. V. Korobeynikov, M.A. Mikhailenko, Advanced Materials for Solid Oxide Fuel Cells and Membrane Catalytic Reactors, Advanced Nanomaterials for Catalysis and Energy: Synthesis, Characterization and Applications (2019) 435–514. https://doi.org/10.1016/B978-0-12-814807-5.00012-7.

[9]   M.S. El-Eskandarany, The history and necessity of mechanical alloying, Mechanical Alloying (2015) 13–47. https://doi.org/10.1016/B978-1-4557-7752-5.00002-4.

[10]   A.K. Geim, K.S. Novoselov, The rise of graphene, Nature Materials 2007 6:3 6 (2007) 183–191. https://doi.org/10.1038/nmat1849.

[11]   V.B. Mbayachi, E. Ndayiragije, T. Sammani, S. Taj, E.R. Mbuta, A. ullah khan, Graphene synthesis, characterization and its applications: A review, Results Chem 3 (2021) 100163. https://doi.org/10.1016/J.RECHEM.2021.100163.

[12]   K.A. Madurani, S. Suprapto, N.I. Machrita, S.L. Bahar, W. Illiya, F. Kurniawan, Progress in Graphene Synthesis and its Application: History, Challenge and the Future Outlook for Research and Industry, ECS Journal of Solid State Science and Technology 9 (2020) 093013. https://doi.org/10.1149/2162-8777/ABBB6F.

[13]   M.S.A. Bhuyan, M.N. Uddin, M.M. Islam, F.A. Bipasha, S.S. Hossain, Synthesis of graphene, International Nano Letters 2016 6:2 6 (2016) 65–83. https://doi.org/10.1007/S40089-015-0176-1.

[14]   K.S. Novoselov, A.K. Geim, S. V. Morozov, D. Jiang, Y. Zhang, S. V. Dubonos, I. V. Grigorieva, A.A. Firsov, Electric field in atomically thin carbon films, Science (1979) 306 (2004) 666–669. https://doi.org/10.1126/SCIENCE.1102896.

[15]   J. Phiri, P. Gane, T.C. Maloney, General overview of graphene: Production, properties and application in polymer composites, Materials Science and Engineering: B 215 (2017) 9–28. https://doi.org/10.1016/J.MSEB.2016.10.004.

[16]   K.S. Novoselov, V.I. Fal'Ko, L. Colombo, P.R. Gellert, M.G. Schwab, K. Kim, A roadmap for graphene, Nature 2012 490:7419 490 (2012) 192–200. https://doi.org/10.1038/nature11458.

[17]   K.S. Novoselov, D. Jiang, F. Schedin, T.J. Booth, V. V. Khotkevich, S. V. Morozov, A.K. Geim, Two-dimensional atomic crystals, Proceedings of the National Academy of Sciences 102 (2005) 10451–10453. https://doi.org/10.1073/PNAS.0502848102.

[18]   R.S. Edwards, K.S. Coleman, Graphene synthesis: relationship to applications, Nanoscale 5 (2012) 38–51. https://doi.org/10.1039/C2NR32629A.

[19]   R. Van Noorden, Production: Beyond sticky tape, Nature 2012 483:7389 483 (2012) S32–S33. https://doi.org/10.1038/483s32a.

[20]   J.Y. Lim, N.M. Mubarak, E.C. Abdullah, S. Nizamuddin, M. Khalid, Inamuddin, Recent trends in the synthesis of graphene and graphene oxide based nanomaterials for removal of heavy metals — A review, Journal of Industrial and Engineering Chemistry 66 (2018) 29–44. https://doi.org/10.1016/J.JIEC.2018.05.028.

[21]   A.B. Bourlinos, V. Georgakilas, R. Zboril, T.A. Sterioti, A.K. Stubos, Liquid-Phase Exfoliation of Graphite Towards Solubilized Graphenes, Small 5 (2009) 1841–1845. https://doi.org/10.1002/SMLL.200900242.

1

[22]   Y. Hernandez, V. Nicolosi, M. Lotya, F.M. Blighe, Z. Sun, S. De, I.T. McGovern, B. Holland, M. Byrne, Y.K. Gun'ko, J.J. Boland, P. Niraj, G. Duesberg, S. Krishnamurthy, R. Goodhue, J. Hutchison, V. Scardaci, A.C. Ferrari, J.N. Coleman, High-yield production of graphene by liquid-phase exfoliation of graphite, Nature Nanotechnology 2008 3:9 3 (2008) 563–568. https://doi.org/10.1038/nnano.2008.215.

[23]   N. Liu, F. Luo, H. Wu, Y. Liu, C. Zhang, J. Chen, One-Step Ionic-Liquid-Assisted Electrochemical Synthesis of Ionic-Liquid-Functionalized Graphene Sheets Directly from Graphite, Adv Funct Mater 18 (2008) 1518–1525. https://doi.org/10.1002/ADFM.200700797.

[24]   C.Y. Su, A.Y. Lu, Y. Xu, F.R. Chen, A.N. Khlobystov, L.J. Li, High-quality thin graphene films from fast electrochemical exfoliation, ACS Nano 5 (2011) 2332–2339. https://doi.org/10.1021/NN200025P.

[25]   F. Liu, C. Wang, X. Sui, M.A. Riaz, M. Xu, L. Wei, Y. Chen, Synthesis of graphene materials by electrochemical exfoliation: Recent progress and future potential, Carbon Energy 1 (2019) 173–199. https://doi.org/10.1002/CEY2.14.

[26]   S. Yang, M.R. Lohe, K. Müllen, X. Feng, New-Generation Graphene from Electrochemical Approaches: Production and Applications, Advanced Materials 28 (2016) 6213–6221. https://doi.org/10.1002/ADMA.201505326.

[27]   A.T. Najafabadi, E. Gyenge, High-yield graphene production by electrochemical exfoliation of graphite: Novel ionic liquid (IL)–acetonitrile electrolyte with low IL content, Carbon N Y 71 (2014) 58–69. https://doi.org/10.1016/J.CARBON.2014.01.012.

[28]   J. Liu, C.K. Poh, D. Zhan, L. Lai, S.H. Lim, L. Wang, X. Liu, N. Gopal Sahoo, C. Li, Z. Shen, J. Lin, Improved synthesis of graphene flakes from the multiple electrochemical exfoliation of graphite rod, Nano Energy 2 (2013) 377–386. https://doi.org/10.1016/J.NANOEN.2012.11.003.

[29]   D. V. Kosynkin, A.L. Higginbotham, A. Sinitskii, J.R. Lomeda, A. Dimiev, B.K. Price, J.M. Tour, Longitudinal unzipping of carbon nanotubes to form graphene nanoribbons, Nature 2009 458:7240 458 (2009) 872–876. https://doi.org/10.1038/nature07872.

[30]   L. Jiao, L. Zhang, X. Wang, G. Diankov, H. Dai, Narrow graphene nanoribbons from carbon nanotubes, Nature 2009 458:7240 458 (2009) 877–880. https://doi.org/10.1038/nature07919.

[31]   A. Hirsch, Unzipping Carbon Nanotubes: A Peeling Method for the Formation of Graphene Nanoribbons, Angewandte Chemie International Edition 48 (2009) 6594–6596. https://doi.org/10.1002/ANIE.200902534.

[32]   N. Li, Z. Wang, K. Zhao, Z. Shi, Z. Gu, S. Xu, Large scale synthesis of N-doped multi-layered graphene sheets by simple arc-discharge method, Carbon N Y 48 (2010) 255–259. https://doi.org/10.1016/J.CARBON.2009.09.013.

[33]   J. Wang, X.-M. Wang, Y.-F. Chen, al -, H. Li, L. Liu, H.-B. Li, S. Karmakar, N. V Kulkarni, A.B. Nawale, N.P. Lalla, R. Mishra, V.G. Sathe, S. V Bhoraskar, A.K. Das, A novel approach towards selective bulk synthesis of few-layer graphenes in an electric arc, J Phys D Appl Phys 42 (2009) 115201. https://doi.org/10.1088/0022-3727/42/11/115201.

[34]   D. Zhang, K. Ye, Y. Yao, F. Liang, T. Qu, W. Ma, B. Yang, Y. Dai, T. Watanabe, Controllable synthesis of carbon nanomaterials by direct current arc discharge from the inner wall of the chamber, Carbon N Y 142 (2019) 278–284. https://doi.org/10.1016/J.CARBON.2018.10.062.

[35]   Y. Zhang, L. Sheng, Y. Fang, K. An, L. Yu, Y. Liu, X. Zhao, Synthesis of 3C-SiC nanowires

from a graphene/Si configuration obtained by arc discharge method, Chem Phys Lett 678 (2017) 17–22. https://doi.org/10.1016/J.CPLETT.2017.04.008.

[36]   B. Qin, T. Zhang, H. Chen, Y. Ma, The growth mechanism of few-layer graphene in the arc discharge process, Carbon N Y 102 (2016) 494–498. https://doi.org/10.1016/J.CARBON.2016.02.074.

[37]   S. Kim, Y. Song, J. Wright, M.J. Heller, Graphene bi- and trilayers produced by a novel aqueous arc discharge process, Carbon N Y 102 (2016) 339–345. https://doi.org/10.1016/J.CARBON.2016.02.049.

[38]   K.E. Whitener, P.E. Sheehan, Graphene synthesis, Diam Relat Mater 46 (2014) 25–34. https://doi.org/10.1016/J.DIAMOND.2014.04.006.

[39]   G. Deokar, J. Avila, I. Razado-Colambo, J.L. Codron, C. Boyaval, E. Galopin, M.C. Asensio, D. Vignaud, Towards high quality CVD graphene growth and transfer, Carbon N Y 89 (2015) 82–92. https://doi.org/10.1016/J.CARBON.2015.03.017.

[40]   Z.Y. Juang, C.Y. Wu, A.Y. Lu, C.Y. Su, K.C. Leou, F.R. Chen, C.H. Tsai, Graphene synthesis by chemical vapor deposition and transfer by a roll-to-roll process, Carbon N Y 48 (2010) 3169–3174. https://doi.org/10.1016/J.CARBON.2010.05.001.

[41]   D.A.C. Brownson, C.E. Banks, The electrochemistry of CVD graphene: progress and prospects, Physical Chemistry Chemical Physics 14 (2012) 8264–8281. https://doi.org/10.1039/C2CP40225D.

[42]   L. Sun, G. Yuan, L. Gao, J. Yang, M. Chhowalla, M.H. Gharahcheshmeh, K.K. Gleason, Y.S. Choi, B.H. Hong, Z. Liu, Chemical vapour deposition, Nature Reviews Methods Primers 2021 1:1 1 (2021) 1–20. https://doi.org/10.1038/s43586-020-00005-y.

[43]   X. Li, W. Cai, J. An, S. Kim, J. Nah, D. Yang, R. Piner, A. Velamakanni, I. Jung, E. Tutuc, S.K. Banerjee, L. Colombo, R.S. Ruoff, Large-area synthesis of high-quality and uniform graphene films on copper foils, Science (1979) 324 (2009) 1312–1314. https://doi.org/10.1126/SCIENCE.1171245.

[44]   X. Wang, H. You, F. Liu, M. Li, L. Wan, S. Li, Q. Li, Y. Xu, R. Tian, Z. Yu, D. Xiang, J. Cheng, Large-Scale Synthesis of Few-Layered Graphene using CVD, Chemical Vapor Deposition 15 (2009) 53–56. https://doi.org/10.1002/CVDE.200806737.

[45]   E. Dervishi, Z. Li, F. Watanabe, A. Biswas, Y. Xu, A.R. Biris, V. Saini, A.S. Biris, Large-scale graphene production by RF-cCVD method, Chemical Communications (2009) 4061–4063. https://doi.org/10.1039/B906323D.

[46]   S.J. Chae, F. Güneş, K.K. Kim, E.S. Kim, G.H. Han, S.M. Kim, H. Shin, S.M. Yoon, J.Y. Choi, M.H. Park, C.W. Yang, D. Pribat, Y.H. Lee, Synthesis of Large-Area Graphene Layers on Poly-Nickel Substrate by Chemical Vapor Deposition: Wrinkle Formation, Advanced Materials 21 (2009) 2328–2333. https://doi.org/10.1002/ADMA.200803016.

[47]   Y.W. Yap, N. Mahmed, M.N. Norizan, S.Z. Abd Rahim, M.N. Ahmad Salimi, K. Abdul Razak, I.S. Mohamad, M.M.A.B. Abdullah, M.Y. Mohamad Yunus, Recent Advances in Synthesis of Graphite from Agricultural Bio-Waste Material: A Review, Materials 16 (2023). https://doi.org/10.3390/MA16093601.

[48]   D.D.L. Chung, Review: Graphite, J Mater Sci 37 (2002) 1475–1489. https://doi.org/10.1023/A:1014915307738.

[49]   O.O. Abakumov, I.B. Bychko, A.I. Trypolskii, Structural Characteristics of Graphene Oxide Reduced by Hydrazine and Hydrogen, Theoretical and Experimental Chemistry 57

(2021) 289–296. https://doi.org/10.1007/S11237-021-09697-Z.

[50]   G.G. Gebreegziabher, A.S. Asemahegne, D.W. Ayele, M. Dhakshnamoorthy, A. Kumar, One-step synthesis and characterization of reduced graphene oxide using chemical exfoliation method, Mater Today Chem 12 (2019) 233–239. https://doi.org/10.1016/J. MTCHEM.2019.02.003.

[51]   A.F. Betancur, N. Ornelas-Soto, A.M. Garay-Tapia, F.R. Pérez, Á. Salazar, A.G. García, A general strategy for direct synthesis of reduced graphene oxide by chemical exfoliation of graphite, Mater Chem Phys 218 (2018) 51–61. https://doi.org/10.1016/J. MATCHEMPHYS.2018.07.019.

[52]   D.R. Dreyer, A.D. Todd, C.W. Bielawski, Harnessing the chemistry of graphene oxide, Chem Soc Rev 43 (2014) 5288–5301. https://doi.org/10.1039/C4CS00060A.

[53]   XIII. On the atomic weight of graphite, Philos Trans R Soc Lond 149 (1859) 249–259. https://doi.org/10.1098/RSTL.1859.0013.

[54]   L. Staudenmaier, Verfahren zur Darstellung der Graphitsäure, Berichte Der Deutschen Chemischen Gesellschaft 31 (1898) 1481–1487. https://doi.org/10.1002/ CBER.18980310237.

[55]   U. Hofmann, E. König, Untersuchungen über Graphitoxyd, Z Anorg Allg Chem 234 (1937) 311–336. https://doi.org/10.1002/ZAAC.19372340405.

[56]   W.S. Hummers, R.E. Offeman, Preparation of Graphitic Oxide, J Am Chem Soc 80 (1958) 1339. https://doi.org/10.1021/JA01539A017/ASSET/JA01539A017.

[57]   A. Jiříčková, O. Jankovský, Z. Sofer, D. Sedmidubský, Synthesis and Applications of Graphene Oxide, Materials 15 (2022). https://doi.org/10.3390/MA15030920.

[58]   S. Pei, Q. Wei, K. Huang, H.M. Cheng, W. Ren, Green synthesis of graphene oxide by seconds timescale water electrolytic oxidation, Nature Communications 2018 9:1 9 (2018) 1–9. https://doi.org/10.1038/s41467-017-02479-z.

[59]   D.R. Dreyer, S. Park, C.W. Bielawski, R.S. Ruoff, The chemistry of graphene oxide, Chem Soc Rev 39 (2009) 228–240. https://doi.org/10.1039/B917103G.

[60]   S. Guo, S. Garaj, A. Bianco, C. Ménard-Moyon, Controlling covalent chemistry on graphene oxide, Nature Reviews Physics 2022 4:4 4 (2022) 247–262. https://doi.org/10.1038/ s42254-022-00422-w.

[61]   D. Chen, H. Feng, J. Li, Graphene oxide: Preparation, functionalization, and electrochemical applications, Chem Rev 112 (2012) 6027–6053. https://doi.org/10.1021/CR300115G.

[62]   H. Zheng, Z. Ji, K.R. Roy, M. Gao, Y. Pan, X. Cai, L. Wang, W. Li, C.H. Chang, C. Kaweeteerawat, C. Chen, T. Xia, Y. Zhao, R. Li, Engineered Graphene Oxide Nanocomposite Capable of Preventing the Evolution of Antimicrobial Resistance, ACS Nano 13 (2019) 11488–11499. https://doi.org/10.1021/ACSNANO.9B04970.

[63]   CRC Handbook of Chemistry and Physics, CRC Handbook of Chemistry and Physics (2016). https://doi.org/10.1201/9781315380476.

[64]   W.B. Jensen, The positions of lanthanum (actinium) and lutetium (lawrencium) in the periodic table, J Chem Educ 59 (1982) 634–636. https://doi.org/10.1021/ED059P634.

[65]   D.A. Johnson, Principles of lanthanide chemistry, J Chem Educ 57 (1980) 475–477. https://doi.org/10.1021/ED057P475.

[66]   S.C. Bart, What is the "Lanthanide Contraction"?, Inorg Chem 62 (2023) 3713–3714. https://doi.org/10.1021/ACS.INORGCHEM.3C00440.

[67]   K. Bernot, C. Daiguebonne, G. Calvez, Y. Suffren, O. Guillou, A Journey in Lanthanide Coordination Chemistry: From Evaporable Dimers to Magnetic Materials and Luminescent Devices, Acc Chem Res 54 (2021) 427–440. https://doi.org/10.1021/ACS.ACCOUNTS.0C00684.

[68]   B.K. Gupta, P. Thanikaivelan, T.N. Narayanan, L. Song, W. Gao, T. Hayashi, A. Leela Mohana Reddy, A. Saha, V. Shanker, M. Endo, A.A. Martí, P.M. Ajayan, Optical bifunctionality of europium-complexed luminescent graphene nanosheets, Nano Lett 11 (2011) 5227–5233. https://doi.org/10.1021/NL202541N.

[69]   S.J. Wang, J.B. Hu, Y.Y. Wang, F. Luo, Coating graphene oxide sheets with luminescent rare-earth complexes, J Mater Sci 48 (2013) 805–811. https://doi.org/10.1007/S10853-012-6799-Y.

[70]   B. Park, S.J. Kim, J. Lim, S. Some, J.E. Park, S.J. Kim, C. Kim, T.J. Lee, S.C. Jun, Tunable wide blue photoluminescence with europium decorated graphene, J Mater Chem C Mater 3 (2015) 4030–4038. https://doi.org/10.1039/C4TC02361G.

[71]   Y. Wang, Y. Li, W. Qi, Y. Song, Luminescent lanthanide graphene for detection of bacterial spores and cysteine, Chemical Communications 51 (2015) 11022–11025. https://doi.org/10.1039/C5CC02889B.

[72]   M. Chen, C. Huo, Y. Li, J. Wang, Selective Adsorption and Efficient Removal of Phosphate from Aqueous Medium with Graphene-Lanthanum Composite, ACS Sustain Chem Eng 4 (2016) 1296–1302. https://doi.org/10.1021/ACSSUSCHEMENG.5B01324.

[73]   L.P. Lingamdinne, S. Lee, J.S. Choi, V.R. Lebaka, V.R.P. Durbaka, J.R. Koduru, Potential of the magnetic hollow sphere nanocomposite (graphene oxide-gadolinium oxide) for arsenic removal from real field water and antimicrobial applications, J Hazard Mater 402 (2021) 123882. https://doi.org/10.1016/J.JHAZMAT.2020.123882.

[74]   H. Gao, Y. Zhou, K. Chen, X. Li, Synthesis of Tb4O7 complexed with reduced graphene oxide for Rhodamine-B absorption, Mater Res Bull 77 (2016) 111–114. https://doi.org/10.1016/J.MATERRESBULL.2016.01.016.

[75]   S. Manavalan, U. Rajaji, S.M. Chen, T.W. Chen, R.J. Ramalingam, T. Maiyalagan, A. Sathiyan, Q. Hao, W. Lei, Microwave-assisted synthesis of gadolinium(III) oxide decorated reduced graphene oxide nanocomposite for detection of hydrogen peroxide in biological and clinical samples, Journal of Electroanalytical Chemistry 837 (2019) 167–174. https://doi.org/10.1016/J.JELECHEM.2019.02.023.

[76]   M.F.P. Da Silva, H.C. De Jesus Fraga Da Costa, E.R. Triboni, M.J. Politi, P.C. Isolani, Synthesis and characterization of CeO 2-graphene composite, J Therm Anal Calorim 107 (2012) 257–263. https://doi.org/10.1007/S10973-011-1924-8.

[77]   Y. Li, G. Wang, K. Pan, B. Jiang, C. Tian, W. Zhou, H. Fu, NaYF4:Er3+/Yb3+–graphene composites: preparation, upconversion luminescence, and application in dye-sensitized solar cells, J Mater Chem 22 (2012) 20381–20386. https://doi.org/10.1039/C2JM34113A.

[78]   M. Zhang, X. Liu, J. Huang, L. Wang, H. Shen, Y. Luo, Z. Li, H. Zhang, Z. Deng, Z. Zhang, Ultrasmall graphene oxide based T1 MRI contrast agent for in vitro and in vivo labeling of human mesenchymal stem cells, Nanomedicine 14 (2018) 2475–2483. https://doi.org/10.1016/J.NANO.2017.03.019.

1

[79]   A.J. Shen, D.L. Li, X.J. Cai, C.Y. Dong, H.Q. Dong, H.Y. Wen, G.H. Dai, P.J. Wang, Y.Y. Li, Multifunctional nanocomposite based on graphene oxide for in vitro hepatocarcinoma diagnosis and treatment, J Biomed Mater Res A 100A (2012) 2499–2506. https://doi.org/10.1002/JBM.A.34148.

[80]   A. Rodríguez-Galván, M. Rivera, P. García-López, L.A. Medina, V.A. Basiuk, Gadolinium-containing carbon nanomaterials for magnetic resonance imaging: Trends and challenges, J Cell Mol Med 24 (2020) 3779–3794. https://doi.org/10.1111/JCMM.15065.

[81]   S.S. Shinde, A. Sami, J.H. Lee, Lanthanides-based graphene catalysts for high performance hydrogen evolution and oxygen reduction, Electrochim Acta 214 (2016) 173–181. https://doi.org/10.1016/J.ELECTACTA.2016.08.050.

[82]   J. Zhang, Z. Zhang, Y. Jiao, H. Yang, Y. Li, J. Zhang, P. Gao, The graphene/lanthanum oxide nanocomposites as electrode materials of supercapacitors, J Power Sources 419 (2019) 99–105. https://doi.org/10.1016/J.JPOWSOUR.2019.02.059.

[83]   R. Rajagopal, K.S. Ryu, Facile hydrothermal synthesis of lanthanum oxide/hydroxide nanoparticles anchored reduced graphene oxide for supercapacitor applications, Journal of Industrial and Engineering Chemistry 60 (2018) 441–450. https://doi.org/10.1016/J.JIEC.2017.11.031.

[84]   S. Karthikeyan, M. Selvapandiyan, A. Sankar, Electrochemical performance of reduced graphene oxide (rGO) decorated lanthanum oxide (La_2O_3) composite nanostructure as asymmetric supercapacitors, Inorg Chem Commun 139 (2022) 109331. https://doi.org/10.1016/J.INOCHE.2022.109331.

[85]   P. Aryanrad, H.R. Naderi, E. Kohan, M.R. Ganjali, M. Baghernejad, A. Shiralizadeh Dezfuli, Europium oxide nanorod-reduced graphene oxide nanocomposites towards supercapacitors, RSC Adv 10 (2020) 17543–17551. https://doi.org/10.1039/C9RA11012G.

[86]   H.R. Naderi, M.R. Ganjali, A.S. Dezfuli, High-performance supercapacitor based on reduced graphene oxide decorated with europium oxide nanoparticles, Journal of Materials Science: Materials in Electronics 29 (2018) 3035–3044. https://doi.org/10.1007/S10854-017-8234-2.

—— CHAPTER 2 ——
Characterisation techniques

In this chapter, the main experimental techniques employed to characterise the carbon nanomaterials synthesised are presented. First, a general description of the technique is given and then, a brief summary of the instrumentation required is presented. Most experiments were carried out at the National Autonomous University of Mexico and the University of Groningen.

2.1. X-ray Diffraction

X-ray diffraction (XRD) is a non-destructive analytical technique used extensively for the characterisation of the crystal structure, but it can also give information on lattice strain, phase composition, and crystallite size.

The X-ray diffraction phenomenon is the consequence of the interaction between the electron clouds of the atoms of a crystalline sample and an incident monochromatic beam of X-rays. When the X-ray beam hits the sample with an incident angle θ the atoms of the top plane of the crystal diffract or scatter part of the light at the same angle θ, while the remaining light passes through with the same angle θ to be in part scattered at the second plane and so on. To create a constructive interference the path length difference between the X-rays scattered from consecutive planes must be equal to an integer number of wavelengths, as expressed by Bragg's law [1,2]:

$$n\lambda = 2d \sin \theta$$

where *n* is any integer, *λ* is the wavelength of the X-ray beam, θ is the incident angle, and *d* is the spacing between diffracting planes (Figure 2.1). Since in a crystal one can define multiple families of parallel planes with different *d*, for X-rays with a certain wavelength *λ*, the Bragg condition will be satisfied for each family of planes at a different incidence angle.
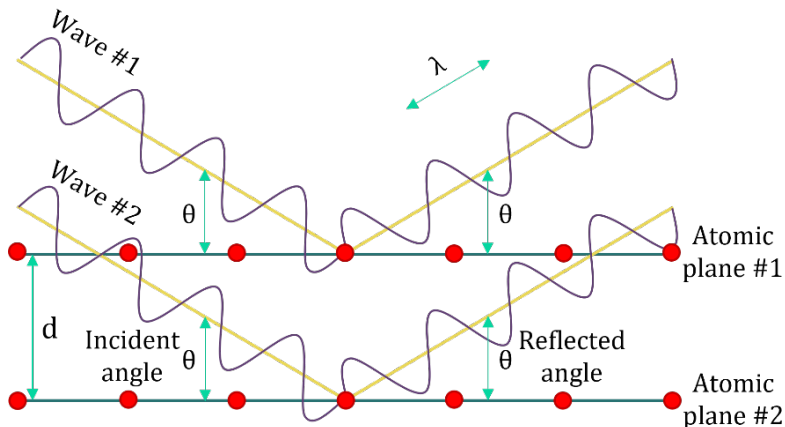
Figure 2.1. Bragg diffraction

2
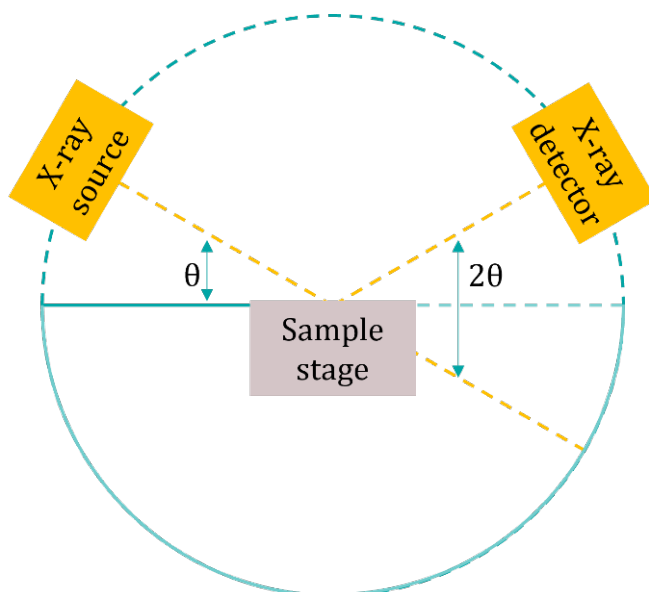
Figure 2.2. Scheme of the X-ray diffractometer

The X-ray equipment consists mainly of three items: An X-ray source, a sample holder, and an X-ray detector, typically using the Bragg-Brentano geometry (Figure 2.2) where the sample is rotated to change the incident angle. First, the X-rays from the source illuminate the sample, and then they are diffracted by the sample and enter the detector. The output, a graph reporting the X-ray intensity measured at the detector as a function of incident angle, is called a diffractogram.

The X-ray diffractograms reported in Chapters 3, 5, and 6 were collected on a D8 Advance Bruker diffractometer in Bragg-Brentano geometry with a monochromatic Cu Kα X-ray source (wavelength of 1.5418 Å) and a Lynxeye detector (RUG). Powder samples were first placed on a zero-background holder. The patterns were recorded in a 2θ range from 5 to 70 °, in steps of 0.02 ° and with a counting time of 0.75 s per step.

2.2. Raman Spectroscopy

Raman spectroscopy is a non-destructive analytical technique capable of detecting vibrational, rotational, and other low-energy modes in a molecule, providing information about a sample's chemical structure and molecular interactions.

When a sample is illuminated with monochromatic light of a certain wavelength, it is scattered either elastically or inelastically by the sample. Rayleigh scattering is the elastic interaction where the wavelength of the scattered light is identical to that of the incoming light. Raman scattering is the inelastic scattering, so the wavelength of scattered light differs from the incident light wavelength (Figure 2.3) and the Raman-responsive bond in the sample in a different rotational or vibration state. Raman scattering occurs if there is a change in bond polarizability associated with the excitation of de-excitation. This change in wavelength value is known as Raman shift and the energy of scattered light can be higher (Stokes scattering) or lower (anti-Stokes scattering) than the incident light. The Raman shift corresponds to the rotational or vibrational energies which in turn are a fingerprint of the presence of certain bonds in the sample studied [3,4].

The Raman setup consists principally of a light source, lenses, a filter, a mirror, and a light detector. Since Raman scattering is much weaker than Rayleigh scattering, the filter serves to block the Rayleigh scattered (Figure 2.4). The output obtained is a spectrum, where the intensity of the scattered light is plotted as a function of the Raman shift given by wavenumber (cm^{-1}).
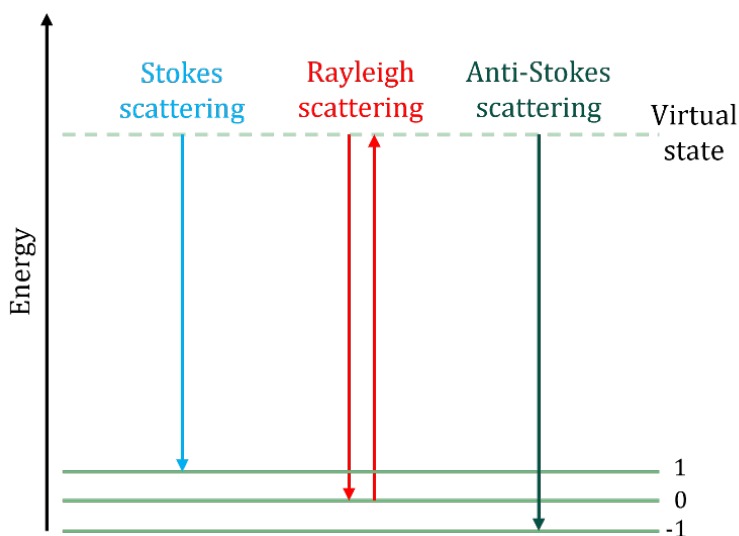
Figure 2.3. Diagram of different types of light scattering
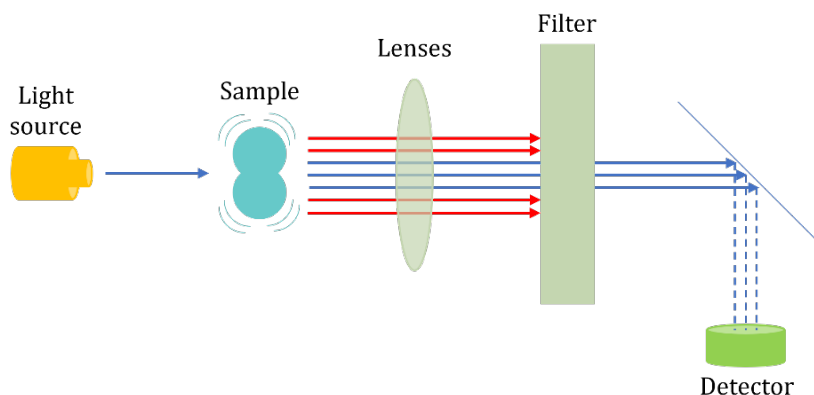
Figure 2.4. Scheme of Raman setup

The Raman spectra reported in Chapters 3 and 6 were collected on a Raman Witec alpha300R (WITec GmbH, Ulm, Germany) using a 532 nm wavelength laser light excitation from an Nd:YVO4 laser (UNAM). The incident laser beam with a power of 2.85 µW was focused on the sample using a 100x objective (Zeiss, 0.9 NA). Raman spectra were acquired in 10 points of every sample in a Raman shift range of 500-4000 cm^{-1}. Each spectrum was the average of 60 scans collected at 0.5 cm^{-1} resolution. The spectra were acquired by the author of the research with the help of Dr. Selene R. Islas at the Spectroscopic Characterisation University Laboratory of the Institute of Applied Sciences and Technology (ICAT) of UNAM.

The Raman spectra reported in Chapter 5 were acquired on a Nicolet Almega XR Dispersive Raman Thermo-Scientific spectrometer using a 532 nm wavelength laser light excitation (UNAM). The incident laser beam with a power of 2.85 µW was focused on the sample using a 100x objective. Raman spectra were collected in 10 points of every sample, in a Raman shift range of 500-4000 cm^{-1}. Each spectrum was the average of 30 scans collected at 0.5 cm^{-1} resolution. The spectra were acquired by the author of the research at the Spectroscopic Characterisation University Laboratory of the Institute of Applied Sciences and Technology (ICAT) of UNAM.

2.3. Fourier-Transform Infrared Spectroscopy

Fourier-transform infrared spectroscopy (FTIR) is a non-destructive analytical technique useful for identifying different functional groups present in a sample from the absorption of light with wavelengths in the infrared region.

2

Infrared spectroscopy harnesses the fact that molecules absorb photons at particular frequencies that are distinctive for different bonds. Infrared spectroscopy can detect changes in dipole moment after infrared radiation is passed through a sample, where some radiation is absorbed, and some is transmitted [5,6]. The absorbed radiation can be related to the characteristic vibrational frequencies of different functional groups.

The FTIR equipment consists of a light source, a beam splitter, a set of mirrors, a sample system, and a detector (Figure 2.5). The IR radiation beam coming from the broadband light source, typically a globar, passes through a Michelson interferometer, from which the outgoing beam is passed through the sample before being collected in the detector. Depending on the optical pathlength to and from the scanning mirror, different wavelengths reach the sample. The wavelength is calibrated with the help of a laser beam, which also passes through the interferometer. A Fourier Transform is employed to convert the output into a spectrum where the y-axis shows absorbance intensity, and the x-axis is the wavenumber (cm^{-1}).
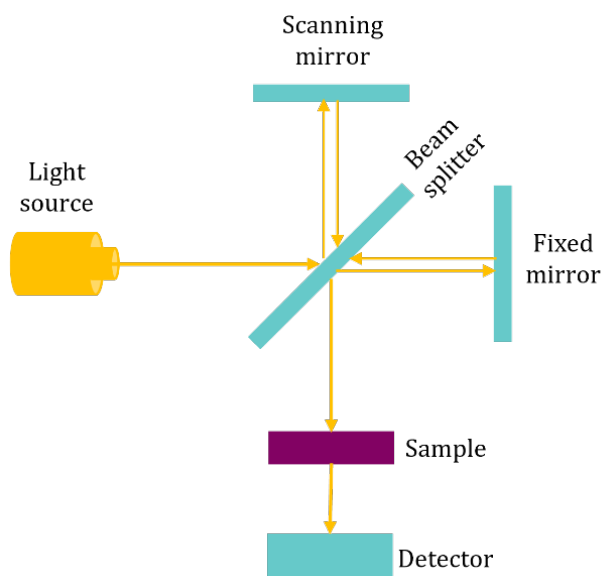

Figure 2.5. Scheme of a typical FTIR spectrometer

2

The FTIR spectra reported in Chapters 3, 5, and 6 were recorded under ambient conditions in the range of 500-4000 cm^{-1} on a Nicolet iS50R Thermo-Scientific spectrometer (UNAM). Each spectrum was the average of 32 scans, collected at 4 cm^{-1} resolution. The spectra were acquired by the author of the research at the Spectroscopic Characterisation University Laboratory of the Institute of Applied Sciences and Technology (ICAT) of UNAM.

2.4. X-ray Photoelectron Spectroscopy

X-ray photoelectron spectroscopy (XPS) is an analytical technique employed to determine the elemental composition, different chemical environments, and electronic states at the surface of a material.

XPS is based on the photoelectric effect. When a sample is irradiated with a monochromatic X-ray beam photoelectrons are emitted from the inner shells (see Figure 2.6(a)) travel through the sample to the surface, and, if the kinetic energy is higher than the work function, are able to leave the solid to be collected in the detector. There, both the number of photoelectrons, as well as their kinetic energy, are measured. The binding energy of a photoelectron can be determined utilising the following energy conservation law, as illustrated in the sketch in Figure 2.6 (b):

$$hv = E_{BE} + E_{KE} + \varphi$$

where *hv* is the energy of the X-ray beam, E_{KE} is the measured kinetic energy of the photoelectron, E_{BE} is the binding energy, and φ is the spectrometer work function [7–9]. The binding energy is characteristic of the elements and the core level from which the electron was emitted and also varies depending on the chemical environment the atom is in. The number of photoemitted electrons from a certain element (XPS intensity) is directly proportional to the number of atoms present in the probed volume, hence the binding energy can be used to identify and the XPS peak intensity to quantify the elemental composition. Measurements are conducted in ultrahigh vacuum so that the photoelectrons, which have lost energy not more than once on their way from the photoemitting atom to the sample surface can be related to the binding energy. For how long an electron of a certain kinetic energy can travel in the sample is given by the elastic mean free path but typically the XPS signal comes from the first 1-10 nm from the sample surface. Hence XPS is a surface-sensitive technique.

2
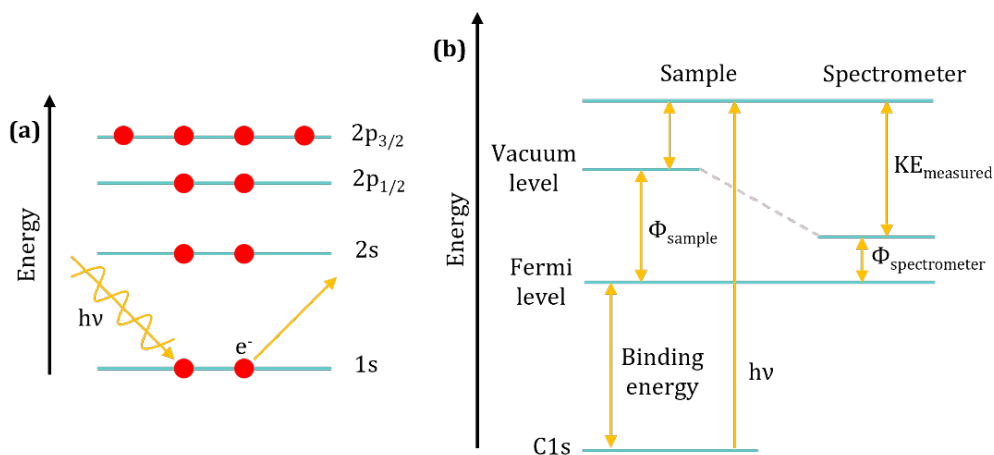
Figure 2.6. (a) Sketch of the core level photoemission process, (b) scheme of energy conservation law for X-ray photoelectron spectroscopy

The XPS instrument generally consists of a source of monochromatized X-rays, a sample stage, extraction lenses, a hemispherical analyser, and a detector, everything lodged within an ultra-high vacuum environment. First, the X-ray beam illuminates the sample and photoelectrons are emitted. Then, the photoelectrons are collected by the extraction lenses where their energy is usually retarded and lastly reach the analyser, as sketched in Figure 2.7. Only electrons with specific kinetic energy travel through the analyser and reach the detector; electrons that are too slow end up in the lower hemisphere, while the ones which are too fast, hit the outer hemisphere. The ensuing XPS spectrum reports the number of photoelectrons detected as a function of the binding energy.

Hemispherical
analyser

Electron
retarding lenses

Detector

Extraction
lenses

Electron
collection lenses

X-ray
beam

Sample

Stage
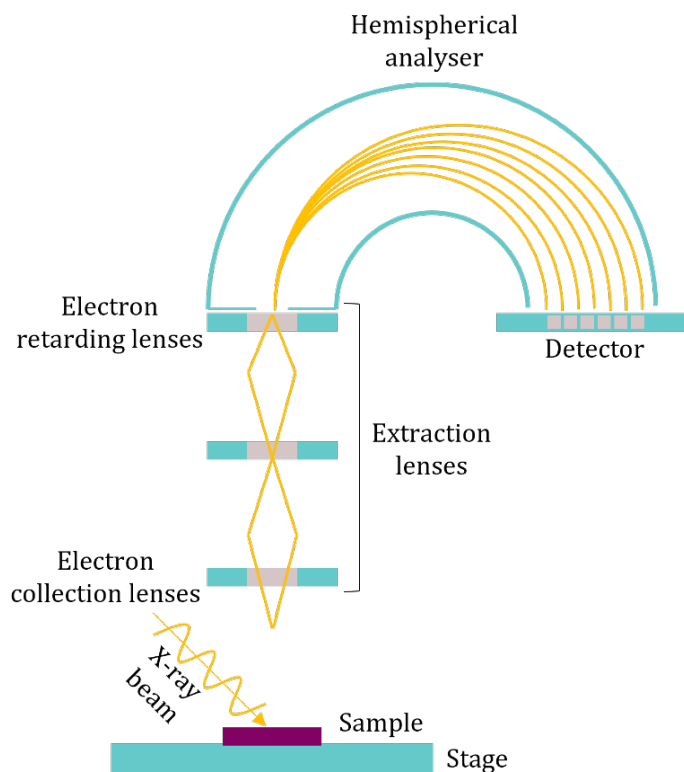
Figure 2.7. Scheme of a typical XPS instrument

The XPS spectra reported in Chapters 3 and 5 were collected with a Scanning XPS microprobe PHI5000 VersaProbe II system, equipped with a monochromatic Al Kα X-ray source ($h\nu$ = 1486.6 eV) (UNAM); the pressure in the chamber was maintained at 7×10^{-10} mbar during data acquisition and the electron take-off angle with respect to the surface normal was 45°. The XPS data were acquired by using a spot size of 100 μm in diameter and the energy resolution was 0.56 eV for the detailed spectra of core level regions; the programs PHI Multipack© version 9.6.0.15 and SDP© v 4.1 were employed for the deconvolution analysis. The measurements were performed by Lázaro Huerta from the Materials Research Institute (IIM) of UNAM.

The XPS spectra reported in Chapter 6 were collected with a Surface Science Instruments SSX-100 ESCA instrument with a monochromatic Al Kα X-ray source ($h\nu$ = 1486.4 eV) (RUG); the pressure in the chamber was maintained at 1×10^{-9} mbar during data acquisition and the electron take-off angle with respect to the surface normal was 37°. The XPS data were acquired on a spot size of 1000 μm in diameter and the

energy resolution was 1.3 eV for both the survey and the detailed spectra of core level regions; XPS spectra were analysed using the least-squares curve-fitting program Winspec (developed at the LISE laboratory of the University of Namur, Belgium). Deconvolution of the spectra included a Shirley [10] baseline and fitting with a minimum of peaks consistent with the chemical structure of the sample, taking into account the experimental resolution. The profile of the peaks was taken as a convolution of Gaussian and Lorentzian functions. The uncertainty in the peak intensity determination is 2 % for all core levels reported.

Binding energies (BEs) were referenced to the Au $4f_{7/2}$ photoemission peak [11] centred at 84.0 eV and accurate to ± 0.1 eV when deduced from the fitting procedure. All data were normalized to the number of scans and corrected for the sensitivity factor of the spectrometer. The transmission function of the analyser was corrected by the Atomic Sensitivity Factor (ASF) reported by Scofield [12] with the lanthanides reference materials. For all measurements, powder samples were dispersed in isopropanol, sonicated for 5 min, and drop-casted on a thin gold film, grown on mica. All measurements were carried out on freshly prepared samples; data were collected on three spots in each case to check for homogeneity.

2.5. Scanning Electron Microscopy

Scanning electron microscopy (SEM) provides information about the morphology of a sample by scanning its surface with a focused electron beam producing detailed and magnified images of the electrons coming back from the sample. When the electrons interact with the sample atoms, they lose energy because of scattering and absorption processes and produce secondary electrons, backscattered electrons, and characteristic X-rays that are collected by different types of detectors. Secondary electrons carry information about morphological features, backscattered electrons about the distribution of different elements with different atomic masses, and X-rays can be used to identify and quantify the elements present in the sample [13,14]. The latter is called Energy Dispersive X-ray Spectroscopy, or EDS. It is important to note that SEM can give information about the lateral size of morphological features but not about their height.

In a scanning electron microscope, the principal components are the electron source, the electromagnetic lenses, the scanning coils, the objective lenses, a sample stage, and different detectors, everything housed in a vacuum environment, as sketched

in Figure 2.8. The electron beam coming from the electron gun is narrowed in lateral size with the condenser lenses. Then, the beam is deflected using the deflecting coils and focused with the objective lenses. Finally, the electron beam interacts with the sample and the secondary electrons, backscattered electrons, and X-rays are produced and collected with the appropriate detectors.

The SEM images reported in Chapters 3 and 5 were collected with a JEOL JSM 6510LV microscope operated at a voltage of 20 kV (UNAM); the backscattered mode was employed. The SEM instrument was coupled to an INCA Energy 250 Energy Dispersive X-ray (EDS) Microanalysis System from Oxford Instruments. The measurements were performed by Dr. Victor Meza-Laguna from the Nuclear Science Institute (ICN) of UNAM.
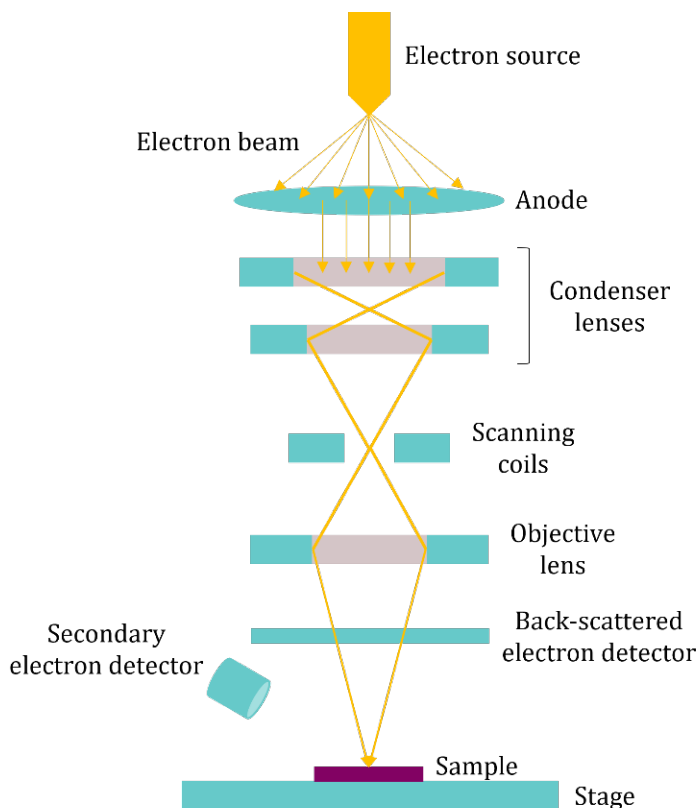
Figure 2.8. Scheme of typical SEM setup

The SEM images reported in Chapters 4 and 6 were recorded at the University of Groningen with an FEI NovaNano SEM 650 microscope operating at an acceleration voltage of 20 kV and fitted with an Ametek EDAX-TLS electron backscatter diffraction (EBSD) system.

2.6. Transmission Electron Microscopy

Transmission electron microscopy (TEM) is a technique employed to study the size, morphology, and crystal structure of small samples.

The TEM images are acquired by using a high-energy electron beam impinging perpendicular to a thin sample, and then the scattered and transmitted electrons can form an image [15,16]. Multiple detectors can be utilised for imaging, such as the bright-field (BF), the dark-field (DF), and the high-angle annular dark-field (HAADF) detector. Scanning Transmission Electron Microscopy (STEM) can be employed as an alternative to TEM; while in TEM a parallel electron beam is perpendicularly focused with respect to the sample plane, in STEM the electron beam is focused at a large angle which converges into a focal point.

The transmission electron microscope consists of mainly three parts, an electron gun, electromagnetic lenses, the sample stage, a fluorescent screen, and a digital camera arranged as sketched in Figure 2.9. The electron beam coming from the electron gun is focused utilising the condenser lens to obtain a small and coherent beam that hits the sample and if the sample is thin enough, a large part of the electrons is transmitted and focused using objective lenses onto a phosphor screen or a camera. In the image, the darker areas represent parts of the sample where fewer electrons are transmitted; in lighter areas, more electrons are transmitted.
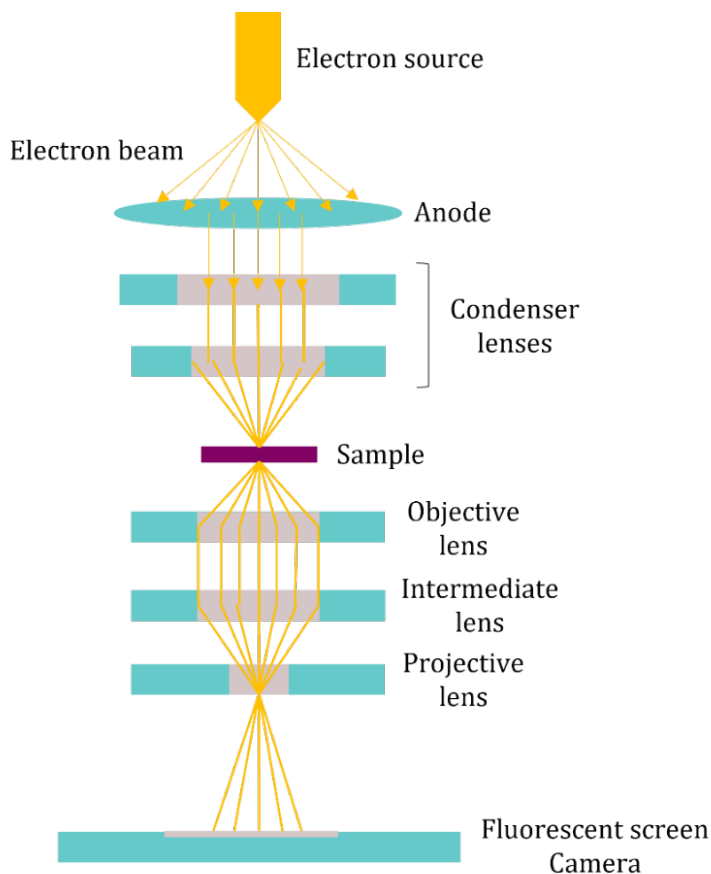
Figure 2.9. Scheme of typical TEM setup

The DF-TEM images reported in Chapters 3 and 4 were collected with a JEOL JEM-ARM200F STEM operated at 1.0 Å resolution and 200 kV voltage and provided with a Schottky field emission gun. This instrument is located at UNAM. Samples were dispersed in isopropanol, sonicated for 5 min, and drop-casted using standard grids with collodion support films. The images were collected by Josué Esau Romero-Ibarra from the Materials Research Institute (IIM) of UNAM.

The DF-STEM images reported in Chapters 5 and 6 were collected with an FEI NovaNano SEM 650 system at an acceleration voltage of 20 kV; this system is located at the University of Groningen. Samples were dispersed in isopropanol, sonicated for 5 min, and drop-casted using standard Cu grids with holey carbon films.

2.7. Thermogravimetric Analysis

Thermogravimetric analysis (TGA) serves to study the thermal stability of different types of materials such as composites and polymers. Thermogravimetric analysis monitors the weight changes of a sample as a function of increasing temperature or time (heated at a constant rate) when a gas passes over it. These changes can indicate processes like physisorption, chemisorption, phase transitions, sublimation, desolvation, and decomposition [16,17].

The TGA instrument consists of a very sensitive balance to measure mass changes and a furnace that can be programmed to control the heating rate of the sample (Figure 2.10). First, the weight of a sample is measured using a balance inside the furnace that is filled with constant gas flow. Then, the sample is heated, and its mass change is recorded. The output is a plot of the weight as a function of either temperature or time.
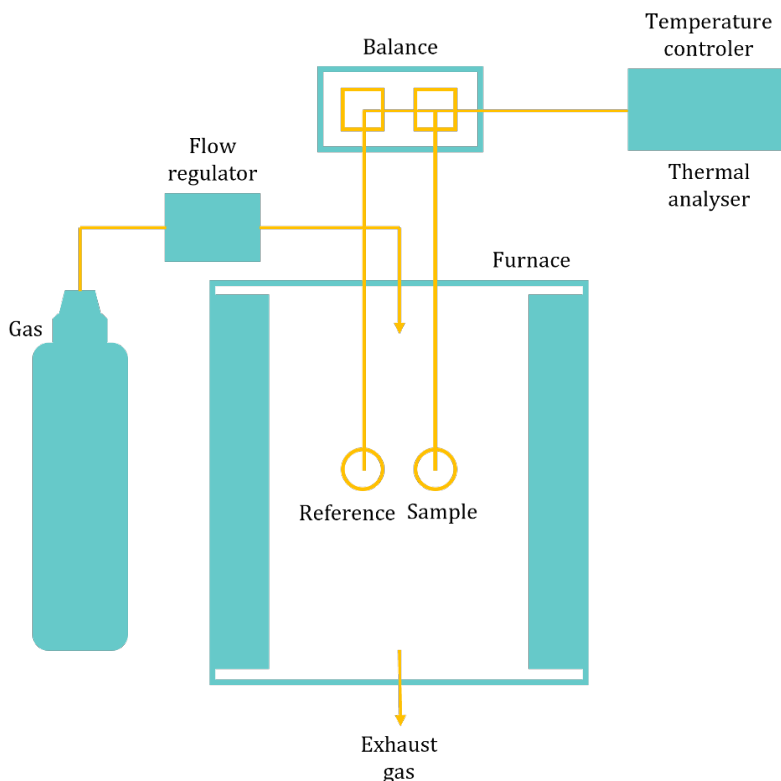
Figure 2.10. Scheme of typical TGA setup

For the TGA-DTA thermograms reported in Chapters 3 and 6, the data were collected at the University of Groningen on an SDT 2960 Simultaneous DSC-TGA analyser from TA Instruments in air; the airflow was 100 mL/min and a heating ramp of 10 °C/min was applied until 1000 °C were reached. Samples of approximately 5 mg were used.

For the TGA-DTA thermograms reported in Chapter 5, the weight losses were recorded on an STA 449 C Jupiter analyser from Netzsch-Gerätebau GmbH in air located at UNAM; the airflow was 50 mL/min and a heating ramp of 10 °C/min was applied until 1000 °C were reached. Samples of approximately 5 mg were used. The measurements were performed by Dr. Edgar Álverez-Zauco from the Faculty of Sciences of UNAM.

References

[1]   N. Raval, R. Maheshwari, D. Kalyane, S.R. Youngren-Ortiz, M.B. Chougule, R.K. Tekade, Importance of Physicochemical Characterization of Nanoparticles in Pharmaceutical Product Development, Basic Fundamentals of Drug Delivery (2019) 369–400. https://doi.org/10.1016/B978-0-12-817909-3.00010-8.

[2]   M. Gumustas, C.T. Sengel-Turk, A. Gumustas, S.A. Ozkan, B. Uslu, Effect of Polymer-Based Nanoparticles on the Assay of Antimicrobial Drug Delivery Systems, Multifunctional Systems for Combined Delivery, Biosensing and Diagnostics (2017) 67–108. https://doi.org/10.1016/B978-0-323-52725-5.00005-8.

[3]   D.D. Le Pevelen, NIR FT-Raman, Encyclopedia of Spectroscopy and Spectrometry (2017) 98–109. https://doi.org/10.1016/B978-0-12-409547-2.12150-X.

[4]   A.K. Adya, E. Canetta, Nanotechnology and Its Applications to Animal Biotechnology, Animal Biotechnology: Models in Discovery and Translation (2014) 247–263. https://doi.org/10.1016/B978-0-12-416002-6.00014-6.

[5]   N.N. Daéid, FORENSIC SCIENCES | Systematic Drug Identification, Encyclopedia of Analytical Science: Second Edition (2005) 471–480. https://doi.org/10.1016/B0-12-369397-7/00197-7.

[6]   S. Wen, J. Liu, J. Deng, Methods for the detection and composition study of fluid inclusions, Fluid Inclusion Effect in Flotation of Sulfide Minerals (2021) 27–68. https://doi.org/10.1016/B978-0-12-819845-2.00003-X.

[7]   R.R. Mather, Surface modification of textiles by plasma treatments, Surface Modification of Textiles (2009) 296–317. https://doi.org/10.1533/9781845696689.296.

[8]   M. Omidi, A. Fatehinya, M. Farahani, Z. Akbari, S. Shahmoradi, F. Yazdian, M. Tahriri, K. Moharamzadeh, L. Tayebi, D. Vashaee, Characterization of biomaterials, Biomaterials for Oral and Dental Tissue Engineering (2017) 97–115. https://doi.org/10.1016/B978-0-08-100961-1.00007-4.

[9]   F.A. Stevie, C.L. Donley, Introduction to x-ray photoelectron spectroscopy, Journal of Vacuum Science & Technology A 38 (2020) 063204. https://doi.org/10.1116/6.0000412/1024200.

[10]   D.A. Shirley, High-Resolution X-Ray Photoemission Spectrum of the Valence Bands of Gold, Phys Rev B 5 (1972) 4709. https://doi.org/10.1103/PhysRevB.5.4709.

[11]   J.F. Moulder, W.F. Stickle, P.E. Sobol, K.D. Bomben, Handbook of X-Ray Photoelectron Spectroscopy (Perkin-Elmer, Eden Prairie, MN, 1992), Google Scholar (2002) 128. https://books.google.com/books/about/Handbook_of_X_ray_Photoelectron_Spectros.html?hl=es&id=A_XGQgAACAAJ (accessed July 17, 2023).

[12]   J.H. Scofield, Hartree-Slater subshell photoionization cross-sections at 1254 and 1487 eV, J Electron Spectros Relat Phenomena 8 (1976) 129–137. https://doi.org/10.1016/0368-2048(76)80015-1.

[13]   A.K. Singh, Experimental Methodologies for the Characterization of Nanoparticles, Engineered Nanoparticles (2016) 125–170. https://doi.org/10.1016/B978-0-12-801406-6.00004-2.

[14]   T.A. Silva, J.S. Stefano, B.C. Janegitz, Sensing Materials: Nanomaterials, Encyclopedia of Sensors and Biosensors: Volume 1-4, First Edition 1–4 (2023) 212–230. https://doi.org/10.1016/B978-0-12-822548-6.00023-6.

[15]   P. Sciau, Transmission Electron Microscopy: Emerging Investigations for Cultural Heritage Materials, Advances in Imaging and Electron Physics 198 (2016) 43–67. https://doi.org/10.1016/BS.AIEP.2016.09.002.

[16]   M. Nasrollahzadeh, M. Atarod, M. Sajjadi, S.M. Sajadi, Z. Issaabadi, Plant-Mediated Green Synthesis of Nanostructures: Mechanisms, Characterization, and Applications, Interface Science and Technology 28 (2019) 199–322. https://doi.org/10.1016/B978-0-12-813586-0.00006-7.

[17]   K.R. Rajisha, B. Deepa, L.A. Pothan, S. Thomas, Thermomechanical and spectroscopic characterization of natural fibre composites, Interface Engineering of Natural Fibre Composites for Maximum Performance (2011) 241–274. https://doi.org/10.1533/9780857092281.2.241.

—— CHAPTER 3 ——

Solvothermal synthesis of lanthanide-functionalised graphene oxide nanocomposites

In this chapter, we present a facile approach to the preparation of graphene oxide composites with lanthanide oxide/hydroxide nanoparticles (Ln = La, Eu, Gd, Tb) under relatively mild conditions by two different procedures of solvothermal synthesis. The mechanism of graphene oxide-lanthanide nanocomposite formation is thought to involve the initial coordination of Ln^{3+} ions to the oxygen-containing groups of graphene oxide as nucleation sites, followed by Ln_2O_3 and $Ln(OH)_3$ nanoparticle growth. The nanocomposites obtained preserve the intrinsic planar honeycomb-like structures of graphene as proven by the typical G and D bands in the Raman spectra. Fourier-transform infrared and X-ray photoelectron spectroscopy confirmed the interaction between oxygen-containing groups of graphene oxide and lanthanide ions. The size and distribution of Ln oxide/hydroxide nanoparticles on graphene oxide sheets, estimated from scanning and transmission electron microscopy images, vary broadly for the different lanthanides. The size can span from sub-nm dimensions for Eu oxide to more than 10 μm for Eu hydroxide nanoparticles. The most homogeneous distribution of lanthanide oxide/hydroxide nanoparticles was found in La-containing composites. Thermogravimetric analysis demonstrated that all the graphene oxide-lanthanide nanocomposites are thermally less stable, by up to 30 °C than pristine graphene oxide.

3.1. Introduction

The graphene "gold rush" has resulted in the development of countless applications including electrochemical energy storage, sensors, and catalysts, using graphene (G) and graphene oxide (GO)-based materials. Surface functionalization with different metal species - single ions, neutral atoms, or nanoparticles [1–3] - is a frequently explored approach to the development of metal-graphene composites. Among the most attractive metals are lanthanides, whose electronic configuration consists of filled [Xe]6s levels and 4f orbitals that are gradually filled as the atomic number increases. These 4f orbitals are strongly shielded from the external environment by the 5s5p6s orbitals, and therefore the ligands of lanthanide complexes cause only small perturbations in the 4f electron structure, and the lanthanides retain their properties [4]. Lanthanide ions are preferred dopants for diverse nanoparticles due to their outstanding properties such as stable luminescence, high fluorescence quantum efficiency, long luminescence lifetimes, and low toxicity [5–9]. The combination of the unique characteristics of carbon nanomaterials, in particular graphene, with those of lanthanides, opens a way to the preparation of novel materials with unusual magnetic, luminescent, catalytic, biological, and other properties useful for a broad spectrum of applications in different areas of science, technology, and medicine [10–15].

Using graphene oxide as a solid support for lanthanide deposition can be advantageous because of the presence of oxygen-containing functional groups that promote the nucleation of metal-containing nanoparticles [16–21].

Many previously published works are focused on the interaction of lanthanide compounds with GO. However, most of them are limited to considering Ln ion and/or complex adsorption on different active sites, particularly the carboxylic groups of GO. Ashour et al. [22] reported the adsorption of La(III), Nd(III), Gd(III) and Y(III) ions as a dependent effect of the pH, because higher values of pH increase the degree of GO deprotonation and the negative charges on the GO surface promote the electrostatic interaction with Ln(III) ions. Narayanam *et al.* [23] studied the luminescence tunability of Eu(III) functionalized GO sheets in green and red wavelength regions but Eu(III) does not form nanoparticles, instead, its isolated ions bind with oxygen functionalities of GO. Pang et al. [24] designed and synthesized a luminescent terbium complex containing GO. In this case, Tb does not form nanoparticles, instead, it complexes with N2,N6-bis(4-aminobutyl)pyridine-2,6-dicarboxamide, forming a coordination compound, whose synthesis is a multi-step and ecologically unfriendly process. Wang *et al.* [25] described the preparation of Eu^{3+} and Tb^{3+} complex with GO for the detection of bacterial spores and cysteine, but first GO has to be covalently modified by grafting 1,2-Bis(2-

aminoethoxy)ethane and ethylenediamine tetraacetic acid dianhydride (EDTAD) and later the coordination with Eu^{3+} and Tb^{3+} ions is achieved. Although these studies emphasise in adsorption and coordination of Ln(III) ions, reports on lanthanide-containing nanoparticles deposition onto GO (that is, on the synthesis of genuine GO-Ln nanocomposites) are much scarce. Jenkins et al. [26] and Jabeen et al. [27] reported the preparation of GO-Ln_2O_3 (namely Sm_2O_3, Dy_2O_3, Gd_2O_3, and Er_2O_3) nanocomposites showing AFM images revealing a particle size distribution in the nano range from 10 to 60 nm and agglomerates around 150 nm. Zhang et al. [28] synthesized a reduced GO/lanthanum oxide nanocomposite as an electrode material in a supercapacitor where La_2O_3 nanorods obtained have a diameter of about 20 nm utilising a long-time heating reflux reaction. Aryanrad *et al.* [29] produced a GO/europium oxide nanorods nanocomposite where Eu nanorods present a diameter larger than 30 nm, but europium oxide nanorods have to be prepared previous their integration with GO as a self-assembly approach.

Subasri et al. [30] reported simple solvothermal reduction as a method to prepare a novel nanohybrid of $La(OH)_3$ electrostatically anchored onto 2D-graphene nanosheets and investigated as an electrode material for supercapacitors; unfortunately, this methodology required long reaction times, as well as DMF as reaction media and the previous preparation of $La(OH)_3$ nanoparticles, not to mention that it was tested only for lanthanum, and not for lanthanides having partially or totally filled 4*f* orbitals. Nanoparticle size in $La(OH)_3$/GO nanocomposite is around 7 nm and it is estimated by employing XRD, but it is not confirmed by microscopy studies (the use of transmission electron microscopy, TEM, is highly desirable or even mandatory). Sharma *et al.* [31] developed a hydrothermal method-assisted synthesis of Ce, Tb, and Ce/Tb-doped binary GO nanocomposites, using ionic liquid (1-butyl-3-methyl tetrafluoroborate) as reaction medium and fluorinating agents; the sizes of the reported nanoparticles are of 20-29 nm for CeF_3:Tb^{3+}-GO and LaF_3:Ce^{3+}/Tb^{3+}-GO and around 80 nm for BaF_2:Ce^{3+}-GO and BaF_2:Ce^{3+}/Tb^{3+}-GO nanocomposites.

Thus, the traditional synthetic routes for the preparation of composites based on carbon nanomaterials and lanthanides are carried out in an organic solvent, the amount of organic solvent used is large, compared with the amount of nanomaterial used, which is undesirable given the harmful effects on the environment and human health these solvents can produce. Other significant disadvantages one should mention are elevated costs, difficulties in impurity removal, and special equipment requirements. For this reason, molten medium methods are a great alternative when it comes to developing more scalable, facile, and efficient processes for different types of nanoparticles [32,33]. Furthermore, solvothermal synthesis is a well-known one-step

technique for obtaining nanomaterials with high yields and at low cost. In addition to offering advantageous features like fast and uniform heating of the material and mild reaction conditions [34–39], this method can yield thermodynamically stable as well as metastable materials, which cannot be easily obtained through other synthetic routes. The ability to control the size and shape of target nanoparticles makes solvothermal synthesis especially valuable for applications in nanocircuits and devices. The process employs solvents under moderate to high pressure (typically between 1 and 10,000 atm) and temperature (typically between 100 °C and 1000 °C), which considerably facilitates the interaction of precursors during synthesis [40]. For example, Li *et al.* [41] employed solvothermal synthesis to decorate nitrogen-doped graphene with Fe_2O_3 and obtained uniformly dispersed and chemically bonded Fe_2O_3 nanocrystals that can be used as synergistic microwave absorbers. Another example is the synthesis of nanocomposites with carbon dots and Ag nanoparticles/TiO_2 studied by Wang *et al.* [42] to produce photocatalysts for environmental remediation.

However, in terms of the application of a broader variety of lanthanides and more environmentally friendly reaction media, the preparation of Ln-functionalized GO [30,31] deserves further exploration and improvements. Accordingly, the study described here focused on the solvothermal synthesis of lanthanide-functionalized graphene oxide nanocomposites. Two different preparation pathways for GO decorated with lanthanide oxide and hydroxide nanoparticles were tested for La, Eu, Gd and Tb. The nanocomposites obtained were characterized by several spectroscopic, microscopic, and thermal analysis techniques.

3.2. Experimental

3.2.1. Materials

La(III), Eu(III), Gd(III) and Tb(III) acetate hydrates (all having 99.9 % purity), ethyl alcohol (CH_3CH_2OH, ≥ 99.5 %), citric acid ($C_6H_8O_7$, ≥ 99.5 %), and potassium hydroxide (KOH, ≥ 85 %) were purchased from Sigma-Aldrich and used as received. Single-layer graphene oxide was purchased from Cheap Tubes, Inc. (>99 wt% purity, sheet size of 300-800 nm and thickness of 0.7-1.2 nm).

3.2.2. Solvothermal synthesis

Two series of GO-Ln nanocomposites were prepared using the solvothermal

synthetic approach (Figure 3.1.).

3.2.2.1. Series 1 labelled as GO-Ln-1

20 mg of GO was mixed with 2 mg of Ln(III) acetate hydrate in 10 mL of ethyl alcohol. The mixture was stirred for 5 min. Then, the solution was transferred to a Teflon-lined stainless-steel autoclave (25 mL) and heated at 170 °C for 4 h. Once the reaction was finished, the resulting mixture was dried under ambient conditions. The powder obtained was further heated at 300 °C for 3 h in air. The samples obtained are denoted hereafter as GO-La-1, GO-Eu-1, GO-Gd-1, and GO-Tb-1.

3.2.2.2. Series 2 labelled as GO-Ln-2

2 mg of Ln(III) acetate hydrate and 0.25 mmol of citric acid were dissolved in 20 mL of deionized water. At the same time, a 10 mL aqueous solution containing 10 wt% potassium hydroxide and 20 mg GO was prepared. The lanthanide solution was added to the KOH solution and stirred for 5 min. The prepared mixture was transferred to a Teflon-lined stainless-steel autoclave (50 mL) and heated at 170 °C for 4 h. Once the reaction was finished, the product was centrifuged to collect the solid phase, which was washed three times with deionized water (this methodology was adapted from the one described in [43]). The samples obtained are denoted hereafter as GO-La-2, GO-Eu-2, GO-Gd-2, and GO-Tb-2.
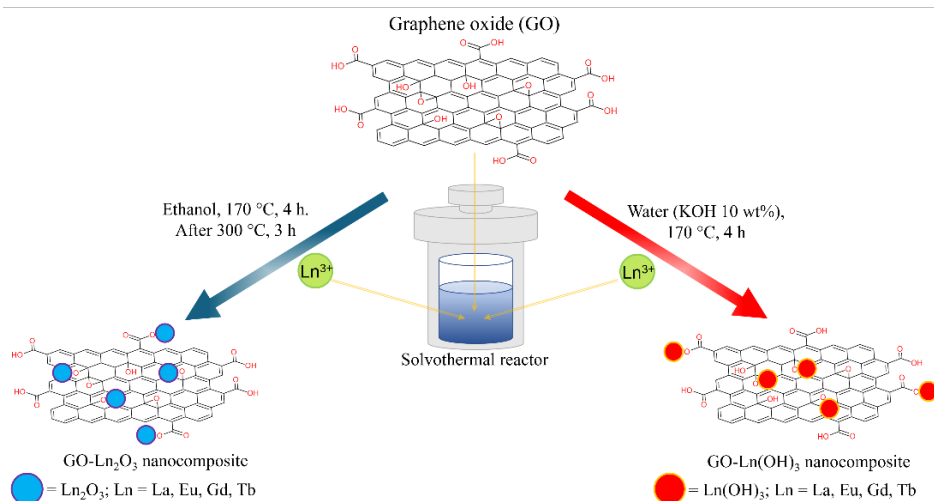
Figure 3.1. Solvothermal synthesis employed for the preparation of GO-Ln oxides and hydroxides nanocomposites

3.3. Results and discussion

Detailed information on the composition, morphology, and structure of the nanohybrid materials was obtained from Fourier-transform infrared spectroscopy (FTIR), Raman spectroscopy, energy dispersive spectroscopy (EDS), X-ray photoelectron spectroscopy (XPS), X-ray diffraction (XRD), scanning electron microscopy (SEM) and high-resolution transmission electron microscopy (HRTEM), as well as thermogravimetric analysis (TGA) and differential thermal analysis (DTA).

The Raman spectra of all samples (Figure 3.2) showed the presence of the characteristic D band centred at about 1350 cm^{-1}, which is related to C-C bond disorder (sp^3-hybridized carbon atoms), and the G band located at 1595 cm^{-1}, which is caused by stretching vibrations of C=C of the sp^2 hybridized carbon backbone [44–47]. For both series, the ratio between D and G band intensities (I_D/I_G) did not exhibit tangible changes: I_D/I_G amounted to 0.99 for pristine GO to 1.00 for all GO-Ln hybrids, thus implying that neither the solvothermal treatment nor the interaction of lanthanide ions with the GO affected the ratio between sp^3- and sp^2-hybridized carbon atoms.
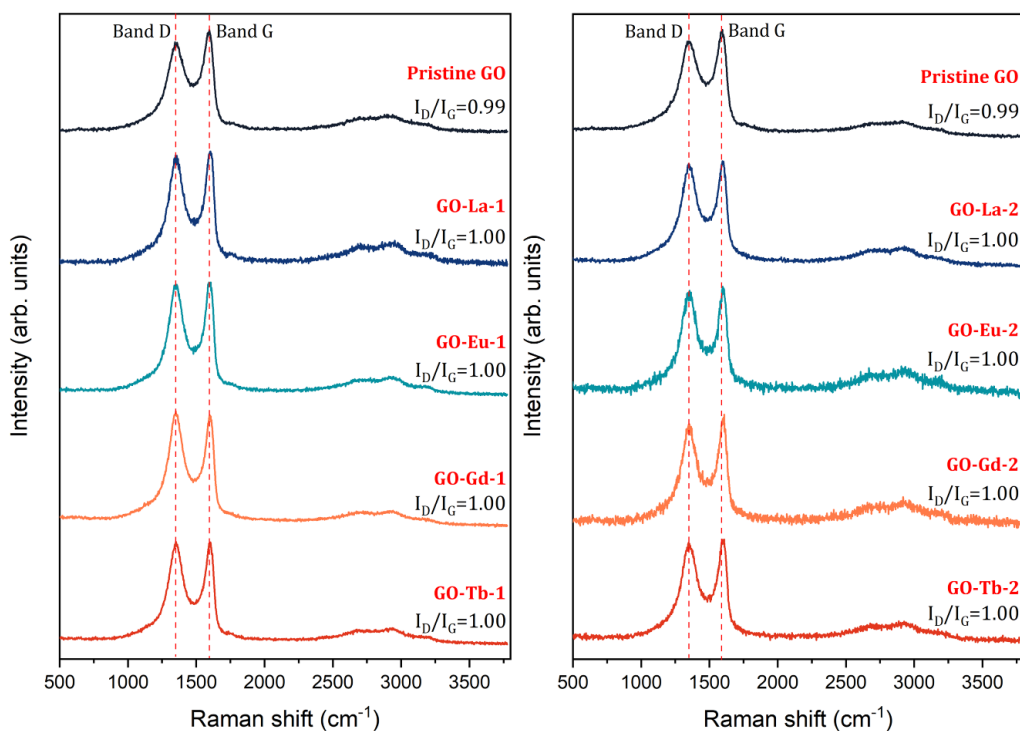
Figure 3.2. Comparison of the Raman spectra of GO-Ln-1 and GO-Ln-2 samples

The FTIR analysis (Figure 3.3) revealed evident changes upon the solvothermal chemical modification of GO sheets. Pristine GO showed typical peaks due to the presence of oxygen-containing functional groups [48,49]: the broad stretching hydroxyl ν_{OH} band at 3363 cm^{-1} and the corresponding deformation δ_{OH} band at 1618 cm^{-1}, stretching $\nu_{C=O}$ vibrations in COOH groups at 1720 cm^{-1}, a strong band at 1224 cm^{-1} due to asymmetric and symmetric stretching modes of epoxy C-O-C groups, a band at 1052 cm^{-1} associated with C-O stretching vibrations, and a shoulder at 965 cm^{-1} due to unsaturated ketone groups. Weak symmetric and asymmetric ν_{C-H} bands at 2981 and 2959 cm^{-1} and a signal of unoxidized sp^2 C=C bonds at 1552-1593 cm^{-1} could be observed as well.

While in the FTIR spectra of GO-Ln samples for both Series 1 and 2, the intensity of the broad hydroxyl ν_{OH} stretching band at 3363 cm^{-1} significantly decreased, and some differences were found depending on the particular synthetic approach. The most noticeable changes observed for the samples of Series 1 were the frequency shift of the epoxy band to 1232 cm^{-1} for GO-La-1, 1208 cm^{-1} for GO-Eu-1, and 1201 cm^{-1} for both GO-Gd-1 and GO-Tb-1, indicating an epoxide ring opening reaction. Figure 3.3 shows
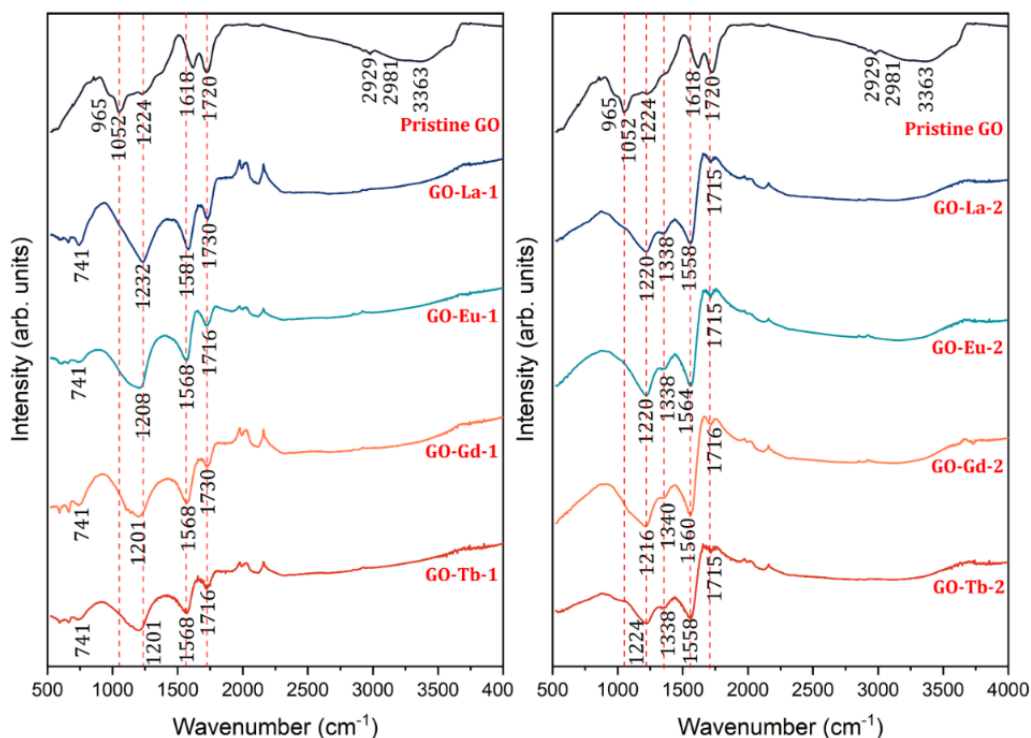

Figure 3.3. Comparison of the FTIR spectra of GO-Ln-1 and GO-Ln-2 samples

a decrease in the intensity of the COOH band and an almost total disappearance of the C-O signal at 1052 cm^{-1} for all GO-Ln-1 samples. On the other hand, one can see an intensity increase for the band corresponding to the vibrations of unoxidized sp^2 C=C bonds at 1568-1581 cm^{-1}, as well as emerging bands at 724-550 cm^{-1} related to the Ln-O vibrations. For the Series 2 samples, the epoxy band ($\sim$1220 cm^{-1}) increased in intensity and became broader. In addition, the band intensity due to the COOH group decreased, along with the total disappearance of the C-O signal at 1041 cm^{-1}, an intensity increase of the band due to sp^2 C=C bond vibrations at 1552-1593 cm^{-1}, and the appearance of a band near 1340 cm^{-1} corresponding to stretching C-O bond vibrations in alcohols. As a whole, all the FTIR spectra presented are indicative of structural changes in the oxygen-containing groups of GO, which can be interpreted as pointing to the chemical bonding of Ln ions to GO sheets by replacing H atoms of OH, COOH functionalities or breaking C-O-C bonds. The pH media apparently plays an important role for Series 2, where the use of KOH and water media in the solvothermal process fosters the interaction of Ln ions with COOH groups, rather than the interaction with epoxy groups.

Further details of the chemical bonding in GO-Ln samples in comparison to pristine GO were obtained from XPS measurements. XPS spectra of the C1s, O1s and Ln 3d core level regions are shown in Figure 3.4, Figure 3.5 and Figure 3.6, respectively; the corresponding binding energies and the percentages indicating the relative at% are listed in Table 3.1, Table 3.2, Table 3.3, and Table 3.4. The fit of the C1s core level spectrum of pristine GO (Figure 3.4) requires six components at binding energies (BEs) of 284.2, 285.0, 285.9, 287.2, 288.2 and 289.3 eV, attributed respectively to the presence of CH-CH, C-C, C-CH$_2$, C-O, C=O and COOH bonds. Their contributions to the total C1s spectral intensity amounted to 8.6, 25.8, 16.9, 32.9, 8.5 and 7.5 %, respectively. After the solvothermal treatment, with the incorporation of Ln(III) ions on GO, the most remarkable change for both sample series was the appearance of a new component at a BE of 287.5-287.8 eV, attributed to the bond between Ln atoms and GO oxygenated functionalities. The relative contribution of this component to the total C1s spectral intensity varies from 6.4 % for La to 19.6 % for Gd. Although the bonding nature in lanthanide compounds is still under discussion [50], this effect might be linked to the difference in the electron configuration of the two lanthanide ions, which is [Xe]4f^0 for La^{3+} and [Xe]4f^7 for Gd^{3+}. Therefore, with a higher number of 4f electrons, the Gd^{3+} ion can exhibit a higher coordination number, i.e. form a larger number of chemical bonds with functional groups in the reaction medium: in the present case, with oxygenated functionalities of GO. To put it in a different way, as the Ln atomic number increases, the ionic radius decreases and hence the charge density of the cation increases, leading to the differences observed. The peak related to C-O for all GO-Ln samples downshifts by approximately 0.6 eV (to 286.5 eV), and the contributions related to

C=O and COOH exhibited similar shift higher binding energies, namely to 288.9 and 290.5 eV, respectively, indicating that the integration of Ln ions can also change the electronic charge of oxygen-containing groups of GO. Also, the relative intensity related to the oxygen-containing groups decreases for C-O to 13.5-27.9 %, for C=O to 5.4-8.9 % and for COOH to 1.7-4.8 % of the total C1s intensities. It can be said, hence, that the solvothermal conditions promote the chemical reaction of C-O, C=O, and COOH groups to C-O-Ln bonds and change the nature of oxygen functional groups of GO.
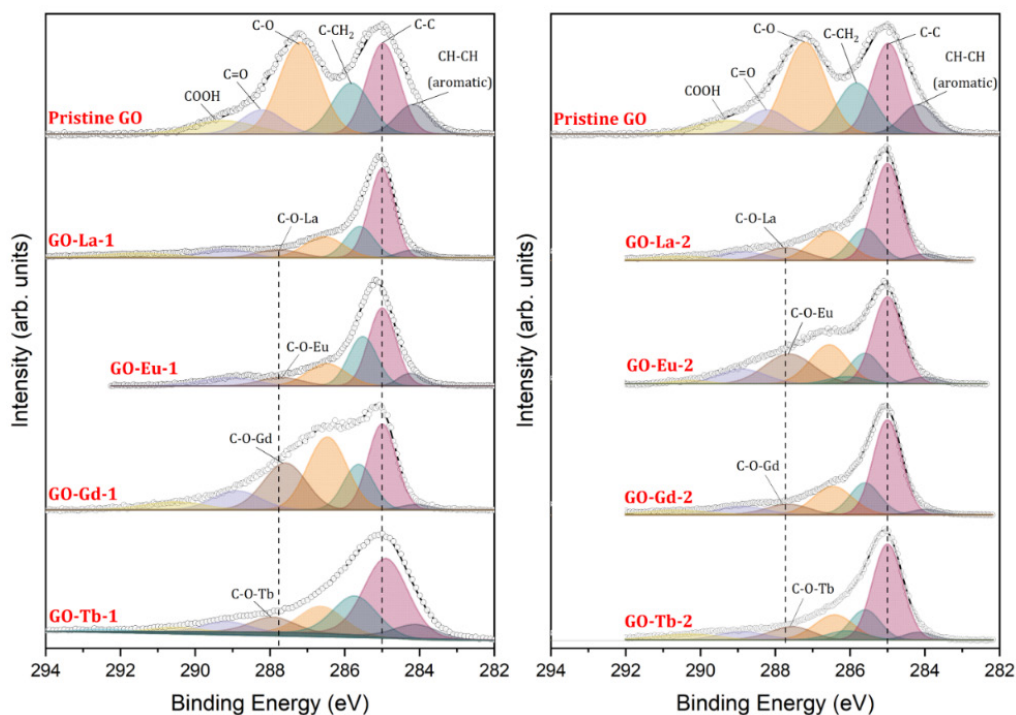

Figure 3.4. Comparison of the XPS spectra of the C1s core level region of GO-Ln-1 and GO-Ln-2 samples. The corresponding fits are also shown

Table 3.1. XPS binding energies of the C1s core level components of GO-Ln-1 and GO-Ln-2 samples

Sample	Binding energies (eV) of C1s components due to different bonding environments							
	CH-CH	C-C	C-CH$_3$	C-CH$_2$	C-O	C-O-Ln	C=O	COOH
Pristine GO	284.2	285.0		285.9	287.2		288.2	289.3
Series 1								
GO-La	284.2	285.0	285.6		286.6	287.8	289.2	
GO-Eu	284.2	285.0	285.5		286.5	287.7	289.1	
GO-Gd	284.1	285.0	285.6		286.5	287.6	288.9	290.5
GO-Tb	284.1	284.9	285.7		286.6	287.8	289.2	290.5
Series 2								
GO-La	284.0	285.0	285.6		286.5	287.7	288.9	290.6
GO-Eu	284.0	285.0	285.6	286.1	286.6	287.6	288.9	290.3
GO-Gd	284.0	285.0	285.6		286.5	287.7	288.9	290.7
GO-Tb	284.2	285.0	285.6	286.1	286.4	287.6	288.9	290.3

The O1*s* line of the pristine GO sample, presented in Figure 3.5, can be deconvoluted into four components at 531.0, 531.9, 532.6 and 533.5 eV, which are assigned respectively to COOH, C=O, C-OH, and C-O. The contributions of these deconvoluted peaks to the total O1*s* spectral intensity amounted to 5.0 %, 15.5 %, 38.4 % and 36.6 %, respectively. After the solvothermal reactions with the Ln salts, new components appear at 530.5-531.4 eV due to Ln-O bonding and the relative intensity goes from 0.6 % to 13.3 % of the total O1*s* line intensity depending on the Ln composite, in accordance with the changes observed in C1*s* line. Also, a slight shift of 0.1-0.4 eV can be observed for the peak assigned to the C=O component, while the binding energy of the contribution due to C-OH bonds does not change. Therefore, it can be observed that while the C=O and COOH component shifts to higher BEs in the C1*s* peak, they shift to lower BEs in the O1*s* peak, conversely to the C-O component, confirming the change in electronic distribution in oxygen groups of GO. The relative intensity of C=O varies in the range of 18.4-37.0 % between the different Ln composites; that of C-OH decreases to 11.9-27.0 % and the one of C-O increases to 20.1-39.8 % of the total O1*s* peak. This supports the claim that C-OH groups replace H atoms to form a chemical bond with Ln ions.
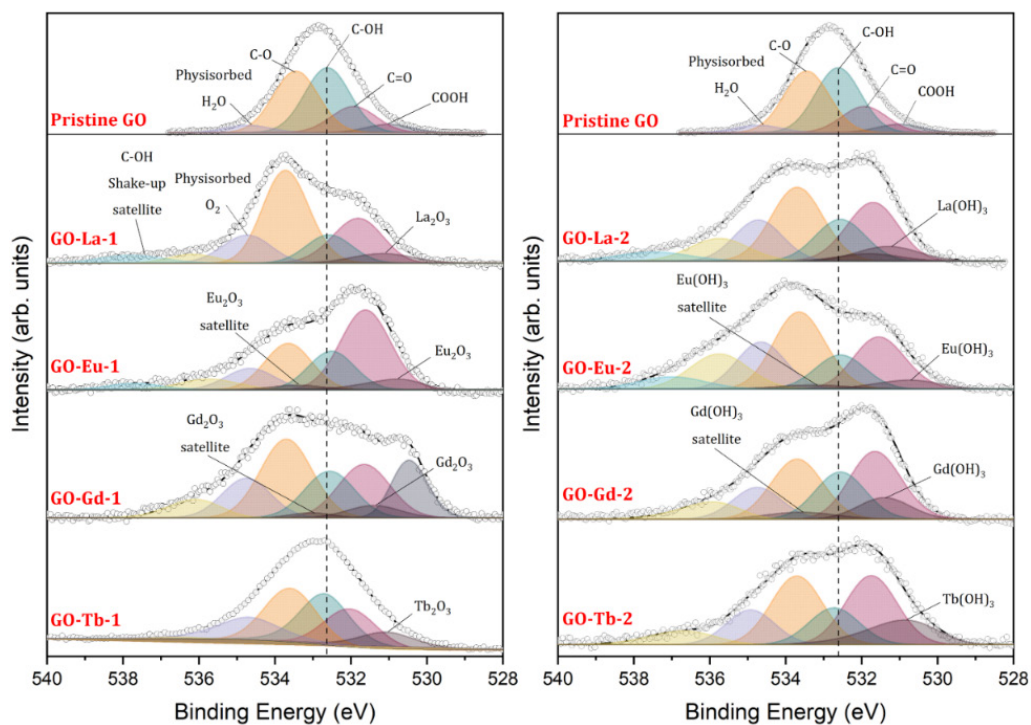
Figure 3.5. Comparison of the XPS spectra of the O1s core level region of GO-Ln-1 and GO-Ln-2 samples. The corresponding fits are also shown

Table 3.2. XPS binding energies for O1s core level components of GO-Ln-1 and GO-Ln-2 samples

Sample	Binding energies (eV) of O1s components due to different bonding environments								
	COOH	C=O	C-OH	C-O	Physis. H_2O	Physis. O_2	Shake-up satel. C-OH	Ln-O	Satel.
Pristine GO	531.0	531.9	532.6	533.5	534.7				
	Series 1								
GO-La		531.8	532.6	533.7	534.7	536.2	537.8	531.2	
GO-Eu		531.6	532.5	533.7	534.7	535.8	537.7	530.8	533.4
GO-Gd	530.5	531.6	532.6	533.7	534.8	536.1		531.4	533.1
GO-Tb		531.9	532.7	533.6	534.7	536.5		531.0	
	Series 2								
GO-La		531.7	532.6	533.7	534.7	535.8	537.5	531.3	531.8
GO-Eu		531.6	532.6	533.7	534.7	535.8	537.0	530.8	533.3
GO-Gd		531.5	532.6	533.7	534.8	535.9		531.4	533.6
GO-Tb		531.8	532.7	533.7	534.8	536.6		531.1	

A number of previous studies [51–53] have demonstrated that variations in ligand nature and/or coordination number of lanthanides cause changes in the relative intensities of satellites and main Ln 3*d* signals. The assignment of final states related to the 3*d* core level peaks is a difficult task due to the existence of satellite features next to the main spectral components. The Ln 3*d* photoemission lines observed for several compounds can be accompanied by shake-up, shake-down and multiplet splittings, which leads to a very complex fine structure [54,55]. In our case (Figure 3.6), the XPS spectra of the La $3d_{5/2}$ core level for GO-La-1 and GO-La-2 show the main component at 834.8 eV and satellites appearing at about 838.5 and 836.7 eV that are indicative of the presence of La^{3+} [56,57]. The difference between the two samples concerns one more satellite located at a BE of 832.7 eV for GO-La-1, and at 840.5 eV for GO-La-2. The Eu 3*d* XPS spectra for europium-containing samples are qualitatively similar to each other. For GO-Eu-1, the main peaks are observed at 1164.8 eV and 1135.0 eV, respectively, and these binding energies are typical for Eu^{3+} [58]. One can also see minor components at
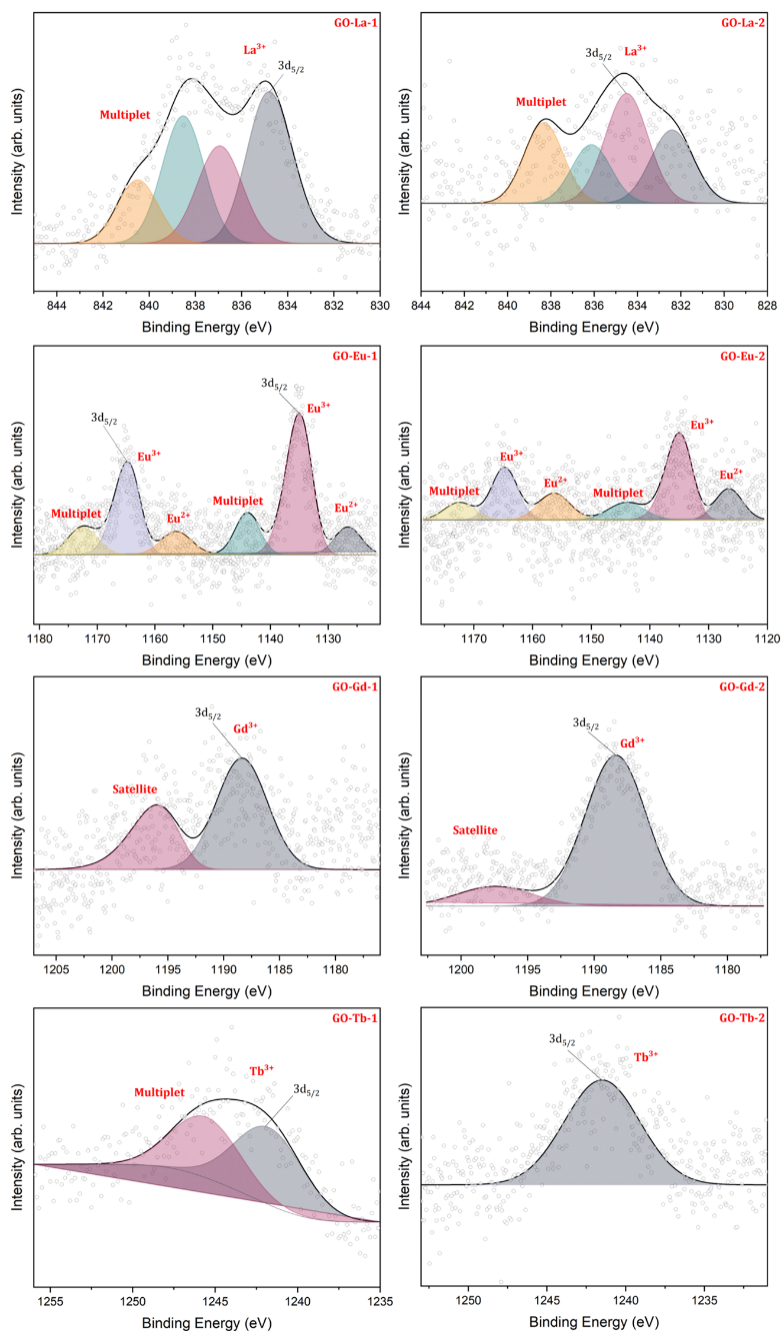
Figure 3.6. Comparison of the XPS spectra of the Ln 3d core level region of GO-Ln-1 and GO-Ln-2 samples and corresponding fits

1156.3 eV and 1126.6 eV, which can be attributed to Eu^{2+} [58], with additional multiplet features at BEs of 1144.0 and 1172.5 eV. For GO-Eu-2, the component located at 1152.3 eV is shifted by 4.0 eV with respect to the Eu^{2+} peak at 1156.3 eV for GO-Eu-1. In the Gd $3d_{5/2}$ core level spectrum for GO-Gd-1, the main peak due to Gd^{3+} [59] appears at 1187.4 eV and its satellite at 1196.0 eV. For GO-Gd-2, the main component is found at 1188.4 eV (1.0 eV higher than for GO-Gd-1) and its satellite at 1197.5 eV. The main peak in the Tb $3d_{5/2}$ spectrum appears at a BE of 1241.7 eV for GO-Tb-1, and at 1241.5 eV for GO-Tb-2, with a multiplet additionally present in the case of GO-Tb-1 sample. All the samples show differences between the BEs components of $3d_{5/2}$ core levels due to the interactions related to oxides and hydroxides.

Table 3.3. XPS binding energies for La $3d_{5/2}$, Eu 3d, Gd $3d_{5/2}$, and Tb $3d_{5/2}$ core level components in GO-Ln-1 and GO-Ln-2 samples

Sample	Binding energies (eV) Ln 3d core level lines					
	Series 1					
GO-La $3d_{5/2}$	834.8	838.5	836.9	840.5		
GO-Eu 3d	1135.0	1164.8	1126.6	1156.3	1144.0	1172.5
GO-Gd $3d_{5/2}$	1187.4	1196.0				
GO-Tb $3d_{5/2}$	1241.7	1245.6				
	Series 2					
GO-La $3d_{5/2}$	834.8	838.6	836.4		832.7	
GO-Eu 3d	1135.0	1164.8	1126.6	1152.3	1144.0	1172.5
GO-Gd $3d_{5/2}$	1188.4	1197.5				
GO-Tb $3d_{5/2}$	1241.5					

The atomic percentages of the elements present in all the samples were calculated and are presented in Table 3.4. The estimated La content in GO-La-1 is 0.6 at%, for Eu in GO-Eu-1 we found 0.8 at%, for Gd in GO-Gd-1 0.7 at%, for Tb in GO-Tb-1 0.3 at%, for La inGO-La-2 0.4 at%, for Eu in GO-Eu-2 0.6 at%, for Gd in GO-Gd-2 0.9 at%, and Tb in GO-Tb-2 0.5 at%. The amount of lanthanide in the nanocomposites is slightly lower for La^{3+} and Tb^{3+} than for Eu^{3+} and Gd^{3+} in both series, indicating a different nanoparticle formation efficiency. As could be seen from the relative contributions of C-O-Ln components to the total C1*s* intensity, this can be attributed to the differences in the electronic configuration of the four lanthanides, where also half-filled electron shell effect can influence the ability to bond with oxygen functionalities of GO as well as the

Table 3.4. Elemental composition (at%) of GO-Ln-1 and GO-Ln-2 samples as deducted from the XPS spectra

	at% XPS	
	Series 1	**Series 2**
GO-La	C: 81.5	C: 83.3
	O: 17.9	O: 16.3
	La: 0.6	La: 0.4
GO-Eu	C: 77.1	C: 75.7
	O: 22.1	O: 23.7
	Eu: 0.8	Eu: 0.6
GO-Gd	C: 77.9	C: 78.4
	O: 21.4	O: 20.7
	Gd: 0.7	Gd: 0.9
GO-Tb	C: 73.0	C: 80.8
	O: 26.7	O: 18.7
	Tb: 0.3	Tb: 0.5

stability of such bonds.

The XRD pattern of pristine GO (Figure 3.7) presents a characteristic sharp peak at 11.4° consistent with a basal spacing of d_{001} = 7.8 Å that is associated with the presence of hydroxyl, epoxy, and carbonyl groups and possibly intercalated water between the GO sheet surfaces [48,60]. After the solvothermal reaction, the XRD patterns of GO-Ln samples of both series 1 and 2 show a broad peak that points to exfoliation of the GO sheets; the maximum at around 25.1° corresponds to a basal spacing of d_{002} = 3.5 Å that can be explained by a partial reconstruction of the sp^2 carbon network involving the epoxy ring-opening reactions as reported by Fan *et al*. using aluminum powder [61,62] and agrees with the sp^2 C=C band increase observed in the FTIR results. In the case of GO-Ln-1 samples, no peaks attributable to Ln oxides were observed, which can be explained by the very small dimensions and low crystallinity of Ln nanoparticles formed [63]. At the same time, the diffractograms obtained for GO-Ln-2 samples exhibit a series of characteristic peaks corresponding to the hexagonal crystal structure of lanthanide hydroxides and indicate larger Ln nanoparticles than for GO-Ln-1 [64–67]. This confirms that even using shorter reaction times than Zheng reported [43] it is possible to obtain nanoparticles anchored to the GO surface employing the solvothermal technique.

3
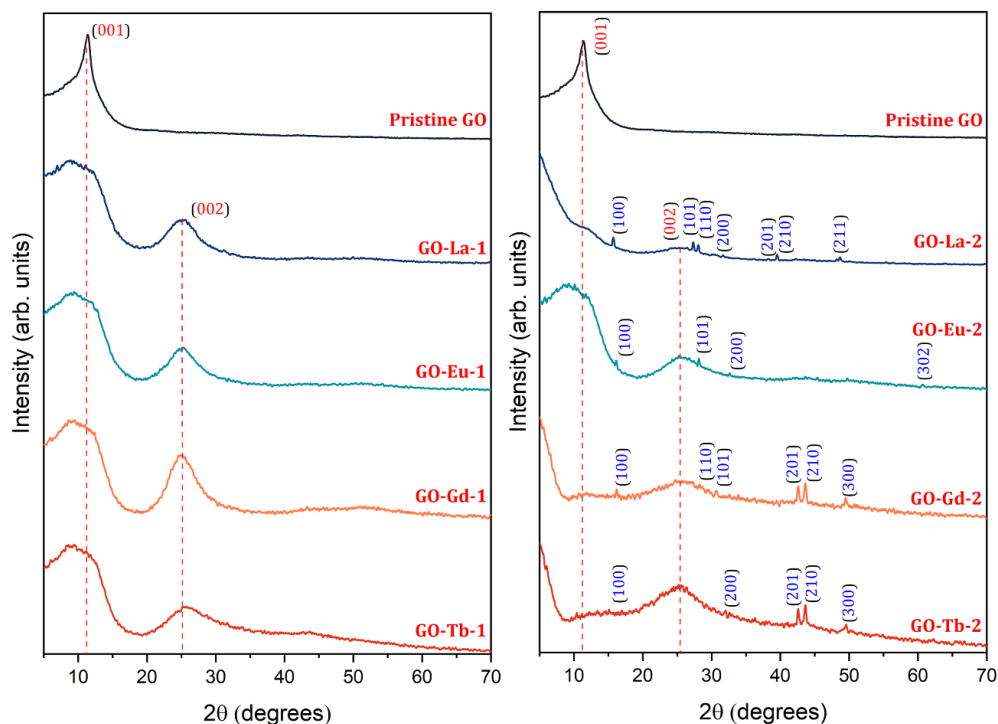
Figure 3.7. Comparison of the XRD diffractograms of GO-Ln-1 and GO-Ln-2 samples. (Red nimbers correspond to GO peaks and blue numbers correspond to lanthanide hydroxide peaks)

The morphology of the GO-Ln hybrids was investigated at different length scales with the help of SEM and TEM. SEM images acquired in the backscattered electron composition (BEC) mode, where light and heavy elements appear with different contrast, are presented in Figure 3.8 and Figure 3.9. The micrographs show GO sheets covered by lanthanide-containing particles of variable size as can be seen in the particle distribution histograms (Figure 3.10 and Figure 3.11): for the GO-Ln-1 series, the particle sizes range from approximately 100 to 800 nm with a mean size of (387 ± 127) nm for GO-La-1, (300 ± 48) nm for GO-Eu-1, (472 ± 99) nm for GO-Gd-1, and (357 ± 80) nm, whereas, for the GO-Ln-2 series, the particle size varies roughly between 800 and 7000 nm, with a mean size of (2169 ± 203) nm for GO-La-2, (2774 ± 1446) nm for GO-Eu-2, (1170 ± 131) nm for GO-Gd-2, and (935 ± 401) nm for GO-Tb-2. The samples of the GO-Ln-1 series exhibit a much more homogeneous particle distribution compared to the GO-Ln-2 series. There is also a difference between particle shapes: most striking when comparing GO-La-1 and GO-La-2 is the presence of large rod-shaped particles in the latter. The corresponding EDS spectra were probed at 10 different spots, representative results shown in Figure 3.12 and Figure 3.13 allow to

estimate the Ln content, which was found to amount to (0.86-0.98) wt% for GO-La-1; (1.22-2.84) wt% for GO-Eu-1; (3.98-6.82) wt% for GO-Gd-1 and (4.29-8.28) wt% for GO-Tb-1; it was higher for the second series, namely (2.69-5.84) wt% for GO-La-2; (1.50-3.45) wt% for GO-Eu-2; (2.42-9.35) wt% for GO-Gd-2 and (2.86-7.16) wt%, for GO-Tb-2. The EDS also confirmed that there were no other contaminant species present. The Ln content expressed in at% (Figure 3.12 and Figure 3.13) agrees with that derived from the XPS results (Table 3.4) within the experimental error.
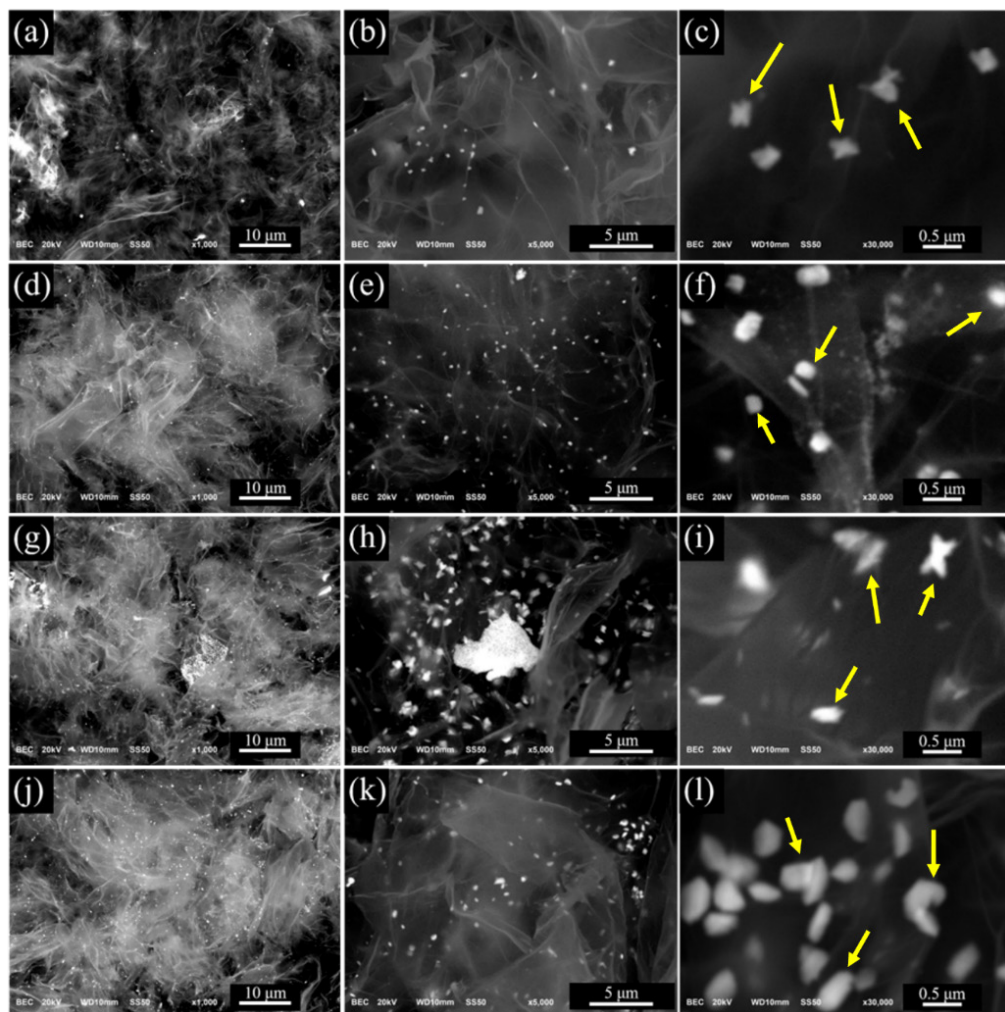
Figure 3.8. SEM images collected in backscattered composition mode (BEC) at different magnifications of (a-c) GO-La-1, (d-f) GO-Eu-1, (g-i) GO-Gd-1, and (j-l) GO-Tb-1. (Yellow arrows point to lanthanide oxide particles)

Figure 3.9. SEM images collected in backscattered composition mode (BEC) at different magnifications of (a-c) GO-La-2, (d-f) GO-Eu-2, (g-i) GO-Gd-2, and (j-l) GO-Tb-2. (Yellow arrows point to lanthanide hydroxide particles)

Figure 3.10. Particle distribution histogram deduced from the SEM images for (a) GO-La-1, (b) GO-Eu-1, (c) GO-Gd-1, and (d) GO-Tb-1

Figure 3.11. Particle distribution histograms deduced from the SEM images for (a) GO-La-2, (b) GO-Eu-2, (c) GO-Gd-2, and (d) GO-Tb-2
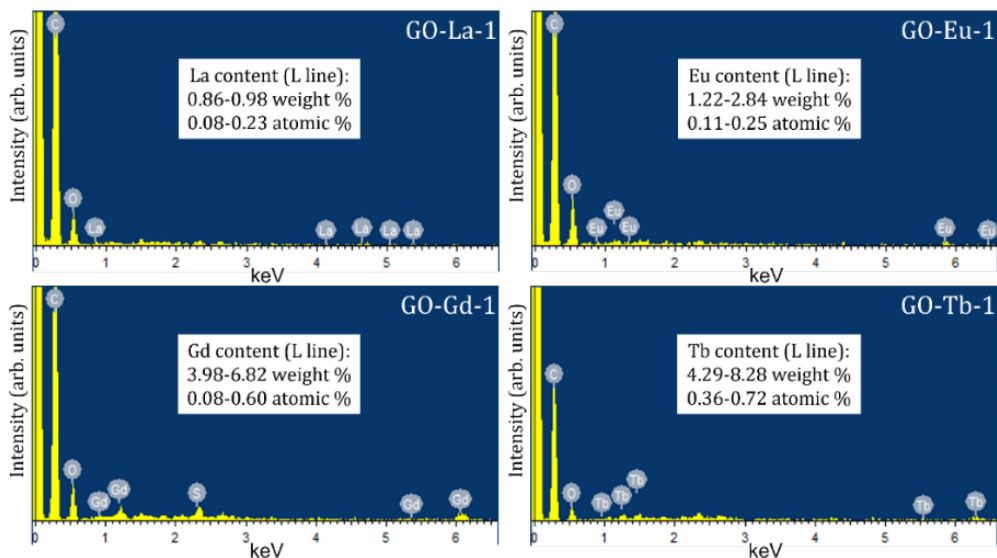
Figure 3.12. EDS spectra of (a) GO-La-1, (b) GO-Eu-1, (c) GO-Gd-1, and (d) GO-Tb-1
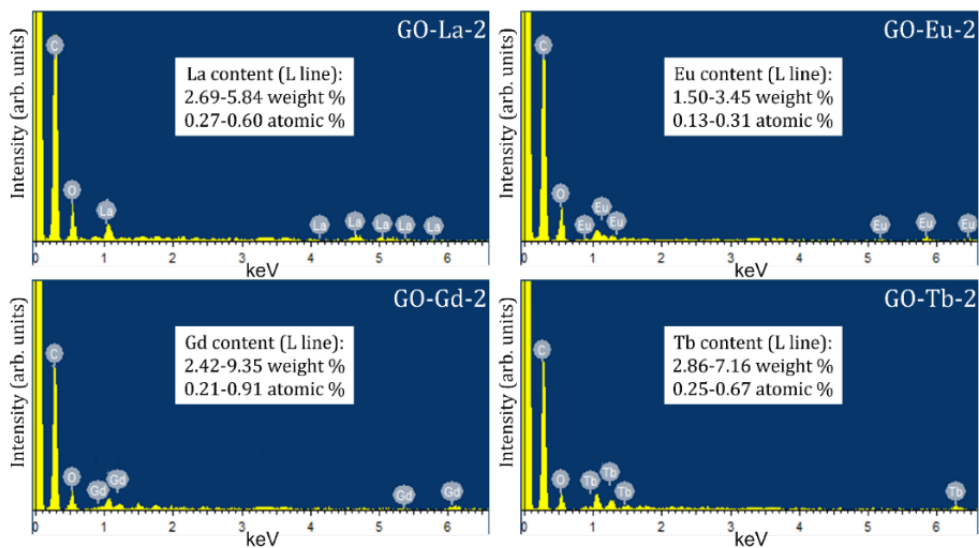
Figure 3.13. EDS spectra of (a) GO-La-2, (b) GO-Eu-2, (c) GO-Gd-2, and (d) GO-Tb-2

To explore the finer details of the size and distribution of the lanthanide-containing particles, we employed dark-field TEM. The images of GO-Ln-1 and GO-Ln-2 samples are presented in Figure 3.14 and Figure 3.15, respectively. One can see that in addition to the larger particles seen in SEM, nanoparticles are also present in both samples, as illustrated in particle distribution histograms (Figure 3.16 and Figure 3.17).

In the case of La, a more uniform distribution on the GO sheets is observed for GO-La-1 (Figure 3.14a, b), where the particle size varies from approximately 2 to 5 nm, with a mean size of (3.4 ± 1.3) nm. Similar features are found in the GO-La-2 image (Figure 3.15a), with almost equally well-distributed nanoparticles, but their size is notably larger, namely up to *ca.* 20 nm but with a mean size of (8.9 ± 4.2) nm. In both cases, the nanoparticle morphology is close to spherical. The particles appearing in both Eu-containing samples are apparently amorphous and smaller, with a mean size of (0.9 ± 0.5) nm for GO-Eu-1 and (8.2 ± 2.0) nm for GO-Eu-2. Also, a more homogeneous coverage can be observed in the case of GO-Eu-1 (Figure 3.14c, d). General similarities were also found between GO-Gd-1 (Figure 3.14e, f) and GO-Gd-2 (Figure 3.15c), where the nanoparticle structure seems to be amorphous as well, with mean sizes of (1.3 ± 0.6) nm for GO-Gd-1 and (6.6 ± 1.5) nm for GO-Gd-2. On the contrary, the nanoparticles observed in GO-Tb-1 (Figure 3.14g, h) exhibit clear facets, forming compact agglomerates with lateral dimensions of roughly 160 nm but the coverage appears to be scarce compared to the nanoparticle distribution in GO-Tb-2 (Figure 3.15d); here, the formations seem to be amorphous as for the Eu- and Gd-containing samples with a mean size of (8.3 ± 3.5) nm. It is interesting to compare our nanoparticle sizes with those reported in the literature for different lanthanide oxides. Jenkins *et al.* [26] used atomic force microscopy to confirm Ln_2O_3 particle size distribution in the nanometer range: in particular, 10-60 nm for Sm_2O_3 and Dy_2O_3, with some up to 120 nm for Sm_2O_3. Gd_2O_3 particle size ranged from 10 to 42.5 nm, while Er_2O_3 has 50 nm with agglomerated bigger particles with diameters around 150 nm. Also, Zhang *et al.* [28] and Aryanrad *et al.* [29] confirmed the possibility of forming La_2O_3 and Eu_2O_3 nanorods, with a diameter of about 20 nm (by TEM) and 30 nm (by SEM), respectively. We can therefore conclude that our approach allows for the preparation of smaller nanoparticles with a considerably larger surface area than previously reported.

Taken together the SEM and TEM results and the Raman, FTIR and XPS studies indicate that not only the solvothermal conditions have an important effect on the interaction of Ln ions with the oxygen functional groups of GO, the morphology and distribution of lanthanide oxide and hydroxide nanoparticles, but also there are differences depending on the type of lanthanide.
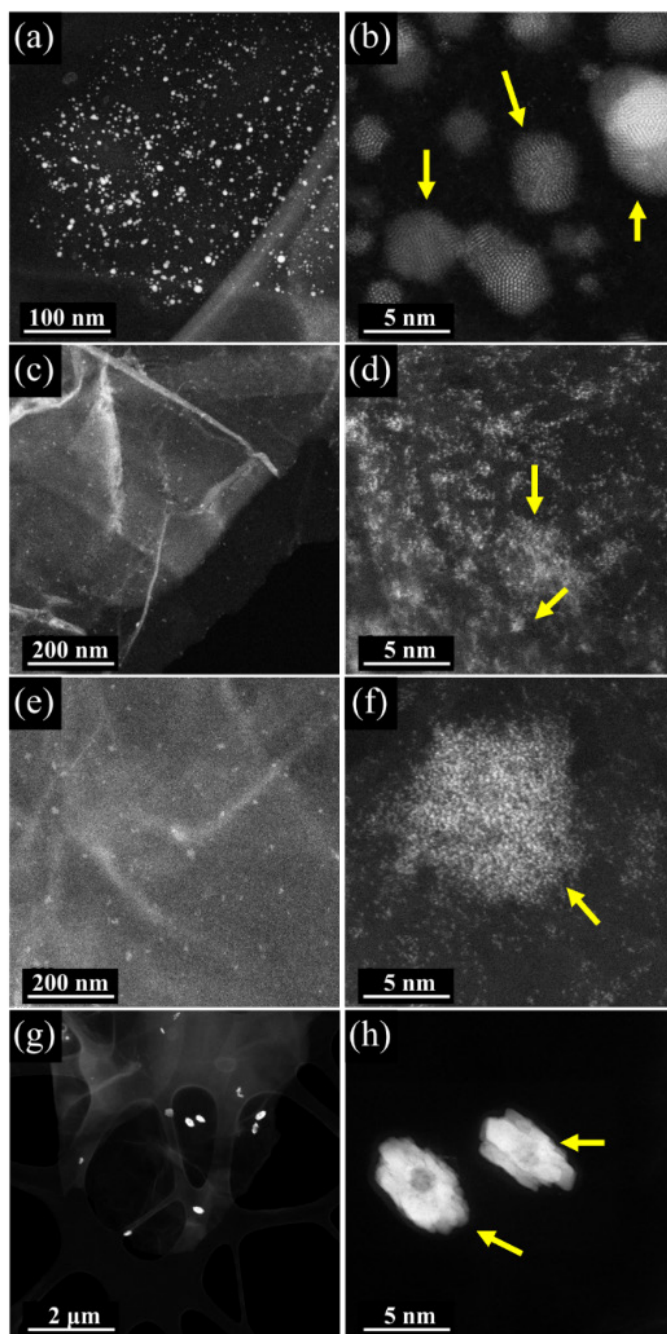
Figure 3.14. Dark-field TEM images at different magnifications of (a, b) GO-La-1, (c, d) GO-Eu-1, (e, f) GO-Gd-1, and (g, h) GO-Tb-1. (Yellow arrows point to lanthanide oxide nanoparticles)
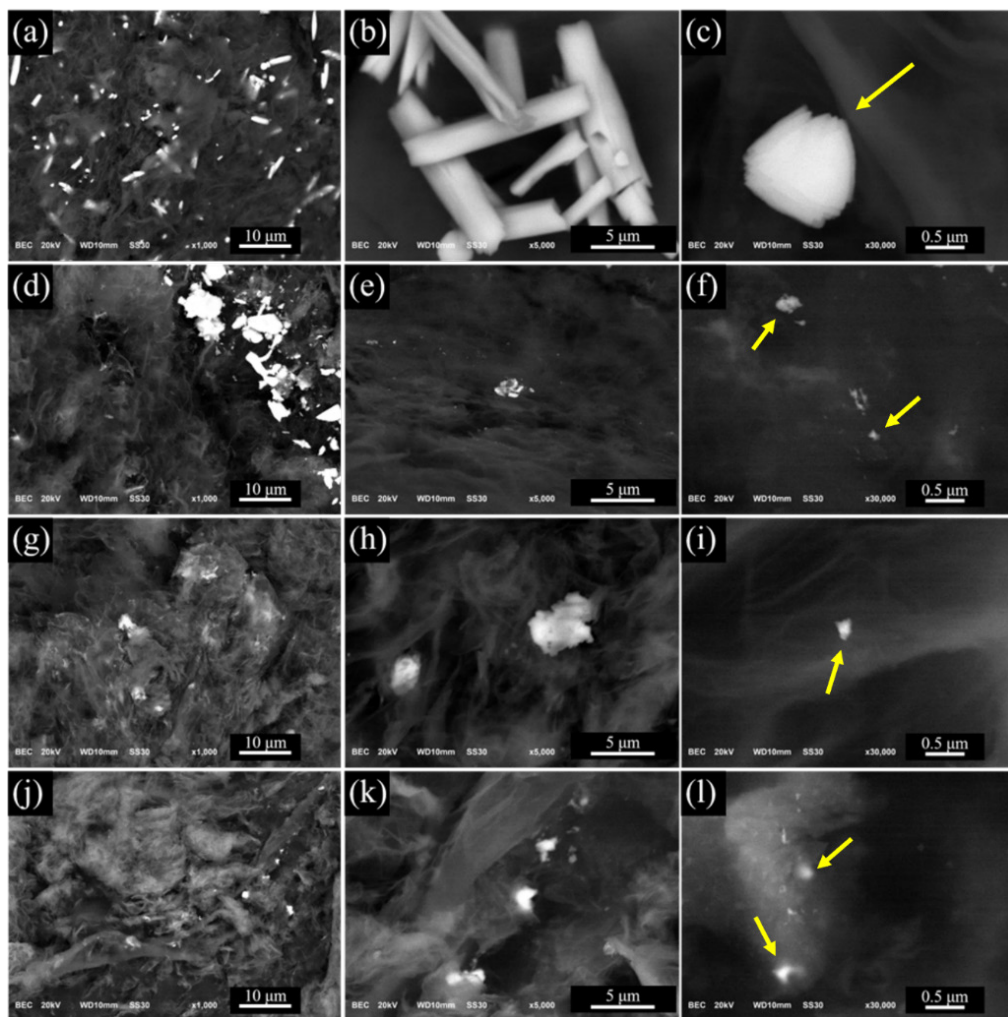
3
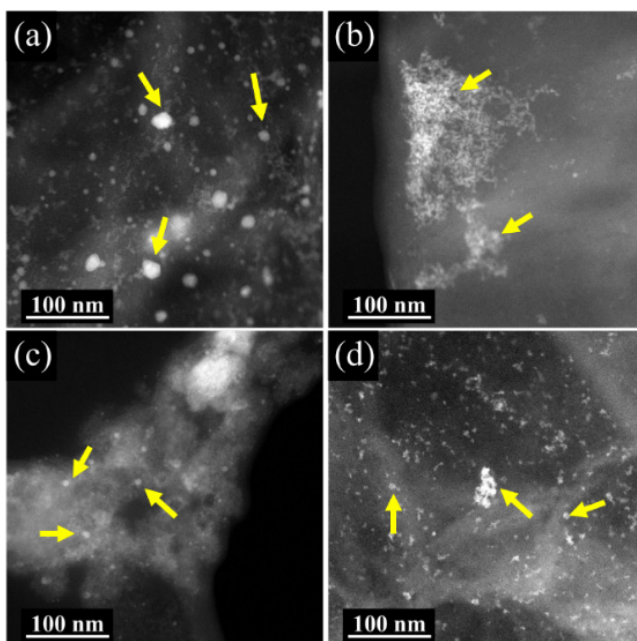
Figure 3.15. Dark-field TEM images of (a) GO-La-2, (b) GO-Eu-2, (c) GO-Gd-2, and (d) GO-Tb-2. (Yellow arrows point to lanthanide hydroxide nanoparticles)
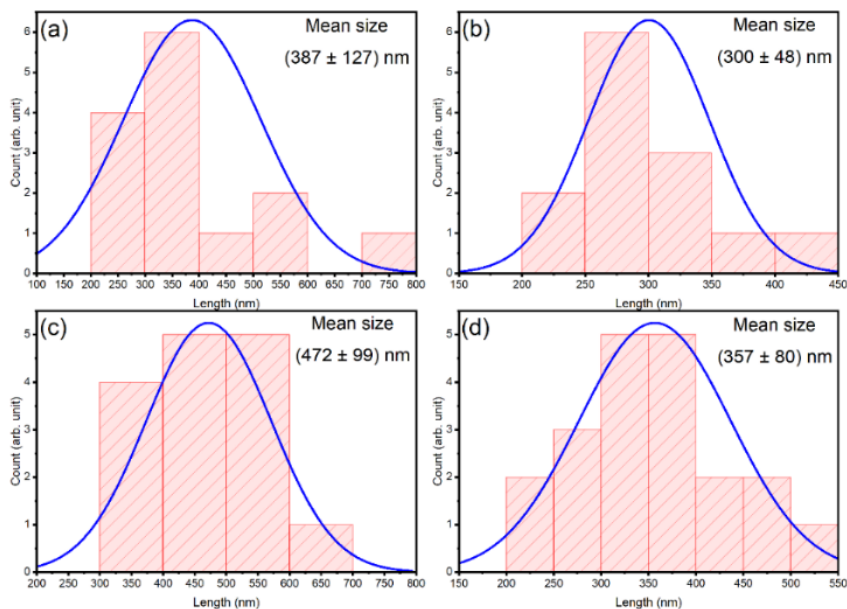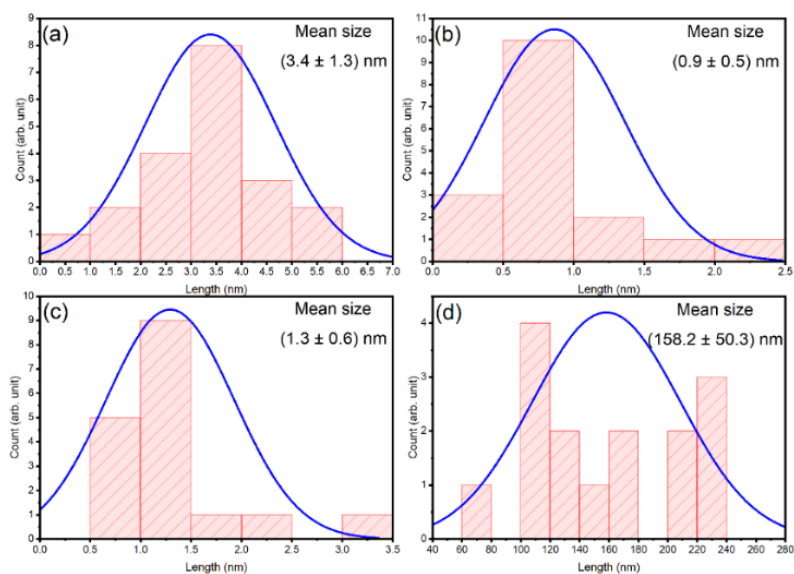

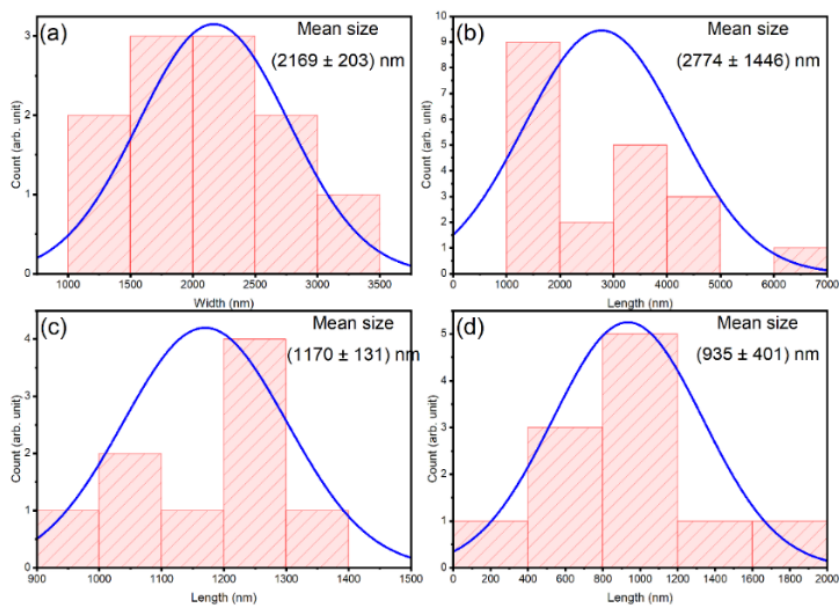*Figure 3.16. Particle distribution histogram deduced from the TEM images for (a) GO-La-1, (b) GO-Eu-1, (c) GO-Gd-1, and (d) GO-Tb-1 samples*
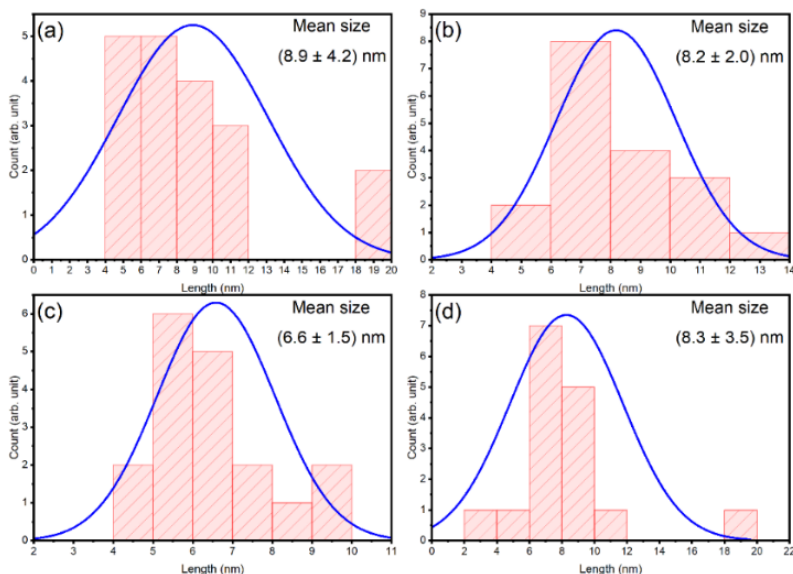
Figure 3.17. Particle distribution histogram deduced from the TEM images for (a) GO-La-2, (b) GO-Eu-2, (c) GO-Gd-2, and (d) GO-Tb-2

The thermal behaviour of GO-Ln nanocomposites was studied by TGA-DTA analysis; the corresponding thermograms are shown in Figure 3.18. The TGA curve for pristine GO (Figure 3.18a) exhibits three main weight loss steps. The first loss of 16.7 % occurs up to 100 °C and is due to the evaporation of physisorbed water. The second loss of 28.7 % is observed up to 241 °C and attributed to the decomposition of the intrinsic oxygen-containing groups of GO. The third weight loss of 51.4 %, ending at 619 °C, corresponds to the decomposition of the graphene backbone. The DTA thermogram contains features at 69, 225 and 509 °C, consistent with the three weight-loss steps in the TGA curve. The thermograms for GO-Ln-1 composites exhibited only two weight loss steps; the first one (due to the elimination of adsorbed water) amounts to 5.5-7.0 % ends at about 120 °C. A similar weight loss can be observed for the GO-Ln-2 series as well, but its magnitude is considerably higher, namely 12.9-14.2 %. The second weight loss in the TGA curves of the GO-Ln-1 series finishes below 600 °C, *viz.* at 589 °C for GO-La-1, 576 °C for GO-Eu-1, 577 °C for GO-Gd-1 and 570 °C for GO-Tb-1, with the corresponding DTA peaks at 503, 518, 512 and 513 °C. In other words, the thermal stability of Ln-containing samples decreases by 30-60 °C compared to the final decomposition temperature of pristine GO, and this decrease can be attributed to a catalytic effect of lanthanide oxides on the combustion of the graphene backbone. This final weight loss for GO-Ln-1 samples is matched by the second (of a total of three) weight loss step for the GO-Ln-2 series, ending at 575 °C for GO-La-2, at 560 °C for GO-Eu-2, at 581 °C for GO-Gd-2 and at 595 °C

for GO-Tb-2; again, the thermal stability of the Ln-containing samples is lower than that of pristine GO. The corresponding DTA thermograms exhibit a more complex structure, with the main maxima observed at lower temperatures than for the GO-Ln-1 series, *i.e.* at 404 °C for GO-La-2, 399°C for GO-Eu-2, 496 °C for GO-Gd-2 and 487 °C for GO-Tb-2. The final (third) weight loss step for the GO-Ln-2 samples ends at temperatures as high as 1000 °C and represents the main difference between the two series: it confirms in fact that Ln species exist as hydroxides in the GO-Ln-2 samples, which are dehydrated at temperatures higher than 600 °C. From the analysis of TGA curves, it was possible to estimate that the lanthanide oxide content in GO-La-1 amounts to 11.8 %, in GO-Eu-1 to 12.5 %, in GO-Gd-1 to 9.0 % and in GO-Tb-1 it is 12.6 % (Figure 3.9). For the GO-Ln-2 series, the Ln hydroxide content, roughly approximated from the horizontal ramp at around 700 °C, corresponds to values of 22 % (La), 25 % (Eu), 25 % (Gd) and 23 % (Tb). It may seem confusing that for both GO-Ln-1 and GO-Ln-2, the estimated content of Ln oxide or hydroxide is considerably higher than the atomic percentages for Ln obtained from EDS, but one has to remember that TGA allows quantifying not only the content of Ln oxide of hydroxide present after synthesis but also measures the Ln oxide content that forms during heating in air in the thermogravimetric analysis.
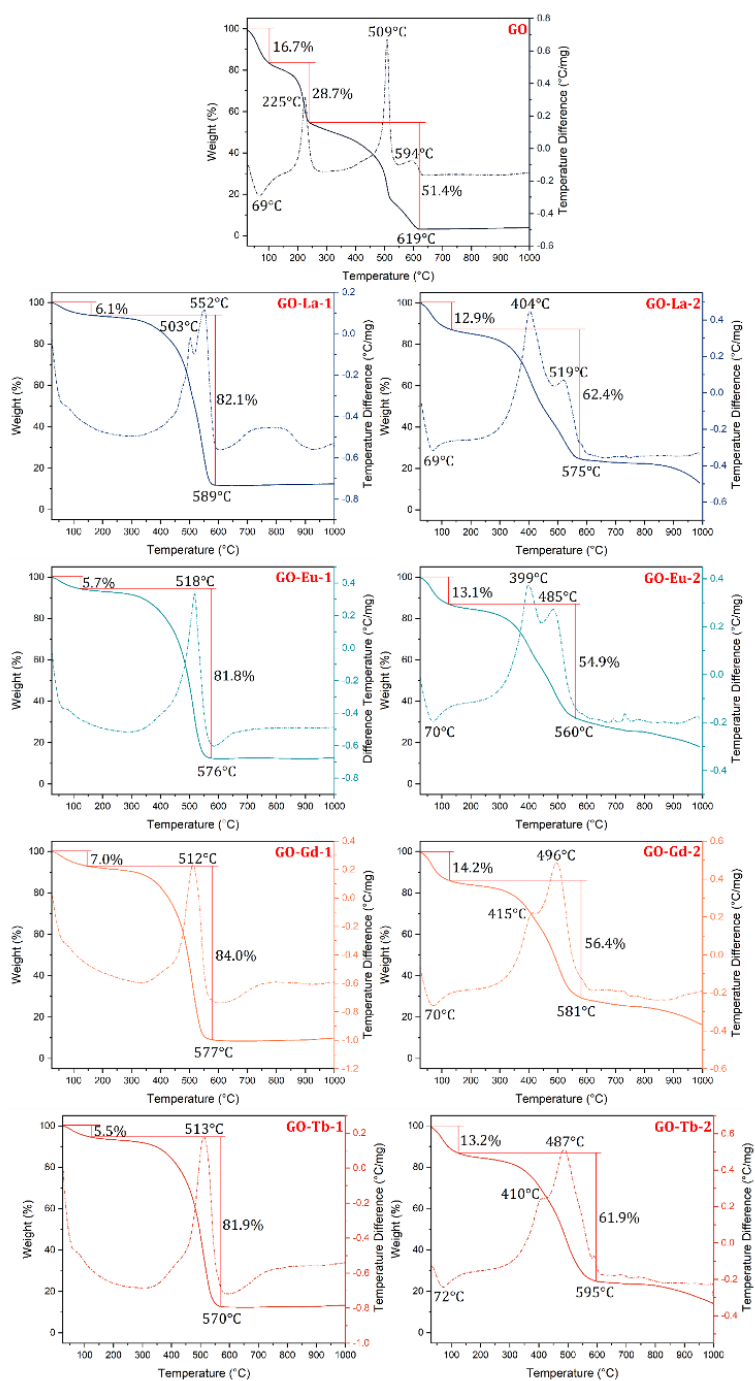
3

Figure 3.18. Comparison of TGA-DTA curves of GO-Ln-1 and GO-Ln-2 samples

3.4. Conclusions

In this chapter we describe a facile, time-saving approach for the preparation of GO-Ln_2O_3 and GO-$Ln(OH)_3$ nanocomposites under relatively mild conditions, applying two different pathways of solvothermal synthesis. One can suggest that the mechanism of GO-Ln nanocomposite formation involves the initial coordination of Ln^{3+} ions to the oxygen-containing groups of GO as nucleation sites, followed by the formation of Ln_2O_3 and $Ln(OH)_3$ nanoparticles. Although FTIR and XRD present an increase in sp^2-hybridized carbon, all the nanocomposites obtained preserve the I_D/I_G ratio of sp^3 defects present in the GO before solvothermal processing, but the presence of graphene-like honeycomb structures is confirmed by the typical G and D bands in the Raman spectra. FTIR and XPS spectra support the interaction between oxygen-containing groups of GO and Ln ions. The size and distribution of Ln oxide/hydroxide nanoparticles on the GO sheets, estimated from SEM and TEM images, varies broadly, *e.g*. for the composites with Eu, the size spans from sub-nm dimensions (as seen by TEM) in the case of GO-Eu-1 to more than 10 μm large particles (seen by SEM) for GO-Eu-2. The most homogeneous distribution of Ln oxide/hydroxide nanoparticles was found in GO-La-1 and GO-La-2. TGA-DTA measurements demonstrated that all the GO-Ln nanocomposites are less thermally stable than pristine GO by up to 30 °C. The results demonstrate that GO-Ln_2O_3 and GO-$Ln(OH)_3$ nanocomposites can be prepared simply, efficiently, and eco-friendly by solvothermal synthesis.

References

[1]   X. Zhou, X. Huang, X. Qi, S. Wu, C. Xue, F.Y.C. Boey, Q. Yan, P. Chen, H. Zhang, In situ synthesis of metal nanoparticles on single-layer graphene oxide and reduced graphene oxide surfaces, Journal of Physical Chemistry C. 113 (2009) 10842–10846. https://doi.org/10.1021/JP903821N.

[2]   C. Xu, X. Wang, J. Zhu, Graphene - Metal particle nanocomposites, Journal of Physical Chemistry C. 112 (2008) 19841–19845. https://doi.org/10.1021/JP807989B.

[3]   P. V. Kamat, Graphene-based nanoarchitectures. Anchoring semiconductor and metal nanoparticles on a two-dimensional carbon support, Journal of Physical Chemistry Letters. 1 (2010) 520–527. https://doi.org/10.1021/JZ900265J.

[4]   A.L. Jenkins, Polymer based lanthanide fluorometric sensors for the detection of chemical agents, Univerdity of Maryland, 1998.

[5]   K. Chen, H. Gao, B. Bai, W. Liu, X. Li, Microwave Hydrothermal Synthesis of Terbium Ions Complexed with Porous Graphene for Effective Absorbent for Organic Dye, Nanoscale Res Lett. 12 (2017) 1–8. https://doi.org/10.1186/S11671-017-1962-7.

[6]   M. Latva, H. Takalob, V.M. Mukkala, C. Matachescu, J.C. Rodríguez-Ubis, J. Kankare,

Correlation between the lowest triplet state energy level of the ligand and lanthanide(III) luminescence quantum yield, J Lumin. 75 (1997) 149–169. https://doi.org/10.1016/S0022-2313(97)00113-0.

[7]   X. Fan, K. Shang, B. Sun, L. Chen, S. Ai, Decoration of surface-carboxylated graphene oxide with luminescent Sm 3+-complexes, J Mater Sci. 49 (2014) 2672–2679. https://doi.org/10.1007/S10853-013-7975-4.

[8]   P. Li, Y. Wang, H. Li, G. Calzaferri, Luminescence Enhancement after Adding Stoppers to Europium(III) Nanozeolite L, Angewandte Chemie International Edition. 53 (2014) 2904–2909. https://doi.org/10.1002/ANIE.201310485.

[9]   Y. Chen, Y. Chi, H. Wen, Z. Lu, Sensitized Luminescent Terbium Nanoparticles: Preparation and Time-Resolved Fluorescence Assay for DNA, Anal Chem. 79 (2006) 960–965. https://doi.org/10.1021/AC061477H.

[10]   V.A. Basiuk, O. V. Prezhdo, E. V. Basiuk, Adsorption of Lanthanide Atoms on Graphene: Similar, Yet Different, Journal of Physical Chemistry Letters. 13 (2022) 6042–6047. https://doi.org/10.1021/ACS.JPCLETT.2C01580.

[11]   X. Liu, C.Z. Wang, M. Hupalo, W.C. Lu, M.C. Tringides, Y.X. Yao, K.M. Ho, Metals on graphene: correlation between adatom adsorption behavior and growth morphology, Physical Chemistry Chemical Physics. 14 (2012) 9157–9166. https://doi.org/10.1039/C2CP40527J.

[12]   Y.J. Li, M. Wang, M.Y. Tang, X. Tian, S. Gao, Z. He, Y. Li, T.G. Zhou, Spin and orbital magnetic moments and spin anisotropy energies of light rare earth atoms embedded in graphene: A first-principles study, Physica E Low Dimens Syst Nanostruct. 75 (2016) 169–173. https://doi.org/10.1016/J.PHYSE.2015.09.017.

[13]   S. Li, M. Zhou, G. Li, F. Zheng, P. Zhang, Strong bonding and high spin-polarization of lanthanide atoms on vacancies in graphene, AIP Adv. 7 (2017) 105207. https://doi.org/10.1063/1.4994714/977122.

[14]   V.A. Basiuk, D.A. Acevedo-Guzmán, V. Meza-Laguna, E. Álvarez-Zauco, L. Huerta, M. Serrano, M. Kakazey, E. V. Basiuk, High-energy ball-milling preparation and characterization of Ln2O3–graphite nanocomposites, Mater Today Commun. 26 (2021) 102030. https://doi.org/10.1016/J.MTCOMM.2021.102030.

[15]   A. Rodríguez-Galván, M. Rivera, P. García-López, L.A. Medina, V.A. Basiuk, Gadolinium-containing carbon nanomaterials for magnetic resonance imaging: Trends and challenges, J Cell Mol Med. 24 (2020) 3779–3794. https://doi.org/10.1111/JCMM.15065.

[16]   C. Lee, X. Wei, J.W. Kysar, J. Hone, Measurement of the elastic properties and intrinsic strength of monolayer graphene, Science (1979). 321 (2008) 385–388. https://doi.org/10.1126/SCIENCE.1157996.

[17]   K.S. Novoselov, A.K. Geim, S. V. Morozov, D. Jiang, Y. Zhang, S. V. Dubonos, I. V. Grigorieva, A.A. Firsov, Electric field in atomically thin carbon films, Science (1979). 306 (2004) 666–669. https://doi.org/10.1126/SCIENCE.1102896.

[18]   K. Wang, J. Ruan, H. Song, J. Zhang, Y. Wo, S. Guo, D. Cui, Biocompatibility of Graphene Oxide, Nanoscale Res Lett. 6 (2010) 8. https://doi.org/10.1007/s11671-010-9751-6.

[19]   S.F. Kiew, L.V. Kiew, H.B. Lee, T. Imae, L.Y. Chung, Assessing biocompatibility of graphene oxide-based nanocarriers: A review, Journal of Controlled Release. 226 (2016) 217–228. https://doi.org/10.1016/J.JCONREL.2016.02.015.

3

[20]   M. Lundie, Ž. Šljivančanin, S. Tomić, Electronic and optical properties of reduced graphene oxide, J Mater Chem C Mater. 3 (2015) 7632–7641. https://doi.org/10.1039/C5TC00437C.

[21]   Y. Wang, Y. Wang, Y. Tian, M. Rasheed, S. Shihab, O.W. Sabah, An investigation of the Structural, Electrical and Optical Properties of Graphene-Oxide Thin Films Using Different Solvents, J Phys Conf Ser. 1795 (2021) 012052. https://doi.org/10.1088/1742-6596/1795/1/012052.

[22]   R.M. Ashour, H.N. Abdelhamid, A.F. Abdel-Magied, A.A. Abdel-Khalek, M.M. Ali, A. Uheida, M. Muhammed, X. Zou, J. Dutta, Rare Earth Ions Adsorption onto Graphene Oxide Nanosheets, 35 (2017) 91–103. https://doi.org/10.1080/07366299.2017.1287509.

[23]   P.K. Narayanam, K. Sankaran, Luminescence tunability of europium functionalized graphene oxide sheets, Mater Res Express. 5 (2018) 065039. https://doi.org/10.1088/2053-1591/AACA77.

[24]   S. Pang, Z. Zhou, Q. Wang, Terbium-containing graphene oxide and its opto-electrochemical response for hypochlorite in water, Carbon N Y. 58 (2013) 232–237. https://doi.org/10.1016/J.CARBON.2013.03.004.

[25]   Y. Wang, Y. Li, W. Qi, Y. Song, Luminescent lanthanide graphene for detection of bacterial spores and cysteine, Chemical Communications. 51 (2015) 11022–11025. https://doi.org/10.1039/C5CC02889B.

[26]   A.L.J. David P Ziegler, Preparation and Properties of Luminescent Lanthanide Based Graphene Oxide, J Phys Chem Biophys. 03 (2013). https://doi.org/10.4172/2161-0398.1000120.

[27]   F. Jabeen, M.S. Sajid, B. Fatima, A. Saeed, M.N. Ashiq, M. Najam-ul-Haq, Graphene oxide–metal oxide nanocomposites for on-target enrichment and analysis of phosphorylated biomolecules, J Sep Sci. 44 (2021) 3137–3145. https://doi.org/10.1002/JSSC.202001276.

[28]   J. Zhang, Z. Zhang, Y. Jiao, H. Yang, Y. Li, J. Zhang, P. Gao, The graphene/lanthanum oxide nanocomposites as electrode materials of supercapacitors, J Power Sources. 419 (2019) 99–105. https://doi.org/10.1016/J.JPOWSOUR.2019.02.059.

[29]   P. Aryanrad, H.R. Naderi, E. Kohan, M.R. Ganjali, M. Baghernejad, A. Shiralizadeh Dezfuli, Europium oxide nanorod-reduced graphene oxide nanocomposites towards supercapacitors, RSC Adv. 10 (2020) 17543–17551. https://doi.org/10.1039/C9RA11012G.

[30]   A. Subasri, K. Balakrishnan, E.R. Nagarajan, V. Devadoss, A. Subramania, Development of 2D La(OH)3 /graphene nanohybrid by a facile solvothermal reduction process for high-performance supercapacitors, Electrochim Acta. 281 (2018) 329–337. https://doi.org/10.1016/J.ELECTACTA.2018.05.142.

[31]   R.K. Sharma, M. Ghora, Y.N. Chouryal, T. Ganguly, D. Acharjee, D.J. Mondal, S. Konar, S. Nigam, P. Ghosh, Multifunctional Lanthanide-Doped Binary Fluorides and Graphene Oxide Nanocomposites Via a Task-Specific Ionic Liquid, ACS Omega. (2021). https://doi.org/10.1021/ACSOMEGA.1C06875.

[32]   A. Javadi, S. Pan, C. Cao, G. Yao, X. Li, Facile synthesis of 10 nm surface clean TiB2 nanoparticles, Mater Lett. 229 (2018) 107–110. https://doi.org/10.1016/J.MATLET.2018.06.054.

[33]   J. Yuan, G. Yao, S. Pan, N. Murali, X. Li, Size Control of In Situ Synthesized TiB2 Particles in Molten Aluminum, Metall Mater Trans A Phys Metall Mater Sci. 52 (2021) 2657–2666.

3

https://doi.org/10.1007/S11661-021-06260-2.

[34]   P. Lidström, J. Tierney, B. Wathey, J. Westman, Microwave assisted organic synthesis—a review, Tetrahedron. 57 (2001) 9225–9283. https://doi.org/10.1016/S0040-4020(01)00906-1.

[35]   J.A. Gerbec, D. Magana, A. Washington, G.F. Strouse, Microwave-Enhanced Reaction Rates for Nanoparticle Synthesis, J Am Chem Soc. 127 (2005) 15791–15800. https://doi.org/10.1021/ja052463g.

[36]   F. Bensebaa, N. Patrito, Y. Le Page, P. L'Ecuyer, D. Wang, Tunable platinum–ruthenium nanoparticle properties using microwave synthesis, J Mater Chem. 14 (2004) 3378–3384. https://doi.org/10.1039/B404280H.

[37]   J. Lai, W. Niu, R. Luque, G. Xu, Solvothermal synthesis of metal nanocrystals and their applications, Nano Today. 10 (2015) 240–267. https://doi.org/10.1016/J.NANTOD.2015.03.001.

[38]   S. Chella, P. Kollu, E.V.P.R. Komarala, S. Doshi, M. Saranya, S. Felix, R. Ramachandran, P. Saravanan, V.L. Koneru, V. Venugopal, S.K. Jeong, A.N. Grace, Solvothermal synthesis of MnFe2O4-graphene composite—Investigation of its adsorption and antimicrobial properties, Appl Surf Sci. 327 (2015) 27–36. https://doi.org/10.1016/J.APSUSC.2014.11.096.

[39]   Y.J. Tong, L.D. Yu, J. Zheng, G. Liu, Y. Ye, S. Huang, G. Chen, H. Yang, C. Wen, S. Wei, J. Xu, F. Zhu, J. Pawliszyn, G. Ouyang, Graphene Oxide-Supported Lanthanide Metal-Organic Frameworks with Boosted Stabilities and Detection Sensitivities, Anal Chem. 92 (2020) 15550–15557. https://doi.org/10.1021/ACS.ANALCHEM.0C03562.

[40]   B Gersten, Solvothermal synthesis of nanoparticles, Chemfiles. 5 (2005) 11–12.

[41]   Z. Li, X. Li, Y. Zong, G. Tan, Y. Sun, Y. Lan, M. He, Z. Ren, X. Zheng, Solvothermal synthesis of nitrogen-doped graphene decorated by superparamagnetic Fe3O4 nanoparticles and their applications as enhanced synergistic microwave absorbers, Carbon N Y. 115 (2017) 493–502. https://doi.org/10.1016/J.CARBON.2017.01.036.

[42]   C. Wang, K. Yang, X. Wei, S. Ding, F. Tian, F. Li, One-pot solvothermal synthesis of carbon dots/Ag nanoparticles/TiO2 nanocomposites with enhanced photocatalytic performance, Ceram Int. 44 (2018) 22481–22488. https://doi.org/10.1016/J.CERAMINT.2018.09.017.

[43]   H. Zheng, Z. Ji, K.R. Roy, M. Gao, Y. Pan, X. Cai, L. Wang, W. Li, C.H. Chang, C. Kaweeteerawat, C. Chen, T. Xia, Y. Zhao, R. Li, Engineered Graphene Oxide Nanocomposite Capable of Preventing the Evolution of Antimicrobial Resistance, ACS Nano. 13 (2019) 11488–11499. https://doi.org/10.1021/ACSNANO.9B04970.

[44]   A. Kaniyoor, S. Ramaprabhu, A Raman spectroscopic investigation of graphite oxide derived graphene, AIP Adv. 2 (2012) 32183. https://doi.org/10.1063/1.4756995/21084.

[45]   R. Kumar, B.R. Mehta, M. Bhatnagar, R. S, S. Mahapatra, S. Salkalachen, P. Jhawar, Graphene as a transparent conducting and surface field layer in planar Si solar cells, Nanoscale Res Lett. 9 (2014) 1–9. https://doi.org/10.1186/1556-276X-9-349.

[46]   L. Xu, L. Cheng, Graphite oxide under high pressure: A Raman spectroscopic study, J Nanomater. 2013 (2013). https://doi.org/10.1155/2013/731875.

[47]   Z. Ni, Y. Wang, T. Yu, Z. Shen, Raman spectroscopy and imaging of graphene, Nano Res. 1 (2008) 273–291. https://doi.org/10.1007/S12274-008-8036-1.

[48]   M. Acik, G. Lee, C. Mattevi, A. Pirkle, R.M. Wallace, M. Chhowalla, K. Cho, Y. Chabal, The role of oxygen during thermal reduction of graphene oxide studied by infrared absorption spectroscopy, Journal of Physical Chemistry C. 115 (2011) 19761–19781. https://doi.org/10.1021/JP2052618.

[49]   T. Rattana, S. Chaiyakun, N. Witit-Anun, N. Nuntawong, P. Chindaudom, S. Oaew, C. Kedkeaw, P. Limsuwan, Preparation and characterization of graphene oxide nanosheets, Procedia Eng. 32 (2012) 759–764. https://doi.org/10.1016/J.PROENG.2012.02.009.

[50]   T. Vitova, P.W. Roesky, S. Dehnen, Open questions on bonding involving lanthanide atoms, Communications Chemistry 2022 5:1. 5 (2022) 1–4. https://doi.org/10.1038/s42004-022-00630-6.

[51]   O.P. Ivanova, L.A. Vasilyev, A. V. Naumkin, V. V. Kantsel, XPS studies of natural monazite and relative compounds under ion bombardment, Appl Surf Sci. 72 (1993) 307–312. https://doi.org/10.1016/0169-4332(93)90367-K.

[52]   Y.A. Teterin, A.Y. Teterin, A.M. Lebedev, K.E. Ivanov, Secondary electronic processes and the structure of X-ray photoelectron spectra of lanthanides in oxygen-containing compounds, J Electron Spectros Relat Phenomena. 137–140 (2004) 607–612. https://doi.org/10.1016/J.ELSPEC.2004.02.016.

[53]   H. Berthou, C.K. Jørgensen, C. Bonnelle, Influence of the ligands on 3d photoelectron spectra of the first four lanthanides, Chem Phys Lett. 38 (1976) 199–206. https://doi.org/10.1016/0009-2614(76)85135-4.

[54]   A. Novosselov, E. Talik, A. Pajaczkowska, An X-ray photoelectron spectroscopy study on electron structure of some Ln-containing (Ln = La, Pr, Nd and Gd) oxide crystals, J Alloys Compd. 351 (2003) 50–53. https://doi.org/10.1016/S0925-8388(02)01064-2.

[55]   B. Glorieux, R. Berjoan, M. Matecki, A. Kammouni, D. Perarnau, XPS analyses of lanthanides phosphates, Appl Surf Sci. 253 (2007) 3349–3359. https://doi.org/10.1016/J.APSUSC.2006.07.027.

[56]   M.F. Sunding, K. Hadidi, S. Diplas, O.M. Løvvik, T.E. Norby, A.E. Gunnæs, XPS characterisation of in situ treated lanthanum oxide and hydroxide using tailored charge referencing and peak fitting procedures, J Electron Spectros Relat Phenomena. 184 (2011) 399–409. https://doi.org/10.1016/J.ELSPEC.2011.04.002.

[57]   J.P.H. Li, X. Zhou, Y. Pang, L. Zhu, E.I. Vovk, L. Cong, A.P. Van Bavel, S. Li, Y. Yang, Understanding of binding energy calibration in XPS of lanthanum oxide by in situ treatment, Physical Chemistry Chemical Physics. 21 (2019) 22351–22358. https://doi.org/10.1039/C9CP04187G.

[58]   F. Mercier, C. Alliot, L. Bion, N. Thromat, P. Toulhoat, XPS study of Eu(III) coordination compounds: Core levels binding energies in solid mixed-oxo-compounds EumXxOy, J Electron Spectros Relat Phenomena. 150 (2006) 21–26. https://doi.org/10.1016/J.ELSPEC.2005.08.003.

[59]   D. Raiser, J.P. Deville, Study of XPS photoemission of some gadolinium compounds, J Electron Spectros Relat Phenomena. 57 (1991) 91–97. https://doi.org/10.1016/0368-2048(91)85016-M.

[60]   A.B. Bourlinos, D. Gournis, D. Petridis, T. Szabó, A. Szeri, I. Dékány, Graphite Oxide: Chemical Reduction to Graphite and Surface Modification with Primary Aliphatic Amines and Amino Acids, Langmuir. 19 (2003) 6050–6055. https://doi.org/10.1021/LA026525H.

[61]   Z. Fan, K. Wang, T. Wei, J. Yan, L. Song, B. Shao, An environmentally friendly and efficient route for the reduction of graphene oxide by aluminum powder, Carbon N Y. 48 (2010) 1686–1689. https://doi.org/10.1016/J.CARBON.2009.12.063.

[62]   K. Muthoosamy, R. Geetha Bai, I.B. Abubakar, S.M. Sudheer, H.N. Lim, H.S. Loh, N.M. Huang, C.H. Chia, S. Manickam, Exceedingly biocompatible and thin-layered reduced graphene oxide nanosheets using an eco-friendly mushroom extract strategy, Int J Nanomedicine. 10 (2015) 1505–1519. https://doi.org/10.2147/IJN.S75213.

[63]   H.R. Naderi, M.R. Ganjali, A.S. Dezfuli, High-performance supercapacitor based on reduced graphene oxide decorated with europium oxide nanoparticles, Journal of Materials Science: Materials in Electronics. 29 (2018) 3035–3044. https://doi.org/10.1007/S10854-017-8234-2.

[64]   C. Hu, H. Liu, W. Dong, Y. Zhang, G. Bao, C. Lao, Z.L. Wang, La(OH)3 and La2O3 Nanobelts—Synthesis and Physical Properties, Advanced Materials. 19 (2007) 470–474. https://doi.org/10.1002/ADMA.200601300.

[65]   J.G. Kang, Y. Jung, B.K. Min, Y. Sohn, Full characterization of Eu(OH)3 and Eu2O3 nanorods, Appl Surf Sci. 314 (2014) 158–165. https://doi.org/10.1016/J.APSUSC.2014.06.165.

[66]   J.G. Kang, B.K. Min, Y. Sohn, Synthesis and characterization of Gd(OH)3 and Gd2O3 nanorods, Ceram Int. 41 (2015) 1243–1248. https://doi.org/10.1016/J.CERAMINT.2014.09.053.

[67]   Y. Sohn, Structural and spectroscopic characteristics of terbium hydroxide/oxide nanorods and plates, Ceram Int. 40 (2014) 13803–13811. https://doi.org/10.1016/J.CERAMINT.2014.05.096.

3

—— CHAPTER 4 ——

Lanthanide-modified graphene oxide nanocomposites and their antimicrobial properties

This chapter reports on the study of the antimicrobial properties of two series of nanocomposites containing graphene oxide and lanthanide oxide/hydroxide nanoparticles (La, Eu, Gd, Tb) synthesised by the solvothermal method. The graphene oxide-lanthanide oxide nanocomposites presented a strong dose-dependent bactericidal behaviour against two different types of bacteria, *Escherichia coli* and *Corynebacterium glutamicum*; this effect was especially strong for the graphene oxide-La$_2$O$_3$ nanocomposite. On the other hand, graphene oxide-lanthanide hydroxide nanocomposites did not show any antibacterial properties. Scanning and transmission electron microscopy evidenced that these outcomes might be related to the distribution, shape, and size of the lanthanide-containing nanoparticles on the graphene oxide surface.

4.1. Introduction

Over the last decade, infectious diseases caused by bacteria have been one of the major threats to human health, and this danger has been worsened by the rapid progression of antimicrobial resistance which reduces the efficiency of current antibiotics and treatments [1,2]. Significant efforts have been devoted to exploring new strategies to produce materials with broader antimicrobial properties and one of the most promising strategies in this context is focused on developing and designing graphene nanomaterials (GNMs) that could be employed as disinfectants, antibacterial coatings, or additives in clinical devices [3–7]. GNMs using graphene oxide (GO) have been demonstrated to possess a broad range of antibacterial activity attributed to the physical and chemical interactions with bacteria that cause the degradation of the cell membrane components, proteins, lipids, and nucleic acids [8–12].

The mechanisms responsible for the bactericidal properties are driven by the physicochemical characteristics of GO such as sheet size, number of layers, morphology, and surface chemistry leading to different types of interactions when the graphene sheets have contact with bacterial cells [8,9,13]. The large surface area and sharp edges of graphene cause mechanical membrane stress or mechanical wrapping [14–16] by mechanisms including "nano-knives" insertion [17–19], lipid extraction [20–22], or pore formation [23,24]. The latter two originate in the van der Waals interactions between the hydrophobic interface and membrane lipids. Moreover, oxidative stress induced by the oxygen-containing groups on the GO surface results in lipid peroxidation as well as the oxidation of proteins and nucleic acids that can ultimately lead to the destruction of the cell membrane [19,25,26].

The chemically rich nature of GO including epoxy (C-O-C), hydroxyl (-OH) and carboxylic groups (-COOH) offers a great opportunity to synthesise GO-based nanocomposites by covalent and non-covalent functionalisation of the surface. Such surface modifications can be specifically designed to enhance the interaction with cell membranes and therefore improve the antimicrobial properties. Lanthanide species possess a strong chemical affinity to phosphate groups, proteins, or carbohydrates and can create pores in the bacteria cell wall, which makes them ideal candidates for GO nanocomposites with superior antibacterial properties [27,28]. A powerful synergetic effect can be achieved by the combination of GO and lanthanides, even capable of overcoming evolving genetic adaptations [29].

In the study described in this chapter, we explored the antimicrobial properties of GO-lanthanide oxide and GO-lanthanide hydroxide nanocomposites against *Escherichia*

coli and *Corynebacterium glutamicum* by performing optical density measurements to observe the evolution of the bacteria population growth.

4.2. Experimental

4.2.1. Synthesis of GO-lanthanide oxide/hydroxide nanocomposites

The GO-lanthanide oxide/hydroxide nanocomposites were synthesised employing the solvothermal technique, as described in Chapter 3 Section 2.2.

4.2.2. Antimicrobial tests

For the determination of the antimicrobial activity, initially, 100 μL of bacterial population was taken from stock bacterial populations of the Gram-negative *Escherichia coli* BL21DE3 strain and Gram-positive strain *Corynebacterium glutamicum* stored in glycerol and inoculated in 5 mL of fresh Lysogeny Broth (LB). The preculture was incubated at 37 °C overnight under constant stirring at 180 rpm. After the overnight incubation, the preculture absorbance was measured at 600 nm and diluted with fresh LB so that the new culture reached an optical density (OD) of about 0.08. The new culture was incubated at 37 °C under stirring at 180 rpm for about 2 h until the bacterial population passed the exponential phase and presented an OD of 0.2–0.5. The culture was then centrifuged at 4000 rpm for 5 minutes. The resulting supernatant was discarded, and the bacterial precipitate was redissolved in saline (0.9 % w/v NaCl). Then, three successive washes of the bacterial pellet with saline were performed and finally, the pellet was redissolved in an equal volume of the culture. Then, cells of a Gram-negative strain *E. coli* ($\sim 10^7$ CFU mL^{-1}) and a Gram-positive strain *C. glutamicum* ($\sim 10^7$ CFU mL^{-1}) in the exponential phase were added to aqueous dispersions (containing 0.9 wt% NaCl) of the different nanocomposites at various concentrations up to 400 μg mL^{-1}. The samples were kept at a constant temperature of 37 °C for 12 h while being continuously agitated at 180 rpm. Then, 25 μL of each sample was added each time to a Nunclon™ Delta 96-Well MicroWell™ Plate (Thermo Scientific) containing 225 μL of a sterile LB broth medium, and the absorbance value of OD600 was recorded each hour for a total of eight hours. Finally, the growth curves of the two bacterial populations, both in the presence and absence of the corresponding samples were prepared. (The antimicrobial tests were performed by Dr. Archontoula Giannakopoulou in the University of Ioannina)

4.3. Results and discussion

A widely employed method to estimate microbial growth in a liquid cell culture is the measurement of the optical density at 600 nm (OD_{600}) [30]. Since the absorbance scales linearly with the number of cells, one can employ a spectrophotometer to measure the light scattered by the bacteria population within a cell culture in order to know how the population changes over time (Figure 4.1.a). A wavelength of 600 nm is utilised because most bacteria do not have pigments that absorb this wavelength; moreover, it minimises cell damage and does not affect growth.

Monitoring the change of a bacterial population over time results in a growth curve where four phases can be observed: the lag phase, the log phase, the stationary phase, and the death phase, as sketched in (Figure 4.1.b). After the inoculation, in the lag phase, bacteria need to adapt to the culture media, thus no cell division takes place, and OD_{600} does not change. In the log phase, bacteria have adapted to the environment and cells start to replicate. Each bacterium doubles rapidly resulting in an exponential bacterial growth and OD_{600} increases linearly because it is defined as the logarithm of the ratio between the incident light, I_0, and the intensity of the light after passing through the sample, I: $OD_{600} = \log(I_0/I)$. In the stationary phase, when cell density reaches its maximum, reproduction is limited by the amount of nutrients available in the culture media. Hence, the bacteria stop dividing, and OD_{600} remains constant. In the death phase, due to the lack of enough nutrients, the accumulation of waste products like acids and ethanol, and changes in the pH media, the bacteria population decreases along with the OD_{600}.
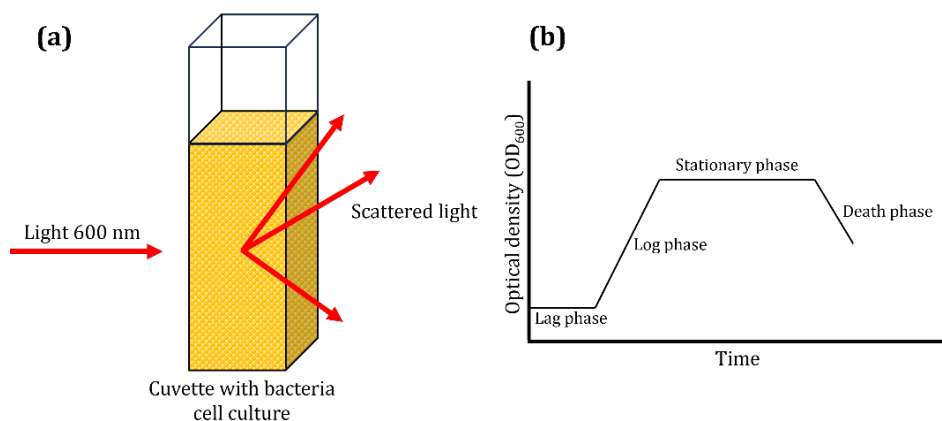
Figure 4.1. (a) Optical Density measurement, (b) Phases of cell growth as observed in an OD_{600} measurement

To observe the antimicrobial activity of all the GO-Ln oxide and GO-Ln hydroxide nanocomposites against *Escherichia coli* and *Corynebacterium glutamicum*, OD_{600} measurements were performed; the results are shown in Figures 4.3, 4.4, 4.6 and 4.7, and the OD_{600} values reported in Tables 4.1-4.4.

<u>*Escherichia coli*</u>

Escherichia coli is a pathogenic bacterium commonly found in the gastrointestinal tracts of humans and warm-blooded animals [31,32]. It is a gram-negative (Gram⁻) rod-shaped bacterium and its envelope consists of three layers (Figure 4.2): The outer membrane, the peptidoglycan cell wall, and the cytoplasmic membrane or inner membrane [33]. The outer membrane is mainly formed of a lipid bilayer with phospholipids in the inner leaflet and glycolipids (lipid-A) in the outer leaflet, as well as lipopolysaccharides and proteins. Lipid-A and phospholipids have a hydrophilic head containing a negatively charged phosphate group and two hydrophobic tails that are long fatty acids. The lipopolysaccharides are molecules containing lipids and long-chain polymeric carbohydrates known as polysaccharides. The peptidoglycan is a large macromolecule formed of repeating units of two amino sugars, namely *N*-acetylglucosamine and *N*-acetylmuramic acid cross-linked by peptide side chains made of three to five amino acids. The inner membrane is made of a phospholipid bilayer and proteins.
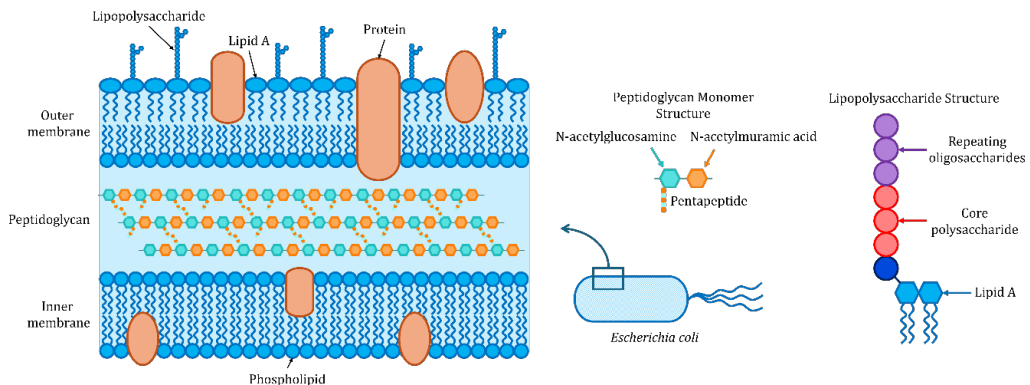
Figure 4.2. The cell membrane structure of gram-negative (Gram⁻) bacteria and its components

The measurements of OD_{600} of *E. coli* growth in the presence of GO-lanthanide oxide nanocomposites are shown in Figure 4.3. The exponential growth (log phase) in the control group started after three hours and the same occurred in the presence of 50 µg/mL of GO-La_2O_3 and GO-Gd_2O_3 (Figure 4.3), while for GO-Eu_2O_3 and GO-Tb_2O_3 the log phase started after four hours. After eight hours, the OD_{600} values obtained (Table 4.1) are slightly higher for the four nanocomposites than for the control group, which can be explained by the fact that the presence of the nanocomposites in the media increases the amount of scattered light, so for nanocomposite concentrations of 50 µg/mL no evident antimicrobial activity was observed. When the concentration was increased to 200 µg/mL, in the cell culture, the presence of GO-La_2O_3 induced a strong antibacterial activity since bacterial growth was inhibited even for six hours. The addition of GO-Eu_2O_3, GO-Gd_2O_3, and GO-Tb_2O_3 only seems to have slowed down bacterial growth. For concentrations of 400 µg/mL, all four nanocomposites were found to inhibit bacterial growth for six hours. In the case of GO-Eu_2O_3, GO-Gd_2O_3, and GO-Tb_2O_3, the bacterial population continued to increase and at eight hours the population was largest for the cell culture with GO-Tb_2O_3 followed by that with GO-Gd_2O_3 and then the one with GO-Eu_2O_3. In the cell culture to which GO-La_2O_3 had been added, the bacterial growth was completely inhibited.

4

Figure 4.3. Growth curves of an E. coli population after 8 h of incubation in the presence of various concentrations (50, 100 and 200 µg/mL) of GO-Ln oxide nanocomposites as a function of time. (The standard deviation was less than 5 % in all the cases)

Table 4.1. Optical density values (OD$_{600}$) of E. coli after 8 h of incubation in the presence of various concentrations (50, 100 and 200 µg/mL) of GO-Ln oxide nanocomposites as a function of time. (The standard deviation was less than 5 % in all the cases)

Concentration	Optical Density (600 nm)				
	Control	GO-La$_2$O$_3$	GO-Eu$_2$O$_3$	GO-Gd$_2$O$_3$	GO-Tb$_2$O$_3$
400 µg/mL		0.0121 ± 0.0090	0.0724 ± 0.0001	0.1282 ± 0.0085	0.2220 ± 0.0002
200 µg/mL	0.2693 ± 0.0030	0.0532 ± 0.0001	0.2506 ± 0.0090	0.2789 ± 0.0098	0.2623 ± 0.0090
50 µg/mL		0.2932 ± 0.0090	0.2966 ± 0.0029	0.2998 ± 0.0065	0.3052 ± 0.0087

In the case of GO-Ln hydroxide nanocomposites, bacterial growth started after three hours for concentrations of 50, 200 and 400 µg/mL and the same was observed for the control group (Figure 4.4). Contrary to the GO-Ln oxide nanocomposites, no antimicrobial activity was observed for any of the three concentrations of GO-Ln hydroxide employed for the first eight hours (Table 4.2). Surprisingly, the presence of GO-Ln hydroxide nanohybrids seems to favour bacterial growth for the three concentrations tested; this effect is most prominent for GO-Gd(OH)$_3$, followed by GO-Eu(OH)$_3$ and GO-Tb(OH)$_3$, while it is least pronounced for GO-La(OH)$_3$.
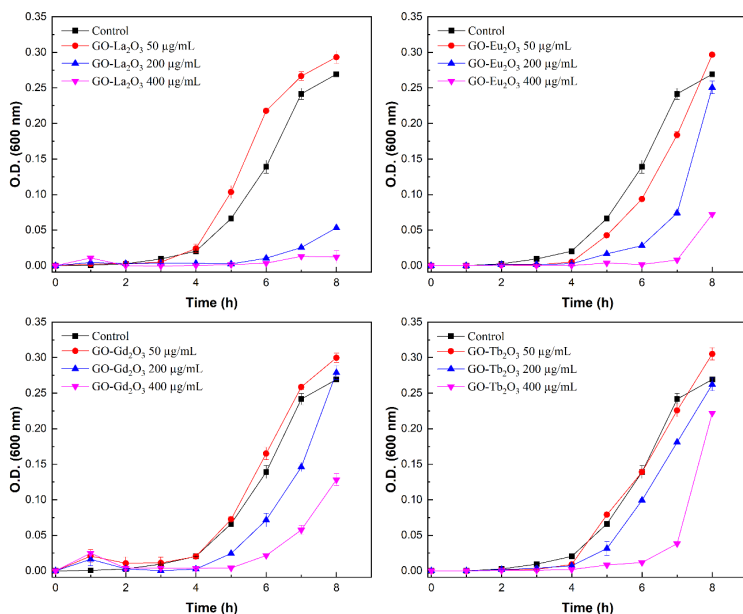
4
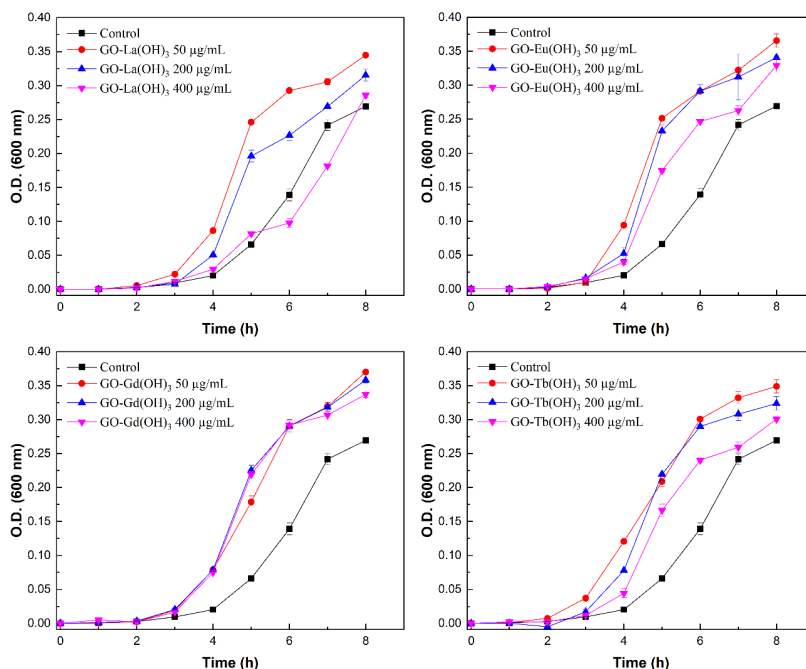
Figure 4.4. Growth curves of an E. coli population after 8 h of incubation in the presence of various concentrations (50, 100 and 200 µg/mL) of GO-Ln hydroxide nanocomposites as a function of time. (The standard deviation was less than 5 % in all the cases)

Table 4.2. Optical density values (OD_{600}) of E. coli after 8 h of incubation in the presence of various concentrations (50, 100 and 200 µg/mL) of GO-Ln hydroxide nanocomposites as a function of time. (The standard deviation was less than 5 % in all the cases)

Concentration	Optical Density (600 nm)				
	Control	GO-La(OH)$_3$	GO-Eu(OH)$_3$	GO-Gd(OH)$_3$	GO-Tb(OH)$_3$
400 µg/mL		0.2858 ± 0.0034	0.3293 ± 0.0098	0.3370 ± 0.0044	0.3005 ± 0.0034
200 µg/mL	0.2693 ± 0.0030	0.3153 ± 0.0090	0.3407 ± 0.0023	0.3581 ± 0.0045	0.3237 ± 0.0098
50 µg/mL		0.3447 ± 0.0023	0.3656 ± 0.0098	0.3700 ± 0.0012	0.3488 ± 0.0096

Previous studies proved that grafting La(OH)$_3$ nanoparticles to the GO surface increases the bactericidal effect against *E. coli* strains, and such nanocomposites are even capable of overcoming the evolution of antimicrobial resistance [29]. The mechanism proposed describes an extracellular multitarget invasion involving successive steps, namely first the association of the GO-La(OH)$_3$ nanocomposite with the outer membrane driven by the strong binding affinity between lanthanum and the phosphate groups [34], followed by lipid dephosphorylation, lipid peroxidation caused by the GO oxygen groups and the peptidoglycan disruption. Since the introduction of lanthanide species to the GO sheets can modify the surface charge and since the association step relies on the electrostatic attraction between the nanocomposite and the negatively charged surface of *E. coli*, Ln-containing nanoparticles are expected to play a very important role in the results obtained. As can be seen in the SEM and TEM micrographs in Figures 4.5 and 4.6, the Ln oxide particles are more homogeneously distributed on the GO surface than the Ln hydroxide particles. It is therefore reasonable that the antimicrobial activity against *E. coli* is higher for the GO-Ln oxide nanocomposites. That among the four GO-Ln oxides, GO-La$_2$O$_3$ shows the strongest activity cannot be related to a more uniform distribution of La$_2$O$_3$ particles on the GO sheets as compared to Eu$_2$O$_3$, Gd$_2$O$_3$ and Tb$_2$O$_3$ but to the fact that the La$_2$O$_3$ nanoparticles present a spherical shape and sizes of around 5 nm. Compared to the mostly amorphous nanoparticles found in GO-Eu$_2$O$_3$, Gd$_2$O$_3$ and Tb$_2$O$_3$ nanocomposites, the spherical-shaped nanoparticles in GO-La$_2$O$_3$ possess a higher surface area, leading to a stronger interaction with the bacteria membrane.
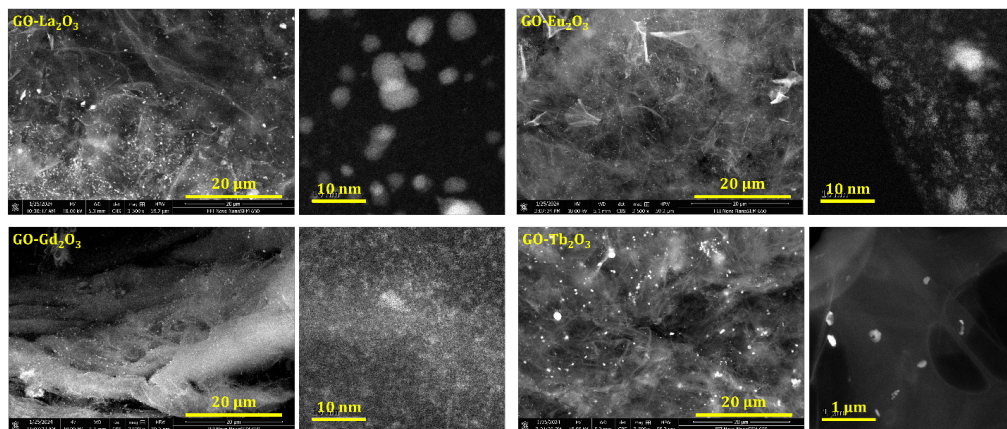
Figure 4.5. SEM and TEM images of GO-lanthanide oxide nanocomposites
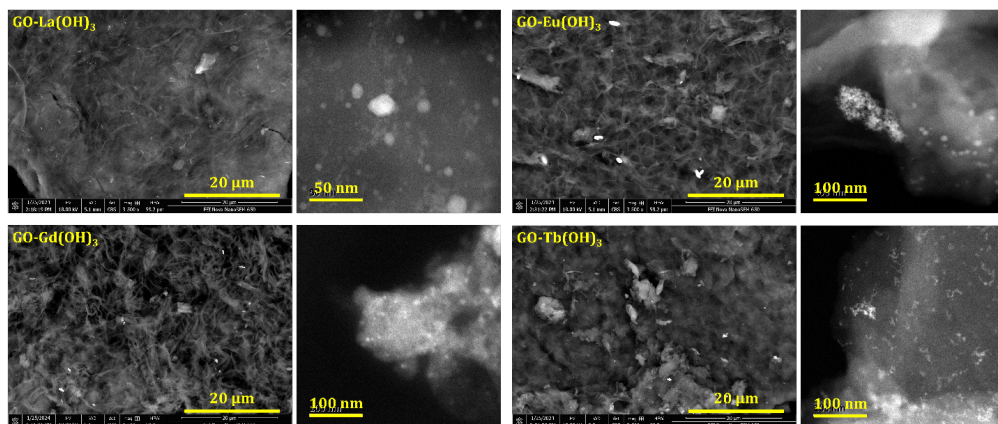
Figure 4.6. SEM and TEM images of GO-lanthanide hydroxide nanocomposites

4

Corynebacterium glutamicum

Corynebacterium glutamicum is a non-pathogenic bacterium usually employed in the large-scale production of amino acids [35]. It is a gram-positive (Gram⁺) rod-shaped bacterium, and its envelope differs from its Gram⁻ bacteria counterpart. The Gram⁺ bacteria do not possess an outer membrane only the peptidoglycan cell wall and the inner membrane, as sketched in Figure 4.7, but the composition is like Gram⁻ bacteria [33]. While the thickness of the Gram⁻ bacteria peptidoglycan cell wall is only 2 to 3 nm thick, for Gram⁺ bacteria its thickness typically reaches 30 to 100 nm, which provides structure and protection to the cell.
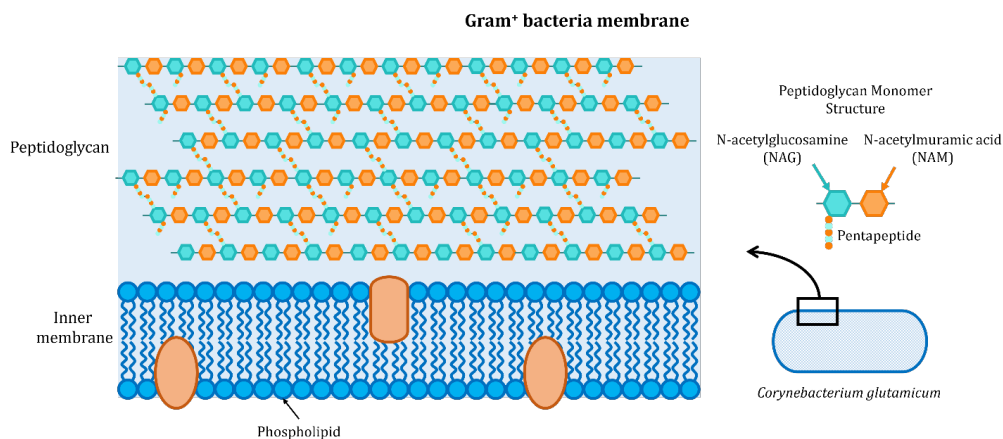
Figure 4.7. The cell membrane structure of gram-positive (Gram⁺) bacteria and its components

The measurements of OD_{600} of *C. glutamicum* growth in the presence of GO-lanthanide oxide nanocomposites are shown in Figure 4.8. The log phase in the control group started after three hours the same occurred in the presence of 50 µg/mL of GO-La$_2$O$_3$, GO-Gd$_2$O$_3$, and GO-Tb$_2$O$_3$, while for GO-Eu$_2$O$_3$ the start was delayed by hour compared to the other nanocomposites. After eight hours, there is no evidence of antimicrobial activity of any of the GO-Ln oxide nanocomposites when concentrations of 50 µg/mL were employed. When the concentration increased to 200 µg/mL, GO-La$_2$O$_3$ showed the strongest antibacterial activity since it completely inhibited bacterial growth even for six hours, while GO-Eu$_2$O$_3$, GO-Gd$_2$O$_3$, and GO-Tb$_2$O$_3$ only seemed to slow down bacterial growth, similar to what was observed against *E. coli*. For concentrations of 400 µg/mL of GO-La$_2$O$_3$ bacterial growth started only after 7 h, while the same concentration of GO-Eu$_2$O$_3$, GO-Gd$_2$O$_3$, and GO-Tb$_2$O$_3$ was less effective since there the log phase could be seen only after 7, 6, 6 and 5 hours, respectively. At eight hours at this high concentration, the bacterial population had increased the most for GO-Gd$_2$O$_3$ followed by GO-Tb$_2$O$_3$ and GO-La$_2$O$_3$ and the lowest value was recorded for GO-Eu$_2$O$_3$ (Table 4.3). This proves that GO-La$_2$O$_3$ and GO-Eu$_2$O$_3$ present the strongest antimicrobial activity and almost completely inhibit bacterial growth.

Figure 4.8. Growth curves of C. glutamicum population after 8 h of incubation in the presence of various concentrations (50, 100 and 200 µg/mL) of GO-Ln oxide nanocomposites as a function of time. (The standard deviation was less than 5 % in all the cases)

Table 4.3. Optical density values (OD_{600}) of C. glutamicum after 8 h of incubation in the presence of various concentrations (50, 100 and 200 µg/mL) of GO-Ln oxide nanocomposites as a function of time. (The standard deviation was less than 5 % in all the cases)

Concentration	Control	Optical Density (600 nm)			
		GO-La_2O_3	GO-Eu_2O_3	GO-Gd_2O_3	GO-Tb_2O_3
400 µg/mL		0.0532 ± 0.0003	0.0316 ± 0.0075	0.1672 ± 0.0017	0.1322 ± 0.0017
200 µg/mL	0.2603 ± 0.0098	0.0885 ± 0.0060	0.1829 ± 0.0095	0.2757 ± 0.0067	0.2692 ± 0.0095
50 µg/mL		0.3043 ± 0.0089	0.2681 ± 0.0096	0.3154 ± 0.0078	0.2781 ± 0.0021

As illustrated in Figure 4.9, in the case of GO-Ln hydroxide nanocomposites, the bacterial growth started already after two and three hours for cell cultures with concentrations of 50, 200 and 400 µg/mL, just like for the control group. No antimicrobial activity was observed with any of the three concentrations employed at eight hours and like the results obtained against *E. coli*, the presence of GO-Ln hydroxide nanocomposites seems to favour bacterial growth for the three concentrations tested. However, here the effect was strongest for GO-Tb(OH)$_3$ followed by GO-Gd(OH)$_3$ and GO-Eu(OH)$_3$, while GO-Tb(OH)$_3$ was only in third place in terms of effectiveness. in most of the cases. GO-La(OH)$_3$ has the lowest growth-promoting effect in most of the cases (Table 4.4), but more detailed investigations would be required to discard the hypothesis that the increase of OD$_{600}$ values is a consequence of poor interaction between nanocomposites and bacteria.
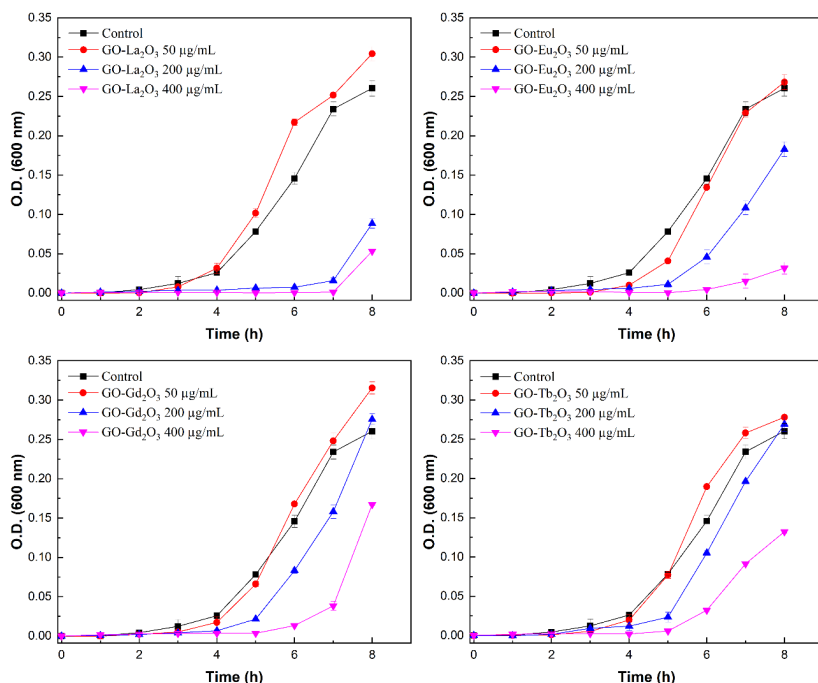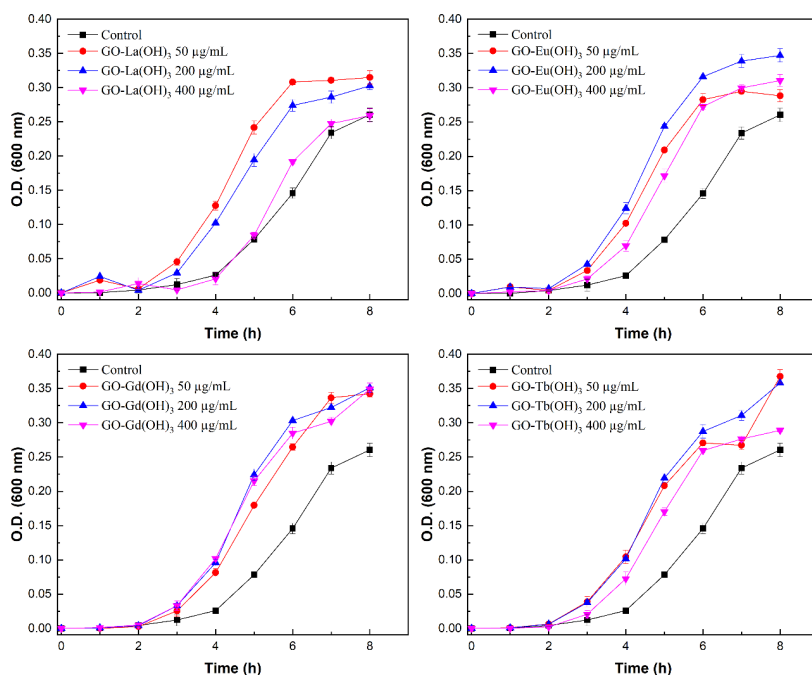

Figure 4.9. Growth curves of C. glutamicum population after 8 h of incubation in the presence of various concentrations (50, 100 and 200 µg/mL) of GO-Ln hydroxide nanocomposites as a function of time. (The standard deviation was less than 5 % in all the cases)

Table 4.4. Optical density (OD_{600}) of C. glutamicum after 8 h of incubation in the presence of various concentrations (50, 100 and 200 µg/mL) of GO-Ln hydroxide nanocomposites as a function of time. (The standard deviation was less than 5 % in all the cases)

Concentration	Optical Density (600 nm)				
	Control	GO-La(OH)$_3$	GO-Eu(OH)$_3$	GO-Gd(OH)$_3$	GO-Tb(OH)$_3$
400 µg/mL	0.2603 ± 0.0098	0.2891 ± 0.0023	0.3105 ± 0.0087	0.3490 ± 0.0089	0.2891 ± 0.0023
200 µg/mL		0.3580 ± 0.0023	0.3472 ± 0.0097	0.3510 ± 0.0067	0.3580 ± 0.0023
50 µg/mL		0.3675 ± 0.0098	0.2884 ± 0.0087	0.3423 ± 0.0045	0.3675 ± 0.0098

As a consequence of a strong binding between GO-La(OH)$_3$ and peptidoglycan molecules based on their affinity, a massive disruption of the molecular arrangement in the cell wall is possible [29], so antimicrobial activity against Gram[+] bacteria could be expected. As observed for the activity against *E. coli*, the antimicrobial activity against *C. glutamicum* is stronger for GO-Ln oxide than for GO-Ln hydroxide nanocomposites due to the size, shape and distribution of the Ln-containing particles. Among the four GO-Ln oxides employed, the GO-La$_2$O$_3$ sample has the strongest effect because La$_2$O$_3$ nanoparticles are mostly spherical, as previously discussed.

4.4. Conclusions

The antimicrobial activity of the GO-lanthanide oxide and GO-lanthanide hydroxide nanocomposites against *Escherichia coli* and *Corynebacterium glutamicum*. While the GO-lanthanide hydroxide did not show any negative effect on bacterial growth in both cases but even seemed to favour cell division. GO-lanthanide oxides exhibited a dose-dependent behaviour. The best growth inhibition was achieved by adding a concentration of 400 µg/mL of GO-La$_2$O$_3$ to the cell culture; in fact, under these conditions, the nanocomposite was able to inhibit completely the proliferation of *E. coli* for 8 hours. The SEM micrographs revealed that the differences in antibacterial activity are not related to the type of lanthanides employed but to the shape and size of the nanoparticles as well as to their distribution, throughout the GO surface. These findings show that nanocomposites of graphene oxide and lanthanide-oxide nanoparticles are promising antibacterial agents against both Gram[-] and Gram[+] bacteria.

References

[1] D.E. Bloom, D. Cadarette, Infectious disease threats in the twenty-first century: Strengthening the global response, Front Immunol 10 (2019) 445106. https://doi.org/10.3389/FIMMU.2019.00549.

[2] F. Prestinaci, P. Pezzotti, A. Pantosti, Antimicrobial resistance: a global multifaceted phenomenon, Pathog Glob Health 109 (2015) 309–318. https://doi.org/10.1179/2047773215Y.0000000030.

[3] H. Liu, J. Cheng, F. Chen, F. Hou, D. Bai, P. Xi, Z. Zeng, Biomimetic and cell-mediated mineralization of hydroxyapatite by carrageenan functionalized graphene oxide, ACS Appl Mater Interfaces 6 (2014) 3132–3140. https://doi.org/10.1021/AM4057826.

[4] V. Rosa, Z. Zhang, R.H.M. Grande, J.E. Nör, Dental Pulp Tissue Engineering in Full-length Human Root Canals, Http://Dx.Doi.Org/10.1177/0022034513505772 92 (2013) 970–975. https://doi.org/10.1177/0022034513505772.

[5] L. Karimi, M.E. Yazdanshenas, R. Khajavi, A. Rashidi, M. Mirjalili, Using graphene/TiO2 nanocomposite as a new route for preparation of electroconductive, self-cleaning, antibacterial and antifungal cotton fabric without toxicity, Cellulose 21 (2014) 3813–3827. https://doi.org/10.1007/S10570-014-0385-1.

[6] C.M. Santos, M.C.R. Tria, R.A.M. V. Vergara, F. Ahmed, R.C. Advincula, D.F. Rodrigues, Antimicrobial graphene polymer (PVK-GO) nanocomposite films, Chemical Communications 47 (2011) 8892–8894. https://doi.org/10.1039/C1CC11877C.

[7] H. Zheng, R. Ma, M. Gao, X. Tian, Y.Q. Li, L. Zeng, R. Li, Antibacterial applications of graphene oxides: structure-activity relationships, molecular initiating events and biosafety, Sci Bull (Beijing) 63 (2018) 133–142. https://doi.org/10.1016/J.SCIB.2017.12.012.

[8] X. Zou, L. Zhang, Z. Wang, Y. Luo, Mechanisms of the Antimicrobial Activities of Graphene Materials, J Am Chem Soc 138 (2016) 2064–2077. https://doi.org/10.1021/JACS.5B11411.

[9] H. Mohammed, A. Kumar, E. Bekyarova, Y. Al-Hadeethi, X. Zhang, M. Chen, M.S. Ansari, A. Cochis, L. Rimondini, Antimicrobial Mechanisms and Effectiveness of Graphene and Graphene-Functionalized Biomaterials. A Scope Review, Front Bioeng Biotechnol 8 (2020) 498689. https://doi.org/10.3389/FBIOE.2020.00465.

[10] F. Perreault, A.F. De Faria, S. Nejati, M. Elimelech, Antimicrobial Properties of Graphene Oxide Nanosheets: Why Size Matters, ACS Nano 9 (2015) 7226–7236. https://doi.org/10.1021/ACSNANO.5B02067.

[11] J. Zhu, J. Wang, J. Hou, Y. Zhang, J. Liu, B. Van der Bruggen, Graphene-based antimicrobial polymeric membranes: a review, J Mater Chem A Mater 5 (2017) 6776–6793. https://doi.org/10.1039/C7TA00009J.

[12] H.E. Karahan, C. Wiraja, C. Xu, J. Wei, Y. Wang, L. Wang, F. Liu, Y. Chen, Graphene Materials in Antimicrobial Nanomedicine: Current Status and Future Perspectives, Adv Healthc Mater 7 (2018) 1701406. https://doi.org/10.1002/ADHM.201701406.

[13] S. Bhatt, R. Pathak, V.D. Punetha, M. Punetha, Recent advances and mechanism of antimicrobial efficacy of graphene-based materials: a review, Journal of Materials Science 2023 58:19 58 (2023) 7839–7867. https://doi.org/10.1007/S10853-023-08534-Z.

[14] V.T.H. Pham, V.K. Truong, M.D.J. Quinn, S.M. Notley, Y. Guo, V.A. Baulin, M. Al Kobaisi,

4

R.J. Crawford, E.P. Ivanova, Graphene Induces Formation of Pores That Kill Spherical and Rod-Shaped Bacteria, ACS Nano 9 (2015) 8458–8467. https://doi.org/10.1021/ACSNANO.5B03368.

[15]   J. Li, G. Wang, H. Zhu, M. Zhang, X. Zheng, Z. Di, X. Liu, X. Wang, Antibacterial activity of large-area monolayer graphene film manipulated by charge transfer, Scientific Reports 2014 4:1 4 (2014) 1–8. https://doi.org/10.1038/srep04359.

[16]   O. Akhavan, E. Ghaderi, A. Esfandiar, Wrapping bacteria by graphene nanosheets for isolation from environment, reactivation by sonication, and inactivation by near-infrared irradiation, Journal of Physical Chemistry B 115 (2011) 6279–6288. https://doi.org/10.1021/JP200686K.

[17]   W. Hu, C. Peng, W. Luo, M. Lv, X. Li, D. Li, Q. Huang, C. Fan, Graphene-based antibacterial paper, ACS Nano 4 (2010) 4317–4323. https://doi.org/10.1021/NN101097V.

[18]   S. Liu, T.H. Zeng, M. Hofmann, E. Burcombe, J. Wei, R. Jiang, J. Kong, Y. Chen, Antibacterial activity of graphite, graphite oxide, graphene oxide, and reduced graphene oxide: Membrane and oxidative stress, ACS Nano 5 (2011) 6971–6980. https://doi.org/10.1021/NN202451X.

[19]   I. Sengupta, P. Bhattacharya, M. Talukdar, S. Neogi, S.K. Pal, S. Chakraborty, Bactericidal effect of graphene oxide and reduced graphene oxide: Influence of shape of bacteria, Colloid Interface Sci Commun 28 (2019) 60–68. https://doi.org/10.1016/J.COLCOM.2018.12.001.

[20]   Y. Tu, M. Lv, P. Xiu, T. Huynh, M. Zhang, M. Castelli, Z. Liu, Q. Huang, C. Fan, H. Fang, R. Zhou, Destructive extraction of phospholipids from Escherichia coli membranes by graphene nanosheets, Nature Nanotechnology 2013 8:8 8 (2013) 594–601. https://doi.org/10.1038/nnano.2013.125.

[21]   L. Wu, L. Zeng, X. Jiang, Revealing the nature of interaction between graphene oxide and lipid membrane by surface-enhanced infrared absorption spectroscopy, J Am Chem Soc 137 (2015) 10052–10055. https://doi.org/10.1021/JACS.5B03803.

[22]   B. Luan, T. Huynh, R. Zhou, Complete wetting of graphene by biological lipids, Nanoscale 8 (2016) 5750–5754. https://doi.org/10.1039/C6NR00202A.

[23]   J. Chen, G. Zhou, L. Chen, Y. Wang, X. Wang, S. Zeng, Interaction of Graphene and its Oxide with Lipid Membrane: A Molecular Dynamics Simulation Study, Journal of Physical Chemistry C 120 (2016) 6225–6231. https://doi.org/10.1021/ACS.JPCC.5B10635.

[24]   M. Moghayedi, E.K. Goharshadi, K. Ghazvini, H. Ahmadzadeh, M.N. Jorabchi, Antibacterial activity of Ag nanoparticles/phosphomolybdate/reduced graphene oxide nanocomposite: Kinetics and mechanism insights, Materials Science and Engineering: B 262 (2020) 114709. https://doi.org/10.1016/J.MSEB.2020.114709.

[25]   T. Pulingam, K.L. Thong, M.E. Ali, J.N. Appaturi, I.J. Dinshaw, Z.Y. Ong, B.F. Leo, Graphene oxide exhibits differential mechanistic action towards Gram-positive and Gram-negative bacteria, Colloids Surf B Biointerfaces 181 (2019) 6–15. https://doi.org/10.1016/J.COLSURFB.2019.05.023.

[26]   T. Pulingam, K.L. Thong, J.N. Appaturi, C.W. Lai, B.F. Leo, Mechanistic actions and contributing factors affecting the antibacterial property and cytotoxicity of graphene oxide, Chemosphere 281 (2021) 130739. https://doi.org/10.1016/J.CHEMOSPHERE.2021.130739.

[27]   M.T. Kaczmarek, M. Zabiszak, M. Nowak, R. Jastrzab, Lanthanides: Schiff base complexes,

4

applications in cancer diagnosis, therapy, and antibacterial activity, Coord Chem Rev 370 (2018) 42–54. https://doi.org/10.1016/J.CCR.2018.05.012.

[28]   M. Wang, Y. Su, Y. Liu, Y. Liang, S. Wu, N. Zhou, J. Shen, Antibacterial fluorescent nano-sized lanthanum-doped carbon quantum dot embedded polyvinyl alcohol for accelerated wound healing, J Colloid Interface Sci 608 (2022) 973–983. https://doi.org/10.1016/J.JCIS.2021.10.018.

[29]   H. Zheng, Z. Ji, K.R. Roy, M. Gao, Y. Pan, X. Cai, L. Wang, W. Li, C.H. Chang, C. Kaweeteerawat, C. Chen, T. Xia, Y. Zhao, R. Li, Engineered Graphene Oxide Nanocomposite Capable of Preventing the Evolution of Antimicrobial Resistance, ACS Nano 13 (2019) 11488–11499. https://doi.org/10.1021/ACSNANO.9B04970.

[30]   J.A. Myers, B.S. Curtis, W.R. Curtis, Improving accuracy of cell and chromophore concentration measurements using optical density, BMC Biophysics 2013 6:1 6 (2013) 1–16. https://doi.org/10.1186/2046-1682-6-4.

[31]   J.B. Kaper, J.P. Nataro, H.L.T. Mobley, Pathogenic Escherichia coli, Nature Reviews Microbiology 2004 2:2 2 (2004) 123–140. https://doi.org/10.1038/nrmicro818.

[32]   N. Allocati, M. Masulli, M.F. Alexeyev, C. Di Ilio, Escherichia coli in Europe: An Overview, International Journal of Environmental Research and Public Health 2013, Vol. 10, Pages 6235-6254 10 (2013) 6235–6254. https://doi.org/10.3390/IJERPH10126235.

[33]   T.J. Silhavy, D. Kahne, S. Walker, The Bacterial Cell Envelope, Cold Spring Harb Perspect Biol 2 (2010). https://doi.org/10.1101/CSHPERSPECT.A000414.

[34]   M. Kawase, T. Suzuki, K. Miura, Growth mechanism of lanthanum phosphate particles by continuous precipitation, Chem Eng Sci 62 (2007) 4875–4879. https://doi.org/10.1016/J.CES.2007.02.032.

[35]   V. Gopinath, K.M. Nampoothiri, Corynebacterium glutamicum, Encyclopedia of Food Microbiology: Second Edition (2014) 504–517. https://doi.org/10.1016/B978-0-12-384730-0.00076-8.

4

—— CHAPTER 5 ——

High-energy ball-milling preparation and characterisation of Ln_2O_3-graphite nanocomposites

The combination of lanthanide species with graphite and related carbon nanomaterials (including graphene and graphene oxide) is a pathway to hybrid materials and nanocomposites with unique properties. Mechanical processing is an especially efficient and attractive way to generate such nanostructured materials since it results in the progressive exfoliation of graphite and can yield a variety of carbon nanostructures with sp^2 hybridization, derived from graphene building blocks. However, the knowledge of how lanthanides interact with graphite upon mechanical processing is very scarce. The study reported in this chapter aimed to obtain composites of graphite and selected Ln_2O_3 oxides (Ln = La, Eu, Gd and Lu) via high-energy ball-milling. According to scanning electron microscopy and X-ray diffraction analysis, the materials obtained can be qualified as nanocomposites, combining nanosized graphite and Ln_2O_3 particles, whose size depends on particular lanthanide species. The nanocomposites were characterized by Raman, fluorescence, and X-ray photoelectron spectroscopy, as well as thermogravimetric and differential thermal analysis. Density functional theory calculations were employed to provide insight into the strength of interactions between Ln^{3+} ions and graphene sheets, as well as into the distribution of charge and spin density depending on a particular lanthanide.

5.1. Introduction

The combination of different lanthanide species with graphite and especially related carbon nanomaterials such as graphene and graphene oxide (GO) is a pathway to hybrid materials with unique and potentially useful properties. Some particular aspects of interest are the fabrication of luminescent nanocomposites for medical diagnostics, bioimaging and environmental monitoring [1–4], catalysts for high-performance hydrogen evolution and oxygen reduction [5], components of proton membranes for fuel cells, water electrolysers [6], sensors for detection of hydrogen peroxide in biological and clinical samples [7,8] and dye-sensitised solar cells [9], contrast agents for magnetic resonance imaging [10–12], as well as model systems for the research in nuclear waste management [13].

Combining lanthanide compounds with graphite received much less attention. It was studied mainly in the context of graphite intercalation compounds, which can be obtained under relatively harsh conditions such as the treatment of graphite with lanthanide metal vapour, the compression and heating of mixtures of graphite and metal powders at 400–500 °C [14], the interaction of graphite and lanthanide metals in molten chlorides at up to 400 °C [15], or intercalation by chemical vapour transport of lanthanide trichlorides at about 700–800 °C [16].

In view of the global focus on nanomaterials, the importance of graphite-based composites with lanthanide compounds seems rather obvious at first glance: compact graphite does not exhibit the unique properties of nanosized graphene. A gap still exists between the two carbon varieties, due to the fact that the fabrication of graphene from graphite through traditional 'chemical' processing routes is labour and time-intensive; moreover, it can also be considered environmentally unfriendly because requires a relatively large amount of chemicals.

Nevertheless, in the case of graphite, one can approach the 'top-down structuring' in a different way. It is well-known that mechanical processing (MP) can serve to generate nanostructured materials [17]. In particular, it has been shown that high-energy ball milling results in progressive exfoliation of graphite and yields a variety of carbon nanostructures with sp^2 hybridization, derived from the graphene backbone [18]. On the other hand, the knowledge of how lanthanides interact with graphite upon MP is scarce. J. Tang showed how ball milling induces amorphization of graphite and increases its solubility in Ag-Gd solid solution [19], O. Mao and G. Rixecker and colleagues reported attempts to synthesise interstitial carbide-type permanent magnets by the mechanochemical blending of lanthanide-iron intermetallides and

graphite [20,21], and X. Zheng et al. studied MP of rare earth trihydrides and graphite for the fabrication related of lithium storage materials [22].

While in the previous chapters, we employed the solvothermal method as an environmentally friendly approach, the goal of the study presented in this chapter was to obtain composites of graphite and selected Ln_2O_3 oxides (Ln = La, Eu, Gd and Lu) by means of high-energy ball-milling as a solvent-free synthesis technique and to characterise them by several spectroscopy and electron microscopy techniques, as well as by thermal analysis. The main question we intended to address was whether the composites obtained can be qualified as nanocomposites, combining nanosized graphite and Ln_2O_3 particles. Density functional theory (DFT) calculations were employed to provide insight into the mechanism of interactions of Ln^{3+} ions with graphene sheets, taken as the structural elements of graphite.

5.2. Experimental

5.2.1. Materials

Lanthanide oxides La_2O_3, Eu_2O_3, Gd_2O_3 and Lu_2O_3 (all having 99.9 % purity), as well as graphite powder (particle size of <20 μm) were purchased from Sigma-Aldrich and used as received.

5.2.2. Mechanical processing

For MP, we used Ln_2O_3–graphite mixtures with 20 wt% of lanthanide oxide. Graphite powder (10 g) and Ln_2O_3 (2.5 g) were placed into a 100 mL tungsten carbide (WC) reactor together with 30 WC balls of 20 mm diameter. The balls:mixture ratio was 22:1 w/w. After sealing the reactor, each sample was subjected to high-energy ball-milling for 8 h at 400 rpm, by using a Planetary Ball-Mill PM 400/2 from Retsch, Inc.

5.2.3. Theoretical calculations

The DFT approach of choice was the Perdew-Burke-Ernzerhof (PBE) [23] correlation functional within general gradient approximation (GGA). Since accounting for dispersion interactions is crucial when analysing noncovalently bonded systems, the PBE functional was complemented with the empirical correction developed by Grimme [24]. This combination, commonly referred to as PBE-D (or also PBE-D2), has been

frequently used for DFT studies of noncovalent, covalent and coordination interactions of a wide variety of chemical species with graphene and GO models [25–33].

The software employed for calculations was the DMol^3 numerical-based module [34–37] of the Materials Studio package. The PBE-D functional was used in conjunction with the double numerical basis set DNP [37], where a polarisation d-function was added on all non-hydrogen atoms, and a polarisation p-function on all H atoms. The quasi-relativistic effective core potentials (ECP) [38,39] were utilised to describe the interactions of core electrons. All the calculations were spin unrestricted. 'Fine' computation quality and convergence criteria were set for full geometry optimization and electronic parameter calculations, namely: 10^{-5} Ha energy gradient, 0.002 Ha/Å maximum force, 0.005 Å maximum displacement, and 10^{-6} self-consistent field (SCF) tolerance. The value of 5.8 Å was used for the global orbital cutoff for all the systems studied.

The model systems containing Ln species, which are 4*f* elements, and carbon nanoclusters were found to be a very difficult case of SCF convergence [32,33]. Setting orbital occupancy directly to 'Fermi' allows for successful SCF convergence in very rare (rather fortuitous) cases. Therefore, the use of thermal smearing was necessary, whose value was reduced stepwise starting from 0.005 Ha [33,40]. Nevertheless, for most (especially central) lanthanides even this auxiliary measure did not help to complete computations with Fermi orbital occupancy. Since the use of sufficiently low smearing of 10^{-4} Ha was shown to yield results identical to those obtained with Fermi occupancy [33], our attempted goal was to complete the whole series of calculations at this value (successful for La^{3+}, Pr^{3+}, Eu^{3+}, Yb^{3+} and Lu^{3+}). As a last resource, for a few lanthanide species (Ce^{3+}, Nd^{3+}, Ho^{3+}, Er^{3+} and Tm^{3+}) the geometry optimization was performed at $5 \cdot 10^{-4}$ Ha, but electronic parameters were refined at 10^{-4} Ha, as recommended in our previous study [33]. The most difficult cases turned out to be the systems containing Pm^{3+}, Sm^{3+}, Gd^{3+}, Tb^{3+} and Dy^{3+}, for which even this relaxed computational strategy failed (the results obtained with higher smearing values are not presented here).

The formation energies ΔE_{Ln+G} (hereafter ΔE for simplicity) for the complexes of Ln^{3+} species were calculated with a graphene cluster model [33] according to the following equation:

$$\Delta E = E_{Ln+G} - (E_{Ln} + E_G)$$

where E$_i$ is the corresponding absolute energy.

5.3. Results and discussion

5.3.1. Experimental results

The changes in particle size and morphology of graphite and lanthanide oxides due to MP can be best illustrated by means of SEM. As shown in the micrographs presented in Figure 5.1, the size of pristine graphite particles was roughly around 10 μm, and platelets smaller than 10 μm were generally absent (Figure 5.1a, c). While at lower magnifications (e.g., 1000×; Figure 5.1d, g, j, m) the four lanthanide oxides exhibited similar morphology, the images taken at higher magnifications (e.g., 30,000×; Figure 5.1f, i, l, o) reveals important differences between them. Individual particles of pristine La_2O_3 and Lu_2O_3 appear as irregularly shaped compact formations (Figure 5.1f, o). The La_2O_3 particle size was found to vary, mostly between 200 nm and 5 μm, whereas in the case of Lu_2O_3, it was more uniform within a few micrometres. The fine morphological features observed for pristine Eu_2O_3 and Gd_2O_3 samples (Figure 5.1i, l) revealed that the individual oxide particles were actually agglomerates of globular structural elements. These round structures are smaller (of ca. 50 nm) and loosely packed (with distinguishable empty spaces between them) in the case of Eu_2O_3, whereas they are roughly 100−300 nm in size and densely compressed for Gd_2O_3. At the same time, it is interesting to note that the density of these oxides is approximately the same, 7.42 and 7.41 g/cm^3, respectively (for comparison, the density of La_2O_3 and Lu_2O_3 is very different, namely 6.51 and 9.42 g/cm^3, respectively).

5

Figure 5.1. Representative SEM images (taken at different magnifications) of the starting materials: (a-c) pure graphite powder; (d-f) La₂O₃; (g-i) Eu₂O₃; (j-l) Gd₂O₃; (m-o) Lu₂O₃. Scale bar: (a, d, g, j, m) 10 μm; (b, e, h, k, n) 5 μm; and (c, f, i, l, o) 0.5 μm

As expected, high-energy MP dramatically changed the features described above. At first glance, one can say that the SEM images of all the ball-milling processed samples, including pure graphite, look alike (Figure 5.2), (Figure 5.2a-c). Since graphite is a dominating component of the mixtures (80 wt%), it is its MP-induced morphology, which defines the general appearance of the sample in the micrographs. All of them show the presence of globular agglomerates of broadly variable sizes. For graphite, La₂O₃–graphite and Eu₂O₃–graphite (Figure 5.2c, f, i) the smallest features were nanometre-sized, of the order of 100 nm. On the other hand, the presence of such nanometre-sized

formations is less evident in the case of Gd_2O_3–graphite (Figure 5.2l) and for the Lu_2O_3–graphite mixture (Figure 5.2o) they can be hardly found at all. The morphology in Figure 5.2o can be better described as a combination of features typical for pristine individual graphite and for Lu_2O_3 (Figure 5.1c, o), though with notably smaller particle sizes. This observation suggests that MP efficiency is different for different lanthanide oxides.
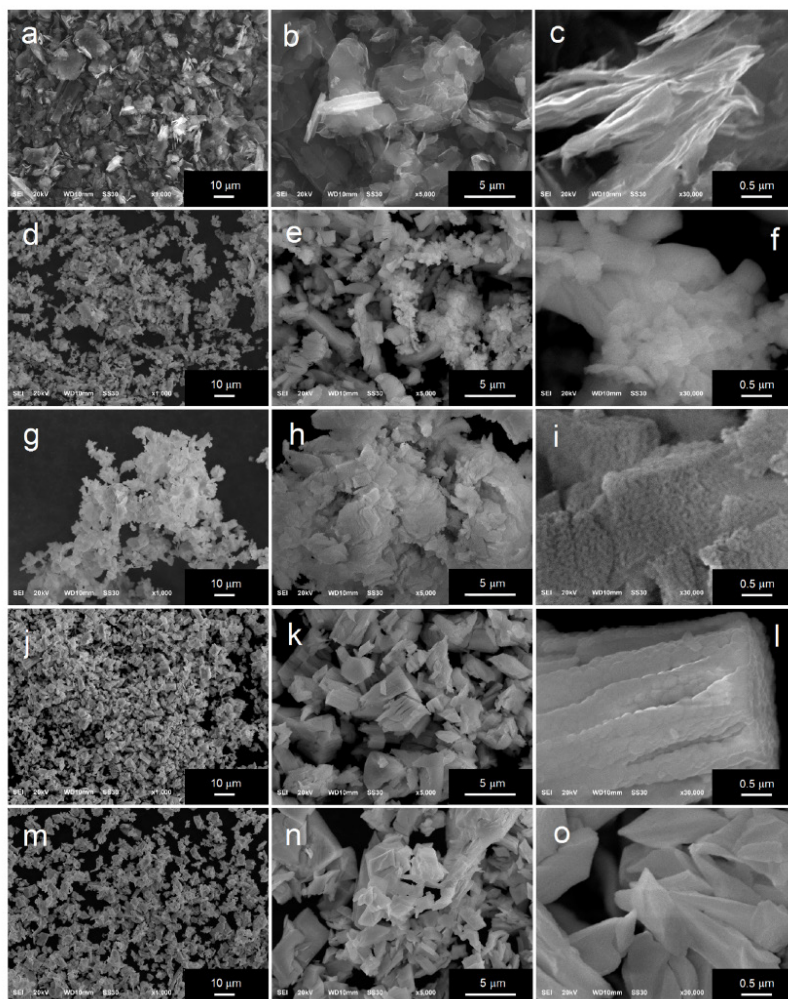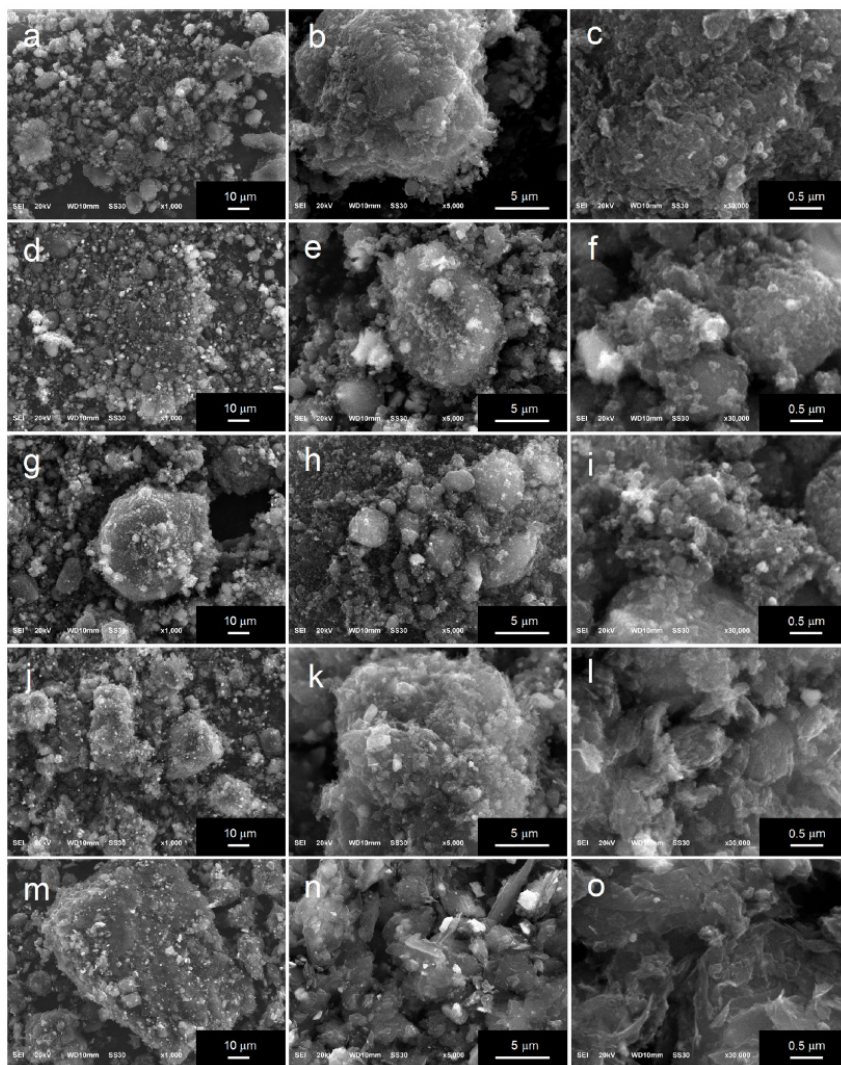

Figure 5.2. Representative SEM images (taken at different magnifications) of mechanically processed materials: (a-c) pure graphite powder; (d-f) La_2O_3-graphite; (g-i) Eu_2O_3-graphite; (j-l) Gd_2O_3-graphite; (m-o) Lu_2O_3-graphite. Scale bar: (a, d, g, j, m) 10 µm; (b, e, h, k, n) 5 µm; and (c, f, I, l, o) 0.5 µm.

Since the High-Angle Annular Dark Field (HAADF) mode is a STEM mode where elements with different Z numbers appear with distinct contrast, it was employed to have a better insight into the lanthanide oxide particles. The micrographs shown in Figure 5.3 confirmed that all the Ln$_2$O$_3$-graphite mixtures present globular-shaped Ln$_2$O$_3$ nanoparticles with sizes around 50-125 nm for La$_2$O$_3$-graphite, 50-100 nm for Eu$_2$O$_3$-graphite, 40-115 nm for Gd$_2$O$_3$-graphite, and 90-180 nm for Lu$_2$O$_3$.
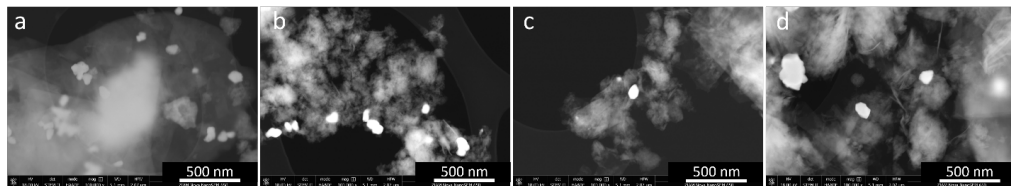
Figure 5.3. Representative STEM-HAADF images for mechanically processed materials: (a) La$_2$O$_3$-graphite; (b) Eu$_2$O$_3$-graphite; (c) Gd$_2$O$_3$-graphite; and (d) Lu$_2$O$_3$-graphite. Scale bar: (a-d) 500 nm.

Another technique which can serve as a quantitative measure of the efficiency of the ball-milling is powder XRD. For pure graphite the XRD patterns in Figure 5.4 show that although the platelets have sizes roughly around 10 μm when observed by SEM (Figure 5.1a-c), the size of crystallites forming them is about 9.5 nm, as estimated from the width of the (002) peak at about 25.6°. After 8 h of MP, the crystallite size reduces 4–5 times to an average of 2.2 nm, which is very close to the value of 2.3 nm reported by Shen et al. [41] for similar ball-milling conditions. It is impossible to estimate the graphite crystallite size in processed La$_2$O$_3$–graphite (Figure 5.3) since the (002) peak at 25.6° coincides with a signal from La$_2$O$_3$. In the case of Eu$_2$O$_3$–graphite we found approximately the same crystallite size as for pure milled graphite. However, for Gd$_2$O$_3$–graphite and Lu$_2$O$_3$–graphite, the crystallite size was found to be much larger, about 7 and 8 nm, respectively, suggesting that MP is less efficient for these two mixtures than for La and Eu-containing materials. As regards the crystallite size reduction for lanthanide oxides, it depends on Ln species as well. The strongest effect was found for La$_2$O$_3$, with a three-fold decrease in crystallite size, from 67 to 22 nm (by 67 %), followed by Eu$_2$O$_3$, for which crystallite size is reduced from 40 to 31 nm (by 23 %), then by Gd$_2$O$_3$ where it decreased from 35 to 25 nm (by 29 %) and finally by Lu$_2$O$_3$, where we found only an 11 % decrease from 37 to 33 nm. In other words, the efficiency of MP in terms of crystallite size reduction clearly correlates with Ln$_2$O$_3$ density, which decreases in the series as follows: La$_2$O$_3$ < Gd$_2$O$_3$ < Eu$_2$O$_3$ < Lu$_2$O$_3$.
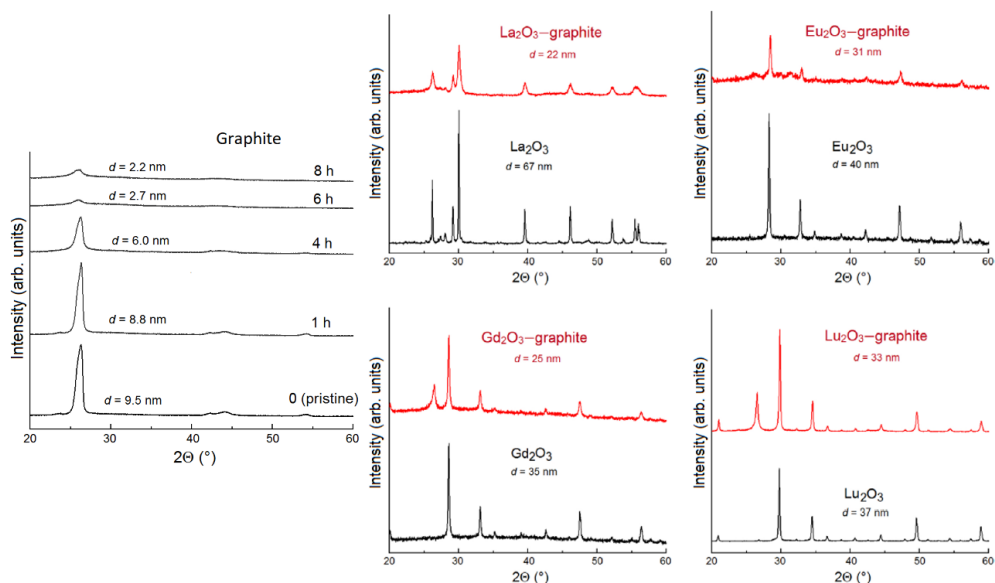
Figure 5.4. XRD diffractograms before and after MP (left) graphite; (right) different Ln2O3-graphite mixtures here the diffractograms in red after 8 h and the diffractograms in black refer to the unprocessed materials. For each diffractogram, the crystallite size, as deduced from the FWHM of the (002) peak with the help of the Scherrer equation, is also reported.

5

For graphite, in addition to the decrease in crystallite size, MP also implies the generation of a large number of structural defects, equivalent to an increase in the number of sp^3-hybridised carbon atoms. This can be conveniently monitored by Raman spectroscopy [22,41,42], as illustrated in Figure 5.5. For unprocessed graphite, its most prominent characteristic D, G and 2D bands are observed at 1339, 1569 and 2687 cm^{-1}, respectively, with an approximate intensity ratio between the D and the G band (due to a high noise level), I_D/I_G, of 0.32. As a result of MP, for pure graphite I_D/I_G value dramatically increases to 1.08. A similar effect was found for La$_2$O$_3$–graphite, with I_D/I_G = 1.15. No interference of La$_2$O$_3$ bands was observed since the peaks due to this compound are all below 500 cm^{-1} with the exception of the most intense feature at 3608 cm^{-1} [43]. On the contrary, Eu$_2$O$_3$ exhibits a very rich Raman spectrum precisely in the range of interest between 1300 and 4000 cm^{-1}, thus making even a very rough estimate of the I_D/I_G ratio impossible. For the remaining two samples, Gd$_2$O$_3$–graphite and Lu$_2$O$_3$–graphite, the signals due to lanthanide oxides do not interfere significantly and all three characteristic graphite bands D, G and 2D are clearly seen. It is interesting to note that the I_D/I_G ratio for Gd and Lu-containing samples was found to amount to 0.35 and 0.37, respectively, i.e. to values much closer to that for pristine graphite than the one for milled graphite. We also attempted FTIR characterisation, however, due

to the low quality typical for infrared spectra of powder graphite samples, no useful information was afforded.
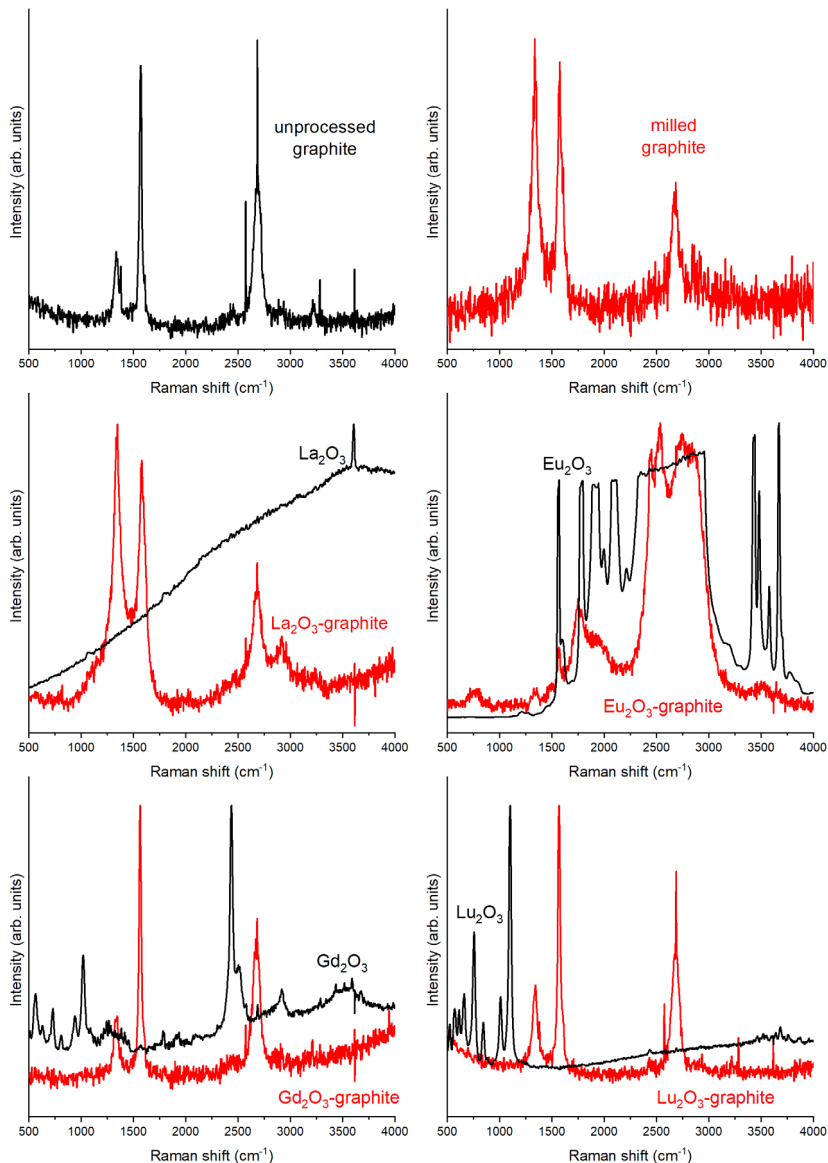
Figure 5.5. Comparison of Raman spectra (without baseline adjustment) for mechanically processed samples (in red) and starting materials (graphite and lanthanide oxides; in black).

Raman scattering and fluorescence emission are two competing phenomena. They have a similar origin, and the fluorescence effect can lead to a gradual increase of the baseline of the Raman spectrum from lower to higher wavenumbers, which is evident for neat La_2O_3, Gd_2O_3 and Lu_2O_3 and their composites with graphite after MP (Figure 5.4). In general, fluorescence is an important feature of many lanthanide compounds, and that is why we also employed this kind of spectroscopy for comparative characterization of the samples obtained. The results are presented in Figure 5.6. According to Cui and Hope [43], La_2O_3 does not exhibit fluorescence emissions in the visible region. In our case, upon excitation at 405 nm, we only observed weak emission in the near-infrared region at 838 nm (Figure 5.6a). This weak emission, which is barely present in ball-milled graphite, can be also detected in La_2O_3–graphite after MP. For Lu_2O_3, its mixture with graphite and pure milled graphite (Figure 5.5d) no reliable differences can be found in the emission spectra. The absence of bright features for La and Lu-based systems is due to the absence of unpaired $4f$ electrons in these lanthanide species. As opposed to La^{3+} and Lu^{3+}, Eu^{3+} and Gd^{3+} ions have six and seven $4f$ electrons, respectively. Generally, chemical compounds and materials containing central lanthanide species are fluorescent. One should note, however, that gadolinium complexes are more widely known for their outstanding magnetic properties, whereas their fluorescence is comparatively weak and needs to be enhanced by adding usually Eu^{3+} [44–46], or in more rare cases Ho^{3+} [47], Er^{3+}, Tb^{3+}, and Dy^{3+} [48]. In our study, pure Eu_2O_3 when excited at 394 nm, exhibits a series of emission bands (Figure 5.5b) corresponding to $^5D_0$-^7F_J transitions [49,50]. The most intense feature is the $^5D_0$-$^7F_2$ transition observed at 613 nm [50], followed by the one at 593 nm ($^5D_0$-$^7F_1$), and then by less intense bands at 581, 588, 624 and 629 nm. All these emissions appear to be quenched in Eu_2O_3–graphite after MP. The only likely contribution of Eu_2O_3 fluorescence is a slight 2 nm shift of the band observed for milled graphite at 595 nm. A similar effect has been reported by Mo *et al.* [51] who observed fluorescence quenching for Eu_2O_3 after deposition onto a carbon nanotube template; to the authors' surprise, after calcination of the composite at >620 °C, when carbon nanotubes were burnt, the resulting Eu_2O_3 nanotubes exhibited very strong emission bands at around 540 and 580 nm, due to the $^5D_0$-$^7F_0$ and $^5D_0$-$^7F_1$ forced electric dipole transition of Eu^{3+} ions. In other words, quenching of Eu_2O_3 fluorescence by a carbon material is an already documented phenomenon.

5
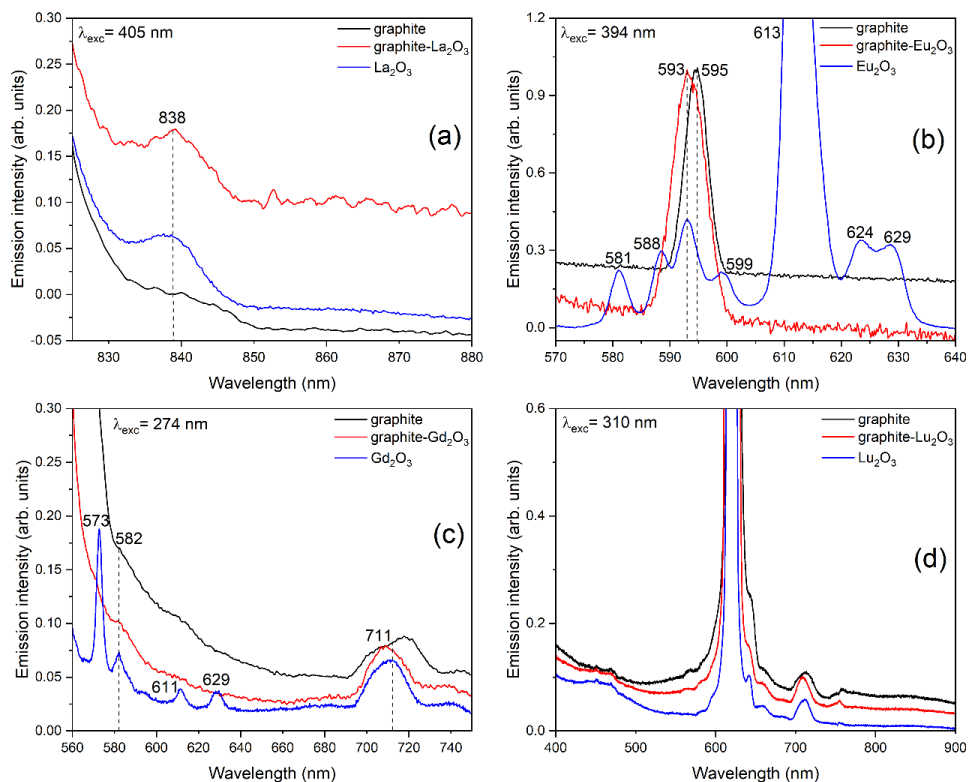
Figure 5.6. Comparison of fluorescence spectra for mechanically processed Ln$_2$O$_3$-graphite mixtures, pure ball-milled graphite, and unprocessed lanthanide oxides: (a) La$_2$O$_3$; (b) Eu$_2$O$_3$; (c) Gd$_2$O$_3$; (d) Lu$_2$O$_3$.

As mentioned above, in the case of gadolinium compounds fluorescence is comparatively weak but can be strongly enhanced by means of doping with ions of other central lanthanides [44–48]. To be precise, pure cubic and monoclinic Gd$_2$O$_3$ polymorphs exhibit an intrinsic luminescence due to "defective" Gd^{3+} ions (at 315 nm); the luminescence is excited according to the 4f–4f intracentral mechanism at 232 and 275 nm [52]. At the same time, for the above polymorphs, no luminescence is observed in the spectral range of 300-900 nm. In our study, the fluorescence spectrum of pure unprocessed Gd$_2$O$_3$ (Figure 5.5c; excitation at 274 nm) contains a series of peaks in the visible range at 573 (most intense), 582, 611, 629 and 711 nm; nevertheless, they are much weaker compared to those observed for neat Eu$_2$O$_3$ (Figure 5.5b). Similarly, in the case of Eu$_2$O$_3$, the latter peaks results totally quenched for Gd$_2$O$_3$–graphite after MP, and their possible contribution is apparently limited to a minor increase in fluorescence at 582 and 711 nm. Interestingly, as opposed to the quenching effect of carbon nanotubes

on Eu_2O_3 fluorescence reported by Mo *et al.* [51], Yue *et al.* [53] revealed that covering ultrasmall Gd_2O_3 particles with a thin carbon layer results in a broad emission between 410 and 600 nm (with a maximum at about 460 nm) due to the nanocarbon phase.

The most direct information on possible rearrangements in chemical bonds can be obtained from XPS. As a necessary reference point, we first addressed the question of whether graphite itself can undergo substantial changes upon MP. While the reactor is hermetically sealed, the presence of minor amounts of residual atmospheric oxygen is inevitable. Consequently, high-energy ball-milling can, in principle, cause partial oxidation of graphite. As one can see from the C1s core level spectrum presented in Figure 5.7, the same carbon-containing groups are present before and after MP but the amount of oxygenated species somewhat increases after ball milling: this can be seen from the intensities of CH=O (288.4–288.5 eV), C–OH (285.5 eV [54,55]) and CH–O (286.7–287.0 eV) components, as well as from comparison of the entire C1s peak profiles (the inset in Figure 5.6). Fine features of the O1s core level peak (centred at 532.8 eV) are impossible to resolve; one can only say that its intensity increases by about 50 % due to MP.
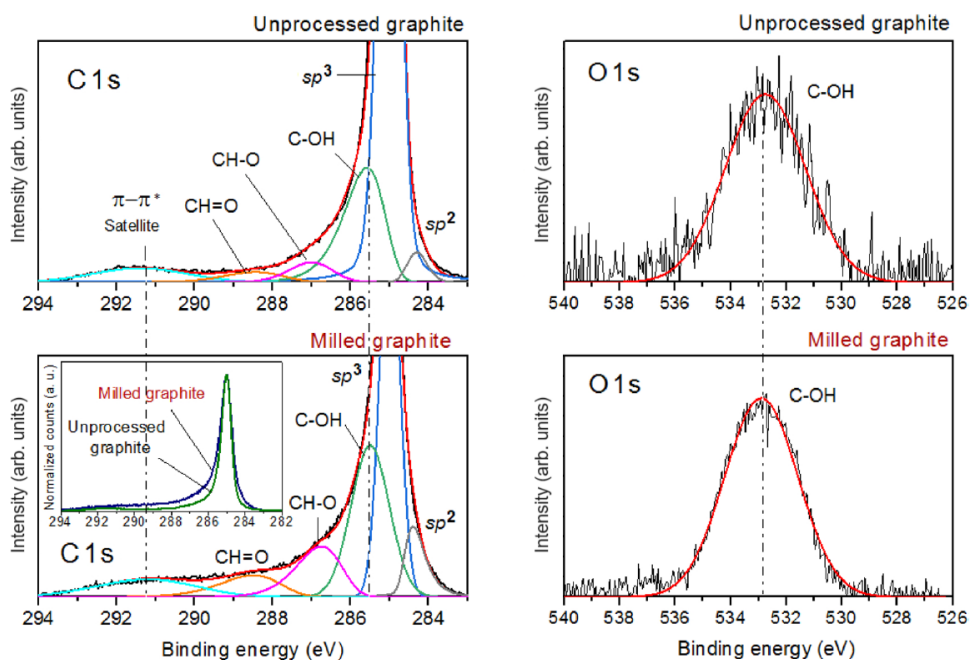
Figure 5.7. Comparison of the C1s and O1s core level regions in XPS spectra of unprocessed and ball-milled graphite. The inset shows differences in the corresponding C1s profiles. Raw data are shown in black, and the sum of the fitted components, in red.

The C1s spectra of all ball-milled Ln$_2$O$_3$–graphite mixtures (Figure 5.7) are similar to the spectrum of pure milled graphite, which is expected since it is the dominating component (80 wt%). At the same time, one should note that in the case of La and Eu, the contribution due to CH-O bonds at 286.6–286.8 and to C-OH bonds at 285.5–285.6 eV is larger than for Gd and Lu. This correlates with the differences in graphite milling efficiency suggested by the results of SEM (Figure 5.2), XRD (Figure 5.4) and Raman spectroscopy (Figure 5.5).
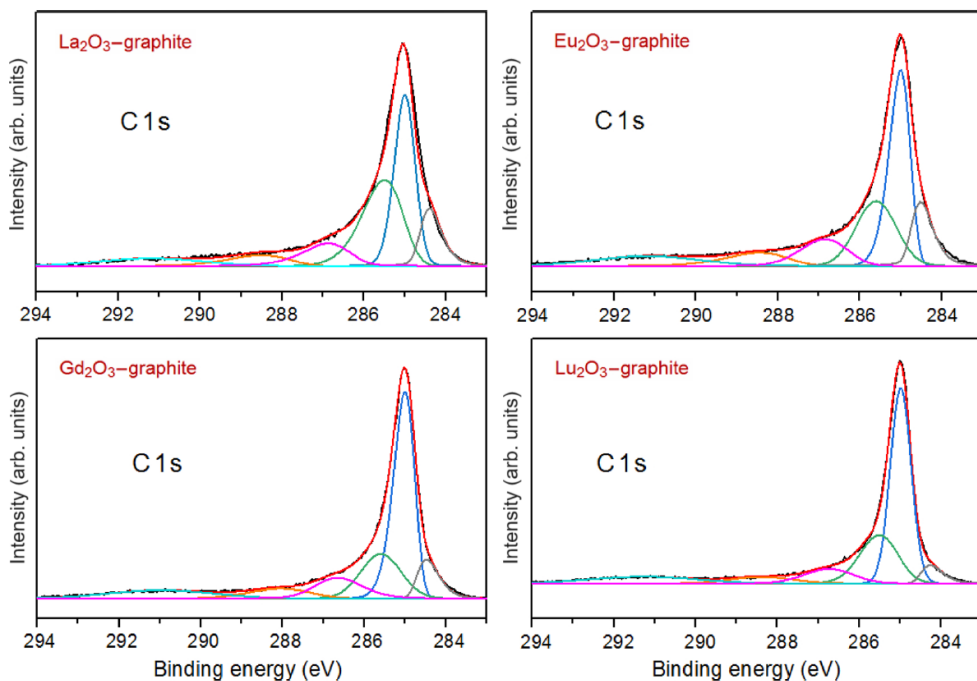
Figure 5.8. Comparison of the C1s core level region of the XPS spectra for mechanically processed Ln$_2$O$_3$-graphite mixtures. Raw data are shown in black, and sum of fitted components in red.

Table 5.1. XPS binding energies (eV) for La 3d$_{5/2}$, Eu 3d, Gd 3d$_{5/2}$, Lu 4f, O1s and C1s core levels in ball-milled Ln$_2$O$_3$-graphite mixtures and the corresponding pure Ln$_2$O$_3$ oxides as a reference.

	Binding energy (eV)										
	La 3d$_{5/2}$	Eu 3d$_{5/2}$	Gd 3d$_{5/2}$	Lu 4f	O1s	C1s					
Sample	La-O	Eu-O	Gd-O	Lu-O	O-Ln	sp^2	sp^3	C-OH	CH-O	CH=O	π – π*
Graphite						284.4	285.0	285.5	286.8	288.5	291.2
La$_2$O$_3$-graphite	837.1				531.8	284.4	285.0	285.5	286.9	288.5	291.2
La$_2$O$_3$	835.2				531.8[a]		285.0				
Eu$_2$O$_3$-graphite		1135.5			529.8	284.5	285.0	285.6	286.9	288.4	291.2
Eu$_2$O$_3$		1134.1			529.8[b]		285.0				
Gd$_2$O$_3$-graphite			1188.2		530.9	284.5	285.0	285.6	286.7	288.0	291.0
Gd$_2$O$_3$			1187.3		529.3[a]		285.0				
Lu$_2$O$_3$-graphite				8.2	530.3	284.3	285.0	285.6	286.7	288.4	291.3
Lu$_2$O$_3$				7.4	529.2[c]		285.0				

[a] Ref. [56]; [b] Ref. [57]; [c] Ref. [58]

The XPS data for Ln$_2$O$_3$–graphite mixtures in terms of deconvolution of O1s, La3d$_{5/2}$, Eu3d$_{5/2}$, Gd3d$_{5/2}$ and Lu4f core level components are presented in Figure 5.9 and Table 5.1. In the O1s spectra, the major peak is always due to oxidised functionalities (C–OH) in graphite. At the same time, the contribution of O–Ln bonds is clearly seen at 529.8–531.8 eV. The O–Ln binding energy (BE) for the Ln$_2$O$_3$–graphite composite remains the same as for pure lanthanide oxide in the case of La and Eu but shifts to higher BE by 1.1 and 1.6 eV for Lu and Gd, respectively. The latter trend can be seen also for the La3d$_{5/2}$, Eu3d$_{5/2}$, Gd3d$_{5/2}$ and Lu4f components. The largest BE difference of 1.9 eV was found for Ln$_2$O$_3$–graphite vs. pure Ln$_2$O$_3$ (La3d$_{5/2}$ peak), followed by 1.4 eV for Eu$_2$O$_3$–graphite vs. pure Eu$_2$O$_3$ (Eu3d$_{5/2}$ peak), 0.9 eV for Gd$_2$O$_3$–graphite vs. pure Gd$_2$O$_3$ (Gd3d$_{5/2}$ peak), and finally, the smallest one of 0.8 eV was obtained for Lu$_2$O$_3$–graphite vs. pure Lu$_2$O$_3$ (Lu4f). The larger BE difference between Ln$_2$O$_3$–graphite and pure Ln$_2$O$_3$ in the case of La and Eu, again, goes in line with a higher milling efficiency (compared to Gd and Lu composites), suggested by SEM imaging (Figure 5.2), XRD (Figure 5.4) and Raman spectroscopy (Figure 5.5), which results in a larger fraction of lanthanide oxide nanoparticles found in direct contact with graphite, which induces the corresponding BE shift.
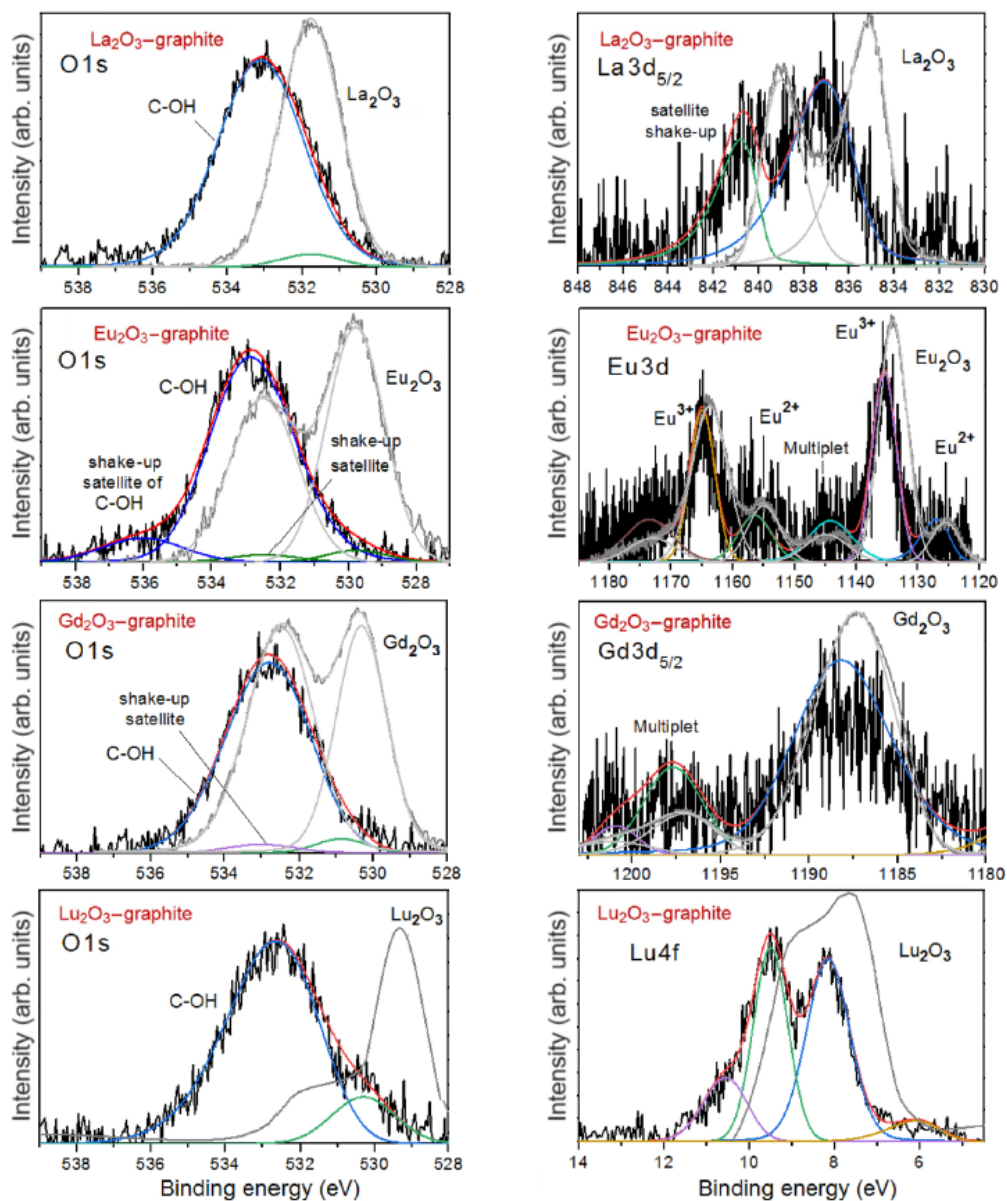
Figure 5.9. XPS spectra of the O1s, La3d$_{5/2}$, Eu3d, Gd3d$_{5/2}$ and Lu4f core level regions of ball milled Ln_2O_3-graphite mixtures. Raw data are shown in black, and sum of the fitted components in red. Spectra in grey correspond to pure corresponding Ln_2O_3 as a reference [47–49].

The last but not least aspect of interest is how MP and the presence of lanthanide oxide influence the thermal stability of graphite. It was addressed by TGA–DTA analysis; the results are shown in Figure 5.10. Ball-milling of pure graphite results in a dramatic reduction of the final combustion temperature from 969 °C (main DTA peak at 759 °C; Figure 5.9a) to 783 °C (DTA peak at 648 °C; Figure 5.9b), which can be explained by a sharp increase in the total graphite surface exposed to air, as well as by the formation of a large number of reactive defects. This effect is even more pronounced for La_2O_3–graphite and Eu_2O_3–graphite mixtures (Figure 5.9c, d), for which the final combustion temperatures are 759 and 756 °C (main DTA peaks at 572 and 474 °C), respectively. In part, this can be attributed to the abrasive action of lanthanide oxides, which helps more efficient MP: for example, note that I_D/I_G = 1.15 for La_2O_3–graphite mixture (calculated from Raman spectra in Figure 5.5) is somewhat higher than the value of 1.08 obtained for pure ball-milled graphite. In addition, a catalytic effect of Ln_2O_3, which reduces the final combustion temperature of graphite, is in principle, possible as well. Still, the first explanation seems to be more plausible, taking into account that for Gd_2O_3–graphite and Lu_2O_3–graphite mixtures (Figure 5.9e, f), the much more moderate decrease in final combustion temperatures of 835 and 873 °C (main DTA peaks at 647 and 723 °C), respectively, correlates with the much less significant increase in I_D/I_G ratio (estimated from Raman spectra in Figure 5.5) and with less-pronounced reduction in Ln_2O_3 crystallite size (especially for Lu_2O_3; Figure 5.4) due to MP.

5

5

Figure 5.10. Thermogravimetric analysis (black) and differential thermal analysis (red) of (a) unprocessed graphite powder and of lanthanide-oxide graphite composites after mechanical processing; (b) pure graphite; (c) La$_2$O$_3$-graphite; (d) Eu$_2$O$_3$-graphite; (e) Gd$_2$O$_3$-graphite; (f) Lu$_2$O$_3$-graphite.

5.3.2. Theoretical modelling

DFT calculations can provide additional insights into the mechanisms of interaction of lanthanide species with carbon materi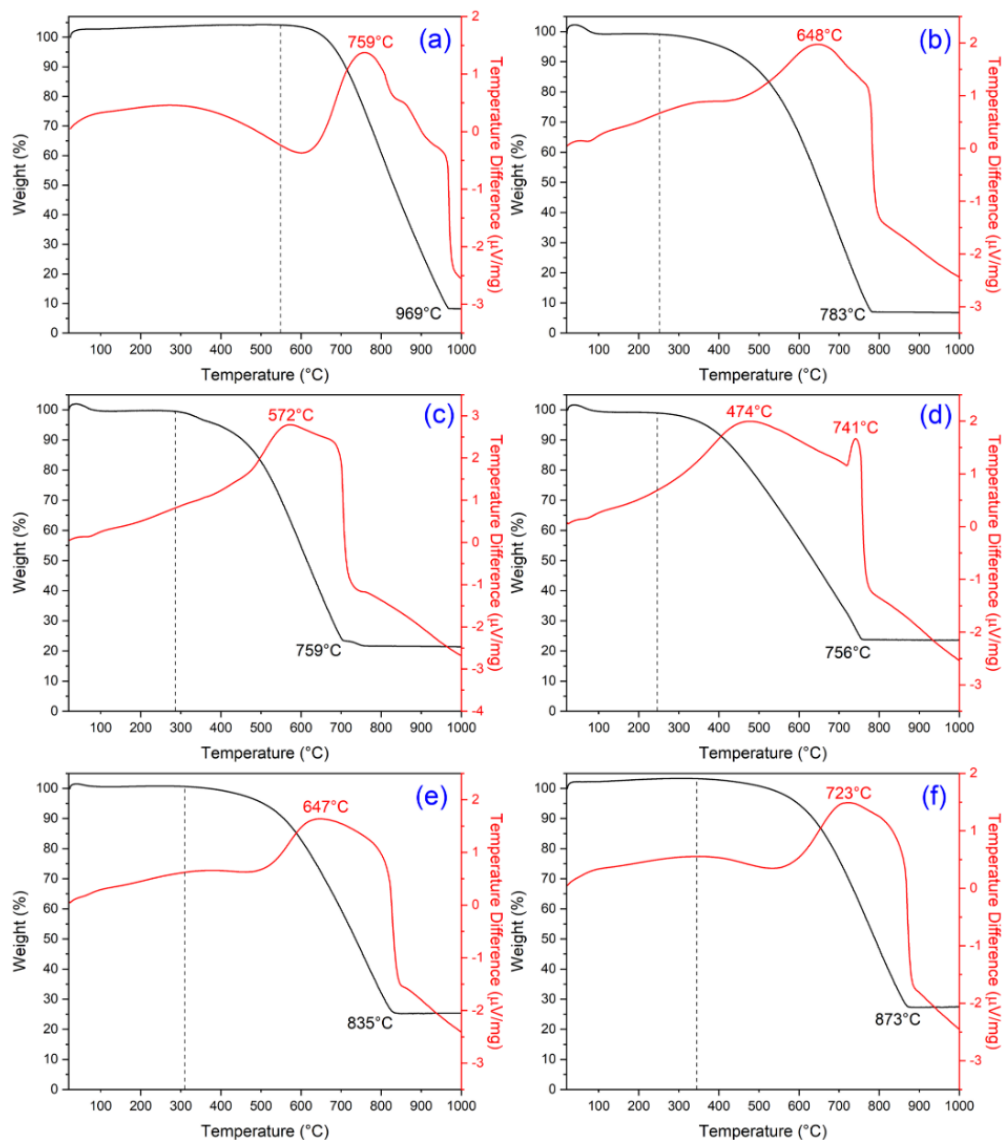als. In the present context, the ideal approach would be to consider the interaction of a Ln_2O_3 *phase* with graphene sheet models, but, unfortunately, such a theoretical treatment it is not feasible in the near future due to the known difficulties with SCF convergence when running calculations on the model systems containing *f*-electrons. In our case, even though the model systems contained *only one* lanthanide species, completion of the step-by-step computations on some Ln^{3+}+G complexes required up to one month when using PCs with 8–12 parallel processes and 64GB RAM. Furthermore, it turns out that even studies related to bonding of *single* lanthanide atoms and ions to graphene sheets are extremely scarce. The examples we are aware of concern the adsorption, density-of-states and magnetization characteristics of La atoms interacting with pristine [59] and single vacancy-containing graphene [60], the attachment and spin-polarization of lanthanide (Ln =La-Gd) atoms on graphene containing single and double vacancies [61], the interaction of La and Lu atoms and their trivalent cations with topological (pentagon-based) defects in graphene [32], as well as the optimization of the DFT computational strategy by employing thermal smearing when using both cluster and periodic models for the graphene sheet [33].

A special comment should be made on the choice of a cluster versus a periodic model for graphene. While cluster models are unable to match the quasi-continuity of the graphene skeleton, they are more versatile in other regards, due to the possibility to account for changeable chemical periphery (edge-terminating hydrogen atoms and oxygen functionalities such as COOH groups) [28–33], as well as to incorporate defects other than vacancies (isolated pentagonal rings, pyracylene units, etc.) [29–33]. The systems containing peripheral groups and topological defects are of particular focus in our other studies, which explains the same choice of a cluster model in the present work.

While experimental limitations did not allow us to include the full series of lanthanide oxides, we attempted to expand the variety of Ln^{3+} species considered in DFT calculations to the highest extent possible. Nevertheless, due to persistent SCF convergence problems, the results with the necessary level of credibility were impossible to obtain for Pm^{3+}, Sm^{3+}, Gd^{3+}, Tb^{3+} and Dy^{3+} (see section *2.4. Theoretical calculations*). Thus, the discussion presented below comprises ten of fifteen possible Ln^{3+} species.

The cluster model of choice was supercoronene (hereafter referred to as G;

5

Figure 5.11), whose peripheral dangling bonds were filled with hydrogen atoms (brutto formula $C_{54}H_{18}$)[33]. In the starting geometry, a Ln^{3+} ion was placed over the central hexagonal ring, so that lanthanide species was hexacoordinated (i.e., η^6 hapticity) in all cases. The coordination pattern did not change upon geometry optimization. Nevertheless, we observed an interesting effect consisting of G model bending to a degree, which depends on Ln^{3+} species adsorbed, as exemplified for Lu^{3+}, Nd^{3+} and Eu^{3+} in Figure 5.11. This phenomenon results from a very strong interaction between lanthanide ion and the graphene model and implies that the latter suffers a variable degree of tension, which must increase its energy. In other words, this effect must be taken into account when estimating the bonding strength between Ln^{3+} species and the G model.

The calculated formation energies ΔE for $Ln^{3+}+G$ complexes are presented in Table 5.2. The attraction between the strongly positively charged lanthanide species and the π-electron rich graphene model explains the very low negative ΔE values, spanning from -374.2 ($La^{3+}+G$) down to -672.1 kcal/mol ($Tm^{3+}+G$). *A priori*, one could expect that the interaction strength must depend on the atomic number of lanthanide chemical element and the number of unpaired electrons in Ln^{3+} (referred to as n_{ue}). A graphical analysis of these two
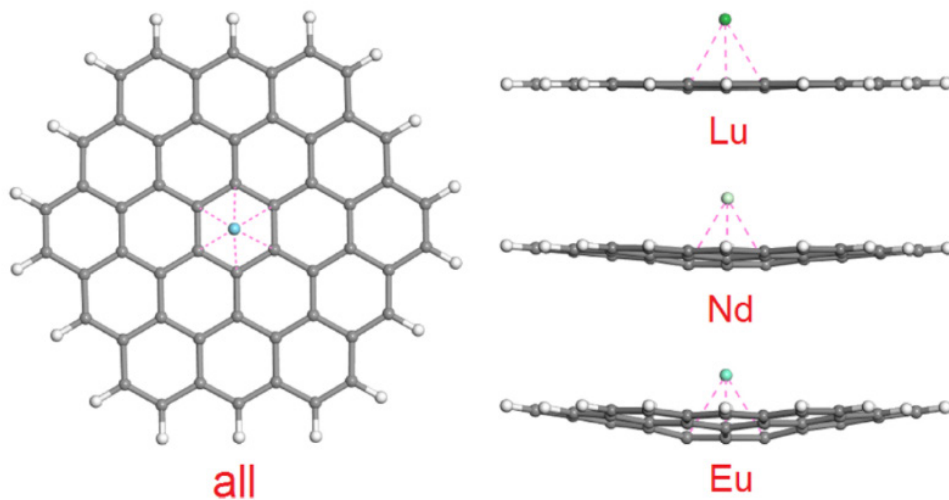
5

Figure 5.11. Optimised geometries for the complexes of Ln^{3+} ions with supercoronene cluster model (G), represetative of the graphene sheet, showing the coordination pattern (η^6 hapticity in all cases) and different degree of G model bending depending on Ln^{3+} species adsorbed.

interrelations is presented in Figure 5.12a, b, respectively. In Figure 5.12a one can see that ΔE steadily (almost linearly) decreases from La to Ho, then remains approximately the same until Yb, and finally for Lu dramatically jumps back up to bonding energy values close to those calculated for La and Ce. It is interesting to note that in terms of electronic configuration, Lu^{3+} ([Xe] $4f^{14}$) is more similar to Yb^{3+} ([Xe]$4f^{13}$) than to La^{3+} ([Xe]) and Ce^{3+} ([Xe]$4f^{1}$). The same can be said about their ionic radii, which are 0.86, 0.87, 1.03 and 1.01 Å for Lu^{3+}, Yb^{3+}, La^{3+} and Ce^{3+}, respectively. On the other hand, in the plot of ΔE vs. n_{ue}, the position of Lu is much closer to the one of La and Ce. This plot includes several pairs of Ln^{3+} ions having the same n_{ue} value (namely, La^{3+} and Lu^{3+}, Ce^{3+} and Yb^{3+}, Pr^{3+} and Tm^{3+}, Nd^{3+} and Er^{3+}), which form two series of data points, comprising the early (upper series) and late (lower series) lanthanides and converging on the point of Eu^{3+}.

As it was mentioned above, the very strong interaction between lanthanide ion and G induces strong distortion of the latter. The corresponding increase in energy (i.e. decrease in its absolute value) of the graphene model, referred to hereafter as ΔE_{dist}, can be calculated as the total energy difference between the optimised (relaxed) energy of the isolated G model and the single-point energy of G extracted from the optimised Ln^{3+}+G complex. The formation energy ΔE thus contains two components, namely:

$$\Delta E = \Delta E_{dist} + \Delta E_{bond}$$

where ΔE_{bond} is the remaining fraction responsible just for bonding between lanthanide ion and graphene model. That is,

$$\Delta E_{bond} = \Delta E - \Delta E_{dist}$$

The ΔE_{dist} and ΔE_{bond} values calculated for each Ln^{3+}+G complex are listed in Table 5.2. Even though the ΔE_{dist} component can vary within roughly one order of magnitude, from 1.3 (Er^{3+}+G) to 16.2 kcal/mol (Eu^{3+}+G), on the entire scale of ΔE values its contribution does not seem to be significant. In particular, the general trends observed in the plots of ΔE_{bond} vs. atomic number (Figure 5.12c) and ΔE_{bond} vs. n_{ue} (Figure 5.12f) are essentially the same as those found in the plots of ΔE vs. atomic number and ΔE vs. n_{ue} discussed above (Figure 5.12a, b). As regards the graphic interrelations of ΔE_{dist} vs. atomic number (Figure 5.12c) and ΔE_{dist} vs. n_{ue} (Figure 5.12d), they suggest that the distortion of G (see also Figure 5.11) and the corresponding increase in energy are much more significant for central lanthanides with n_{ue} = 5–7, which are represented here by Eu^{3+} (electronic configuration [Xe]$4f^{6}$). However, to make more definitive conclusions, the relevant data for Pm^{3+}, Sm^{3+}, Gd^{3+}, Tb^{3+} and Dy^{3+} would be necessary.

Table 5.2. Formation energies (ΔE) and their components ΔE$_{dist}$ and ΔE$_{bond}$ (all in kcal/mol), the shortest distances d$_{Ln...C}$ (in Å), charge and spin of Ln species (based on Mulliken population analysis), as calculated for Ln^{3+}+G complexes with PBE GGA functional with Grimme´s dispersion correction in conjunction with DNP basis set and ECP pseudopotentials.

Ln^{3+}+G complex	ΔE (kcal/mol)	ΔE$_{dist}$ (kcal/mol)	ΔE$_{bond}$ (kcal/mol)	d$_{Ln...C}$ (Å)	Charge of Ln	Spin of Ln
La^{3+}+G	-374.2	1.8	-376.0	2.887-2.893	1.430	0.894
Ce^{3+}+G	-395.9	3.2	-399.1	2.580-2.625	1.450	1.307
Pr^{3+}+G	-479.2	2.3	-481.5	2.557-2.576	0.946	2.793
Nd^{3+}+G	-519.2	4.8	-524.0	2.557	0.920	3.905
Eu^{3+}+G	-587.9	16.2	-604.1	2.455	1.177	7.030
Ho^{3+}+G	-658.6	4.2	-662.8	2.521	1.255	-3.031
Er^{3+}+G	-669.7	1.3	-671.0	2.715	1.380	2.032
Tm^{3+}+G	-672.1	1.8	-673.9	2.649	1.344	1.021
Yb^{3+}+G	-669.8	1.6	-671.4	2.598-2.604	1.320	0.009
Lu^{3+}+G	-408.8	2.0	-410.8	2.605-2.634	0.995	-1.057

5

One could expect that stronger interactions are accompanied by shorter distances $d_{Ln...C}$ between the lanthanide ion and the carbon atoms of the G model. The values are presented in Table 5.2, and the plots of $d_{Ln...C}$ vs. ΔE and $d_{Ln...C}$ vs. ΔE$_{dist}$ are shown in Figure 5.12g, h. This suggests that the shortest $d_{Ln...C}$ distances can be found for Ln^{3+}+G complexes corresponding to central lanthanides, represented by Eu^{3+}, but again, the values calculated for Pm^{3+}, Sm^{3+}, Gd^{3+}, Tb^{3+} and Dy^{3+} are required to make more definitive conclusions. The span of $d_{Ln...C}$ distances is not very broad if the values of 2.887-2.893 Å calculated for La^{3+} (having no 4f electrons) are discarded: they vary from 2.455 (Eu^{3+}+G) to 2.715 Å (Er^{3+}+G), that is, within 0.260 Å.
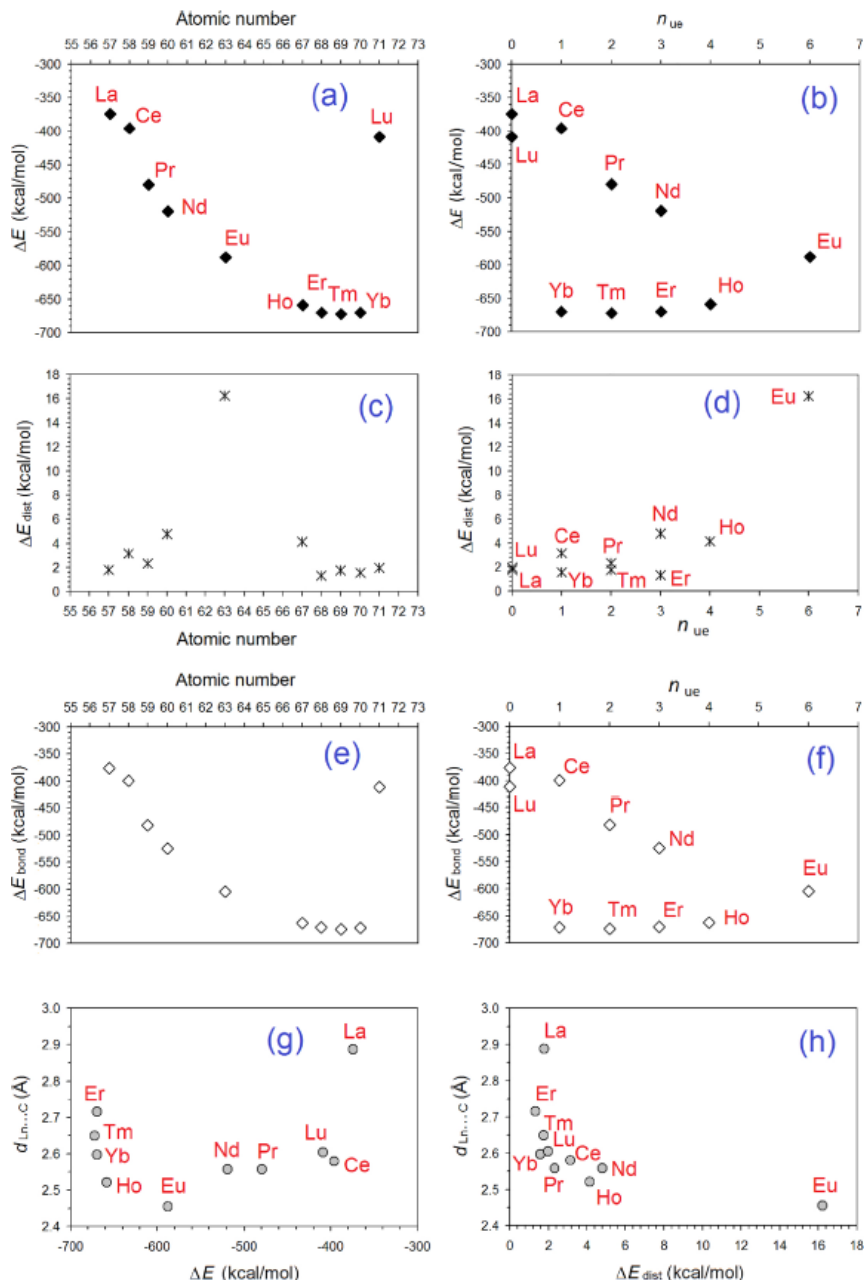
Figure 5.12. Interrelations between the calculated formation energies ΔE for Ln³⁺+G complexes, their components ΔE_dist and ΔE_bond, the shortest distances d_Ln...C, Ln atomic numbers and numbers of unpaired electrons (n_ue) in Ln³⁺ ions: (a) ΔE vs. atomic number; (b) ΔE vs. n_ue; (c) ΔE_dist vs. atomic number; (d) ΔE_dist vs. n_ue; (e) ΔE_bond vs. atomic number; (f) ΔE_bond vs. n_ue; (g) d_Ln...C vs. ΔE; (h) d_Ln...C vs. ΔE_dist.

The charge transfer observed in the complexes studied is rather significant in all cases. The degree of compensation of 3+ charge on the lanthanide species at the cost of π-electrons of the G model is always of more than 50 %, so that the resulting positive charge on Ln ion fluctuates from 0.920 (Nd^{3+}+G; Table 5.2) to 1.450 (Ce^{3+}+G), with no evident correlation with atomic number and/or n_{ue}. The spin of Ln species (Table 5.2) varies within an even broader range, with the lowest absolute value of 0.009 *e* calculated for the Yb^{3+}+G complex, and the highest one of 7.030 *e* found for Eu^{3+}+G. In most complexes, it is composed of 'spin-up' electrons and thus has a positive value (blue lobes in the spin density plots shown in Figure 5.13); the two exceptions are Ho^{3+}+G and Lu^{3+}+G, for which the spin of the Ln species results from 'spin-down' electrons (yellow lobes in the spin density plots; Figure 5.12). When analysing the entire distribution of spin density, one can see that three general situations are possible: (1) the entire population of unpaired electrons is 'spin-up' (the cases of Ce, Eu, Er, Tm and Yb); (2) the spin of Ln species is composed by 'spin-up' electrons, and that of G, by 'spin-down' electrons (La, Pr and Nd); (3) the spin of Ln species is composed by 'spin-down' electrons, and that of G by 'spin-up' electrons (Ho and Lu).

It is especially interesting to analyse to what degree the spin of Ln species in the corresponding complex matches the n_{ue} value in isolated Ln^{3+} ions. It turns out that such agreement is observed only for Ce (1.307 *e* vs. n_{ue} = 1). Instead, most lanthanide species acquire additional spin density, in particular: La (0.894 *e* vs. n_{ue} = 0), Lu (-1.057 *e* vs. n_{ue} = 0), Pr (2.793 *e* vs. n_{ue} = 2), Nd (3.905 *e* vs. n_{ue} = 3), and Eu (7.030 *e* vs. n_{ue} = 6). An opposite effect was found for Yb (0.009 *e* vs. n_{ue} = 1), Tm (1.021 *e* vs. n_{ue} = 2),
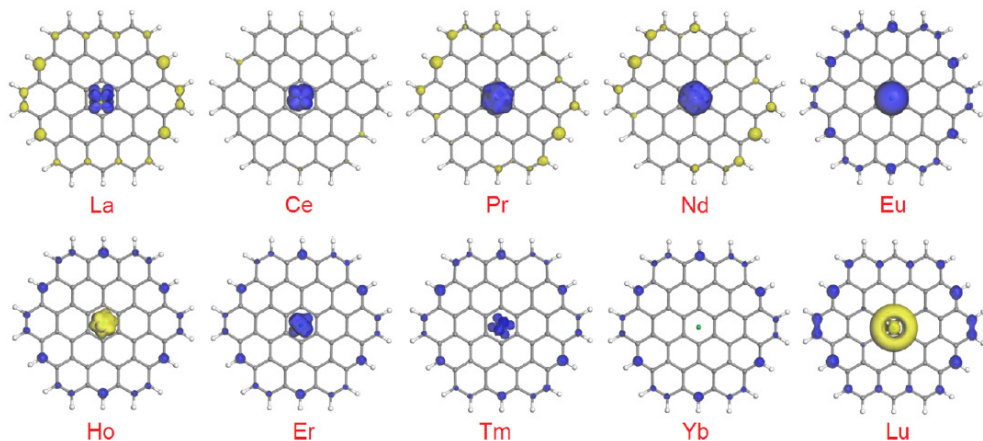
Figure 5.13. Spin density plots (isosurfaces at 0.02 a. u.) for Ln^{3+}+G complexes studied. Blue lobes correspond to ´spin-up' density; yellow lobes, to ´spin-down´ density.

Er (2.032 *e* vs. n_{ue} = 3), and Ho (-3.031 *e* vs. n_{ue} = 4). In other words, Ln^{3+} ions of the early lanthanides (with the exception of Ce) acquire approximately one additional unpaired electron, whereas, for the late lanthanides, the trend is to lose one unpaired electron.

5.4. Conclusions

The study presented in this chapter demonstrates that mechanical processing can effectively produce Ln_2O_3-graphite nanocomposites. As evidenced by electron microscopy, high-energy ball-milling produces a large number of globular graphite agglomerates of broadly variable sizes, with the smallest spheres having a diameter of the order of 100 nm, whereas the size of pristine graphite particles is roughly around 10 μm. For La_2O_3–graphite, Eu_2O_3–graphite, and Gd_2O_3-graphite the smallest Ln_2O_3 spheres are of the order of 50 nm in diameter and for Lu_2O_3–graphite is of the order of 90 nm in diameter.

According to the results of powder XRD for pure graphite, the size of crystallites forming them is about 9.5 nm. After 8-h MP, their size reduces by 4–5 times to an average of 2.2 nm. In the case of Ln_2O_3–graphite mixtures, the reduction of the graphite crystallites is approximately to values between 2 and 8 nm. As regards the crystallite size reduction for lanthanide oxides, it depends on Ln species as well. The strongest effect was found for La_2O_3, with a three-fold decrease in crystallite size from 67 to 22 nm (by 67 %). It was followed by Eu_2O_3, Gd_2O_3 and Lu_2O_3, for which the crystallite size reduced from 40 to 31 nm (by 23 %), from 35 to 25 nm (by 29 %) and from 37 to 33 nm (by only 11 %), respectively.

Altogether with SEM and XRD results, Raman spectroscopy confirmed that MP efficiency is different for different lanthanide oxides. XPS evidenced the introduction of oxygen-functional groups to graphite after the mechanical processing and a BE shift for the $La3d_{5/2}$, $Eu3d_{5/2}$, $Gd3d_{5/2}$ and Lu4f core level components revealed a chemical interaction between such oxygen functionalities and the Ln ions. Lastly, thermogravimetric analysis showed that Ln_2O_3-graphite nanocomposites are less thermally stable than pristine graphite.

5

References

[1] S.J. Wang, J.B. Hu, Y.Y. Wang, F. Luo, Coating graphene oxide sheets with luminescent rare-earth complexes, J Mater Sci. 48 (2013) 805–811. https://doi.org/10.1007/S10853-012-6799-Y.

[2] B. Park, S.J. Kim, J. Lim, S. Some, J.E. Park, S.J. Kim, C. Kim, T.J. Lee, S.C. Jun, Tunable wide blue photoluminescence with europium decorated graphene, J Mater Chem C Mater. 3 (2015) 4030–4038. https://doi.org/10.1039/C4TC02361G.

[3] Y. Wang, Y. Li, W. Qi, Y. Song, Luminescent lanthanide graphene for detection of bacterial spores and cysteine, Chemical Communications. 51 (2015) 11022–11025. https://doi.org/10.1039/C5CC02889B.

[4] B.K. Gupta, P. Thanikaivelan, T.N. Narayanan, L. Song, W. Gao, T. Hayashi, A. Leela Mohana Reddy, A. Saha, V. Shanker, M. Endo, A.A. Martí, P.M. Ajayan, Optical bifunctionality of europium-complexed luminescent graphene nanosheets, Nano Lett. 11 (2011) 5227–5233. https://doi.org/10.1021/NL202541N.

[5] S.S. Shinde, A. Sami, J.H. Lee, Lanthanides-based graphene catalysts for high performance hydrogen evolution and oxygen reduction, Electrochim Acta. 214 (2016) 173–181. https://doi.org/10.1016/J.ELECTACTA.2016.08.050.

[6] X. Zhang, S. Wang, T. Yan, J. Zhang, F. Luo, 3D lanthanide-organic supramolecular-graphene oxide composites: A simple and effective method significantly improve the proton conductivity of proton exchange membrane, Inorg Chem Commun. 111 (2020) 107634. https://doi.org/10.1016/J.INOCHE.2019.107634.

[7] S. Manavalan, U. Rajaji, S.M. Chen, T.W. Chen, R.J. Ramalingam, T. Maiyalagan, A. Sathiyan, Q. Hao, W. Lei, Microwave-assisted synthesis of gadolinium(III) oxide decorated reduced graphene oxide nanocomposite for detection of hydrogen peroxide in biological and clinical samples, Journal of Electroanalytical Chemistry. 837 (2019) 167–174. https://doi.org/10.1016/J.JELECHEM.2019.02.023.

[8] M.F.P. Da Silva, H.C. De Jesus Fraga Da Costa, E.R. Triboni, M.J. Politi, P.C. Isolani, Synthesis and characterization of CeO 2-graphene composite, J Therm Anal Calorim. 107 (2012) 257–263. https://doi.org/10.1007/S10973-011-1924-8.

[9] Y. Li, G. Wang, K. Pan, B. Jiang, C. Tian, W. Zhou, H. Fu, NaYF4:Er3+/Yb3+–graphene composites: preparation, upconversion luminescence, and application in dye-sensitized solar cells, J Mater Chem. 22 (2012) 20381–20386. https://doi.org/10.1039/C2JM34113A.

[10] M. Zhang, X. Liu, J. Huang, L. Wang, H. Shen, Y. Luo, Z. Li, H. Zhang, Z. Deng, Z. Zhang, Ultrasmall graphene oxide based T1 MRI contrast agent for in vitro and in vivo labeling of human mesenchymal stem cells, Nanomedicine. 14 (2018) 2475–2483. https://doi.org/10.1016/J.NANO.2017.03.019.

[11] A.J. Shen, D.L. Li, X.J. Cai, C.Y. Dong, H.Q. Dong, H.Y. Wen, G.H. Dai, P.J. Wang, Y.Y. Li, Multifunctional nanocomposite based on graphene oxide for in vitro hepatocarcinoma diagnosis and treatment, J Biomed Mater Res A. 100A (2012) 2499–2506. https://doi.org/10.1002/JBM.A.34148.

[12] A. Rodríguez-Galván, M. Rivera, P. García-López, L.A. Medina, V.A. Basiuk, Gadolinium-containing carbon nanomaterials for magnetic resonance imaging: Trends and challenges, J Cell Mol Med. 24 (2020) 3779–3794. https://doi.org/10.1111/JCMM.15065.

5

[13]   Y. Sun, Q. Wang, C. Chen, X. Tan, X. Wang, Interaction between Eu(III) and graphene oxide nanosheets investigated by batch and extended X-ray absorption fine structure spectroscopy and by modeling techniques, Environ Sci Technol. 46 (2012) 6020–6027. https://doi.org/10.1021/ES300720F.

[14]   M. El Makrini, D. Guérard, P. Lagrange, A. Hérold, Intercalation of rare earth metals in graphite, Physica B+C. 99 (1980) 481–485. https://doi.org/10.1016/0378-4363(80)90282-X.

[15]   R. Hagiwara, M. Ito, Y. Ito, Graphite intercalation compounds of lanthanide metals prepared in molten chlorides, Carbon N Y. 34 (1996) 1591–1593. https://doi.org/10.1016/S0008-6223(96)00109-1.

[16]   S. Cahen, R. Vangelisti, Versatile behavior upon intercalation by chemical vapor transport of lanthanide trichlorides into graphite, Carbon N Y. 49 (2011) 1834–1841. https://doi.org/10.1016/J.CARBON.2011.01.005.

[17]   C. Suryanarayana, Mechanical alloying and milling, Prog Mater Sci. 46 (2001) 1–184. https://doi.org/10.1016/S0079-6425(99)00010-9.

[18]   C. Patiño-Carachure, S. Martínez-Vargas, J.E. Flores-Chan, G. Rosas, Synthesis of carbon nanostructures by graphite deformation during mechanical milling in air, 28 (2020) 869–876. https://doi.org/10.1080/1536383X.2020.1776264.

[19]   J. Tang, Ball Milling Induced Amorphization of Graphite and High Solubility in Ag-Gd Solid Solution, Materials Science Forum. 225–227 (1996) 477–482. https://doi.org/10.4028/WWW.SCIENTIFIC.NET/MSF.225-227.477.

[20]   O. Mao, J.O. Ström-Olsen, Z. Altounian, J. Yang, Characteristics of Sm2Fe17Cx compounds prepared from ball-milled blends of Sm2Fe17 and graphite, J Appl Phys. 79 (1996) 4619–4621. https://doi.org/10.1063/1.361682.

[21]   G. Rixecker, K.H.J. Buschow, H. Bakker, Can Rare Earth-Transition Metal Compounds Be Carburized by Mechanical Alloying?, Materials Science Forum. 269–272 (1998) 75–80. https://doi.org/10.4028/WWW.SCIENTIFIC.NET/MSF.269-272.75.

[22]   X. Zheng, C. Yang, X. Chang, T. Wang, M. Ye, J. Lu, H. Zhou, J. Zheng, X. Li, Synergism of Rare Earth Trihydrides and Graphite in Lithium Storage: Evidence of Hydrogen-Enhanced Lithiation, Advanced Materials. 30 (2018) 1704353. https://doi.org/10.1002/ADMA.201704353.

[23]   J.P. Perdew, K. Burke, M. Ernzerhof, Generalized Gradient Approximation Made Simple, Phys Rev Lett. 77 (1996) 3865. https://doi.org/10.1103/PhysRevLett.77.3865.

[24]   S. Grimme, Semiempirical GGA-type density functional constructed with a long-range dispersion correction, J Comput Chem. 27 (2006) 1787–1799. https://doi.org/10.1002/JCC.20495.

[25]   Y. Wang, Z. Xu, Y.N. Moe, On the performance of local density approximation in describing the adsorption of electron donating/accepting molecules on graphene, Chem Phys. 406 (2012) 78–85. https://doi.org/10.1016/J.CHEMPHYS.2012.08.008.

[26]   P.L. Silvestrelli, A. Ambrosetti, Including screening in van der Waals corrected density functional theory calculations: The case of atoms and small molecules physisorbed on graphene, Journal of Chemical Physics. 140 (2014). https://doi.org/10.1063/1.4869330/211902.

[27]   Q. Zhou, W. Ju, X. Su, Y. Yong, X. Li, Adsorption behavior of SO2 on vacancy-defected

5

graphene: A DFT study, Journal of Physics and Chemistry of Solids. 109 (2017) 40–45. https://doi.org/10.1016/J.JPCS.2017.05.007.

[28]   E. V. Basiuk, M. Martínez-Herrera, E. Álvarez-Zauco, L.V. Henao-Holguín, I. Puente-Lee, V.A. Basiuk, Noncovalent functionalization of graphene with a Ni(II) tetraaza[14]annulene complex, Dalton Transactions. 43 (2014) 7413–7428. https://doi.org/10.1039/C3DT52645C.

[29]   V.A. Basiuk, N. Alzate-Carvajal, L. V. Henao-Holguín, E. V. Rybak-Akimova, E. V. Basiuk, Coordination functionalization of graphene oxide with tetraazamacrocyclic complexes of nickel(II): Generation of paramagnetic centers, Appl Surf Sci. 371 (2016) 16–27. https://doi.org/10.1016/J.APSUSC.2016.02.166.

[30]   V.A. Basiuk, E. V. Rybak-Akimova, E. V. Basiuk, Graphene oxide and nanodiamond: same carboxylic groups, different complexation properties, RSC Adv. 7 (2017) 17442–17450. https://doi.org/10.1039/C7RA01685A.

[31]   V.A. Basiuk, L.M. Bolivar-Pineda, V. Meza-Laguna, E. V. Rybak-Akimova, E. V. Basiuk, Carbon Nanotubes and Graphene Promote Pyrolysis of Free-Base Phthalocyanine, Journal of Physical Chemistry Letters. 9 (2018) 4420–4427. https://doi.org/10.1021/ACS.JPCLETT.8B02141.

[32]   V.A. Basiuk, M. Kakazey, M. Vlasova, E. V. Basiuk, Effect of structural defects on the strength of adsorption of La and Lu species on graphene, Diam Relat Mater. 100 (2019) 107597. https://doi.org/10.1016/J.DIAMOND.2019.107597.

[33]   V.A. Basiuk, O. V. Prezhdo, E. V. Basiuk, Thermal smearing in DFT calculations: How small is really small? A case of La and Lu atoms adsorbed on graphene, Mater Today Commun. 25 (2020) 101595. https://doi.org/10.1016/J.MTCOMM.2020.101595.

[34]   B. Delley, An all-electron numerical method for solving the local density functional for polyatomic molecules, J Chem Phys. 92 (1990) 508–517. https://doi.org/10.1063/1.458452.

[35]   B. Delley, Fast Calculation of Electrostatics in Crystals and Large Molecules, Journal of Physical Chemistry. 100 (1996) 6107–6110. https://doi.org/10.1021/JP952713N.

[36]   B.D.-T.J. of chemical physics, undefined 2000, From molecules to solids with the approach, Pubs.Aip.Org. (n.d.). https://pubs.aip.org/aip/jcp/article-abstract/113/18/7756/458395 (accessed August 13, 2023).

[37]   B. Delley, D.E. Ellis, A.J. Freeman, E.J. Baerends, D. Post, Binding energy and electronic structure of small copper particles, Phys Rev B. 27 (1983) 2132. https://doi.org/10.1103/PhysRevB.27.2132.

[38]   A. Bergner, M. Dolg, W. Küchle, H. Stoll, H. Preuß, Ab initio energy-adjusted pseudopotentials for elements of groups 13–17, 80 (2006) 1431–1441. https://doi.org/10.1080/00268979300103121.

[39]   S.J. Clark, M.D. Segall, C.J. Pickard, P.J. Hasnip, M.I.J. Probert, K. Refson, M.C. Payne, First principles methods using CASTEP, Zeitschrift Fur Kristallographie. 220 (2005) 567–570. https://doi.org/10.1524/ZKRI.220.5.567.65075.

[40]   V.A. Basiuk, Electron smearing in DFT calculations: A case study of doxorubicin interaction with single-walled carbon nanotubes, Int J Quantum Chem. 111 (2011) 4197–4205. https://doi.org/10.1002/QUA.23003.

[41]   T.D. Shen, W.Q. Ge, K.Y. Wang, M.X. Quan, J.T. Wang, W.D. Wei, C.C. Koch, Structural disorder

5

and phase transformation in graphite produced by ball milling, Nanostructured Materials. 7 (1996) 393–399. https://doi.org/10.1016/0965-9773(96)00010-4.

[42]   T. Xing, L.H. Li, L. Hou, X. Hu, S. Zhou, R. Peter, M. Petravic, Y. Chen, Disorder in ball-milled graphite revealed by Raman spectroscopy, Carbon N Y. 57 (2013) 515–519. https://doi.org/10.1016/J.CARBON.2013.02.029.

[43]   J. Cui, G.A. Hope, Raman and fluorescence spectroscopy of CeO2, Er2O3, Nd2O3, Tm2O3, Yb2O3, La2O3, and Tb4O7, Journal of Spectroscopy. 2015 (2015). https://doi.org/10.1155/2015/940172.

[44]   H. Peng, B. Cui, Y. Wang, Bifunctional Fe3O4@Gd2O3:Eu3+nanocomposites obtained by the homogeneous precipitation method, Mater Res Bull. 48 (2013) 1767–1771. https://doi.org/10.1016/J.MATERRESBULL.2013.01.001.

[45]   R.K. Tamrakar, K. Upadhyay, I.P. Sahu, D.P. Bisen, Tuning of photoluminescence emission properties of Eu3+ doped Gd2O3 by different excitations, Optik (Stuttg). 135 (2017) 281–289. https://doi.org/10.1016/J.IJLEO.2017.01.081.

[46]   A. García-Murillo, C. Le Luyer, C. Garapon, C. Dujardin, E. Bernstein, C. Pedrini, J. Mugnier, Optical properties of europium-doped Gd2O3 waveguiding thin films prepared by the sol–gel method, Opt Mater (Amst). 19 (2002) 161–168. https://doi.org/10.1016/S0925-3467(01)00214-2.

[47]   X. Tian, Z. Liu, A. Zeng, H. Wang, J. Lou, Y. Wei, Y. Man, L. Li, F. Yang, Evaluation of in vivo immunotoxicity for Ho3+-doped Gd2O3 nanoparticles as dual-modality nanoprobes, Mater Today Commun. 23 (2020) 100899. https://doi.org/10.1016/J.MTCOMM.2020.100899.

[48]   W. Kuznik, M.G. Brik, I. Cieślik, A. Majchrowski, L. Jaroszewicz, N.S. Alzayed, A.M. El-Naggar, I. Sildos, S. Lange, V. Kiisk, I. V. Kityk, Changes of fluorescent spectral features after successive rare earth doping of gadolinium oxide powders, J Alloys Compd. 511 (2012) 221–225. https://doi.org/10.1016/J.JALLCOM.2011.09.040.

[49]   M. Elbanowski, S. Lis, B. Mąkowska, Fluorescence of lanthanide(III) complexes in aqueous solutions the influence of pH and solution composition, Monatshefte Für Chemie Chemical Monthly. 116 (1985) 901–911. https://doi.org/10.1007/BF00809183.

[50]   H. Yang, D. Zhang, L. Shi, J. Fang, Synthesis and strong red photoluminescence of europium oxide nanotubes and nanowires using carbon nanotubes as templates, Acta Mater. 56 (2008) 955–967. https://doi.org/10.1016/J.ACTAMAT.2007.10.052.

[51]   Z. Mo, Z. Deng, R. Guo, Q. Fu, C. Feng, P. Liu, Y. Sun, Synthesis and luminescence properties for europium oxide nanotubes, Materials Science and Engineering: B. 177 (2012) 121–126. https://doi.org/10.1016/J.MSEB.2011.09.040.

[52]   D.A. Zatsepin, D.W. Boukhvalov, A.F. Zatsepin, Y.A. Kuznetsova, M.A. Mashkovtsev, V.N. Rychkov, V.Y. Shur, A.A. Esin, E.Z. Kurmaev, Electronic structure, charge transfer, and intrinsic luminescence of gadolinium oxide nanoparticles: Experiment and theory, Appl Surf Sci. 436 (2018) 697–707. https://doi.org/10.1016/J.APSUSC.2017.12.086.

[53]   H. Yue, S. Marasini, M.Y. Ahmad, S.L. Ho, H. Cha, S. Liu, Y.J. Jang, T. Tegafaw, A. Ghazanfari, X. Miao, K.S. Chae, Y. Chang, G.H. Lee, Carbon-coated ultrasmall gadolinium oxide (Gd2O3@C) nanoparticles: Application to magnetic resonance imaging and fluorescence properties, Colloids Surf A Physicochem Eng Asp. 586 (2020) 124261. https://doi.org/10.1016/J.COLSURFA.2019.124261.

[54]   X. Chen, X. Wang, D. Fang, A review on C1s XPS-spectra for some kinds of carbon materials,

5

(2020) 1048–1058. https://doi.org/10.1080/1536383X.2020.1794851.

[55]   K.S. Rao, J. Senthilnathan, Y.F. Liu, M. Yoshimura, Role of Peroxide Ions in Formation of Graphene Nanosheets by Electrochemical Exfoliation of Graphite, Scientific Reports 2014 4:1. 4 (2014) 1–6. https://doi.org/10.1038/srep04237.

[56]   Y.A. Teterin, A.Y. Teterin, Structure of X-ray photoelectron spectra of lanthanide compounds, Russian Chemical Reviews. 71 (2002) 347–381. https://doi.org/10.1070/RC2002V071N05ABEH000717.

[57]   F. Mercier, C. Alliot, L. Bion, N. Thromat, P. Toulhoat, XPS study of Eu(III) coordination compounds: Core levels binding energies in solid mixed-oxo-compounds EumXxOy, J Electron Spectros Relat Phenomena. 150 (2006) 21–26. https://doi.org/10.1016/J.ELSPEC.2005.08.003.

[58]   V. V. Kaichev, T.I. Asanova, S.B. Erenburg, T. V. Perevalov, V.A. Shvets, V.A. Gritsenko, Atomic and electronic structures of lutetium oxide Lu{sub 2}O{sub 3}, Journal of Experimental and Theoretical Physics. 116 (2013) 323–329. https://doi.org/10.1134/S1063776113020131.

[59]   I.A. Pašti, A. Jovanović, A.S. Dobrota, S. V. Mentus, B. Johansson, N. V. Skorodumova, Atomic adsorption on pristine graphene along the Periodic Table of Elements – From PBE to non-local functionals, Appl Surf Sci. 436 (2018) 433–440. https://doi.org/10.1016/J.APSUSC.2017.12.046.

[60]   I.A. Pašti, A. Jovanović, A.S. Dobrota, S. V. Mentus, B. Johansson, N. V. Skorodumova, Atomic adsorption on graphene with a single vacancy: systematic DFT study through the periodic table of elements, Physical Chemistry Chemical Physics. 20 (2018) 858–865. https://doi.org/10.1039/C7CP07542A.

[61]   S. Li, M. Zhou, G. Li, F. Zheng, P. Zhang, Strong bonding and high spin-polarization of lanthanide atoms on vacancies in graphene, AIP Adv. 7 (2017) 105207. https://doi.org/10.1063/1.4994714/977122.

5

—— CHAPTER 6 ——

Green mechanochemical fabrication of graphite-lanthanide oxide nanocomposites

In this chapter, we report on a study exploring mechanochemistry as a facile and environmentally friendly approach for the synthesis of graphite-lanthanide oxide (graphite-Ln) nanocomposites. We determined the optimal conditions in which processing mixtures of graphite and lanthanide oxide in a planetary ball mill resulted in exfoliated graphene nanosheets functionalised with Ln oxide particles. The nanocomposites were investigated by a suite of analytical techniques; X-ray photoelectron spectroscopy proved that mechanochemical processing can functionalise the graphene surface in the presence of lanthanide oxides. Raman spectroscopy and X-ray diffraction results evidenced that the mechanochemical treatment can exfoliate graphite and reduce the size of graphite crystallites. Scanning electron microscopy and scanning transmission electron microscopy confirmed the formation of lanthanide oxide nanoparticles and their uniform distribution on the graphene surface and thermogravimetric analysis gave evidence that the graphite-Ln nanocomposites are less thermally stable than pristine graphite. The toxicity of the graphite-Ln nanocomposites was also studied; we found that COS-7 monkey kidney cell growth was not inhibited for more than 5 % in most of the studies.

6.1. Introduction

The development of more sustainable and environmentally friendly protocols for the functionalisation of graphene nanomaterials (GNMs) remains a persistent challenge. Currently, many physicochemical methodologies for the modification of GNMs involve multi-step time-consuming processes and the use of environmentally harmful chemicals. Although many scalable approaches to graphene nanosheet (GN) production have been proposed [1], several of them still rely on harmful solvents such as N,N-dimethylformamide, N-methyl-2-pyrrolidone [2] and strong acids [3], thus generating toxic waste. More sustainable processes like the exfoliation of graphite in water [4–7] often necessitate additives like pyrene derivatives [8,9], surfactants [10], or supercritical CO_2 [11].

A prevalent route for the functionalization of GNs starts with the oxidation of graphite to obtain graphene oxide (GO), where each carbon layer bears reactive oxygen-containing functional groups: hydroxyl and epoxy groups mainly located in the planes and mostly carbonyl and carboxyl groups [12] at the edges. The precise properties of GO depend on the degree of oxidation [13,14] and the oxidation method. Widely used methods are those developed by Brodie [15], Staudenmaier [16], Hofmann [17], and Hummers [18], and their modifications, which all generate corrosive and toxic waste, harmful to the environment and living organisms. Furthermore, the strong oxidising agents introduce several types of defects to the graphene nanosheets, and the subsequent reduction of GO often involves environmentally problematic agents such as hydrazine [19]. Consequently, it is imperative to develop efficient and environmentally friendly synthetic methodologies, which avoid the oxidation step.

In recent years, ball-milling has gained prominence in various areas of chemistry and materials science [20,21], proving effective in nanoparticle synthesis [22,23] and graphite exfoliation [24,25] - a field known as mechanochemistry. Mechanochemistry touted as a sustainable and green technology, enables the functionalisation of carbon nanostructures [26–28] without the use of toxic and hazardous chemicals. Its advantages over solution-based methodologies include higher yields, elimination of the use of organic solvents, cost-effective mass production of graphene [29], scalability, reduced waste generation, improved energy, and atom economy [30].

Several research groups have successfully applied mechanochemical methods to exfoliate and oxidise graphite [31–37] utilising a planetary mill and showed that the oxygen content increases with milling time [33]. The moving balls transfer energy to the milled graphite powder, breaking strong covalent bonds and producing reactive surfaces

[38]. Thus, by combining exfoliation and chemical functionalisation, this approach is conducive to large-scale graphene nanocomposite production.

In our previous work [39] we explored mechanochemistry as a facile one-step strategy for the synthesis of graphite-lanthanide oxide nanocomposites because the last decade has witnessed their fabrication primarily for supercapacitors and dye adsorbents in water remediation [40–47], but only a few studies have explored sustainable synthetic routes using graphite and lanthanide oxides (LnO) as the main precursors. However, in that first attempt, the milling conditions were not optimal, which led to excessive graphite fragmentation and the production of amorphous carbon. In addition, the size of the LnO particles and their distribution on the graphite flakes was not uniform [39] In this chapter, we present the result of the optimisation of the process conditions, which demonstrates mechanochemistry as a robust and environmentally conscious strategy for the fabrication of low-defect graphite-lanthanide oxide nanocomposites.

6.2. Experimental

6.2.1. Materials

Lanthanide (Ln) oxides La_2O_3, Eu_2O_3, Gd_2O_3, and Tb_4O_7 (all having 99.9 % purity), as well as graphite powder (particle size of < 20 μm) were purchased from Sigma-Aldrich and used as received.

6.2.2. Mechanochemical functionalisation

The synthesis of graphite-lanthanide oxide (graphite-Ln) nanocomposites involved the use of mixtures containing 10 wt% lanthanide oxide. For the samples graphite-La, graphite-Eu, graphite-Gd, and graphite-Tb, 3.6 g of graphite powder and 0.4 g of Ln oxide were combined. For the graphite-Eu-Gd sample, 3.6 g of graphite powder, 0.2 g of Eu_2O_3, and 0.2 g of Gd_2O_3 were mixed. Each mixture was placed in a 50 mL tungsten carbide (WC) reactor together with 20 WC balls of 10 mm diameter. The balls:mixture ratio was 22:1 w/w. After sealing the reactor, each sample was subjected to high-energy ball-milling for 48 h at 400 rpm using a Planetary Ball-Mill XQM-0.4A from Tencan. The process is illustrated in Figure 6.1.

6
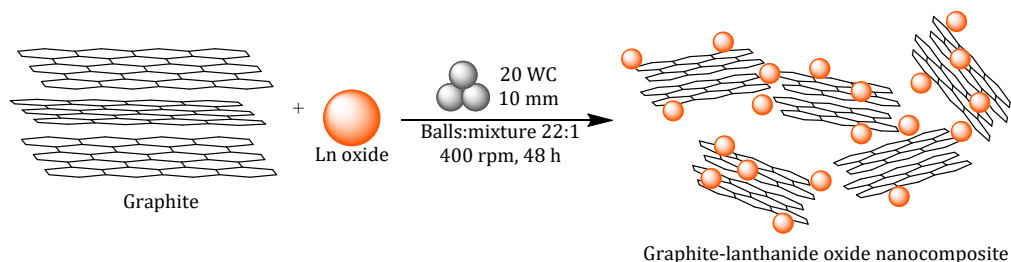
Figure 6.1. Mechanochemical preparation of graphite-Ln nanocomposites.

6.2.3. Cytotoxicity activity

The healthy monkey kidney cell line COS-7 was cultured in RPMI-1640 (Gibco®) supplemented with foetal bovine serum (10 % v/v), nonessential amino acids (1 %v/v), and penicillin-streptomycin solution (1 %v/v) (Corning®). The cells were maintained at 37 °C in a humidified atmosphere with 5 % CO_2. Cytotoxicity was tested by the sulforhodamine B (SRB) assay. Cells were seeded in a 96-well plate and incubated with fresh media or nanomaterial-water dispersions at 50 and 100 µg/mL concentration for 48 h, then cell monolayers were fixed directly to medium supernatant by adding cold trichloroacetic acid (50 %wt/v) to each well. After incubation for 1 h at 4 °C, the plates were gently washed with water and dried at room temperature. To stain the cells, 100 µL of SRB (0.4 %wt/v) were added to each well, left at room temperature for 30 min, and then washed with acetic acid (1 %v/v) to remove the unbound dye. After drying at ambient conditions, the bound dye was solubilised by adding 100 µL tris base solution (10 mM) and shaking on an orbital shaker for 10 min. The absorbance was obtained at 515 nM in a microplate reader (SYNERGY HT, BioTek). Images were captured by an inverted microscope (DIAPHOT 300 Nikon®, Japan) with a digital camera (AmScope MD500) after 48 h treatment. The Growth Inhibition (%) was calculated using the following equation:

$$Growth\ Inhibition\ (\%) = 100 - \left(\frac{Abs.Treatment}{Abs.Control} * 100\right)$$

Experiments were carried out in triplicate. Data are expressed as mean ± standard error of the mean. Statistical analysis was performed with GraphPad Prism 10, using a two-way ANOVA obtained significance with Tukey's multiple comparisons tests.

6.3. Results and discussion

Mechanochemical treatment leads to the production of diverse carbon nanostructures, including multi-layered, few-layered, and single-layered graphene, as well as GO [33,48]. As sketched in Figure 6.2, the milling process subjects graphite crystallites to impacting, compressive, shearing and collision forces. Compressive forces break the graphene sheets, reducing the particle size, while the shear forces induce exfoliation. To gain information on the type of functional groups present before and after mechanochemical processing of graphite alone and of the graphite-lanthanide oxide mixtures, XPS was employed.
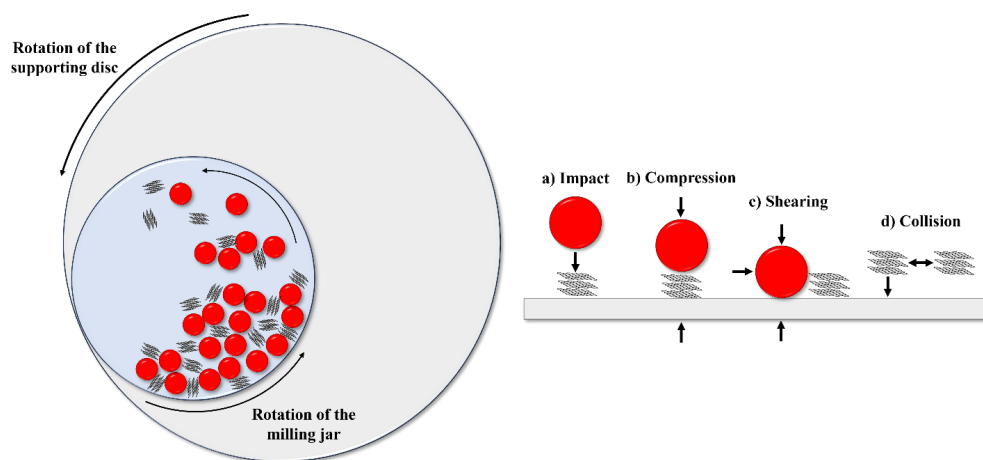
Figure 6.2. Mechanism of graphite processing in a planetary mill and forces to which the graphite flakes are subjected.

6

XPS Analysis of Pristine and Mechanochemically Treated Graphite: The C1*s* core level spectra of pristine and ball-milled graphite, along with the corresponding fits, are shown in Figure 6.3. Table 6.1 provides the binding energy (B.E.) values of the various components deduced from the fits, and Table 6.2 summarises the relative intensities of the components. For pristine graphite, the presence of oxygen functionalities is evident even before the mechanochemical treatment. The observed components are attributed to C=C (at a B.E. of 284.5 eV), C-C/C-H (285.6 eV), C-OH/C-O-C (286.4 eV), C=O (287.8 eV), and O-C=O (289.3 eV), with C=C and C-C/C-H contributing the highest relative spectral intensity to the C1*s* peak as shown in Table 6.2. Considering the stoichiometry, in the pristine material the carbon and oxygen content was deduced to be 94.9 at.% and 5.1 at.%, respectively. Post-milling, the type of bonds detected remained the same, but their relative contribution to the total C1*s* peak intensity changed. Specifically,

the intensity of the component related to C=C bonds (associated with the sp^2 carbon atoms of the graphene lattice) decreased, while that due to C-C/C-H bonds increased, as expected if the size of the graphite flakes is smaller after the mechanochemical treatment [49]. Simultaneously, the oxygen content increased from 5.1 at.% to 14.6 at.% (see Table 6.2), accompanied by an increase in the contribution of C-OH/C-O-C and C=O bonds to the C1*s* peak intensity. This confirms that milling in air creates epoxy, hydroxyl, and carbonyl groups on the graphene sheets, producing a material resembling rGO in composition [50].
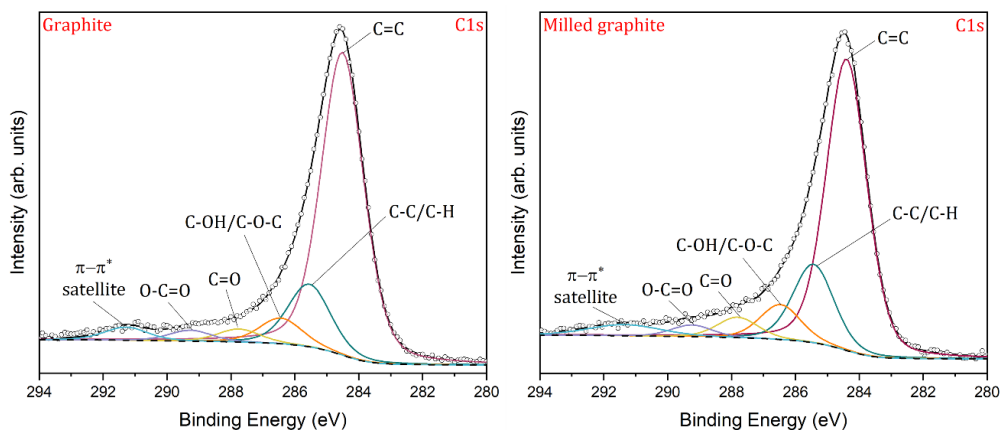
Figure 6.3. Comparison of the C1s core level spectra of pristine graphite and ball-milled graphite and the corresponding fits.

Table 6.1. XPS binding energies (eV) of C1s core level components of pristine graphite and ball-milled graphite, as well as of the graphite-Ln nanocomposites.

Sample	C=C	C-C/C-H	C-OH/C-O-C	C=O	O-C=O
Graphite	284.5	285.6	286.4	287.8	289.3
Ball-milled graphite	284.4	285.4	286.5	287.8	289.2
Graphite-La	284.5	285.5	286.6	288.0	289.3
Graphite-Eu	284.5	285.6	286.7	288.0	289.4
Graphite-Gd	284.5	285.6	286.8	287.8	289.0
Graphite-Tb	284.5	285.5	286.5	287.9	289.3
Graphite-Eu-Gd	284.5	285.6	286.7	288.0	289.4

Table 6.2. Relative contributions of the various components to the total C1s core level photoemission intensity and elemental composition of pristine graphite and ball-milled graphite, as well as of the graphite-Ln nanocomposites.

Sample	Percentage of the relative contribution to the C1s XPS spectra (%)					Composition (at.%)		
	C=C	C-C/C-H	C-OH/C-O-C	C=O	O-C=O	C	O	Ln
Graphite	70.6	14.6	6.0	3.0	2.5	94.9	5.1	-
Ball-milled graphite	63.8	17.2	7.6	4.5	2.6	85.4	14.6	-
Graphite-La	64.6	17.3	7.0	3.3	2.6	82.2	17.6	0.2
Graphite-Eu	64.1	21.4	7.3	2.6	2.4	87.2	12.2	0.6
Graphite-Gd	61.6	19.7	7.8	2.0	2.6	83.4	16.0	0.6
Graphite-Tb	67.5	14.9	7.1	3.2	1.9	82.4	17.2	0.3
Graphite-Eu-Gd	61.0	18.6	7.0	3.9	2.5	85.3	14.1	0.3/0.3

Importantly, the methodology employed in this study is distinctive. In fact, since hydroxyl (C-OH) and epoxy (C-O-C) groups are known to be located mainly on the basal plane, while carbonyl (C=O) and carboxyl (COOH) groups usually decorate the edges of graphene [51,52], we can conclude that both the basal plane and the edges of graphene sheets are functionalised simultaneously under our processing conditions. This contrasts with previous findings [53–58], where mechanochemical functionalisation of graphene was reported to be highly edge-selective, both in the presence of additives like dry ice [53–55], solid urea [56] or oxidants like $KMnO_4$ and $KHSO_4$ [57] and when milling in air as in this study [58].

XPS Analysis of Graphite-Lanthanide Oxide Nanocomposites: The C1s spectra of all the five graphite-Ln nanocomposites (Figure 6.4) exhibit the same components present in pristine and ball-milled graphite, namely C=C, C-C/C-CH, C-OH/O-C-O, C=O, and O-C=O, but the addition of lanthanide oxides to the milling media seems to influence the efficiency of the mechanochemical processing, as we have seen in the past [39]. For all the graphite-Ln nanocomposites, the contribution of the C-OH/O-C-O component to the C1s photoemission line is more important than for pristine graphite, implying the formation of hydroxyl and epoxy groups during ball-milling. More importantly, the C1s line shifts to higher binding energies: by 0.4 eV for graphite-Gd, and by 0.3 eV for graphite-Eu and graphite-Eu-Gd. As to the C=O component, its contribution to the C1s peak is higher for the graphite-Eu-Gd, graphite-La, and graphite-

6

Tb nanocomposites, while for graphite-Eu and graphite-Gd it is lower than for pristine graphite. Besides that, a band shift towards higher binding energies by 0.2 eV is observed for graphite-La, graphite-Eu, and graphite-Eu-Gd nanocomposites. These results suggest that lanthanide ions can be ionically/coordinatively anchored to the oxygen-containing functionalities on the graphene nanosheets. Such line shifts were not observed in our previous study [39], and this implies that the methodology proposed here improves the chemical interaction between the Ln ions and the graphene oxygen functional groups. For all the graphite-Ln nanocomposites, the contribution of the O-C=O component to the C1s peak and its binding energy remains practically unchanged compared with pristine graphite and ball-milled graphite. According to these results, it is clear that the incorporation of lanthanide oxides in the milling media influences the changes in the chemical composition of the graphene sheets, and this effect seems to be stronger in the presence of europium and gadolinium ions, in agreement with our previous work [39].
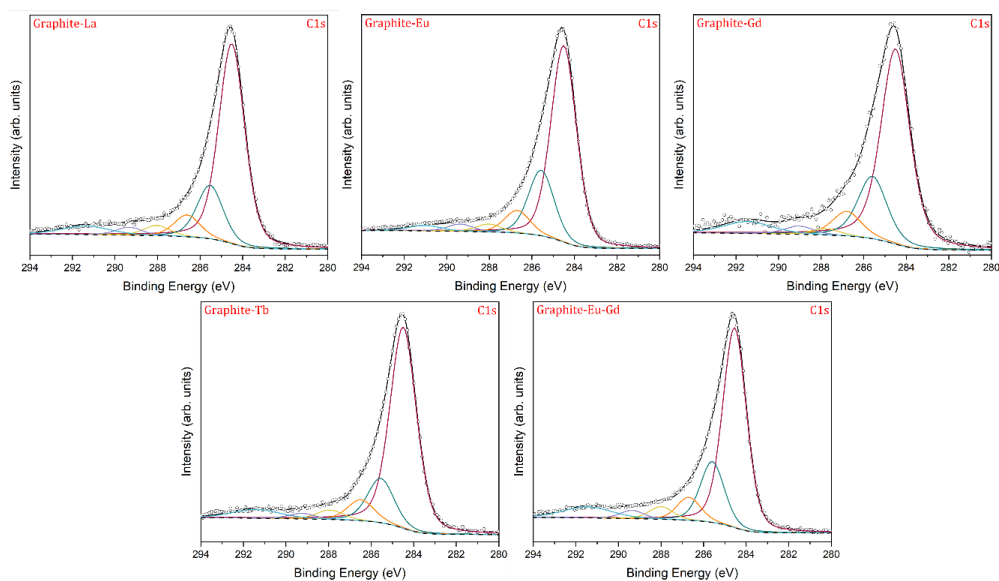

Figure 6.4. Comparison of the C1s core level spectra of graphite-Ln nanocomposites and the corresponding fits. The components are the same as in Figure 6.3 -for details see text.

Raman spectroscopy has been demonstrated to be a powerful non-destructive technique employed to characterise graphitic structures and carbon nanomaterials in general. The Raman spectra of pristine graphite, ball-milled graphite and graphite-Ln nanocomposites are shown in Figure 6.5; the Raman shift for the D, G and 2D bands, as well as the calculated values of the I_D/I_G ratio and crystallite size (L_a), are summarised in Table 6.3. The Raman spectrum of pristine graphite is dominated by the presence of the G band and the 2D band. The G band appears as a strong symmetric sharp peak located at 1578 cm^{-1} attributed to the first-order scattering of the E_{2g} phonon from the in-plane vibration of the sp^2 hybridised carbon lattice [58–61]. The 2D band associated with the ordered stacked graphite structure along the *c*-axis appears at 2716 cm^{-1} and has an asymmetrical shape characteristic of the multilayer nature of the pristine graphite sample [62–67]. Moreover, the D band associated with the vibrational mode A_{1g}, known as the breathing mode, and originating from a disruption in the hexagonal symmetry of the graphene backbone like structural defects, vacancies, crystal edges and sp^3 carbon domains [63,64,66–68], appears as a low-intensity peak located at 1354 cm^{-1}. The estimated I_D/I_G ratio is 0.07, indicating high-quality graphitic structures with large grain sizes [33,48,69,70]. As expected, in the Raman spectrum of ball-milled graphite the intensity of the D band is noticeably higher and the I_D/I_G ratio increases to 0.62, indicating smaller crystallite sizes due to the reduction of the in-plane sp^2 domains, the creation of defects and vacancies promoted by the mechanochemical treatment and an increment of the structural distortion caused by a higher amount of oxygen functionalities such as epoxy, hydroxyl, and carbonyl groups on the graphene sheets corroborated by the XPS results. This differs from what was observed in our previous work as well as in other studies [33,39,48,69], where the Raman spectra of graphite after the mechanochemical treatment look like the typical GO spectrum with I_D/I_G ratios close to 1. These findings confirm that the graphene surface can be functionalised without introducing a high amount of disorder to the lattice if the conditions for mechanochemical processing are optimised. Moreover, the shape of the G band is not symmetrical as for pristine graphite and shows a shoulder around 1605 cm^{-1} known as the D' band, suggesting the presence of few-layered graphene [31–34,56,63,71–73]. This contrasts with the results of the mechanochemical preparation of graphite-phthalocyanine composites, where an effect of 'glueing' between graphite platelets and phthalocyanines was observed under the same milling conditions [74]. Furthermore, the 2D band downshifts to 2709 cm^{-1} and appears symmetrical, showing that ball-milled graphite keeps a proper Bernal stacking of the graphene layers and supporting the interpretation that graphite has been partially exfoliated into few-layer graphene [32–34,69,71,74–78]. In comparison to our previous study, we changed the milling time from 8 to 48 hours and the milling ball size from 20 mm to 10 mm diameter to reduce their impact energy and the apparition of the D' band, as well as the changes in the 2D band, are a clear indication of the improvement

6

over our previous results where the production of few-layered graphene could not be confirmed [39].

Regarding the Raman spectra of the graphite-Ln nanocomposites, the observed changes are practically the same as those for ball-milled graphite; the G band is asymmetrical due to the apparition of the D' band, the 2D band shifts to lower Raman shift values, and the I_D/I_G ratio is higher than that for pristine graphite. All five nanocomposites present a lower I_D/I_G ratio in comparison with ball-milled graphite, and the values were employed to calculate the in-plane sp^2 crystallite size (L_a) of graphite

(Table 6.3) by following the equation given by Cançado *et al.*: [79]

$$L_a = \frac{(2.4 \times 10^{-10})(\lambda_{laser})^4}{I_D/I_G}$$

where λ is the wavelength of the laser source (nm). The graphite crystallite size L_a for all the samples is as follows: pristine graphite (291.5 nm) > graphite-Gd (65.8 nm) > graphite-La (61.8 nm) > graphite-Eu (46.4 nm) > graphite-Eu-Gd (45.3 nm) > graphite-Tb (35.8 nm) > ball-milled graphite (32.9 nm). These results indicate that the addition of lanthanide oxides to the milling media softens the effects of the mechanochemical treatment, reducing the amount of disorder introduced to the graphene lattice without hindering the exfoliation of graphene nanosheets or their surface functionalisation with oxygen functional groups.

6
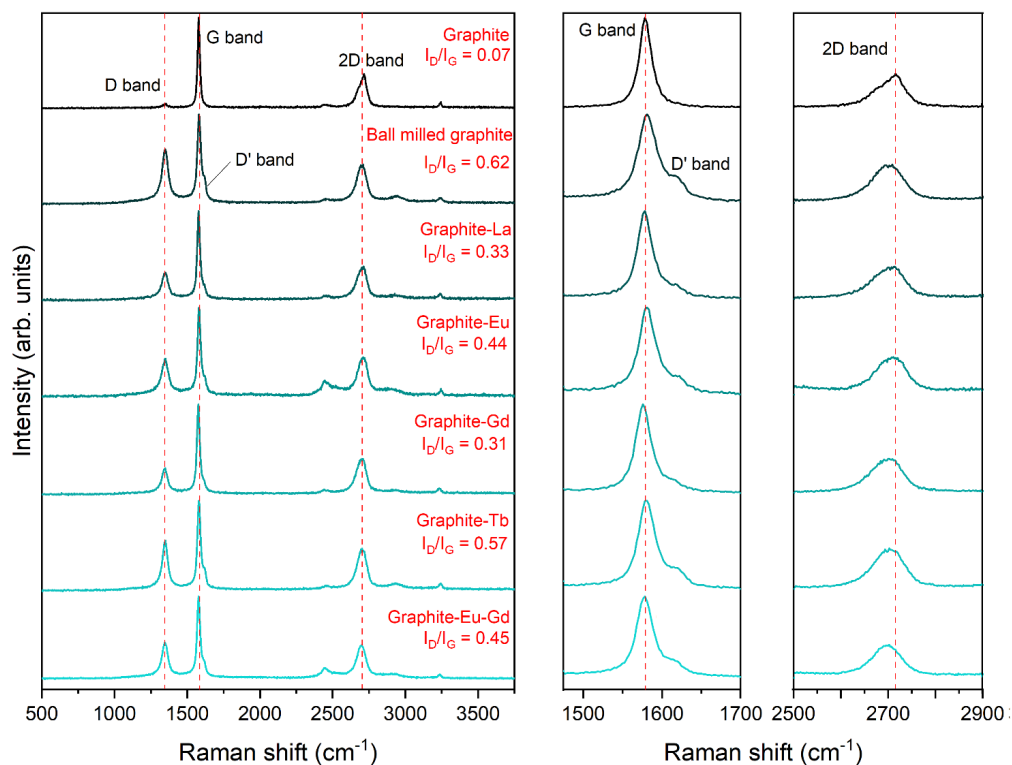
Figure 6.5. Comparison of Raman spectra of pristine graphite, ball-milled graphite, and graphite-Ln nanocomposites.

Table 6.3. Raman shift, I_D/I_G ratio and crystallite L_a size of graphite and ball-milled graphite, as well as of the graphite-Ln nanocomposites.

Sample	D band	G band	2D band	I_D/I_G	L_a (nm)
Graphite	1354	1578	2716	0.07	291.5
Ball-milled graphite	1349	1581	2709	0.62	32.9
Graphite-La	1349	1578	2707	0.33	61.8
Graphite-Eu	1352	1581	2709	0.44	46.4
Graphite-Gd	1349	1576	2702	0.31	65.8
Graphite-Tb	1351	1578	2702	0.57	35.8
Graphite-Eu-Gd	1343	1575	2702	0.45	45.3

6

The X-ray diffraction (XRD) measurements were taken to track the changes in the crystalline nature of graphite and the lanthanide oxides (Figure 6.6) produced by the mechanochemical treatment. The diffractogram of pristine graphite shows two peaks located at 26.5 ° and 54.6 °, corresponding to the diffraction from (002) and (004) planes, respectively. The (002) peak is sharp and the more intense one, a clear indication for a highly ordered material with several graphene layers. The diffractogram of ball-milled graphite exhibits the same two peaks, where the (002) peak exhibits the same shape, showing that the mechanochemical treatment does not affect its position and that graphite does not reach an amorphization stage after 48 h of milling time. The latter fact can be considered an evident advantage compared to what has been reported for milling periods longer than 16 h under different conditions than those used in the experiments described here, which produced a combination of crystalline and amorphous carbon [33,48,69,80]. The position and sharpness of the (002) peak in the diffractograms of graphite-Ln nanocomposite do not change, corroborating that they are still highly ordered materials. However, the (002) peak intensity drastically decreases in all the cases (Figure 6.7), evidencing an even better exfoliation efficiency of graphite after the addition of lanthanide oxides, in agreement with the Raman spectroscopy results. A reasonable explanation for this is that the addition of lanthanide oxides provides a lubrication effect, favouring the impact of the shear forces over the compressive forces involved in the milling mechanism, and fostering the slipping of the graphene sheets. The characteristic peaks of the corresponding lanthanide oxide hexagonal crystal structure can be seen in all the graphite-Ln diffractograms, with lower intensity compared to the graphite (002) peak, due to the ratio of graphite:lanthanide oxide employed, being indicative of the fact that lanthanide oxides keep their crystallinity. The graphite layer-to-layer *d*-spacing was calculated using the Bragg equation, and the interlayer distance is 0.34 nm for all the samples; so it is fair to say that neither the presence of oxygen-containing functional groups confirmed by the XPS results nor the addition of lanthanide oxides affects the stacking pattern of graphene sheets. The apparent crystallite size of graphite through the *c*-axis (L_c) was estimated for all the samples (Table 6.4) and is as follows: pristine graphite (32.3 nm) > graphite-Tb (29.5 nm) > graphite-Eu-Gd (28.5 nm) > graphite-Gd (27.1 nm) > graphite-Eu (26.8 nm) > graphite-La (24.0 nm) > ball-milled graphite (19.6 nm). These results agree with the trend seen in Raman that the lanthanide oxides lead to the formation of smaller graphite crystallites, presumably because their presence in the milling media reduces the abrasive effects of the mechanochemical treatment and therefore produce smaller low-defect crystallites.

6

Table 6.4. Angular position of the (002) peak in the X-ray diffractograms of pristine and ball-milled graphite, as well as of the graphite-Ln nanocomposites produced by ball milling. The full width at half maximum (FWHM), d-spacing and the size of the coherently diffracting domains are also reported

Sample	(002) position	(002) FWHM	d-spacing (nm)	L_c (nm)
Graphite	26.53	0.25	0.34	32.29
Ball-milled graphite	26.51	0.41	0.34	19.55
Graphite-La	26.54	0.34	0.34	24.00
Graphite-Eu	26.53	0.30	0.34	26.77
Graphite-Gd	26.54	0.30	0.34	27.06
Graphite-Tb	26.53	0.27	0.34	29.47
Graphite-Eu-Gd	26.53	0.28	0.34	28.48

6
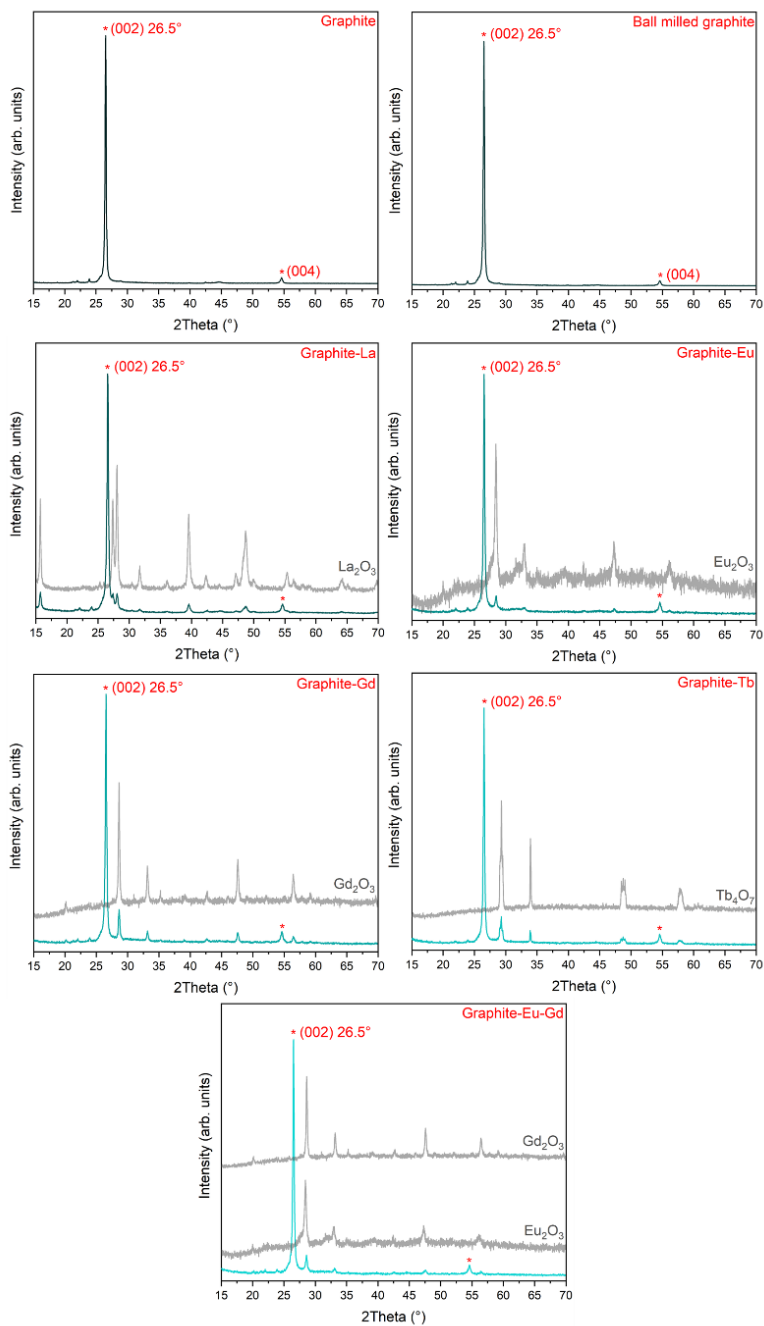
Figure 6.6. XRD diffractograms of pristine graphite, ball-milled graphite and graphite-Ln nanocomposites produced by ball milling
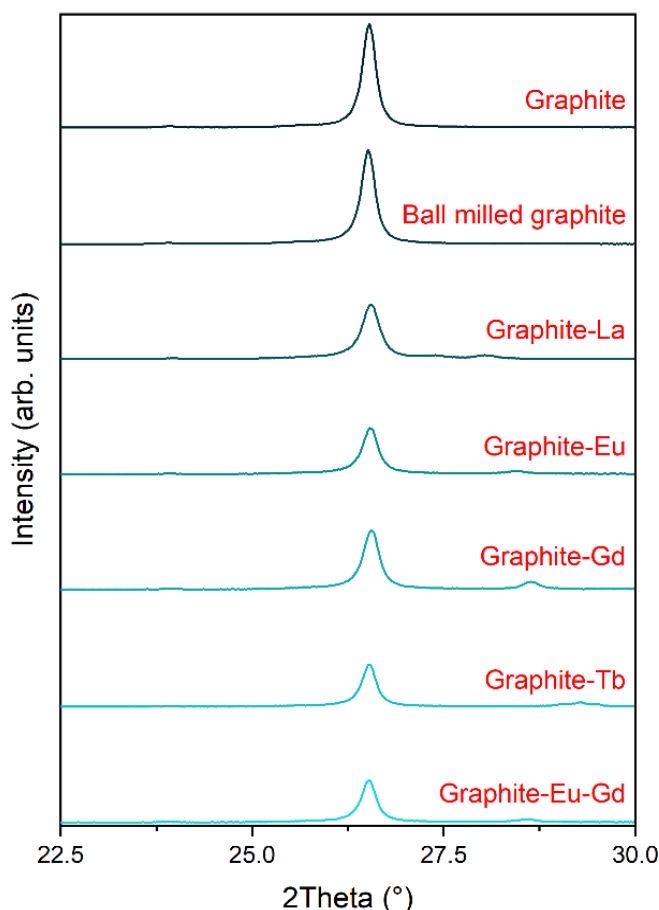
Figure 6.7. Close-up on the (002) peak in the X-ray diffractograms of pristine graphite, ball-milled graphite and graphite-Ln nanocomposites formed through ball milling

The effects of the mechanochemical treatment on graphite morphology can be explored using scanning electron microscopy. The micrographs of pristine graphite presented in Figure 6.8 show thick crystal flakes with sharp edges and smooth surfaces, having broadly variable crystallite sizes ranging from 5 to 20 μm. After the mechanochemical treatment, the crystallite size of ball-milled graphite decreases and now ranges from 1 to 7 μm. The plate-like stacked structure is preserved, in agreement with the results observed in Raman and XRD measurements for both samples, This again confirms an improvement with respect to the milling conditions we previously explored, where we observed the formation of abundant graphite-derived debris after the mechanochemical treatment [39].
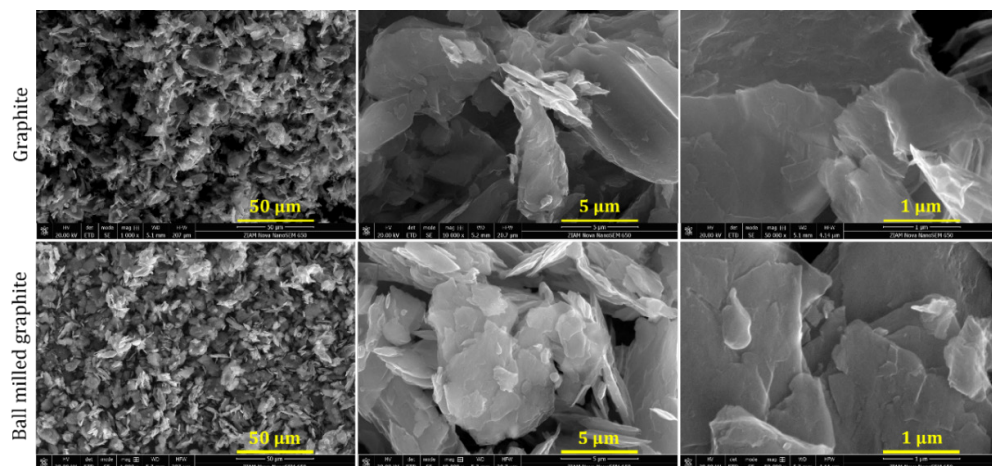
Figure 6.8. SEM-SE micrographs of pristine graphite and ball-milled graphite

The micrographs of the graphite-Ln nanocomposites shown in Figure 6.9, exhibit morphology changes like those observed in ball-milled graphite, with graphite flakes of variable sizes from 1 to 6 μm. The stacked layer structure of the flakes is clearly discernible, confirming the presence of few-layer graphene deduced from the Raman spectra and the XRD data. The backscattered electron detector (BSE) can be employed to differentiate light and heavy elements in a sample, hence SEM-BSE micrographs were acquired to observe the distribution and size of lanthanide oxide particles. The images presented in Figure 6.9 show that they are micro- and nanosized uniformly dispersed throughout the graphite surface in all the areas analysed, confirming that compared to our previous work [39], a better and more homogeneous LnO particle distribution is achieved with the optimised milling conditions. The Eu_2O_3 nanoparticles present the smallest sizes and are also more evenly distributed than the other lanthanide oxides.

Moreover, to have a more detailed look on the lanthanide nanoparticles, scanning transmission electron microscopy with the high-angle annular dark-field detector (STEM-HAADF) was employed. The micrographs, presented in the right column of Figure 6.9, show that most visible (marked with yellow dashed circles) lanthanide oxide particles have a size of around 170–340 nm for graphite-La, 60-140 nm for graphite-Eu, 60–110 nm for graphite-Gd, 80-190 nm for graphite-Tb and 50–200 nm for graphite-Eu-Gd. In addition, a number of even smaller lanthanide oxide particles can be discerned. According to the SEM-BE and the STEM-HAADF micrographs, the Eu_2O_3 and Gd_2O_3 particles present the smaller sizes found among the four lanthanide oxides employed, and that could explain the stronger interaction between the graphene oxygen groups with the lanthanide ions observed in the XPS results.
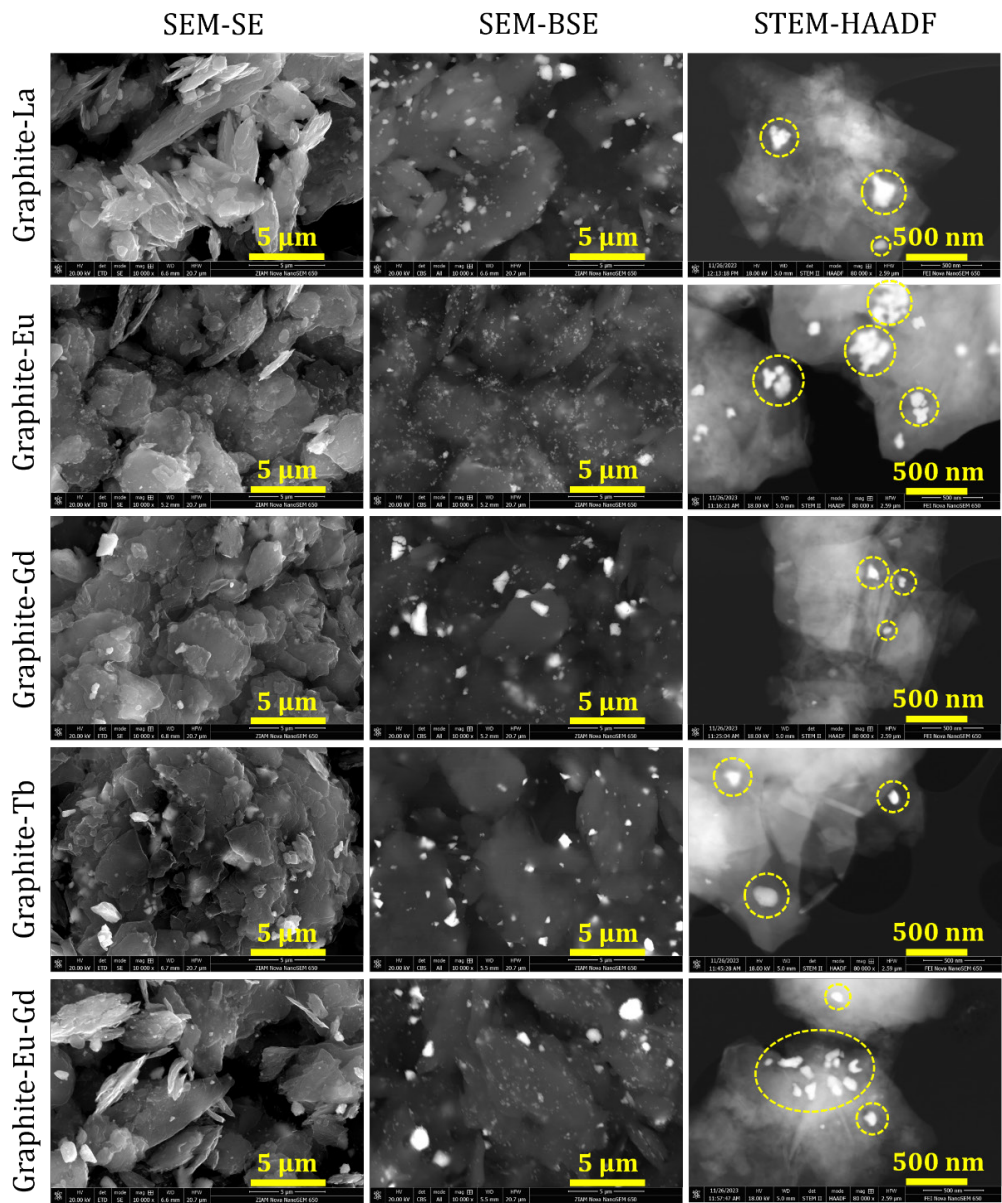
Figure 6.9. Micrographs of graphite-Ln nanocomposites obtained by ball milling collected with different detectors

The thermal behaviour of graphite and the influence of both the mechanochemical treatment and the presence of lanthanide oxides was studied by TGA-DTA; the results are shown in Figure 6.10. The thermogram of pristine graphite presents only one weight loss starting at around 560 °C and ending at 836 °C, associated with the total combustion of the graphitic carbon network, with the corresponding DTA peak centred at 794 °C. Mechanochemical processing reduces the thermal stability of graphite, which can be seen in the thermogram of ball-milled graphite also exhibiting only one weight loss, but here the total combustion starts at around 520 °C and ends at 802 °C, with the DTA peak centred at 745 °C. This can be explained by the introduction of new reactive sites, defects, and oxygen functionalities as a result of the mechanochemical treatment, in agreement with the XPS, Raman, XRD and SEM results. From the thermograms of the graphite-Ln nanocomposites one deduces that the temperature of the final combustion at 750 °C for graphite-La, 792 °C for graphite-Eu, 837 °C for graphite-Gd, 823 °C for graphite-Tb, and 811 °C for graphite-Eu-Gd. As with ball-milled graphite, the weight loss starts below 550 °C in all the graphite-Ln nanocomposites due to the presence of oxygen-containing functional groups. In principle, one could expect that the thermal stability of graphite-Ln nanocomposites would decrease as the Raman I_D/I_G ratio increases, because the higher the number of defects and reactive sites on the graphite structure, the lower the final combustion temperature, but surprisingly such a tend is not observed. Only graphite-La and graphite-Eu show a considerable decrease in the final combustion temperature, to 750 °C and 792 °C, respectively, pointing to a possible catalytic effect of the La and Eu oxide components. On the other hand, despite the disorder and higher oxygen content introduced by the mechanochemical processing, the temperature of the final combustion in graphite-Gd, graphite-Tb and graphite-Eu-Gd samples is not notably influenced, suggesting that the presence of Gd and Tb oxides retards the burning of the carbon backbone.
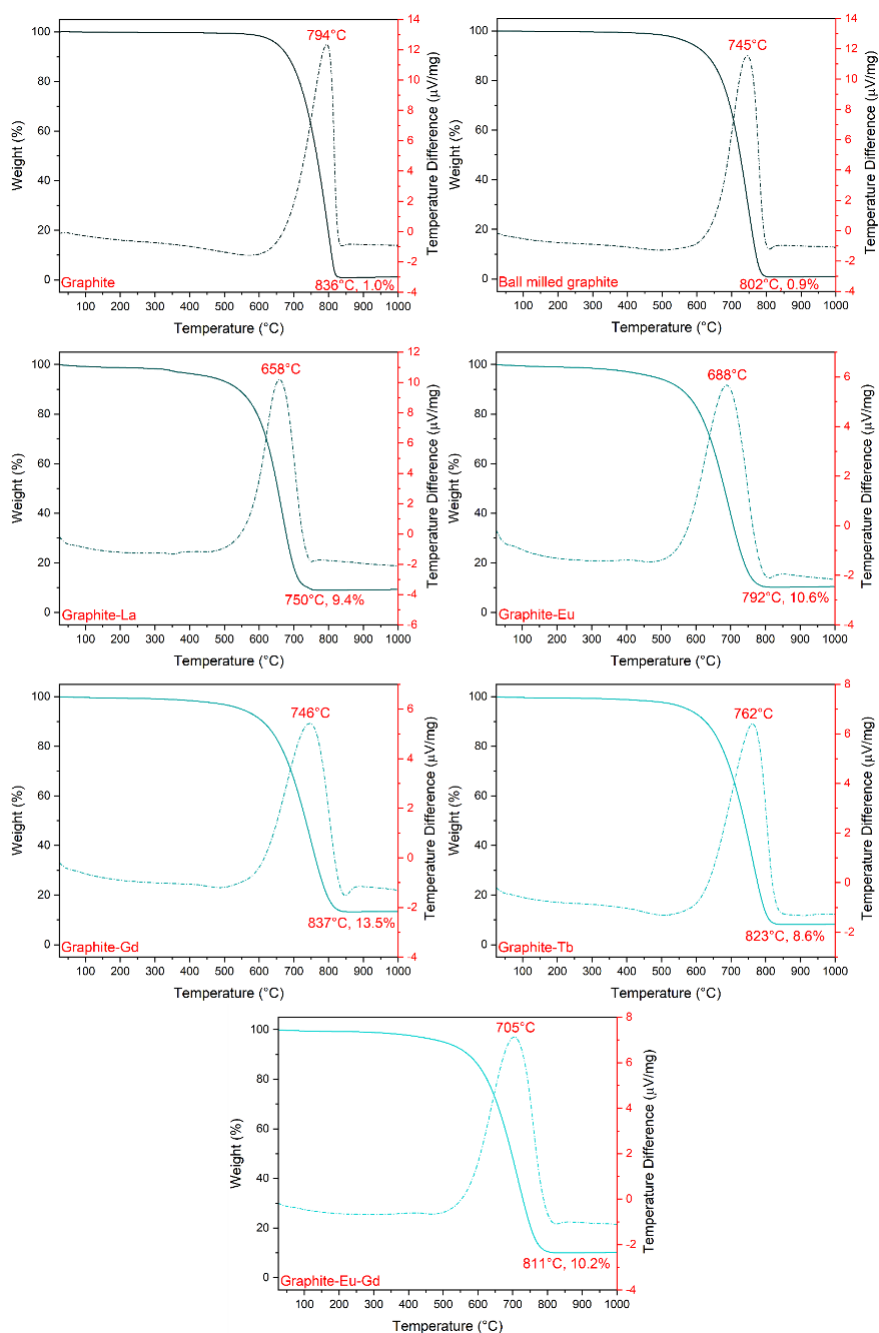
6

Figure 6.10. Thermograms of graphite, ball-milled graphite, and graphite-Ln nanocomposites obtained by ball milling

Elucidating the interaction between graphitic nanomaterials and cells is critical for the safety evaluation of synthesised materials. The literature on the cytotoxicity of these materials is often contradictory, however, it is accepted GO can decrease cell viability and cause cell death depending considerably on the particle surface chemistry, size, purity, and dose [81].

Since cell membranes consist of a phospholipid bilayer, where each phospholipid has a phosphate head group (hydrophilic head) and fatty acid chains (hydrophobic tail), the surface charge of GO, due to the presence of oxygen functionalities, has a significant effect on the interactions between GO and cells. Li *et al.* [82] have reported that GO can interact electrostatically with positively charged, but not with negatively charged or neutral phospholipids. In principle, the phospholipids of mammalian cell membranes are negatively charged or neutral, so the attraction to GO would be unlikely, but Duan *et al.* [83] and Hu *et al.* [84] have indicated that GO can damage the cell membrane through hydrophobic interactions. Li *et al.* [85] investigated the effect of the oxygen content in GO-based materials on lipid membranes and concluded that the cytotoxicity induced is higher for GO than for rGO. Besides that, small-size graphitic nanomaterials can penetrate cell membranes because of their sharp edges, causing leakage of cytoplasm. Moreover, it is possible to see an increment in the cytotoxicity due to the creation of reactive oxygen species that induce lipid peroxidation, which leads to cell death. The presence of impurities has also an important role in the toxicity of graphitic nanomaterials, where metallic impurities, organic solvent contamination, chemical oxidizers and reducing agents employed in the preparation of GO and rGO promote the toxicity of these materials in mammalian cells [81]. For all the reasons exposed above, a proper understanding of the interaction between graphitic nanomaterials and cell membranes is highly desirable to reduce their cytotoxicity when developing more environmentally friendly routes to functionalise and exfoliate graphite flakes.

The introduction of lanthanides to the structure of GO can change the surface charge, and thus the interaction with cell membranes can change as well. Zheng *et al.* [86] have reported the preparation of La@GO composites with a strong bactericidal effect, capable of provoking the phospholipid dephosphorylation, lipid peroxidation of cell membranes, and disruption of cell walls. To investigate the cytotoxicity of the graphite-Ln nanocomposites synthesised as described in this chapter, preliminary studies to determine their ability to affect the growth of COS-7 monkey kidney cells were performed employing an SRB assay, which is widely used as a model in mammal toxicity tests [87]. The results presented in Figure 6.11 and Table 6.5 show that ball-milled graphite is non-cytotoxic for concentrations of 50 and 100 μg/mL. A plausible explanation would be that the negative charge of graphene nanosheet surfaces due to

6

the presence of oxygen-containing groups causes electrostatic repulsion leading to a little interaction between ball-milled graphite and the membranes of COS-7 cells. In general, the growth inhibition is dose-dependent for the graphite-Ln nanocomposites, where for a concentration of 50 μg/mL, the cytotoxicity is less than 3 % for graphite-La (2.7 %) and even lower for graphite-Eu (0.6 %), graphite-Gd (NC) and graphite-Eu-Gd (NC). It is instead considerably higher for graphite-Tb (13.5 %)even at this low dose. For a concentration of 100 μg/mL, the cytotoxicity is again highest for graphite-Tb (17.9 %), followed by graphite-Eu-Gd (5.6 %), graphite-Eu (3.5 %), graphite-La (2.9 %), and graphite-Gd (1.2 %). This trend correlates with the value of the I_D/I_G ratio obtained from Raman spectroscopy. Thus, it seems that not only the presence of lanthanide ions changes the surface charge of graphene nanosheets, the decreased size of graphene nanosheets, reflected in the higher I_D/I_G ratio, increases the cytotoxicity of graphite-Ln nanocomposites. Figure 6.12 shows the morphological micrographs of COS-7 monolayer culture with control and graphite-Ln nanocomposites. Material aggregates were observed for all treatments, but no morphological changes were observed at a concentration of 100 μg/mL. A MTX 1 μM was tested and used as a positive control where it is possible to observe a loss of cell adhesion, dead cells, and a radical change in the morphology of the monolayer culture. These results are comparable with those obtained by Gonzalez *et al*. [76], where the evaluated graphite only presented about 10 % of apoptosis measurement, although, in the present study graphite was the only nanomaterial which does not present cytotoxicity changes in either of the two concentrations tested. Aragón-Muriel *et al*. [88] tested lanthanide complexes against the COS-7 cell line and found that 25 μM of lanthanide complexes inhibited close to 12 % of cell growth. That supports the finding that graphite modified with lanthanides changes the toxicity behaviour.

6

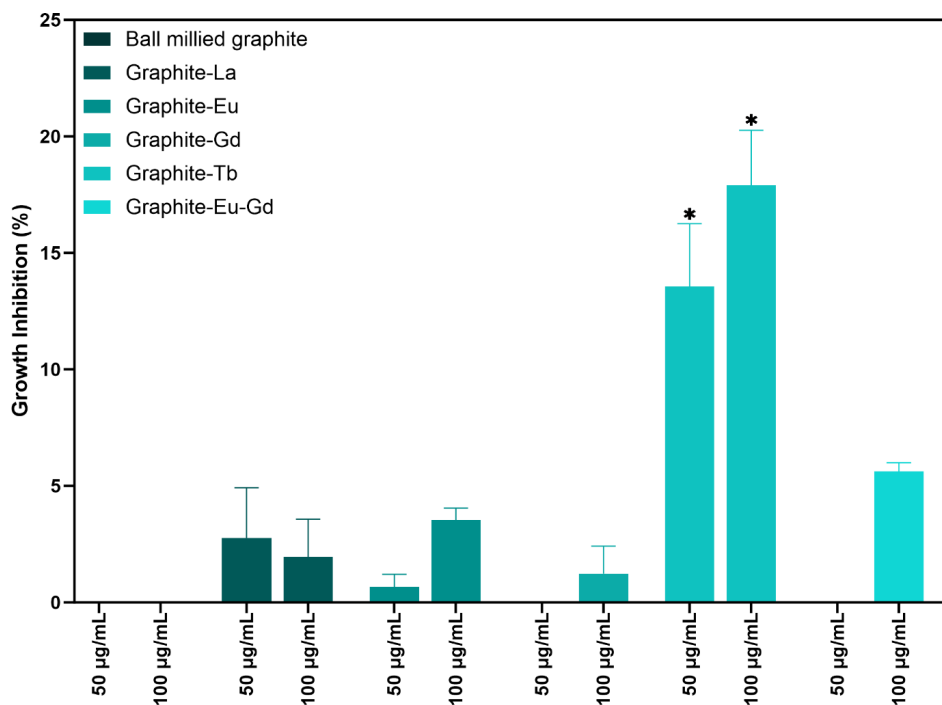*Figure 6.11. Growth inhibition (%) of ball-milled graphite and graphite-Ln nanocomposites at 50 and 100 µg/mL. The data were expressed as the standard error of the mean and * $p < 0.05$ (2-way ANOVA).*
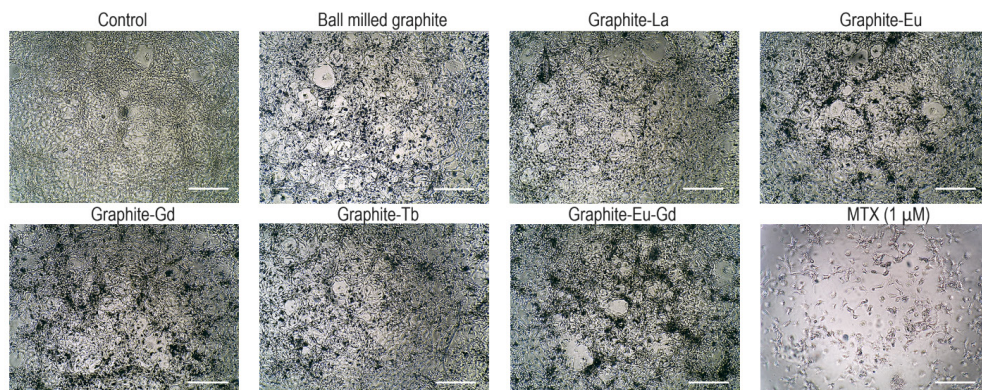

Figure 6.12. Cell culture micrographs of the COS-7 line treated with fresh supplemented media as control, ball-milled graphite and graphite-Ln nanocomposites produced by ball milling at 100 µg/ mL. Scale bar 250 µm.

*Table 6.5. Growth inhibition (%) of ball-milled graphite and graphite-Ln nanocomposites obtained by ball milling against COS-7 cell line at 50 and 100 μg/mL concentration calculated by detection of SRB. NC = non-cytotoxic. The data is expressed as the standard error of the mean and * p < 0.05 (2-way ANOVA).*

	Concentration	
Sample	50 μg/mL	100 μg/mL
Ball-milled graphite	NC	NC
Graphite-La	2.7 ± 2.1	1.9 ± 1.6
Graphite-Eu	0.6 ± 0.5	3.5 ± 0.5
Graphite-Gd	NC	1.2 ± 1.1
Graphite-Tb	13.5 ± 2.7	17.9 ± 2.3
Graphite-Eu-Gd	NC	5.6 ± 0.3

6.4. Conclusions

We present a simple, low-cost, and eco-friendly approach employing the ball milling technique to prepare graphite-Ln nanocomposites. The mechanochemical functionalisation was achieved in the absence of solvents, hazardous chemicals, and oxidant reagents, and only an air atmosphere was needed. Moreover, compared to the findings in our previous studies where we used a milling time of 8 h and balls of 20 mm diameter for the mechanical processing, the optimisation of the experimental conditions employed in the present study, namely a milling time of 48 h and balls of 10 mm diameter, led to a more efficient exfoliation of graphite, as well as a more homogeneous distribution of LnO particles on graphite due to a reduction of the impact energy in the milling process. XPS confirmed the functionalisation of the graphene nanosheets with hydroxyl, epoxy, and carbonyl groups where lanthanide ions could be anchored. Raman spectroscopy revealed the partial exfoliation of graphite into few-layer graphene in all milled samples through the apparition of the D' band, a change in the symmetry and a downshift of the 2D band. XRD showed that all the samples kept a crystalline structure despite the milling time of 48 h, no increment of the *d*-spacing was observed and supported the idea of the graphite exfoliation. The SEM-SE micrographs, as well as Raman evidenced a decrease in the graphite crystallite sizes mainly from 1 to 6 μm, mirrored by the decrease in the size of the coherently diffracting domains as deduced from XRD. The SEM-BEC micrographs showed that the lanthanide oxide particles were micro- and nanosized and uniformly dispersed throughout the graphene

6

nanosheets, while STEM-HAADF micrographs confirmed that all the nanocomposites have lanthanide nanoparticles of at least 50-100 nm. TGA studies corroborated the presence of oxygen functional groups after the mechanochemical treatment, showing that the weight loss started before 550 °C in all the nanocomposites thermograms. On the one hand, TGA revealed a catalytic effect of lanthanum and europium oxides accelerating the graphite combustion, while, gadolinium and terbium oxides were found to retard the combustion process. Additionally, the cytotoxicity tests revealed that the cytotoxicity of graphite-Ln nanocomposites does not reach 6 % of growth inhibition for 50 and 100 µg/mL. except for the graphite-Tb sample, which reached a growth inhibition of 17.9 % for 100 µg/mL.

References

[1]   W. Ren, H.M. Cheng, The global growth of graphene, Nature Nanotechnology 2014 9:10 9 (2014) 726–730. https://doi.org/10.1038/nnano.2014.229.

[2]   M. Lotya, P.J. King, U. Khan, S. De, J.N. Coleman, High-concentration, surfactant-stabilized graphene dispersions, ACS Nano 4 (2010) 3155–3162. https://doi.org/10.1021/NN1005304.

[3]   Y. Hong, Z. Wang, X. Jin, Sulfuric Acid Intercalated Graphite Oxide for Graphene Preparation, Scientific Reports 2013 3:1 3 (2013) 1–6. https://doi.org/10.1038/srep03439.

[4]   J.M. Munuera, J.I. Paredes, M. Enterría, A. Pagán, S. Villar-Rodil, M.F.R. Pereira, J.I. Martins, J.L. Figueiredo, J.L. Cenis, A. Martínez-Alonso, J.M.D. Tascón, Electrochemical Exfoliation of Graphite in Aqueous Sodium Halide Electrolytes toward Low Oxygen Content Graphene for Energy and Environmental Applications, ACS Appl Mater Interfaces 9 (2017) 24085–24099. https://doi.org/10.1021/ACSAMI.7B04802.

[5]   M. Yi, Z. Shen, S. Ma, X. Zhang, A mixed-solvent strategy for facile and green preparation of graphene by liquid-phase exfoliation of graphite, Journal of Nanoparticle Research 14 (2012) 1–9. https://doi.org/10.1007/S11051-012-1003-5.

[6]   M. Buzaglo, M. Shtein, S. Kober, R. Lovrinčić, A. Vilan, O. Regev, Critical parameters in exfoliating graphite into graphene, Physical Chemistry Chemical Physics 15 (2013) 4428–4435. https://doi.org/10.1039/C3CP43205J.

[7]   J.H. Ding, H.R. Zhao, H. Bin Yu, A water-based green approach to large-scale production of aqueous compatible graphene nanoplatelets, Scientific Reports 2018 8:1 8 (2018) 1–8. https://doi.org/10.1038/s41598-018-23859-5.

[8]   X. An, T. Simmons, R. Shah, C. Wolfe, K.M. Lewis, M. Washington, S.K. Nayak, S. Talapatra, S. Kar, Stable aqueous dispersions of noncovalently functionalized graphene from graphite and their multifunctional high-performance applications, Nano Lett 10 (2010) 4295–4301. https://doi.org/10.1021/NL903557P.

[9]   H. Yang, Y. Hernandez, A. Schlierf, A. Felten, A. Eckmann, S. Johal, P. Louette, J.J. Pireaux, X. Feng, K. Mullen, V. Palermo, C. Casiraghi, A simple method for graphene production based on exfoliation of graphite in water using 1-pyrenesulfonic acid sodium salt, Carbon N Y

6

53 (2013) 357–365. https://doi.org/10.1016/J.CARBON.2012.11.022.

[10] M. Lotya, Y. Hernandez, P.J. King, R.J. Smith, V. Nicolosi, L.S. Karlsson, F.M. Blighe, S. De, W. Zhiming, I.T. McGovern, G.S. Duesberg, J.N. Coleman, Liquid phase production of graphene by exfoliation of graphite in surfactant/water solutions, J Am Chem Soc 131 (2009) 3611–3620. https://doi.org/10.1021/JA807449U.

[11] H. Gao, K. Zhu, G. Hu, C. Xue, Large-scale graphene production by ultrasound-assisted exfoliation of natural graphite in supercritical CO2/H2O medium, Chemical Engineering Journal 308 (2017) 872–879. https://doi.org/10.1016/J.CEJ.2016.09.132.

[12] Dimiev A M, Eigler S, Graphene Oxide: Fundamentals and Applications, Wiley, 2016. https://doi.org/10.1002/9781119069447.

[13] K. Krishnamoorthy, M. Veerapandian, K. Yun, S.J. Kim, The chemical and structural analysis of graphene oxide with different degrees of oxidation, Carbon N Y 53 (2013) 38–49. https://doi.org/10.1016/J.CARBON.2012.10.013.

[14] L. Luo, T. Peng, M. Yuan, H. Sun, S. Dai, L. Wang, Preparation of Graphite Oxide Containing Different Oxygen-Containing Functional Groups and the Study of Ammonia Gas Sensitivity, Sensors 2018, Vol. 18, Page 3745 18 (2018) 3745. https://doi.org/10.3390/S18113745.

[15] XIII. On the atomic weight of graphite, Philos Trans R Soc Lond 149 (1859) 249–259. https://doi.org/10.1098/RSTL.1859.0013.

[16] L. Staudenmaier, Verfahren zur Darstellung der Graphitsäure, Berichte Der Deutschen Chemischen Gesellschaft 31 (1898) 1481–1487. https://doi.org/10.1002/CBER.18980310237.

[17] U. Hofmann, E. König, Untersuchungen über Graphitoxyd, Z Anorg Allg Chem 234 (1937) 311–336. https://doi.org/10.1002/ZAAC.19372340405.

[18] W.S. Hummers, R.E. Offeman, Preparation of Graphitic Oxide, J Am Chem Soc 80 (1958) 1339. https://doi.org/10.1021/JA01539A017.

[19] C. Jiang, D. An, Z. Wang, S. Zhang, X. An, J. Bo, G. Yan, K.S. Moon, C. Wong, A sustainable reduction route of graphene oxide by industrial waste lignin for versatile applications in energy and environment, J Clean Prod 268 (2020) 122019. https://doi.org/10.1016/J.JCLEPRO.2020.122019.

[20] J. Andersen, J. Mack, Mechanochemistry and organic synthesis: from mystical to practical, Green Chemistry 20 (2018) 1435–1443. https://doi.org/10.1039/C7GC03797J.

[21] M.N. Temnikov, A.A. Anisimov, P. V. Zhemchugov, D.N. Kholodkov, A.S. Goloveshkin, A. V. Naumkin, S.M. Chistovalov, D. Katsoulis, A.M. Muzafarov, Mechanochemistry – a new powerful green approach to the direct synthesis of alkoxysilanes, Green Chemistry 20 (2018) 1962–1969. https://doi.org/10.1039/C7GC03862C.

[22] S. Menuel, B. Léger, A. Addad, E. Monflier, F. Hapiot, Cyclodextrins as effective additives in AuNP-catalyzed reduction of nitrobenzene derivatives in a ball-mill, Green Chemistry 18 (2016) 5500–5509. https://doi.org/10.1039/C6GC00770H.

[23] R.K. Bhuyan, R.K. Mohapatra, G. Nath, B.K. Sahoo, D. Das, D. Pamu, Influence of high-energy ball milling on structural, microstructural, and optical properties of Mg2TiO4 nanoparticles, Journal of Materials Science: Materials in Electronics 31 (2020) 628–636. https://doi.org/10.1007/S10854-019-02568-3.

[24] X. Li, J. Shen, C. Wu, K. Wu, Ball-Mill-Exfoliated Graphene: Tunable Electrochemistry and

Phenol Sensing, Small 15 (2019) 1805567. https://doi.org/10.1002/SMLL.201805567.

[25]   J. Xu, J. Shui, J. Wang, M. Wang, H.K. Liu, S.X. Dou, I.Y. Jeon, J.M. Seo, J.B. Baek, L. Dai, Sulfur-graphene nanostructured cathodes via ball-milling for high-performance lithium-sulfur batteries, ACS Nano 8 (2014) 10920–10930. https://doi.org/10.1021/NN5047585.

[26]   N. Rubio, C. Fabbro, M.A. Herrero, A. De La Hoz, M. Meneghetti, J.L.G. Fierro, M. Prato, E. Vázquez, Ball-Milling Modification of Single-Walled Carbon Nanotubes: Purification, Cutting, and Functionalization, Small 7 (2011) 665–674. https://doi.org/10.1002/SMLL.201001917.

[27]   R.B.N. Baig, R.S. Varma, Alternative energy input: mechanochemical, microwave and ultrasound-assisted organic synthesis, Chem Soc Rev 41 (2012) 1559–1584. https://doi.org/10.1039/C1CS15204A.

[28]   R.S. Varma, Chemical activation by mechanochemical mixing, microwave and ultrasonic irradiation, Green Chemistry 10 (2008) 1129–1130. https://doi.org/10.1039/B817559B.

[29]   M. Yi, Z. Shen, A review on mechanical exfoliation for the scalable production of graphene, J Mater Chem A Mater 3 (2015) 11700–11715. https://doi.org/10.1039/C5TA00252D.

[30]   E. Colacino, G. Ennas, I. Halász, A. Porcheddu, A. Scano, Mechanochemistry : a practical introduction from soft to hard materials, n.d.

[31]   L. Liu, Z. Xiong, D. Hu, G. Wu, P. Chen, Production of high quality single- or few-layered graphene by solid exfoliation of graphite in the presence of ammonia borane, Chemical Communications 49 (2013) 7890–7892. https://doi.org/10.1039/C3CC43670E.

[32]   V. León, M. Quintana, M.A. Herrero, J.L.G. Fierro, A.D. La Hoz, M. Prato, E. Vázquez, Few-layer graphenes from ball-milling of graphite with melamine, Chemical Communications 47 (2011) 10936–10938. https://doi.org/10.1039/C1CC14595A.

[33]   A.E.D. Mahmoud, A. Stolle, M. Stelter, Sustainable Synthesis of High-Surface-Area Graphite Oxide via Dry Ball Milling, ACS Sustain Chem Eng 6 (2018) 6358–6369. https://doi.org/10.1021/acssuschemeng.8b00147.

[34]   O.Yu. Posudievsky, O.A. Khazieieva, V.G. Koshechko, V.D. Pokhodenko, Preparation of graphene oxide by solvent-free mechanochemical oxidation of graphite, J Mater Chem 22 (2012) 12465. https://doi.org/10.1039/c2jm16073k.

[35]   G. Bharath, R. Madhu, S.M. Chen, V. Veeramani, D. Mangalaraj, N. Ponpandian, Solvent-free mechanochemical synthesis of graphene oxide and Fe3O4–reduced graphene oxide nanocomposites for sensitive detection of nitrite, J Mater Chem A Mater 3 (2015) 15529–15539. https://doi.org/10.1039/C5TA03179F.

[36]   O.Y. Posudievsky, O.A. Kozarenko, O.A. Khazieieva, V.G. Koshechko, V.D. Pokhodenko, Ultrasound-free preparation of graphene oxide from mechanochemically oxidized graphite, J Mater Chem A Mater 1 (2013) 6658–6663. https://doi.org/10.1039/C3TA10542C.

[37]   J. Chen, W. Chen, D. Song, B. Lai, Y. Sheng, L. Yan, The solvent-free mechanochemical synthesis of mildly oxidized graphene oxide and its application as a novel conductive surfactant, New Journal of Chemistry 43 (2019) 7057–7064. https://doi.org/10.1039/C9NJ00529C.

[38]   W. Zhao, M. Fang, F. Wu, H. Wu, L. Wang, G. Chen, Preparation of graphene by exfoliation of graphite using wet ball milling, J Mater Chem 20 (2010) 5817–5819. https://doi.

6

org/10.1039/C0JM01354D.

[39]   V.A. Basiuk, D.A. Acevedo-Guzmán, V. Meza-Laguna, E. Álvarez-Zauco, L. Huerta, M. Serrano, M. Kakazey, E. V. Basiuk, High-energy ball-milling preparation and characterization of Ln2O3–graphite nanocomposites, Mater Today Commun 26 (2021) 102030. https://doi.org/10.1016/J.MTCOMM.2021.102030.

[40]   J. Zhang, Z. Zhang, Y. Jiao, H. Yang, Y. Li, J. Zhang, P. Gao, The graphene/lanthanum oxide nanocomposites as electrode materials of supercapacitors, J Power Sources 419 (2019) 99–105. https://doi.org/10.1016/J.JPOWSOUR.2019.02.059.

[41]   M. Chen, C. Huo, Y. Li, J. Wang, Selective Adsorption and Efficient Removal of Phosphate from Aqueous Medium with Graphene-Lanthanum Composite, ACS Sustain Chem Eng 4 (2016) 1296–1302. https://doi.org/10.1021/ACSSUSCHEMENG.5B01324.

[42]   R. Rajagopal, K.S. Ryu, Facile hydrothermal synthesis of lanthanum oxide/hydroxide nanoparticles anchored reduced graphene oxide for supercapacitor applications, Journal of Industrial and Engineering Chemistry 60 (2018) 441–450. https://doi.org/10.1016/J.JIEC.2017.11.031.

[43]   S. Karthikeyan, M. Selvapandiyan, A. Sankar, Electrochemical performance of reduced graphene oxide (rGO) decorated lanthanum oxide (La2O3) composite nanostructure as asymmetric supercapacitors, Inorg Chem Commun 139 (2022) 109331. https://doi.org/10.1016/J.INOCHE.2022.109331.

[44]   P. Aryanrad, H.R. Naderi, E. Kohan, M.R. Ganjali, M. Baghernejad, A. Shiralizadeh Dezfuli, Europium oxide nanorod-reduced graphene oxide nanocomposites towards supercapacitors, RSC Adv 10 (2020) 17543–17551. https://doi.org/10.1039/C9RA11012G.

[45]   H.R. Naderi, M.R. Ganjali, A.S. Dezfuli, High-performance supercapacitor based on reduced graphene oxide decorated with europium oxide nanoparticles, Journal of Materials Science: Materials in Electronics 29 (2018) 3035–3044. https://doi.org/10.1007/S10854-017-8234-2.

[46]   L.P. Lingamdinne, S. Lee, J.S. Choi, V.R. Lebaka, V.R.P. Durbaka, J.R. Koduru, Potential of the magnetic hollow sphere nanocomposite (graphene oxide-gadolinium oxide) for arsenic removal from real field water and antimicrobial applications, J Hazard Mater 402 (2021) 123882. https://doi.org/10.1016/J.JHAZMAT.2020.123882.

[47]   H. Gao, Y. Zhou, K. Chen, X. Li, Synthesis of Tb4O7 complexed with reduced graphene oxide for Rhodamine-B absorption, Mater Res Bull 77 (2016) 111–114. https://doi.org/10.1016/J.MATERRESBULL.2016.01.016.

[48]   P. Dash, T. Dash, T.K. Rout, A.K. Sahu, S.K. Biswal, B.K. Mishra, Preparation of graphene oxide by dry planetary ball milling process from natural graphite, RSC Adv 6 (2016) 12657–12668. https://doi.org/10.1039/C5RA26491J.

[49]   H. Estrade-Szwarckopf, XPS photoemission in carbonaceous materials: A "'defect'" peak beside the graphitic asymmetric peak, (2004). https://doi.org/10.1016/j.carbon.2004.03.005.

[50]   L.G. Guex, B. Sacchi, K.F. Peuvot, R.L. Andersson, A.M. Pourrahimi, V. Ström, S. Farris, R.T. Olsson, Experimental review: chemical reduction of graphene oxide (GO) to reduced graphene oxide (rGO) by aqueous chemistry, Nanoscale 9 (2017) 9562–9571. https://doi.org/10.1039/C7NR02943H.

[51]   G. Eda, M. Chhowalla, Chemically Derived Graphene Oxide: Towards Large-Area Thin-Film

6

Electronics and Optoelectronics, Advanced Materials 22 (2010) 2392–2415. https://doi.org/10.1002/ADMA.200903689.

[52]   D.R. Dreyer, A.D. Todd, C.W. Bielawski, Harnessing the chemistry of graphene oxide, Chem Soc Rev 43 (2014) 5288–5301. https://doi.org/10.1039/C4CS00060A.

[53]   I.Y. Jeon, Y.R. Shin, G.J. Sohn, H.J. Choi, S.Y. Bae, J. Mahmood, S.M. Jung, J.M. Seo, M.J. Kim, D.W. Chang, L. Dai, J.B. Baek, Edge-carboxylated graphene nanosheets via ball milling, Proc Natl Acad Sci U S A 109 (2012) 5588–5593. https://doi.org/10.1073/PNAS.1116897109.

[54]   I.Y. Jeon, S.Y. Bae, J.M. Seo, J.B. Baek, Scalable Production of Edge-Functionalized Graphene Nanoplatelets via Mechanochemical Ball-Milling, Adv Funct Mater 25 (2015) 6961–6975. https://doi.org/10.1002/ADFM.201502214.

[55]   H. Zhu, Y. Cao, J. Zhang, W. Zhang, Y. Xu, J. Guo, W. Yang, J. Liu, One-step preparation of graphene nanosheets via ball milling of graphite and the application in lithium-ion batteries, J Mater Sci 51 (2016) 3675–3683. https://doi.org/10.1007/s10853-015-9655-z.

[56]   C. Liu, X. Liu, J. Tan, Q. Wang, H. Wen, C. Zhang, Nitrogen-doped graphene by all-solid-state ball-milling graphite with urea as a high-power lithium ion battery anode, J Power Sources 342 (2017) 157–164. https://doi.org/10.1016/j.jpowsour.2016.11.110.

[57]   Y. Wang, H. Meng, Y. Lu, C. Li, Mechanochemical conversion of graphite to highly Cross-linked alkynyl carbon material as excellent mercury (II) sorbent, Chemical Engineering Journal 415 (2021) 129009. https://doi.org/10.1016/j.cej.2021.129009.

[58]   S. Motozuka, M. Tagaya, N. Ogawa, K. Fukui, M. Nishikawa, K. Shiba, T. Uehara, T. Kobayashi, Effective preparation of graphite nanoparticles using mechanochemical solid-state reactions, Solid State Commun 190 (2014) 28–32. https://doi.org/10.1016/j.ssc.2014.03.023.

[59]   G. Zhang, S. Sun, D. Yang, J.P. Dodelet, E. Sacher, The surface analytical characterization of carbon fibers functionalized by H2SO4/HNO3 treatment, Carbon N Y 46 (2008) 196–205. https://doi.org/10.1016/J.CARBON.2007.11.002.

[60]   J. Cao, D. Zhang, X. Zhang, S. Wang, J. Han, Y. Zhao, Y. Huang, J. Qin, Mechanochemical reactions of MnO2 and graphite nanosheets as a durable zinc ion battery cathode, Appl Surf Sci 534 (2020) 147630. https://doi.org/10.1016/J.APSUSC.2020.147630.

[61]   M. Kralj, A. Supina, D. Čapeta, I. Sović, I. Halasz, Mechanochemical oxidation of graphite for graphene-hydrogel applications: Pitfalls and benefits, Materialia (Oxf) 14 (2020) 100908. https://doi.org/10.1016/j.mtla.2020.100908.

[62]   A.A. Green, M.C. Hersam, Solution phase production of graphene with controlled thickness via density differentiation, Nano Lett 9 (2009) 4031–4036. https://doi.org/10.1021/NL902200B.

[63]   D. Graf, F. Molitor, K. Ensslin, C. Stampfer, A. Jungen, C. Hierold, L. Wirtz, Spatially resolved raman spectroscopy of single- and few-layer graphene, Nano Lett 7 (2007) 238–242. https://doi.org/10.1021/NL061702A.

[64]   A.C. Ferrari, J.C. Meyer, V. Scardaci, C. Casiraghi, M. Lazzeri, F. Mauri, S. Piscanec, D. Jiang, K.S. Novoselov, S. Roth, A.K. Geim, Raman spectrum of graphene and graphene layers, Phys Rev Lett 97 (2006) 187401. https://doi.org/10.1103/PHYSREVLETT.97.187401.

[65]   D.S. Lee, C. Riedl, B. Krauss, K. Von Klitzing, U. Starke, J.H. Smet, Raman spectra of epitaxial graphene on SiC and of epitaxial graphene transferred to SiO2, Nano Lett 8 (2008) 4320–

6

4325. https://doi.org/10.1021/NL802156W.

[66] Z. Ni, Y. Wang, T. Yu, Z. Shen, Raman spectroscopy and imaging of graphene, Nano Res 1 (2008) 273–291. https://doi.org/10.1007/S12274-008-8036-1.

[67] L.M. Malard, M.A. Pimenta, G. Dresselhaus, M.S. Dresselhaus, Raman spectroscopy in graphene, Phys Rep 473 (2009) 51–87. https://doi.org/10.1016/J.PHYSREP.2009.02.003.

[68] H. Murphy, P. Papakonstantinou, T.I.T. Okpalugo, Raman study of multiwalled carbon nanotubes functionalized with oxygen groups, Journal of Vacuum Science & Technology B: Microelectronics and Nanometer Structures Processing, Measurement, and Phenomena 24 (2006) 715–720. https://doi.org/10.1116/1.2180257.

[69] J.M. Mendoza-Duarte, F.C. Robles-Hernández, C.D. Gomez-Esparza, J.G. Miranda-Hernández, C.G. Garay-Reyes, I. Estrada-Guel, R. Martínez-Sánchez, Exfoliated graphite preparation based on an eco-friendly mechanochemical route, J Environ Chem Eng 8 (2020) 104370. https://doi.org/10.1016/j.jece.2020.104370.

[70] S. Sharma, D. Susan, N.C. Kothiyal, R. Kaur, Graphene oxide prepared from mechanically milled graphite: Effect on strength of novel fly-ash based cementitious matrix, Constr Build Mater 177 (2018) 10–22. https://doi.org/10.1016/J.CONBUILDMAT.2018.05.051.

[71] L. Liu, N. Solin, O. Inganäs, Scalable lignin/graphite electrodes formed by mechanochemistry, RSC Adv 9 (2019) 39758–39767. https://doi.org/10.1039/C9RA07507K.

[72] K. Zhang, Y. Zhang, S. Wang, Enhancing thermoelectric properties of organic composites through hierarchical nanostructures, Scientific Reports 2013 3:1 3 (2013) 1–7. https://doi.org/10.1038/srep03448.

[73] X. Wang, P.F. Fulvio, G.A. Baker, G.M. Veith, R.R. Unocic, S.M. Mahurin, M. Chi, S. Dai, Direct exfoliation of natural graphite into micrometre size few layers graphene sheets using ionic liquids, Chemical Communications 46 (2010) 4487–4489. https://doi.org/10.1039/C0CC00799D.

[74] V.A. Basiuk, C.U. Mendoza-Domínguez, V. Meza-Laguna, P. Molina-Sevilla, E. Álvarez-Zauco, M. Serrano, M. Vlasova, E. V. Basiuk, Dry ball-milling preparation and characterization of graphite–phthalocyanine composites, Fullerenes, Nanotubes and Carbon Nanostructures (2023). https://doi.org/10.1080/1536383X.2023.2211695.

[75] R. V. Salvatierra, S.H. Domingues, M.M. Oliveira, A.J.G. Zarbin, Tri-layer graphene films produced by mechanochemical exfoliation of graphite, Carbon N Y 57 (2013) 410–415. https://doi.org/10.1016/J.CARBON.2013.02.013.

[76] V.J. González, A.M. Rodríguez, V. León, J. Frontiñán-Rubio, J.L.G. Fierro, M. Durán-Prado, A.B. Muñoz-García, M. Pavone, E. Vázquez, Sweet graphene: exfoliation of graphite and preparation of glucose-graphene cocrystals through mechanochemical treatments, Green Chemistry 20 (2018) 3581–3592. https://doi.org/10.1039/C8GC01162A.

[77] F. Lin, Y. Qiu, X. Zheng, Z. Duanmu, Q. Lu, B. Huang, L. Tang, B. Lu, One-pot mechanochemical assembly of lignocellulose nanofiber/graphite nanocomposites for wearable electronic devices, Chemical Engineering Journal 437 (2022) 135286. https://doi.org/10.1016/j.cej.2022.135286.

[78] A.C. Ferrari, Raman spectroscopy of graphene and graphite: Disorder, electron–phonon coupling, doping and nonadiabatic effects, Solid State Commun 143 (2007) 47–57. https://doi.org/10.1016/J.SSC.2007.03.052.

[79] L.G. Caņado, K. Takai, T. Enoki, M. Endo, Y.A. Kim, H. Mizusaki, A. Jorio, L.N. Coelho, R.

6

Magalhães-Paniago, M.A. Pimenta, General equation for the determination of the crystallite size la of nanographite by Raman spectroscopy, Appl Phys Lett 88 (2006). https://doi.org/10.1063/1.2196057/152616.

[80]   T. Xing, L.H. Li, L. Hou, X. Hu, S. Zhou, R. Peter, M. Petravic, Y. Chen, Disorder in ball-milled graphite revealed by Raman spectroscopy, Carbon N Y 57 (2013) 515–519. https://doi.org/10.1016/J.CARBON.2013.02.029.

[81]   C. Liao, Y. Li, S.C. Tjong, Graphene Nanomaterials: Synthesis, Biocompatibility, and Cytotoxicity, International Journal of Molecular Sciences 2018, Vol. 19, Page 3564 19 (2018) 3564. https://doi.org/10.3390/IJMS19113564.

[82]   S. Li, A.J. Stein, A. Kruger, R.M. Leblanc, Head groups of lipids govern the interaction and orientation between graphene oxide and lipids, Journal of Physical Chemistry C 117 (2013) 16150–16158. https://doi.org/10.1021/JP405991Q.

[83]   G. Duan, Y. Zhang, B. Luan, J.K. Weber, R.W. Zhou, Z. Yang, L. Zhao, J. Xu, J. Luo, R. Zhou, Graphene-Induced Pore Formation on Cell Membranes, Scientific Reports 2017 7:1 7 (2017) 1–12. https://doi.org/10.1038/srep42767.

[84]   X. Hu, H. Lei, X. Zhang, Y. Zhang, Strong hydrophobic interaction between graphene oxide and supported lipid bilayers revealed by AFM, Microsc Res Tech 79 (2016) 721–726. https://doi.org/10.1002/JEMT.22690.

[85]   R. Li, L.M. Guiney, C.H. Chang, N.D. Mansukhani, Z. Ji, X. Wang, Y.P. Liao, W. Jiang, B. Sun, M.C. Hersam, A.E. Nel, T. Xia, Surface Oxidation of Graphene Oxide Determines Membrane Damage, Lipid Peroxidation, and Cytotoxicity in Macrophages in a Pulmonary Toxicity Model, ACS Nano 12 (2018) 1390–1402. https://doi.org/10.1021/ACSNANO.7B07737.

[86]   H. Zheng, Z. Ji, K.R. Roy, M. Gao, Y. Pan, X. Cai, L. Wang, W. Li, C.H. Chang, C. Kaweeteerawat, C. Chen, T. Xia, Y. Zhao, R. Li, Engineered Graphene Oxide Nanocomposite Capable of Preventing the Evolution of Antimicrobial Resistance, ACS Nano 13 (2019) 11488–11499. https://doi.org/10.1021/ACSNANO.9B04970.

[87]   D. Ail, D. Nava, I.P. Hwang, E. Brazhnikova, C. Nouvel-Jaillard, A. Dentel, C. Joffrois, L. Rousseau, J. Dégardin, S. Bertin, J.A. Sahel, O. Goureau, S. Picaud, D. Dalkara, Inducible nonhuman primate models of retinal degeneration for testing end-stage therapies, Sci Adv 9 (2023). https://doi.org/10.1126/SCIADV.ADG8163.

[88]   A. Arag On-Muriel, Y. Liscano-Martínez, E. Rufino-Felipe, D. Morales-Morales, J. O~ Nate-Garz, D. Polo-Cer On, Synthesis, biological evaluation and model membrane studies on metal complexes containing aromatic N,O-chelate ligands, Heliyon (2017) e04126. https://doi.org/10.1016/j.heliyon.2020.e04126.

6

Summary

The research on new graphene nanomaterials for innovative applications and technologies has increased exponentially over the last few years. Tuning the properties of such nanomaterials to make them more efficient for a specific societal need is a challenge and another challenge is upscaling the production while focusing on sustainable and environmentally friendly fabrication methods. Nowadays, graphene-based nanocomposites are applied in a wide range of fields such as catalysis, supercapacitors, solar cells, environmental remediation, and biomedicine. They are synthesised using chemical methods that enable their covalent and non-covalent functionalisation but required long-times, costly equipment, and hazardous reagents. In order to move towards a greener, waste-free and energy frugal economy, novel, more ecologically acceptable strategies for making and modifying such nanocomposites have to be developed. In the PhD project described in this dissertation, we explored the synthesis of graphene-based lanthanide-containing nanocomposites using more environmentally friendly routes.

In **Chapter 1** the principles of green chemistry are introduced. Then the general properties of lanthanides and lanthanide oxides as well as of the carbon materials relevant to the project, namely graphene, graphene oxide and graphite, are described. Moreover, the main routes of synthesis of graphene-based materials and their implications for the environment is discussed.

Chapter 2 briefly describes the principles of the techniques employed for the characterisation of the graphene oxide- and graphite-lanthanide-containing nanocomposites and of the instruments used in the PhD project. These include spectroscopic characterisation (FTIR, Raman, and XPS), microscopy characterisation (SEM, TEM, and STEM), X-ray Diffraction analysis, and thermogravimetric analysis.

This thesis is divided into two parts; the first half (Chapters 3 and 4) is devoted to graphene oxide-lanthanide oxide/hydroxide nanocomposites prepared by solvothermal methods and their properties, and the second part (Chapters 5 and 6) is dedicated to the mechanochemical fabrication of graphite-lanthanide oxide nanocomposites.

In **Chapter 3** the synthesis of graphene oxide-lanthanide oxide and graphene oxide-lanthanide hydroxide nanocomposites (La, Eu, Gd, Tb) employing the solvothermal method is explored. The two experimental methodologies proposed represent a facile environmentally friendlier approach involving reaction times of four hours, as well as ethanol or water reaction media at 170 °C. According to the spectroscopic

characterisation, the chemical environment of GO changes after the incorporation of lanthanide species, showing that a chemical interaction between the oxygen groups of GO and the lanthanide ions is achieved. The X-ray diffraction and electron microscopy studies evidenced that the lanthanide oxide and lanthanide hydroxide particles observed through them seem to have different sizes and distributions, depending on the methodology and lanthanide used. Thermogravimetric analysis showed that the thermal stability decreased after the solvothermal functionalisation.

Chapter 4 details how the antimicrobial properties of graphene oxide-lanthanide oxide/hydroxide nanocomposites prepared as described in Chapter 3 were explored. Due to the differences in the size and distribution of the lanthanide-species particles on GO, the bactericidal effect against *Escherichia coli* (Gram$^-$) and *Corynebacterium glutamicum* (Gram$^+$) was found to be different for the different nanocomposites. $GO-La_2O_3$ presented spherically-shaped nanoparticles as well as the most uniform lanthanide particle distribution and, therefore, also the strongest antimicrobial activity among all the nanocomposites. The different composition between the two types of bacteria membranes did not seem to play an important role in the tests conducted, but lanthanide ions anchored to the GO surface fostered the bactericidal effect. In contrast, the GO-lanthanide hydroxide nanocomposites showed no evidence of antimicrobial activity.

In **Chapter 5** we described how the first approach to the fabrication of graphite-lanthanide oxide nanocomposites employing the high-energy ball milling technique was attempted. The eight hours of mechanochemical treatment of graphite led to a remarkable crystallite size reduction as well as to an increase in the oxygen content, which confirmed the functionalisation of the graphene sheets. The lanthanide oxide particles were found to be uniformly distributed throughout the graphite surface but had broadly variable sizes, mainly in the micro- and nanoscale, depending on the lanthanide oxide employed (La, Eu, Gd, Lu). According to thermogravimetric analysis, lanthanum and europium oxide catalyse the combustion of graphite. Moreover, density functional theory calculations provided insight into the interaction between graphene sheets and the lanthanide ions.

Chapter 6 illustrates the results of an optimisation of the methodology for the synthesis of graphite-lanthanide oxide nanocomposites described in Chapter 5. By changing the milling time from 8 to 48 hours and reducing the size of the milling balls from a diameter of 20 mm to 10 mm, due to the reduction of the impact energy in the milling process, the exfoliation of graphite into a few-layer graphene was achieved successfully and confirmed by Raman and X-ray diffraction studies, as well as their

partial oxidation. Moreover, a strong chemical interaction between the graphene oxygen functional groups and the lanthanide ions was observed in the XPS spectra. Furthermore, the presence of lanthanide oxide particles more homogeneously distributed and with smaller sizes in all the samples was seen employing electron microscopy studies. Lastly, the cell viability of mammal cells was investigated to examine if the presence of lanthanide ions influences the toxicity of the nanocomposites, where the tests revealed that the cytotoxicity of graphite-Ln nanocomposites does not reach 6 % of growth inhibition. except for the graphite-Tb sample, which reached a growth inhibition of 17.9 %. Therefore, the mechanochemical approach can be considered an environmentally friendly methodology to achieve the simultaneous exfoliation and functionalisation of graphite with lanthanide oxides.

Outlook

The research presented in this dissertation explores the synthesis of graphene nanocomposites functionalised with lanthanide-species nanoparticles employing more environmentally friendly methodologies. Moreover, it provides an approach to understanding how interactions between graphene-based materials and cell membranes change because of the presence of lanthanide ions, and the role of the particle size, shape, and distribution in the graphene phase. The results obtained give rise to new questions.

Solvothermal synthesis proved to be an effective method to fabricate graphene oxide-lanthanide-oxide/hydroxide nanocomposites, however, the experimental conditions can be optimised to achieve better control over the distribution, size and shape of the lanthanide-containing nanoparticles. Such changes will allow a more important bactericidal effect. Besides that, further studies to elucidate the antibacterial mechanism are necessary. Also, testing antifungal activity could be a promising line of research.

Mechanochemical milling is a robust approach to the fabrication of graphite-lanthanide oxide nanocomposites, where composites with different features like particle distribution and size can be obtained by manipulating the size of milling balls and reaction times. A broader study exploring their performance in removing dyes from aqueous environments is interesting for future research. Moreover, additional experiments to unveil the causes of the toxicity or biocompatibility with mammal cells that these nanocomposites possess are required.

Samenvatting

Het onderzoek naar nieuwe grafeen-nanomaterialen voor innovatieve toepassingen en technologieën is de afgelopen jaren exponentieel toegenomen. Het afstemmen van de eigenschappen van dergelijke nanomaterialen om ze efficiënter te maken voor een specifieke maatschappelijke behoefte is een uitdaging. Een andere uitdaging is het opschalen van de productie, waarbij de nadruk wordt gelegd op duurzame en milieuvriendelijke synthesemethoden. Tegenwoordig worden op grafeen gebaseerde nanocomposieten toegepast in een breed scala va gebieden, zoals katalyse, supercondensatoren, zonnecellen, milieusanering en biomedische sensoren. Ze worden gesynthetiseerd met behulp van chemische methoden die hun covalente en niet-covalente functionalisering mogelijk maken, maar deze methoden vereisen lange tijd, dure apparatuur en gevaarlijke reagentia. Om te evolueren naar een groenere, afvalvrije en energiezuinige economie moeten nieuwe, ecologisch aanvaardbare strategieën voor het maken en modificeren van dergelijke nanocomposieten worden ontwikkeld. In het PhD-project dat in dit proefschrijft wordt beschreven, hebben we de synthese met behulp van milieuvriendelijkere routes van op grafeen gebaseerde lanthanide-bevattende nanocomposieten onderzocht.

In **Hoofdstuck 1** worden de principes van groene chemie geïntroduceerd. Vervolgens worden de algemene eigenschappen van lanthaniden en lanthanideoxiden beschreven, evenals van de voor het project relevante koolstof materialen, namelijk grafeen, grafeenoxide en grafiet. Bovendien worden de belangrijkste syntheseroutes van op grafeen gebaseerde materialen en hun implicaties voor het milieu besproken.

Hoofdstuk 2 beschrijft kort de principes van de technieken die worden gebruikt voor de karakterisering van de grafeenoxide- en grafiet-lanthanide-bevattende nanocomposieten en van de instrumenten die in het PhD-project worden gebruikt. Deze omvatten spectroscopische karakterisering (FTIR, Raman en XPS), miscrocopische karakterisering (SEM, TEM en STEM), rontgendiffractie analyse en thermogravimetrische analyse.

Dit proefschrift is verdeeld in twee delen; de eerste helft (hoofdstukken 3 en 4) is gewijd aan grafeenoxide-lanthanideoxide/hydroxide nanocomposieten bereid met solvothermische methoden en hun eigenschappen, en het tweede deel (hoofdstukken 5 en 6) is gewijd aan de mechanochemische fabricage van grafiet-lanthanideoxide nanocomposieten.

In **Hoofdstuk 3** wordt uitgelegd hoe de synthese van grafeenoxide-

lanthanideoxide en grafeenoxide-lanthanidehydroxide nanocomposieten (La, Eu, Gd, Tb) met behulp van de solvothermische methode kan worden gerealiseerd. De twee voorgestelde experimentele methodologieën volgen een gemakkelijke, milieuvriendelijkere aanpak met reactietijden van vier uur, evenals ethanol- of waterreactiemedia bij 170 °C. Volgens de spectroscopische karakterisering verandert de chemische omgeving van GO na de integratie van lanthanide soorten, wat aantoont dat een chemische interactie tussen de zuurstof groepen van GO en de lanthanide-ionen wordt bereikt. De röntgendiffractie- en elektronenmicroscopie studies habben aangetoond dat de lanthanideoxide- en lanthanidehydroxide deeltjes die hierdoor worden waargenomen, verschillende afmetingen en verdelingen lijken te hebben, afhankelijk van de gebruikte methodologie en het gebruikte lanthanide. De thermogravimetrische analyse toonde aan dat de thermische stabiliteit afnam na de solvothermische functionaliteit.

Hoofdstuk 4 beschrijft hoe de antimicrobiële eigenschappen van grafeenoxide-lanthanideoxide/hydroxide nanocomposieten, bereid zoals beschreven in Hoofdstuk 3, werden onderzocht. Vanwege de verschillen in de grootte en verdeling van elke soort lanthanide deeltjes op GO, bleek het bateriedodende effect tegen *Escherichia coli* (Gram⁻) en *Corynebacterium glutamicum* (Gram⁺) verschillend te zijn voor alle verschillende nanocomposieten. GO-La_2O_3 presenteerde bolvormige nanodeeltjes en de meest uniforme verdeling van lanthanide deeltjes en daarom ook de sterkste antimicrobiële activiteit van alle nanocomposieten. De verschillende samenstelling tussen de twee soorten bacteriemembranen leek geen belangrijke rol te spelen in de uitgevoerde tests, maar lanthanide-ionen verankerd aan het GO-oppervlak bevorderden het bacteriedodende effect. Daarentegen vertoonden de GO-lanthanidehydroxide-nanocomposieten geen bewijs van antimicrobiële activiteit.

In **Hoofdstuk 5** beschrijven we onze eerste verzoek voor de fabricage van grafiet-lanthanide-oxide nanocomposieten gebruikmakend van de hoogenergetische kogelmolden techniek. De acht uur mechanochemische behandeling van grafiet leidde tot een opmerkelijke verkleining van de kristalliet grootte en tevens tot een toename van het zuurstofgehalte, wat de functionaliteit van de grafeen vllen bevestigde. De lanthanideoxide deeltjes bleken uniform verdeeld over het grafiet opprvlak, maar hadden een breed variabele grootte, voornamelijk op micro- en nanoschaal, afhankelijk van het gebruikte lanthanideoxide (La, Eu, Gd, Lu). Volgens thermogravimetrie en de thermogravimetrische analyse katalyseren lanthaan en europiumoxide de verbranding van grafiet. Bovendien werden DFT berekeningen uitgevoerd om inzicht te verschaffen in de interactie tussen grafeen vellen en de lanthanide-ionen.

Hoofdstuk 6 illustreert de resultaten van een optimalisatie van de methodologie voor de synthese van grafiet-lanthanide-oxide nanocomposieten zoals beschreven in Hoofdstuk 5. Door de maaltijd te veranderen van 8 naar 48 uur en de grootte van de maalkogels te verkleinen van een diameter van 20 mm naar 10 mm, dankzij de vermindering van de impactenergie tijdens het maalproces, wordt de exfoliatie van grafiet tot een paar lagen grafeen met succes bereikt en bevestigd door Raman- en röntgendiffractie studies, evenals hun gedeeltelijke oxidatie. Bovendien werd in de XPS-spectra een sterke chemische interactie waargenomen tussen de functionele zuurstof groepen van grafeen en de lanthanide-ionen. Alle monsters toonden de aanwezigheid van lanthanideoxide deeltjes die homogener verdeeld waren en kleinere afmetingen hadden met behulp van elektronenmicroscopie studies. Ten slotte hebben wij de cel levensvatbaarheid van zoogdiercellen gemeten om te onderzoeken of de aanwezigheid van lanthanide-ionen de toxiciteit van de gesynthesiseerde nanocomposieten verhoogt. Uit de tests bleek dat de cytotoxiciteit van grafiet-Ln-nanocompositen niet 6 % van de groeiremming bereikt, behalve het grafiet-Tb-monster, dat een groeiremming van 17.9 % bereikte. Daarom kan de mechanochemische benadering worden beschouwd als een milieuvriendelijke methologie om de gelijktijdige exfoliatie en functionaliteit van grafiet met lanthanideoxiden te bereiken.

Vooruitzichten

Het onderzoek dat in dit proefshift wordt gepresenteerd, onderzoekt de synthese van grafeen-nanocomposieten gefunctionaliseerd met nanodeeltjes van de lanthanide soort, waarbij gebruik wordt gemaakt van milieuvriendelijkere methologieën en waarbij groene chemie als de belangrijkste rode draad wordt gezien. Bovendien biedt het een benadering om te begrijpen hoe interacties tussen op grafeen gebaseerde materialen en celmembranen veranderen vanwege de aanwezigheid van lanthanide-ionen, en de rol van de deeltjesgrootte, vorm en distributie in the grafeen fase. Deze resultaten roepen nieuwe vragen op.

Solvothermische synthese bleek een effectieve methode om grafeenoxide-lanthanide-oxide/hydroxide nanocomposieten te vervaardigen, maar de experimentele omstandigheden kunnen worden geoptimaliseerd om een betere controle te krijgen over de verdeling grootte en vorm van de lanthanide-bevattende nanodeeltjes. Dergelijke veranderingen zullen een belangrijker bateriedodend effect mogelijk maken. Daarnaast zijn verdere studies nodig om het antibacteriële mechanisme op te helderen. Ook zouden meer experimenten om de antischimmel activiteit te testen een veelbelovende

onderzoekslijn kunnen zijn.

Mehcanochemische syntheses is een robuuste benadering voor de fabricage van grafiet-lanthanide-oxide nanocomposieten, waarbij composieten met verschillende kenmerken, zoals deeltjesverdeling en grootte, kunnen worden verkregen door de grootte van maalkogels van kleurstoffen uit waterige omgevingen is interessant voor toekomstig onderzoek. Bovendien zijn aanvullende experimenten nodig om de oorzaken van de toxiciteit of biocompatibiliteit met zoogdiercellen die deze nanocomposieten bezitten te onthullen.

Resumen

La investigación en busca de nuevos nanomateriales de grafeno para aplicaciones y tecnologías innovadoras ha aumentado exponencialmente durante los últimos años. Modificar las propiedades de dichos nanomateriales y mejorar su eficiencia para una necesidad social específica es un desafío y otro desafío es aumentar la producción al mismo tiempo que centrarse en métodos de fabricación sustentables y más respetuosos con el medio ambiente. Hoy en día, los nanocompósitos basados en grafeno se aplican en una amplia gama de campos como la catálisis, supercapacitadores, celdas solares, remediación ambiental y la biomedicina. Su síntesis se realiza utilizando métodos químicos que permiten su funcionalización covalente y no covalente, pero requieren tiempos largos de reacción, equipos costosos y reactivos peligrosos. Para avanzar hacia una economía más ecológica, libre de residuos y ahorradora de energía, es necesario desarrollar estrategias novedosas y más ecológicamente aceptables para fabricar y modificar dichos nanocompósitos. En el proyecto de doctorado descrito en esta tesis, exploramos la síntesis de nanocompósitos con base de grafeno que contienen lantánidos utilizando rutas más amigables con el medio ambiente.

En el **Capítulo 1** se introducen los principios de la química verde. Después se describen las propiedades generales de los lantánidos y los óxidos de lantánidos, así como de los materiales de carbono relevantes para el proyecto, grafeno, óxido de grafeno y grafito. Además, se discuten las principales rutas de síntesis de materiales con base de grafeno y sus implicaciones para el medio ambiente.

El **Capítulo 2** describe brevemente los principios de las técnicas empleadas para la caracterización de los nanocompósitos de óxido de grafeno y grafito con lantánidos, además de los instrumentos utilizados en el proyecto de doctorado. Estos incluyen la caracterización espectroscópica (FTIR, Raman y XPS), caracterización microscópica (SEM, TEM y STEM), análisis de difracción de rayos X y análisis termogravimétrico.

Esta tesis está dividida en dos partes; la primera mitad (Capítulos 3 y 4) está dedicada a los nanocompósitos óxido de grafeno con óxidos/hidróxidos de lantánido preparados mediante métodos solvotermales y sus propiedades, y la segunda parte (Capítulos 5 y 6) está dedicada a la fabricación mecanoquímica de nanocompósitos de grafito-óxido de lantánido.

En el **Capítulo 3** se explora la síntesis de nanocompósitos de óxido de grafeno-óxido de lantánido y óxido de grafeno-hidróxido de lantánido (La, Eu, Gd, Tb) empleando el método solvotermal. Las dos metodologías experimentales propuestas representan

un enfoque sencillo y amigable con el medio ambiente que emplea tiempos de reacción de cuatro horas, así como etanol y agua como medios de reacción a 170 °C. Según la caracterización espectroscópica, el ambiente químico del GO cambia después de la incorporación de especies de lantánidos, lo que demuestra que se logra una interacción química entre los grupos oxigenados del GO y los iones lantánidos. Los estudios de difracción de rayos X y microscopía electrónica evidenciaron que las partículas de óxido de lantánido e hidróxido de lantánido observadas parecen tener diferentes tamaños y distribuciones, dependiendo de la metodología y del lantánido utilizado. El análisis termogravimétrico mostró que la estabilidad térmica disminuyó después de la funcionalización solvotermal.

El **Capítulo 4** detalla la exploración de las propiedades antimicrobianas de los nanocompósitos de óxido de grafeno-óxido/hidróxido de lantánido preparados como se describe en el Capítulo 3. Debido a las diferencias en el tamaño y la distribución de las partículas de especies de lantánidos en el GO, se encontró que el efecto bactericida contra *Escherichia coli* (Gram[-]) y *Corynebacterium glutamicum* (Gram[+]) era diferente para los diferentes nanocompósitos. GO-La$_2$O$_3$ presentó nanopartículas esféricas, así como una distribución de partículas de lantánido más uniforme y, por lo tanto, la actividad antimicrobiana más fuerte entre todos los nanocompósitos. La diferente composición entre los dos tipos de membranas bacterianas no pareció jugar un papel importante en las pruebas realizadas, pero los iones de lantánidos anclados a la superficie GO fomentaron el efecto bactericida. Por el contrario, los nanocompósitos de hidróxido de lantánido GO no mostraron evidencia de actividad antimicrobiana.

En el **Capítulo 5** describimos el primer acercamiento para la fabricación de nanocompósitos de grafito-óxido de lantánido empleando la técnica de molienda de bolas de alta energía. Las ocho horas de tratamiento mecanoquímico del grafito condujeron a una notable reducción del tamaño de los cristalitos, así como un aumento en el contenido de oxígeno, lo que confirmó la funcionalización de las láminas de grafeno. Se encontró que las partículas de óxido de lantánido estaban distribuidas uniformemente por toda la superficie del grafito, pero tenían tamaños muy variables, principalmente en la micro y nanoescala, dependiendo del óxido de lantánido empleado (La, Eu, Gd, Lu). Según el análisis termogravimétrico, el óxido de lantano y el óxido de europio catalizan la combustión del grafito. Además, los cálculos de la teoría del funcional de la densidad proporcionaron información sobre la interacción entre las láminas de grafeno y los iones de lantánidos.

El **Capítulo 6** ilustra los resultados de la optimización de la metodología para la síntesis de nanocompósitos de grafito-óxido de lantánido descrita en el Capítulo 5.

Cambiando el tiempo de molienda de 8 a 48 horas y reduciendo el tamaño de las bolas de molienda de 20 mm a 10 mm de diámetro, debido a la reducción de la energía de impacto durante el proceso de molienda, se logró con éxito la exfoliación del grafito en grafeno de pocas capas y se confirmó mediante estudios Raman y de difracción de rayos X, así como su oxidación parcial. Además, en los espectros XPS se observó una fuerte interacción química entre los grupos funcionales oxigenados del grafeno y los iones lantánidos. Además, mediante estudios de microscopía electrónica se observó la presencia de partículas de óxido de lantánido distribuidas de forma más homogénea y de menor tamaño en todas las muestras. Por último, se investigó la viabilidad celular de células de mamíferos para examinar si la presencia de iones lantánidos influye en la toxicidad de los nanocompósitos, las pruebas revelaron que la citotoxicidad de los nanocompósitos de grafito-Ln no alcanza el 6 % de inhibición del crecimiento. a excepción de la muestra de grafito-Tb, que alcanzó una inhibición del crecimiento del 17,9 %. Por tanto, el enfoque mecanoquímico puede considerarse una metodología amigable con el medio ambiente para lograr la exfoliación y funcionalización simultánea del grafito con óxidos de lantánidos.

Perspectivas

La investigación presentada en esta tesis explora la síntesis de nanocompósitos de grafeno funcionalizados con nanopartículas de especies de lantánidos empleando metodologías más amigables con el medio ambiente. Además, proporciona un enfoque para comprender cómo cambian las interacciones entre los materiales a base de grafeno y las membranas celulares debido a la presencia de iones lantánidos y el papel del tamaño, la forma y la distribución de dichas partículas en el grafeno. Los resultados obtenidos dan lugar a nuevas preguntas.

La síntesis solvotermal demostró ser un método eficaz para fabricar nanocompósitos de óxido de grafeno-óxido/hidróxido de lantánido; sin embargo, las condiciones experimentales se pueden optimizar para lograr un mejor control sobre la distribución, el tamaño y la forma de las nanopartículas de lantánidos. Tales cambios permitirán un efecto bactericida más importante. Además de eso, son necesarios más estudios para dilucidar el mecanismo antibacteriano. Igualmente, probar la actividad antifúngica podría ser una línea de investigación prometedora.

La molienda mecanoquímica es un enfoque sólido para la fabricación de nanocompuestos de óxido de grafito-lantánido, donde se pueden obtener compósitos

con diferentes características tales como distribución y tamaño de partículas manipulando el tamaño de las bolas de molienda y los tiempos de reacción. Un estudio más amplio que explore su desempeño en la eliminación de tintes de ambientes acuosos es interesante para futuras investigaciones. Además, se requieren experimentos adicionales para desvelar las causas de la toxicidad o biocompatibilidad con células de mamíferos que poseen estos nanocompósitos.

List of publications

Acevedo-Guzmán, D. A., Monroy-Torres, B., Rudolf, P., Basiuk, V. A. and Basiuk, E. V. Green Mechanochemocal Fabrication of Graphite-Lanthanide Oxide Nanocomposites. Draft manuscript.

Acevedo-Guzmán, D. A., Huerta, L., Bizarro, M., Meza-Laguna, V., Rudolf, P., Basiuk, V. A., & Basiuk, E. V. (2023). Solvothermal synthesis of lanthanide-functionalized graphene oxide nanocomposites. Materials Chemistry and Physics, 304, 127840.

Basiuk, V. A., **Acevedo-Guzmán, D. A.**, Meza-Laguna, V., Álvarez-Zauco, E., Huerta, L., Serrano, M., Kakazey, M., & Basiuk, E. V. (2021). High-energy ball-milling preparation and characterization of Ln2O3–graphite nanocomposites. Materials Today Communications, 26, 102030.

Conferences

2023, ZIAM PhD Symposium, University of Groningen, The Netherlands.

2023, LatinXChem 2023, Virtual Conference

2023, IUPAC/Chains 2023, The Netherlands

2022, NWO Chains 2022, The Netherlands

2022, ZIAM PhD Symposium, University of Groningen, The Netherlands.

2022, Vlieland 2022, The Netherlands

2022, Spring Meeting E-MRS, Virtual Conference

The author

Born in Mexico City, Mexico in June 1994, **Diego Armando Acevedo Guzmán** earned a bachelor´s degree in Chemistry at the Faculty of Chemistry, National Autonomous University of Mexico in 2017. In 2019, he completed his Master's in Chemical Sciences at the National Autonomous University of Mexico. His project aimed to develop, study, and functionalise carbon nanomaterials using more environmentally friendly routes and was performed at the Institute of Applied Sciences and Technology under the supervision of Dr. Elena Golovataya Dzhymbeeva. Then, he started a sandwich PhD programme between the National Autonomous University of Mexico and the Zernike Institute for Advanced Materials of the University of Groningen (The Netherlands) under the supervision of Dr. Elena Golovataya Dzhymbeeva and Dr. Petra Rudolf.